OPTIMISING THE MECHANICAL PROPERTIES AND MICROSTRUCTURE OF ARMOURED STEEL PLATE IN THE QUENCHED AND TEMPERED CONDITION

by

MAWEJA KASONDE

Submitted in partial fulfilment of the requirements for the degree

MASTER OF ENGINEERING

(Metallurgical Engineering)

in the Department of Materials Science and Metallurgical Engineering,
Faculty of Engineering, Built Environment and Information Technology,
University of Pretoria

December 2005

To my lovely wife Aimée,
Our daughters and son Gentille, Candide and Artig
And Nelie

ACKNOWLEDGEMENTS

The thesis we are honoured to write today is the blossom of various contribution and influence from divers people and institutions. We are greatly indebted to Many for the learning and training received, idea and discussion shared, question and answer exchanged, hypothesis and verification implemented, financial and spiritual support.

We wish to thank to the Department of Materials Science and Metallurgical Engineering of the University of Pretoria for organising useful advanced courses at postgraduate level and for the logistic and financial supports offered during our studies.

We are grateful to Professor Waldo STUMPF for the illuminating supervision of this work and for his suggestion of the characterisation of the martensite in armour steels using the atomic force microscopy (AFM) and the sake of the direct relationship between microstructure and ballistic performance. This approach methodology has contributed for many in the contraction of project duration and the quality of the results.

″ To measure is to know ″ . More than 350 hours of course, training, work, measurement, analysis and discussion were necessary with the help of the personnel of the Industrial Metals and Minerals Research Institute (IMMRI). We are thankful towards François VERDOORN for the training in dilatometry analysis, his particular intervention during the execution of the project by providing the technical notes and specifications for ballistic materials, the raw materials and samples of armour plates (local and imported), for the organisation of the ballistic testing at Vanderbijlpark and for the discussion during the stressing ballistic testing. Carel COETZEE and Alison TULING for the training, analysis and valuable discussions of the electron microscopy results, which constitute an important part of the proof of the hypothesis advanced in this study.

The presentation and discussion of the mechanical properties as done in this project was inspired by many consideration suggested by Professor Gerrit van ROOYEN. The proposition of the Ballistic Parameter is one example of ideas that were elaborated after discussing with him.

Amount of analysis, measurements and calculus presented in this work were realised with the help of Doctors Sabine VERRYN of the Department of Geology and Nic vander BERG of the Department of Physics.

Thanks also extend to Willem BRITZ and Ian FERREIRA for organising and realising the ballistic testing at the Vanderbijlpark tunnel and for their encouragement during the distressing test. I needed that.

To Daudet TSHIKELE, W. LEE, A. SHIKONGO, Vinod C and J. MUKADI for friendship

OPTIMISING THE MECHANICAL PROPERTIES AND MICROSTRUCTURE OF ARMOURED STEEL PLATE IN THE QUENCHED AND TEMPERED CONDITION

MAWEJA KASONDE

Supervisor: **Professor Waldo STUMPF**

Department of Materials Science and Metallurgical Engineering
Master of Engineering (Metallurgical Engineering)

ABSTRACT

The effect of the chemical composition, austenitisation temperature and tempering temperature and time on the mechanical properties and on the ballistic performance of martensitic steel armour plates was studied.
It was established in this study that the mechanical properties and the ballistic performance of martensitic steels can be optimised by controlling the chemical composition and the heat treatment parameters. However, it was observed that for a given chemical composition of the steel the heat treatment parameters to be applied to advanced ballistic performance armour plates were different from those required for higher mechanical properties. Such a contradiction rendered the relationship between mechanical properties and ballistic performance questionable. Systematic analysis of the microstructure and the fracture mechanism of some martensitic armour plate steels was carried out to explain the improved ballistic performance of steels whose mechanical properties were below that specificied for military and security applications. It was inferred from phase analysis and its quantification by X-ray diffraction, characterisation of the martensite using scanning electron microscopy, transmission electron microscopy and atomic force microscopy that the retained austenite located in the plate interfaces and on grain boundaries of the martensite was the main constituent resisting localised yielding during ballistic impact on thin steel plates.

A part of the kinetic energy is transformed into adiabatic heat where a reaustenitisation of the plate martensite and the formation of new lath martensite was observed. Another part is used to elastically and plastically deform the ballistic impact affected region around the incidence point. Dislocation pile-ups at twinned plate interfaces suggest that the twin interfaces act as barriers to dislocation movement upon high velocity impact loading. The diameter of the affected regions, that determines the volume of the material deforming plastically upon impact, was found to vary as a function of the volume fraction of retained austenite in the martensitic steel. Upon impact, retained austenite transforms to martensite by Transformation Induced Plasticity, the " TRIP " effect. High volume fractions of retained austenite in the martensitic steel were found to yield low values of the ratio yield strength to ultimate tensile strength (YS/UTS) and a high resistance against localised yielding and, therefore, against ballistic perforation.

A Ballistic Parameter was proposed for the prediction of ballistic performance using the volume fraction of retained austenite and the thickness of the armour plate as variables.

Based on the martensite structure and the results of the ballistic testing of 13 armour plate steels a design methodology comprising new specifications was proposed for the manufacture of armour plates whose thicknesses may be thinner than 6mm.

KEYWORDS: Martensite, retained austenite, ratio yield strength to ultimate tensile strength (YS/UTS), ballistic performance, ballistic parameter, reaustenitisation, martensite start temperature.

CHAPTER 1. INTRODUCTION ... 1
1.1. Industrial objective ... 1
1.2. Project aim and methodology ... 2

CHAPTER 2. LITERATURE REVIEW ... 3
2.1 Industrial background ... 3
2.2 Scientific background ... 5
2.2.1. Ballistic material ... 5
2.2.2 Stress waves in solids ... 8
2.2.3. Material behaviour at high strain rates ... 11
2.2.4. Ballistic performance ... 12
2.2.5. Fracture prediction under high-velocity localised impact ... 14
2.2.6. Shock induced transitions and transformations ... 15
2.2.7 Role of material properties ... 16
2.2.8. Prediction of the martensite start temperature M_s and the Driving Force $\Delta G^{\gamma \to M}$ for the martensitic transformation ... 17
2.2.9. Kinetics of the martensitic transformation ... 23
2.2.10. Crystallography and morphology of martensite, general considerations and definition of martensite ... 24
2.3. Tempered martensite and its mechanical properties ... 35
2.3.1 Effect of Carbon additions ... 35
2.3.2 Effect of Sulphur and Manganese content ... 36
2.3.3. Effect of alloying elements ... 38
2.3.4. Ageing of Iron – Carbon martensite at room temperature ... 39
2.3.5. Low temperature tempering of Martensite ... 39
2.4. Mechanical properties of tempered martensitic steels ... 42
2.5. The variations of microstructure with tempering temperature and hold time ... 44
2.6. Diffraction patterns of iron carbides ... 47
2.7. Tensile properties ... 54
2.8. Multiple regression as sequential simple regression ... 54

CHAPTER 3. EXPERIMENTAL TECHNIQUES ... 56
3.1. Hypothesis ... 56
3.1.1. How to improve the Hardenability and the Hardness ... 56
3.1.2. How to improve the Toughness of the martensite ... 56
3.1.3. How to improve the resistance to Shock and to Spalling ... 56
3.1.4. How to improve the Tensile Strength ... 56
3.2. Alloy design ... 57
3.3. The Heat treatment design ... 58
3.4. Experimental Variables ... 59
3.5. Plate manufacturing ... 62
3.6. Mechanical testing ... 62
3.6.1. Hardness measurement ... 63
3.6.2. The tensile strength and elongation ... 65
3.6.3. The Charpy V-notch impact energy ... 66
3.6.4. Fracture analysis ... 67
3.6.5. Microstructure analysis ... 67
3.6.6. Transformation surface relief ... 69
3.7. Martensite start temperatures ... 70
3.8. Ballistic testing ... 70

3.7. Martensite start temperatures 70
3.8. Ballistic testing 70
3.8.1. Specifications for the test 70
3.8.2. Analysis after ballistic testing 70

CHAPTER 4. RESULTS AND DISCUSSION ... 72

4.1. Preliminary results on the steels A and B currently in production in South Africa as well as two imported steels C and D ... 72
  4.1.1. Objective ... 72
  4.1.2. Methodology ... 72
  4.1.3. Results ... 72
Table (4.1.1). Transformation temperatures measured by dilatometric analysis ... 73

4.2. Proposed design for an advanced RB600 armour plate ... 87
4.3 Optimisation of the mechanical properties ... 88
  4.3.1. The optimisation problem ... 88
  4.3.2 The chemical composition ... 89
  4.3.3. The heat treatment cycle ... 89
  4.3.4. Variation of the mechanical properties ... 90
  4.3.4.1 Mechanical properties of Steel E ... 91
  4.3.6. Fracture analysis after the Charpy impact and the tensile tests ... 116
  4.3.7. Martensite start temperatures of the armour steels ... 125

4.4 Results of the ballistic testing (First series) ... 132
  4.4.1. Ballistic report ... 132
  4.4.2. Comparison with the ballistic performance specifications ... 135
  4.4.3. Differences in the microstructures between steels E, F, G, H and I ... 136
  4.4.4. Differences in microstructure between steels E, F, G, H in the tempered condition before ballistic testing ... 141

CHAPTER 5. IMPROVEMENT IN THE BALLISTIC PERFORMANCE 146

5.1 Approach methodology 146
5.2. Ballistic report 147
5.3 The Ballistic Parameters 149

5.3. The fracture mechanism due to the high strain rate during ballistic testing of plates of steels P through to W 157

5.4. Morphology of the martensite and microstructures of the steels P through to W that were tested ballistically 159

5.5. General observation 169

CHAPTER 6. CHARACTERISATION OF THE MARTENSITIC TRANSFORMATION IN ARMOUR STEELS 171

6.1. Background 171
6.1.1 Theories of the martensitic transformation 171
6.1.2. Tetragonality of martensite 172
6.1.3. Techniques used in characterising the martensitic transformation 173

6.2. Characterisation methodology 173
6.3. Characteristics of the martensite formation in the armour steels 173
6.3.1. Crystallographic characteristics 173
6.3.2. Quantitative analysis of the surface relief by means of Atom Force Microscopy 180

CHAPTER 7. REQUIREMENTS FOR ADVANCED PERFORMANCE ARMOUR STEELS 194

CHAPTER 8. CONCLUSION 201

REFERENCES 202

CHAPTER 1. INTRODUCTION

1.1. Industrial objective

The main objective in developing the new armoured steel plate to supersede the currently used steel A and steel B plates, is the manufacture of lighter armoured vehicles by decreasing the required thickness of the steel plates. The new plate should be able to withstand a 5.56 mm R4 round whereas the steel A and steel B plates manufactured currently, need a 8.5 to 20 mm thickness or higher for this ballistic requirement. According to ISCOR [1], the properties listed in Table 1.1 would need to be achieved to meet this objective.

Table 1.1 Specifications for the new armoured steel plate [1]

Property	Specification
Brinell hardness	570-640 BHN
Charpy V-notch transverse impact energy on full size specimens [2]	12 Joules (minimum) at -40 ^0C
Yield strength R_p at 0.2%	1500 MPa (minimum)
Ultimate tensile strength	2000 MPa (minimum)
Elongation of a 50 mm gauge length	7% (minimum)

The process parameters for the new armoured steel plate should be as close as possible to the existing ones for the current steels A and B produced by Mittal Steel South Africa. The processing parameters during hot rolling are more or less fixed, although the post-rolling heat treatment temperatures and times can be slightly adjusted. After preliminary austenitisation of the current steel B, followed by water quenching and a low-temperature tempering, it appears that the harder new armour plate will almost certainly require a change in composition for its higher hardness requirement (Carbon content) and hardenability (Carbon and alloying elements), as well as for its toughness requirement.

To move from the current steel B to the new armour plate, will require an improvement of ballistic properties through optimising the plate's resistance to *impact* or *shock* loading and its resistance to *spalling* as well as meeting the resistance against *localised yielding* and *ballistic perforation*. Minimum *hardness* and *strength* requirements of the alloy should also be realised. The design of the steel alloy and its heat treatment should allow an efficient way for the development and manufacture of the armoured steel plate (steel making, rolling and heat treatment parameters). The assessment of the ballistic performance will be provided after ballistic testing according to the military and civil specifications for South Africa as determined by ARMSCOR. These standardised specifications for ballistic tests in South Africa are presented in Table 1.2. Each test consists of at least five firings of rounds under the prescribed conditions.

Table 1.2: Specification for the assessment of armour plate materials in South Africa [1]

Obliquity	0^0
Muzzle velocity	930 m/s (minimum)
Distance	30 m maximum
Assessment	1. No light path going through the thickness of the plate in the impact region (i.e. no visible through-penetration) 2. No spalling at the rear face of the plate after ballistic testing

1.2. Project aim and methodology

The research project was undertaken with the aim of developing an improved understanding of the relationship between ballistic properties of martensitic armour plate steels and their structures and mechanical properties. By this means design criteria have been proposed that meet the industrial objective outlined in Section 1.1. In the course of the project, benchmarking was carried out using the scientific and industrial background on armour steels currently produced or used in South Africa and throughout the world. Microstructural investigations were used to explain the high or the low ballistic performance of these steels before designing the candidates for the advanced performance RB600. Mechanical testing, fracture analysis, measurement of martensite start temperatures by dilatometry, phase analysis by X-ray diffraction, characterisation of the martensite and surface relief analysis and ballistic tests were conducted to explain the differences in performances and to optimise the ballistic as well as the mechanical properties of the new martensitic armour steels through the control of the chemical composition and the heat treatment parameters.

CHAPTER 2. LITERATURE REVIEW

2.1 Industrial background

Mittal Steel South Africa already manufactures both the steels A and B at its Vanderbijlpark plant that require armour resistance. These steels are used typically in combat vehicles, security vehicles, bulletproof jackets and security doors. The specifications for the chemical compositions of the current armour steels A and B are listed in Table (2.1). From this table, it appears that the compositions for the two products differ mainly in their Nickel and Chromium contents. The ratio of their Nickel to Chromium content are respectively 2 and 0.7 for the respective steels A and B. Steels A and B are fully killed fine-grained steels, which are also calcium treated and vacuum degassed to achieve low sulphur levels and inclusion content. These armour plate steels are quenched and tempered to achieve an ultra high strength with a fine microstructure.

Table (2.1). Specifications for the chemical compositions of the currently produced armour steels A and B

	%C	%Mn	%P	%S	%Si	%Cu	%Ni	%Cr	%Mo
Steel A: specification	0.29-0.31	0.80-0.90	0.0-0.01	0.0-0.003	0.15-0.25	0.0-0.03	2.8-3.0	0.8-1.0	0.45-0.55
Steel A: actual composition	0.317	0.855	0.008	0.002	0.176	0.026	2.8	0.79	0.45
Steel B: specification	0.30-0.32	0.55-0.65	0.0-0.015	0.0-0.005	0.30-0.45	0.0-0.03	1.4-1.5	1.5-1.6	0.55-0.60
Steel B: actual composition	0.253	0.606	0.007	0.002	0.327	0.012	1.41	1.54	0.58

2.1.1. The heat treatment cycle of steel A.

The Brinell hardness range for steel A is:

Table (2.2). Brinell hardness range of steel A armour plate [1]

Thickness [mm]	Brinell hardness
3.5 to 8	460 to 540 BHN
10 to 25	380 to 440 BHN

The typical heat treatment cycle of steel A consists of [1]:

Table (2.3): Typical heat treatment of steel A

Plate Thickness [mm]	Austenitisation temperature [^{0}C]	Austenitisation time [minutes]	Tempering temperature [^{0}C]	Tempering time [minutes]
6	900	20	280	38
8	870	24	400	46

The 3.5 to 4.5mm steel A plates are heated and then quenched in a water-cooled press. Plates from 6 mm to 25 mm thick are heat-treated in a roller quenching plant that subjects the entire plate to a rapid high volume water quench after solution treatment.

The high cooling rate ensures maximum use of the alloying elements to give the required properties throughout the plate thickness [3]. After quenching, plates are tempered in a tempering furnace where the temperature is selected so that the desired degree of hardness for the specific plate thickness is obtained. The 3.5 to 4.5mm steel A plates are not tempered after quenching but are used in the as-quenched condition[1].

2.1.2. The heat treatment cycle of the steel B

The thermomechanical treatment for steel B consists of:

1. Hot rolling in the austenite region (above A_{c3}) to the final thickness;
2. Stack the plates on top of each other for a slow cool to remove possible Hydrogen cracking;
3. Send the cold plates to the Roller Quenching plant;
4. Solution treatment at 910°C;
5. Water quenching in the Roller Quenching plant (for the 3.5 to 4.5 mm plates); and
6. Low temperature tempering.

The steel B Brinell hardness' range is given in Table (2.4).

Table (2.4): Brinell hardness range of steel B Plates

Thickness [mm]	Brinell hardness
6 to 12	477-532 BHN
15 to 25	450-512 BHN

The results after ballistic testing must conform to the ARMSCOR-ARMOUR PLATE SPECIFICATION FOR RSA, specification No. SK112.

- **Storage**: all material, with exception of the 3.5 to 4.5 mm plates, are shot blasted after heat treatment to remove surface scale. The material must preferably be stored under roof to prevent corrosion.

- **Fabrication** [1] :
    1. The hardness, high strength and toughness, as well as the weldability are the main considerations for fabrication of steels A and B;
    2. Due to the high hardness of the materials, bending is not recommended. However, if any form of bending is to be done, it is advised that it be done transverse to the rolling direction and at room temperature of ± 25 °C. Cut edges should be smoothly ground before bending.
    3. Hot rolling: local or general heating must be performed before the final heat treatment, as this could have an effect on the properties of the material. The exposed face of the armour plate on the vehicle can have a higher hardness than the opposite face facing into the vehicle. The latter must have a higher strength.

4. Machining can be performed using high-speed tool steel tips and reducing the speed to 50% of speeds used for normal carbon steels.
5. Flame cutting is not recommended for plate thickness less than 15 mm. For these thicknesses plasma or laser cutting is recommended.
6. Preheating and welding: Preheating usually plays an important role in the application of armour steel plates. Accordingly, a welding specification SK108 has been developed for the correct welding procedures for steels A and B [1] . Preheating of plates is recommended to minimize the adverse effect of welding and flame cutting on the microstructure of the heat-affected-zone (HAZ) by reducing the cooling rate in the HAZ. Rapid cooling after welding and flame cutting result in a hard and brittle martensitic microstructure, which is susceptible to hydrogen cracking. The recommended maximum preheating temperature is $120\,^{0}$C [1].

Direct-quenching and tempering after hot rolling is now a viable technology in the production of high strength steel plate, and it is widely practiced, especially in Japan.

In conventional reheat-quenching and tempering, microstructures and properties are determined by the chemical composition and the tempering conditions. Direct-quenching is an alternative route to reheat-quenching as practised at the Vanderbijlpark plant of Mittal Steel (South Africa)[4].

2.2 Scientific background

2.2.1. Ballistic material

Each class of armour plate is heat treated to provide maximum resistance to ballistic perforation. The microstructure must be homogeneous throughout the section thickness and without inclusions that would act as crack initiators.

The external surface can present a higher hardness for resistance against penetration and compressive impact, whereas the internal surface could have a higher tensile strength [2]. Cast armour has always been more resistant ballistically than rolled armour due mainly to the fundamental difference in mechanical and metallurgical properties between rolled and cast steel [2]. However production of armour plate is not feasible in cast forms.

It is possible to design a casting with smoother contours and higher obliquities than a flat plate, although normally heavier than a corresponding structure fabricated from rolled plate and in many cases with equal or even improved ballistic protection. Cast homogeneous steel armour is still used on Army Combat Vehicles under MIL-S-11356 to produce such components as hulls, turrets, cupolas, hatch covers, etc.

A large amount of empirical data obtained from a variety of tests confirmed that the armour strength or hardness of the steel is a very important parameter in resisting ballistic penetration. According to this design philosophy the candidate armour material should exceed the hardness of the projectile [2]. This can be achieved primarily by thermal or thermomechanical processing.

The assessment criterion of ballistic resistance is that of “no visible light to pass through the impacted plate after the test” as illustrated by Figure 2.1 and quoted from [2].

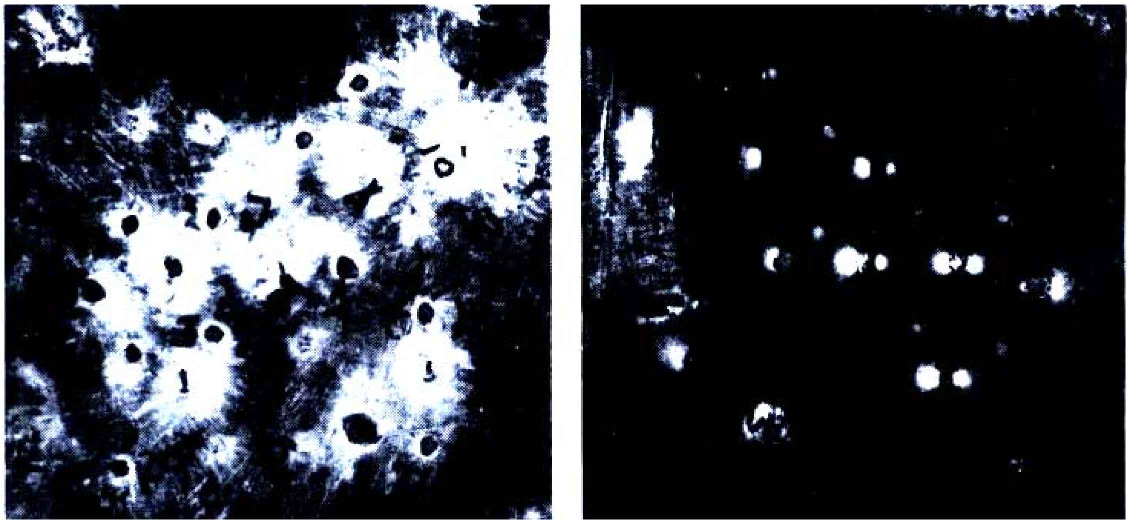

(a) FRONT (b) REAR

Figure.2.1 (a) and (b), Multiple ballistic impact capability of armour plate made from an unidirectionally solidified ingot at a hardness in excess of 55 HRC. Light spots show the difference in sizes between the openings in the front and the rear faces of the impacted plate.

The following figure shows the increase in the ballistic performance versus hardness as a function of technological developments.

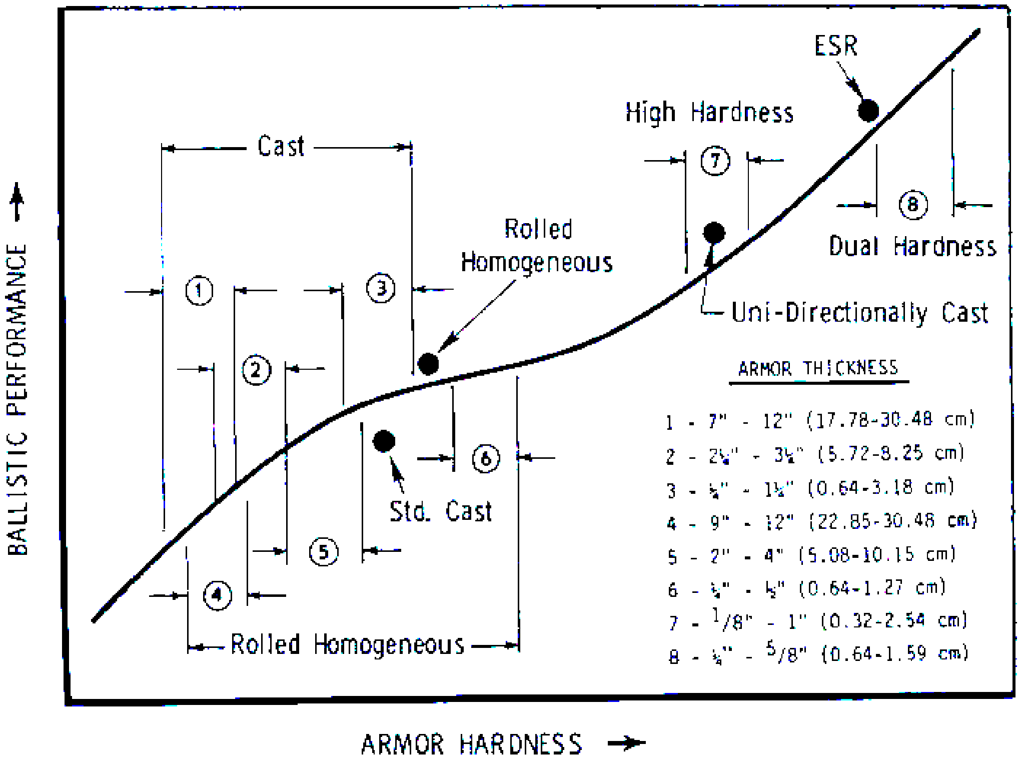

Figure.2.2. Relationship between armour hardness and ballistic performance [2]

There are several additional factors to consider in the choice of alloy for armour plate but the major consideration would be that it should be effective in the field, and it should be light, which in turn gives a variety of advantageous secondary effects.

Above all the armour plate must also be cost-effective. Other considerations are that the armour plate should be amenable to modern fabrication and construction techniques and be readily weldable and capable of being produced in a variety of shapes. Bulk is an important factor because if the armour is bulky even though its area density is low, it will be difficult to provide sufficient room under the armour to meet volume requirements for the crew, gun, ammunition, fuel and power train, etc. For many years various alloy steels have measured up to this requirement very well. Armour application for these steels is well understood and can be made with optimisation of various properties by changing the proportion and presence of the alloying elements.

Although steel is a dense material with a larger area density (i.e. mass per unit area) comparatively to other armour materials, it does offer very good levels of protection against KE (Kinetic Energy) and HESH (Highly Explosive Squash Head) attacks, but its performance against HEAT (Highly Explosive Anti Tank) attack is considerably reduced [2]. Most alloy steels contain some or all of the elements Manganese, Chrome, Nickel, Molybdenum and Vanadium to give the correct blend of high strength and resistance to fracture or toughness.

The major problem with all armour is that if the energy from the projectile is not to be transferred from the armour to the supporting structure then a way has to be found to dissipate the energy before this happens or the secondary effect may be equally fatal.

Experience indicates that homogeneous steel armour (i.e. not a layered combination made from layers of different steels) should be made as hard as possible for defeating small arms and armour piercing (AP) ammunition. However, as homogeneous steel becomes harder it also becomes more brittle and as the material becomes more brittle, its ballistic limit cannot be measured due to severe fracture of the armour. Thus, limits on homogeneous armour hardness have to be established to prevent shatter of the armour due to embrittlement, but not necessarily because of strength limitations on the ballistic limit. This important fact has formed the basic guideline for improved steel armour development programs. That is, to increase the steel armour's ballistic limits by increasing its hardness without increasing the tendency towards brittle failure. An armour hardness of at least 58 to 62 Rockwell C would be required to induce shattering of the projectile upon impact [2]. Various definitions for complete and partial penetration are illustrated in Figure 2.3.

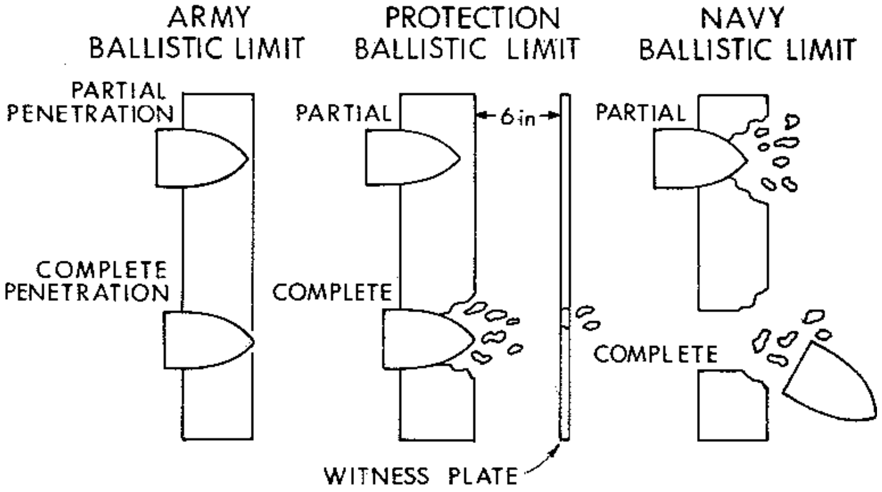

Figure 2.3. Definitions of perforation and partial penetration for defining the ballistic limit

The ballistic superiority of steels of higher metallurgical quality has been demonstrated often. The development of unidirectionally solidified wrought steel armour showed that cast steels with superior ductility could be produced by unidirectional solidification, which produces a cast structure in which columnar grains extend from the chill surface completely through the casting. The resulting solidified steel ingots have been found to be virtually free of gross porosity and with a much finer segregation pattern, factors that contribute to higher ductility [2].

The homogenisation heat treatment, which consists of holding the casting at 1316°C for 64 hours, would virtually eliminate alloy segregation. Steels of armour composition have been produced by this process and have been homogenised, rolled, and heat-treated to hardness levels ranging from 50 to 60 HRC.

The important requirement of structural tank armour is that it should maintain structural integrity at sub-zero temperatures when impacted by overmatching artillery rounds. Test plates are inspected after proof testing for their ability to withstand fracture, spalling, and cracking. The long-standing empirical materials specification, which applies to structural tank armour and its ability to maintain integrity at low temperatures, requires that the material must have a minimum of 27.12 J (20 ft-lbs) transverse Charpy V-notch impact energy at a temperature of $-40\,^{0}$C [1, 2].

2.2.2 Stress waves in solids

The response of materials and structures to intense impact loading is quite complex. For loading conditions that result in stresses below the yield point, materials behave elastically and Hooke’s law is applicable for metals. However the mathematical solutions for various loading conditions in this regime are obtained for semi-infinite bodies. Practical impact problems involve strikers and targets with finite boundaries, which exert considerable influence on their behaviour. As the intensity of the applied load is increased, the material is deformed into the plastic range. The behaviour in this range involves large deformations together with localised heating, and often failure of the colliding solids through a variety of mechanisms. With still further increases in loading intensity, pressures are generated that exceed the strength of colliding solids by several orders of magnitude which, in effect, then start behaving hydrodynamically [5]. Failure modes in impacted plates may be classified as one of the six illustrated in Figure 2.4.

For low intensity excitations, both the geometry of the entire structure as well as the nature of the material from which it is made, play a major role in resisting any external forces. As loading increases, the response tends to become highly localized and is more affected by the constitution of the material in the vicinity of the impact region than the geometry of the structure. The description of the phenomena in terms of elastic, plastic, and shock waves becomes appropriate.

When either a dilatational or distortional wave impinges on a boundary of the solid, waves of both tensile and compressive types are generated. Of particular interest in impact situations is the normal impingement of a strong compressive pulse on a free surface. The pulse is reflected from any discontinuity or a free surface as a tensile wave and if its magnitude is greater than the tensile fracture strength of the material, fractures will occur.

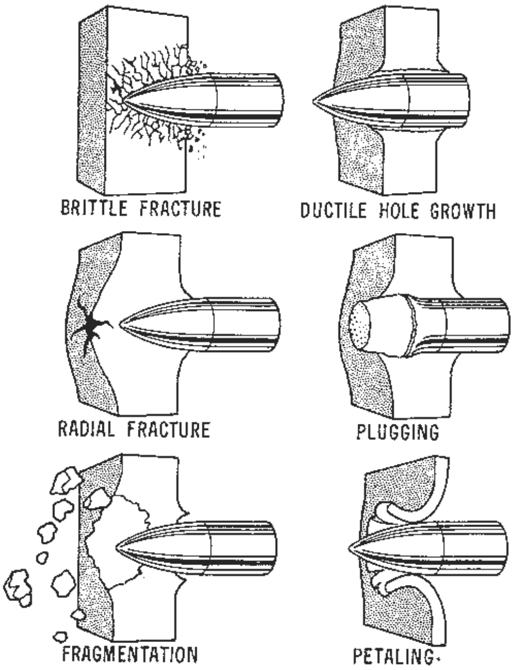

Figure 2.4. Failure modes in impacted plates [2]

Simple analyses predict reasonably well the location of the fracture plane and the size and speed of the ejected material for high strength solids. If after fracture, the magnitude of the stress pulse still exceeds the material's tensile strength, multiple fractures can occur [5]. The reflection of the input compressive pulse and the subsequent formation of a tensile wave are illustrated in Figure 2.5. The evolution of the phenomenon is depicted as different time function of the compressive wavelength λ and the celerity of the light C.

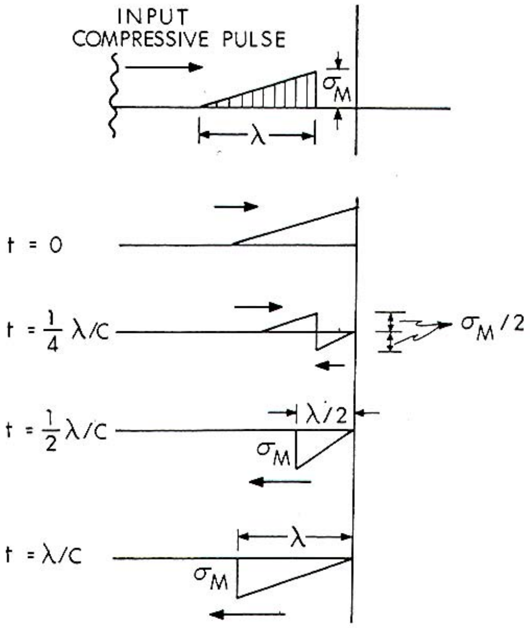

Figure 2.5: Illustration of the propagation and reflection at a free surface of the shock-induced compressive wave and its subsequent conversion into a tensile wave [2]

A high dynamic tensile strength is then required to avoid multiple fractures and spallation during ballistic testing. This observation will be compared later to the experimental results of the ballistic performances in this study on 13 armoured steels. As the intensity of the applied load increases, the material is driven beyond its elastic limit and becomes plastic. Two waves now propagate in the solid, an elastic wave (or precursor) followed by a much slower but more intense plastic wave. The principle is illustrated considering an elastic-linear hardening behaviour for a material whose Young's modulus is E, the yield strength is σ_y and the specific mass is ρ. The elastic wave front propagates at the speed $C_0 = \frac{\sqrt{E}}{\rho}$ whereas the slow plastic wave follows at a velocity $C_1 = \frac{\sqrt{E_1}}{\rho}$ where the two values of E differ because of elastic linear hardening. Figure 2.6 illustrates the delay of the plastic wave front on the elastic wave in the space-stress reference. The same principle may be illustrated in velocity-strain space as in Figure 2.7.

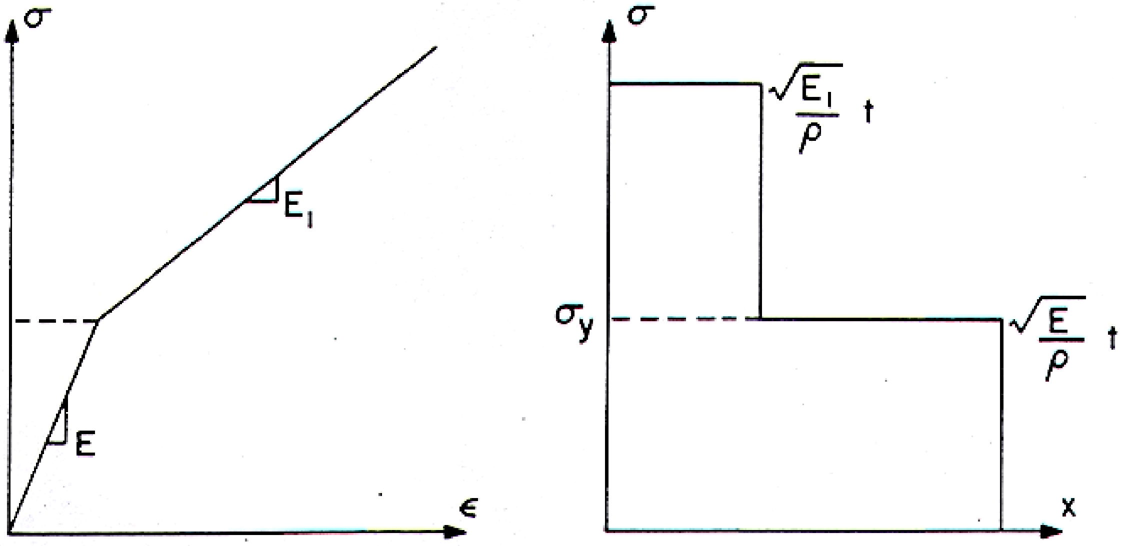

Figure 2.6: Stress-strain relationship and wave-profile for elastic-linear hardened material

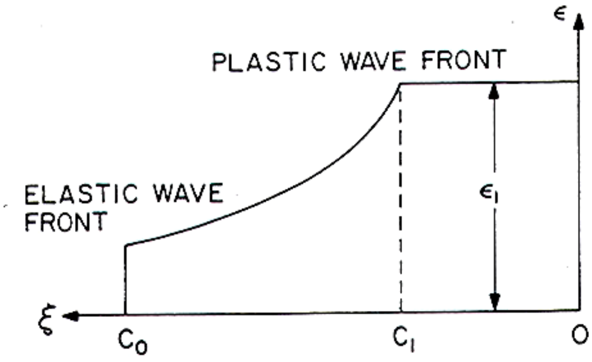

Figure 2.7: Strain distribution in a rod produced by a its constant velocity impact at end. $\xi=x/t$.

If the characteristics of the medium are such that the velocity of propagation of large disturbances is greater than the propagation velocity of smaller ones, the stress pulse develops a steeper and steeper front on passing through the medium, and the width of this front is ultimately determined by the molecular constitution of the medium. The shock wave (or steep pressure pulse) thus formed, differs from the high pressures generated by conventional methods in that it relies on the inertial response of the material to rapid acceleration rather than on static constraints. If the intensity of the loading is so great or its duration so short that the material no longer possesses rigidity, it will behave as though it had the properties of a fluid. Transverse (shear) waves cannot exist then within the body and only a longitudinal wave will be propagated with a velocity c given by:

$$c^2 = \frac{K}{\rho} \qquad \text{(Eq 2.2.2-1)}$$

where K is the bulk elastic modulus and ρ the density. The bulk modulus K may be found from Young's elastic modulus E and Poisson's ratio ν:

$$K = \frac{E}{3(1-2\nu)} \qquad \text{(Eq 2.2.2-2)}$$

In this shock wave regime, extremely high pressures are generated which can lead to changes in the density of materials with changes as large as 30% in steels [5]. The stress response is governed by dilation of the steel, since pressures are typically in the hundreds of kilobars while material strengths are only of the order of a few kilobars. This circumstance led to the development of hydrodynamic theories in which the material strength was neglected and the metal assumed to behave as a perfect fluid with resistance only to dilation. Lee [5] suggests that hydrodynamic theories need to be modified to account for strength effects and finite deformations. Finite strains and strength effects can play a dominant role in determining the stress-wave profile. For fracture problems, this profile is crucial for determining the location and the type of failure.

2.2.3. Material behaviour at high strain rates

The behaviour of materials at high rates of strain has been studied with considerable interest since World War II when dynamic plasticity and plastic-wave propagation first received attention. The most general form of a material-constitutive equation should cover the prediction of material behaviour under the total range of strain rates that may be encountered. However, this can be difficult even for an uniaxial stress and, therefore, the majority of constitutive equations generally cover only a narrow range of strain rates. This is consistent with the physics of the problem since different mechanisms govern the deformation behaviour of materials within different strain-rate regimes.

Five classes of strain rates are identified due to dynamic loadings in metallic structures. The duration of impact, the state of stress and strain as well as the thermal effect accompanying each class, are shown in Table 2.5. From this table it appears that at very high strain rates and the associated short time scale involved, thermodynamic considerations become important. The nominally isothermal conditions then translate to adiabatic conditions.

Table (2.5): Classes of strain rates [5]

Strain rate [s^{-1}]	10^{-8} to 10^{-6}	10^{-2}	10^{0}	10^{2} to 10^{4}	10^{6}
Characteristic time [s]	10^{6} to 10^{4}	10^{2} to 10^{0}	10^{-2}	10^{-4} to 10^{-6}	10^{-8}
	Creep	Quasi-static	Intermediate strain rate	Bar impact	High-velocity plate impact
			Mechanical resonance in machines and specimen	Elastic-plastic wave propagation	Shock wave propagation
Isothermal			Adiabatic		
Inertia forces neglected			Inertia forces important		
Plane stress					Plane strain
→ Increasing stress levels					

2.2.4. Ballistic performance

The development of metallic armour involves a large number of tedious ballistic experiments, since any change in alloy composition or heat treatment parameters significantly alters the ballistic performance. Although considerable knowledge exists on how the alloy compositions and heat treatment parameters affect the mechanical properties, a quantitative understanding of the correlation between the mechanical properties and the ballistic performance is still lacking [6]. Most of the earlier models on ballistic performance focused on the target and the projectile geometry and penetration parameters such as striking velocity and the striking angle. Contrarily most of the actual models are based on the mechanical properties of the projectile and the target, with the latter related to the metallurgical processes. Srivathsa et al [6] suggest that the kinetic energy of the projectile is absorbed in the following three modes:

1. the elastic deformation of the material;
2. the plastic deformation of the material; and
3. the kinetic energy imparted to the target material.

The total energy absorbed in each of the above cases is the product of the energy absorbed per unit volume and the participating volume. In previous work [7] the same authors suggested a model for the calculation of the energy Ψ per unit area-density (ρd) absorbed by the three modes as follows:

$$\frac{\Psi}{\rho d} = \pi t^2 v_r^4 \left[\frac{\alpha_I}{2(1+k_b)^2} + \alpha_{II} \frac{(1+k_e)^2 k^2_\gamma}{2k_j^2} + \frac{1}{k_j}\left(1+\frac{1}{k_p}\right) + \frac{1}{2k_p^2} + \frac{1}{2}\left(1+\frac{1}{k_p}\right)^2 \right] \quad \text{(Eq 2.2.4-1)}$$

where α_I and α_{II} are the fractional widths of the constrained (I) and unconstrained (II) regions, respectively. The non-dimensional parameters k_e, k_p, k_j, k_b and k_f can be computed as described below:

$$k_\gamma = \sqrt{\frac{1-\nu}{(1-2\nu)(1+\nu)}},$$

$$k_e = \frac{V_r}{k_\gamma}\sqrt{\frac{\rho}{E}},$$

$$k_j = \frac{\rho V_r^{\;2}}{\sigma_y},$$

$$k_b = V_r\sqrt{\frac{\rho}{K}} \quad \text{where } K = \frac{E}{3(1-2\nu)},$$

$$k_p = V_r\sqrt{\frac{\rho}{E_p}} \quad \text{where } E_p = \frac{\sigma_u(1+\varepsilon_\gamma)-\sigma_y}{\varepsilon_r},$$

$$\alpha_I = 1-\alpha_{II} = 1-\sqrt{\frac{V_1}{V_0}} \quad \text{where } \nu_I = \frac{-k_\gamma\sqrt{\rho E}+\sqrt{k_\gamma^{\;2}E\rho+10.4\rho\sigma_y}}{2\rho},$$

where ρ is the density, E the elastic modulus, σ_y the yield strength, σ_u the tensile strength, ν is Poisson's ratio, ε_r the reduction in area or the fractional elongation and V_0 the striking velocity, V_F is a material and thickness independent representative of the average velocity, defined as:

$$V_r = \frac{V_0}{1.85}$$

In this model the terms inside the square bracket in the equation 2.2.4-1 correspond to the mechanical properties as well as the striking velocity of interest. Srivathsa et al [6] express the Ballistic Performance Index (BPI) as:

$$\Phi = \left[\frac{\alpha_I}{2(1+k_b)^2} + \alpha_{II}\frac{(1+k_e)^2 k^2{}_\gamma}{2k_j^{\;2}} + \frac{1}{k_j}\left(1+\frac{1}{k_p}\right) + \frac{1}{2k_p^{\;2}} + \frac{1}{2}\left(1+\frac{1}{k_p}\right)^2\right]$$

In the BPI the first two terms represent the elastic components, the third and the fourth terms represent the plastic components and the last term corresponds to the kinetic energy component and Φ is a dimensionless parameter. The strain-hardening rate H is computed as:

$$H = \frac{\sigma_u(1+\varepsilon_r)-\sigma_y}{\varepsilon_r} \qquad (2.1)$$

The strain-hardening rate affects the plastic wave velocity in the material, which essentially determines the extent of plastic deformation in the region of impact.

The authors have applied this model to the following materials:

Table (2.6): Materials tested and their properties [6]

Material	Density [kg/m^3]	Yield strength [MPa]	Tensile strength [MPa]
Mild steel	7800	325	691
Aluminium	2720	130	217
Steel-A	7800	1068	1210
Ti-6Al-4V	4550	990	1050
Al-2024	2770	345	565
Steel-B	7800	1610	1860

They observed that from the ballistic performance:

- Maraging steel is only 1.4 times better than mild steel despite its higher strength. This has been confirmed experimentally [8];
- The BPIs of Steel-S and Steel-B are 1.55 and 2.33, which agreed with the experimental results;
- The Aluminium alloy Al-2024 is nearly 2.2 times better than mild steel. Also, the performance of Ti-6Al-4V is 1.9 times better than that of mild steel.

It can be seen that merely increasing the strength of the material does not necessarily lead to significantly improved performance. This observation is highly significant and will be returned to later in this study on new experimental steels for advanced ballistic performance.

2.2.5. Fracture prediction under high-velocity localised impact

It is well known that the dynamic strength of hard metal sheets and their fracture strength are not identical to those determined for static loading or for low strain rates. Several fracture criteria have been postulated throughout the years. In the present study two of them are presented.

In 2004, Lee and Wierzbicki [9] have postulated that fracture initiates at the critical point of the structure when the accumulated equivalent plastic strain $\bar{\varepsilon}$ with a suitable weighting function, reaches a critical value of:

$$\int_0^{\bar{\varepsilon}_f} f\left(\frac{\sigma_m}{\bar{\sigma}}, \dot{\bar{\varepsilon}}, T\right) d\bar{\varepsilon} = D_C$$

where $\bar{\varepsilon}_f$, the upper limit of the integral, is the equivalent strain to fracture; f is a weighting function dependent on the stress triaxiality and is defined as the ratio of the hydrostatic mean stress σ_m to the von Mises equivalent stress $\bar{\sigma}$, $\dot{\bar{\varepsilon}}$ the strain rate, and T the absolute temperature; D_C is a critical damage value of the specific material. The authors [9] observed three regimes for the fracture mechanisms depending on the stress triaxiality value:

- for a stress triaxiality larger than 1/3 the fracture is controlled by the mechanism of void nucleation, growth and coalescence;
- under negative stress triaxiality the so-called shear decohesion becomes the fracture mechanism; and
- the third regime is a combination of the other two.

It should be pointed out that their study strictly only applies to the prediction of the onset of fracture of uncracked bodies. They further assumed that ductile crack propagation is essentially a process of continuous reinitiation ahead of the crack, so that the same micro-structural events occur in front of the crack tip of previously existing crack, as in the region of a flawless body in which the crack initiates [10]. They have also considered the possible dependence of the fracture criterion on the strain rate and temperature. However Borvik et al. [11-12-13], and Hopperstad et al. [14] have recently shown that the effect of strain rate and temperature on the fracture strain are much smaller than that of any stress triaxiality for Weldox 460E steel.

2.2.6. Shock induced transitions and transformations

The effect of target strength on the perforation of steel plates using different projectile nose shapes, has recently been investigated by Dey and co-workers [15]. They confirm as modelled by Zukas [5], that when a blunt projectile hits the target, the material in front of the projectile accelerates, while the rest of the target is relatively stationary as shown in Figure 2.5.

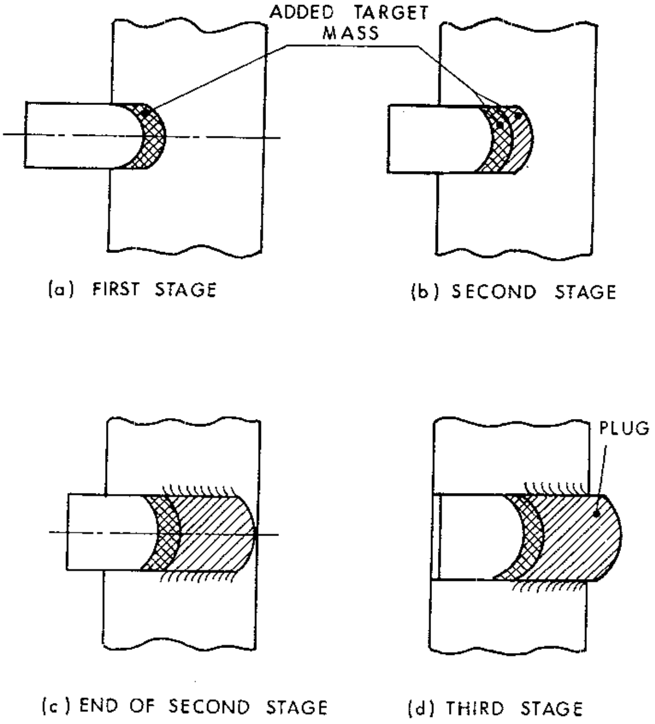

Figure 2.5. Three-stage perforation model showing the increase in the effective mass of the bullet as it progresses through the plate

Hence, the deformation localises in narrow shear bands under adiabatic conditions where the shear strain, shear strain rate and temperature may locally be very high. According to Bai and Dodd [16], these shear bands may either consist of only *deformed* material or *transformed* material, depending on the temperature that was reached in this localised area. Deformation bands are regarded as zones of intense plastic shear only, whereas transformation bands are zones of intense shear in which a phase transformation has occurred. When the localised temperature reaches about $720\,^{0}C$, the steel will undergo a phase transformation. In impact problems involving steel targets, temperatures of this order are produced in micro- or milliseconds, before the band is subsequently quenched by heat flow into the surrounding material.

The common thread is that the spalling-strength of the steel is sufficient as an objective characteristic tensile strength of the material at the microsecond scale of dynamic loading. In reality, a preliminary compression of the material takes place during the passing of the compressive pulse front. If this dynamic compression achieves a critical value, irresistible structural changes within the solid occur before the tensile stresses are generated within the spalling zone of the target. Thus dynamic failure during spallation depends on the plastic instability of the material under compression at the wave front of the loading pulse [17]. The plastic instability can be considered as a strain-rate dependent structural phase transition by means of which the shock wave itself establishes the microstructural features on a mesoscopic scale. Micro-deformation models based on the solution of a non-linear sine-Helmholtz equation, predict a non-stable behaviour of the crystal lattice that is subjected to shear deformation in the non-linear elastic region of loading. This instability leads to the nucleation of large-scale structures such as meso-rotations, shear bands and their combinations. At higher strain gradients a bifurcation transition takes place, which results in the nucleation of structures on a mesoscopic scale commonly seen in microstructural investigations [17]. In accordance with a generally accepted classification (Panin et al., 1982) the microstructural size defining a mesoscopic scale ranges from about 7 to 10 μm.

The transition to a new regime of dynamic deformation can be considered as a structural phase transformation initiated by shock loading. Mescheryakov et al [17] have determined the instability threshold to be at 307 m/s. According to their observation on a set of steels, fracture occurs by a cleavage mechanism at impact velocities less than 307 m/s. However, at impact velocities higher than the instability threshold, blocks of grains and brittle fragmentation become the mechanism of fracture.

2.2.7 Role of material properties

The penetration depth upon impact loading is known to be determined on the basis of a modified Bernoulli equation (Hohler and Stilp, 1990):

$$Y + \frac{1}{2}\rho_{imp}(\nu - u)^2 = \frac{1}{2}\rho_t u^2 + R, \qquad \text{(Eq 2.2.7-1)}$$

where v is the impactor velocity, u is the particle velocity in the material of the target, Y and R are empirical constants defining the dynamic strength for the material of the penetrator and target respectively. It is claimed that the physical meaning of parameters Y and R remains to unclear (Hohler and Stilp, 1990).

The value of R takes into account any deviation in behaviour of the material of the target from the hydrodynamic model of penetration.
Micromechanisms of dynamic deformation responsible for the physical nature and value of R are the subject of investigations on microplasticity. The parameter R is often identified with dynamic hardness H_D which is related to the dynamic yielding limit, Y_D, by the following dependence (Tate, 1967; Lasarev et al., 1993):

$$H_D = (3 - 3.5)Y_D \qquad (2.2.7\text{-}2)$$

The dynamic yielding again is determined by the Hugoniot elastic limit, σ_{HEL}:

$$Y_D = \frac{1-2\nu}{1-\nu}\sigma_{HEL} \qquad (2.2.7\text{-}3)$$

where ν is Poisson's ratio. The main conclusion [17] following from the analysis of peculiarities of high-velocity penetration and also from the analysis of experimental data, is that the strength-component of the resistance of solids to penetration (as a complementary factor for the inertial forces) is determined by the resistance to plastic deformation. This means that if the character of the plastic deformation changes, for example, because of a change of the structural mechanism of deformation, the strength-component of the resistance to penetration changes as well.

Rosenberg et al [18] have investigated the strong dependence of the penetration on a rod's aspect ratio, the so-called " L/D effect ", by rewriting the modified Bernoulli equation as:

$$\frac{1}{2}\rho_{imp}(\nu - u)^2 = \frac{1}{2}\rho_t u^2 + R_t \qquad (2.2.7\text{-}4)$$

They have observed that the term R_t is reasonably independent of the impact velocity as well as the densities of the rod and target, but is strongly dependent on the target strength. R_t may reach critical values as high as 5.5GPa, whereas Y_D may reach only 2GPa.

2.2.8. Prediction of the martensite start temperature M_s and the Driving Force $\Delta G^{\gamma\rightarrow M}$ for the martensitic transformation

Much work has been done to assess the various factors that determine the type or morphology of martensite that forms upon quenching steels from the austenite region. The influence of temperature, composition, magnetic character of the austenite, quench rate, stacking fault energy, shear strength of the austenite and driving force for the martensite formation have been investigated by various authors.

The free energy change accompanying the martensitic transformation may be expressed as:

$$\Delta G^{\gamma\rightarrow m} = \Delta G^{\gamma\rightarrow\alpha} + \Delta G^{\alpha\rightarrow m} + \Delta G^{*} \qquad (2.2.8\text{-}1)$$

$\Delta G^{\gamma \rightarrow m}$ is the driving force required for the transformation from austenite to martensite, $\Delta G^{\gamma \rightarrow \alpha}$ is the sum of the chemical and structural free energy change from the austenite to the ferrite at equilibrium, $\Delta G^{\alpha \rightarrow m}$ is the structural free energy change from ferrite to martensite, ΔG^{*} is Zener's ordering energy from which Zener's ordering parameter Z has been evaluated by Fisher [19] as:

$$\Delta G^{*} = -2.12 \times 10^{5} X_{C}^{2} Z^{2} + 2.77 X_{C} T \phi \text{ J.mol}^{-1} \qquad (2.2)$$

Z = Zener's ordering parameter:

$$\phi = 2(1 - Z)\ln(1 - Z) + (1 + 2Z)\ln(1 + 2Z) \qquad (2.3)$$

The maximum values of Z and ϕ are 1 and 3.295.

$\Delta G^{\alpha \rightarrow m}$ has been evaluated with the assistance of the result for Fe-C [20] as:

$$\Delta G^{\alpha \rightarrow m} = 2.1\sigma + 900 \text{ J.mol}^{-1} \qquad (2.4)$$

in which σ is the yield strength of austenite at the M_S temperature. It may be approximated for Fe-Mn-C systems by [20]:

$$\sigma = 127.4 + 3920 X_{C} + 490 X_{Mn} + 0.265(800 - M_{S}) \text{ MN.m}^{-2} \text{ [20].} \qquad (2.5)$$

Morozov et al [21] studied the transformation in Fe with 0.01% C from low to very high cooling rates. They found four arrest temperatures corresponding to four plateaux and denoted them I, II, III and IV. They identified plateau III with the formation of martensite by slip (lath martensite) and plateau IV with the formation of martensite by twinning (plate martensite). Plateau I is mainly due to the formation of incoherent equiaxed α and plateau II is mainly caused by the transformation of austenite to acicular ferrite (AF) or Widmanstätten ferrite. Depending on the cooling rate there are then two M_S temperatures and not one. The plateaux of transformation are illustrated in Figure 2.6 for the Fe-Ni-C system. The two M_S lines intercept at low M_S temperatures [21].

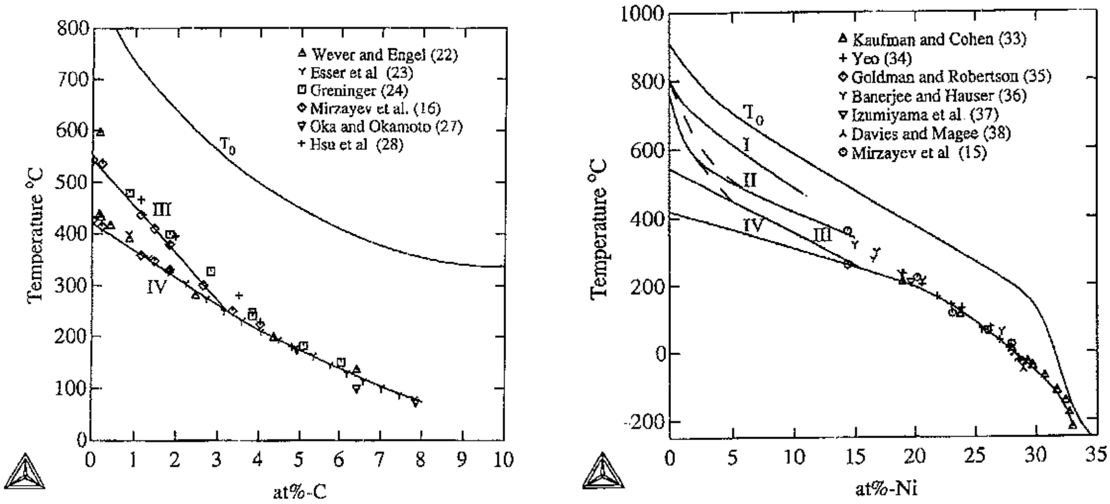

Figure 2.6. Plateaux of transformation and intersection of M_S lines for the Fe-Ni-C system [21]

Table (2.7) presents the intersection temperatures for the two M_s lines as reported by different researchers in varying the cooling rate up to 5×10^5 K/s in Fe – C alloys containing from 0.01% C up to 0.89% C and for some Fe-X systems.

Table (2.7): Temperature [°C] of intersection of the two M_s lines

	Mizrayev et al [16c]	Mizrayev et al [16c]	Shteynberg et al [16d]	Mizrayev et al [16e]	Mizrayev et al [16f]	Zhao and Jin [16g]	Zhao	Wilson	Wilson
Fe-C	342	284			252	250	244	232	
Fe-Ni	392					0	0		200
Fe-Mn			300			346			
Fe-Cr				300			323		

The Lacher, Fowler and Guggenheim (LFG) model for the calculation of $\Delta G^{\gamma\to\alpha}$ in multiple component systems, which was first proposed by Aaronson et al. [22] by incorporation it with Zener's work [23], may be expressed as:

$$\Delta G^{\gamma\to\alpha} = RT(5-16X_C)\ln(1-2X_C) - 4RT(1-X_C)\ln(1-X_C) + 7RTX_C\ln(3-4X_C) -$$
$$4RTX_C\ln 2 - 6RT(1-3X_C)\ln(\delta_\gamma + 1 - 3X_C) + 6RT(1-X_C)\ln(\delta_\gamma + 1 - X_C) - 8RTX_C\ln(\delta_\alpha + 3 - 5X_C)$$
$$+ X_C\left[\left(\Delta\bar{H}_C^{\alpha} - \Delta\bar{H}_C^{\gamma}\right) - \left(\Delta\bar{S}_C^{xs(\alpha)} - \Delta\bar{S}_C^{xs(\gamma)}\right)T\right] + (1+X_C)$$
$$\times\left[141\sum_i X_i\left(\Delta T_{Nm}^{i}\right) + \Delta G_{Fe}^{\gamma\to\gamma} \times \left\{T - 100\sum_i X_i \Delta T_{mag}^{i}\right\}\right] \qquad (2.6)$$

where

$$\delta_\alpha = \left[9(1-X_C)^2 - 4X_C(3-4X_C)J_\alpha\right]^{1/2} \qquad (2.7)$$

$$\delta_\gamma = \left[(1-X_C)^2 - 4X_C(1-2X_C)J_\gamma\right]^{1/2} \qquad (2.8)$$

$$J_{\alpha,\gamma} = 1 - \exp\left(-\omega_{\alpha,\gamma}/RT\right) \qquad (2.9)$$

$\omega_\alpha =$ -25,310 J.mol^{-1}

$\omega_\gamma =$ 1380 J.mol^{-1}

$\Delta\bar{H}_C^{\alpha} =$ 109,680 J.mol^{-1}

$\Delta\bar{H}_C^{\gamma} =$ 38,460 J.mol^{-1}

$\Delta\bar{S}_C^{xs(\alpha)} =$ 39.90 J.mol^{-1}.K^{-1}

$\Delta\bar{S}_C^{xs(\gamma)} =$ 10.65 J.mol^{-1}.K^{-1}

T refers to the M_s temperature in absolute degrees and is the term to be evaluated; X_C and X_i are the mole fractions of Carbon and the ith substitutional alloying element; ΔT_{mag} and ΔT_{Nm} are the magnetic and non-magnetic components respectively affecting the $\Delta G^{\gamma\to\alpha}$ of pure iron, or the displacement in M_s temperature of pure iron by 1 at.% of alloying element. From the Aaronson, Domian and Pound (ADP) model [21] ΔT_{mag} =-35.5 K and ΔT_{Nm} =-37.5 K.

Wang et al [24] have developed an advanced set of equations in which combined binary effects between sets of alloying elements were taken into account for the estimation of the M_s temperatures. The nominal concentration of binary terms was defined as the square root of the products of the mass percentages of two chemical constituents.

$w_{i-j} = \sqrt{w_i w_j}$ leading to the general equation: $M_s = k_0 + \sum k_{ij}\sqrt{w_i w_j}$

$$\begin{aligned} Ms\left({}^0C\right) &= 540 - 584.9w_C - 23.1w_{Si} - 117.7w_{Mn} - 42.5w_{Cr} - 49w_{Mo} - 62.5w_{C-Si} \\ &+ 178.3w_{C-Mn} - 10.0w_{C-Cr} + 52.5w_{C-Mo} + 117.2w_{Si-Mn} + 50.9w_{Si-Cr} - 142.2w_{Si-Mo} \\ &- 129.2w_{Mn-Cr} - 9.7w_{Mn-Mo} + 69.9w_{Cr-Mo} \end{aligned} \quad (2.10)$$

This equation may be applied to typical steel compositions in the range of 0.2 to 0.5%C, 0.5 to 2%Si, 0.5 to 2.0%Mn, 0.5 to 2.0%Cr and 0.1 to 0.7%Mo.

Note that with binary interaction effects, some positive changes in the M_s temperature are to be expected as opposed to the generally negative effects with single element considerations. Other formulae proposed for the M_s estimation in ferrous steels are summarised in the following table:

Table (2.8). Different formulae for the estimation of M_S temperatures in steels

Reference	**M_S [K], all compositions in wt.%**
[27]	$772 - 316.7C - 33.3Mn - 11.1Si - 27.8Cr - 16.7Ni - 11.1Mo - 11.1W$
[28]	$811 - 361C - 38.9Mn - 38.9Cr - 19Ni - 27.8Mo$
[29]	$785 - 453C - 15Cr - 16.9Ni - 217(C)^2 - 71.5(C)(Mn) - 67.6(C)(Cr)$

All these attempts that were made at modelling the compositional dependency of M_s using linear regression or similar methods, are classified as non-adaptative [30] because the 'shape' of the function is predetermined by the authors rather than adapted to the data. Neural networks, as opposed to traditional linear or polynomial regression methods, do not impose a shape of the function on the data. In contrast, neural network methods that are currently under development are adaptive functions.

From these empirical formulae it appears that Nitrogen decreases the M_s temperature more largely than Carbon. This is attributed to its stronger stabilisation of the austenitic matrix due to a larger solid solution strengthening effect. The same observation [30] may be arrived at on the effects of Manganese and Molybdenum due to a difference in solid solution strengthening. Hayzelden et al [31] have investigated the effect of the austenite grain size and the dislocation density on the M_s temperature. In an Fe - 0.38%C - 26.13%Ni alloy and in the absence of a change in dislocation density, M_s was found to be determined by the grain size of the austenite. For a given grain size, the M_s is raised by an increase in dislocation density. In this case the microhardness of the austenite is unaffected by a reduction in grain size but is raised by an increase in dislocation density within the grains.

The depression in M_S in the fine-grained alloy could not be explained by the Hall – Petch strengthening of the austenite and was believed to result from the segregation of active martensite nuclei into a few small grains, a suppression of the autocatalytic stimulation of martensite plates between adjacent grains and a possible reduction in the number of potential martensite nuclei.

From their study on the heterogeneous nucleation of martensite within the vicinity of grain boundaries using an SEM-EBSD method, Ueda et al [32], observed that only some grain boundaries with a specific character could activate martensitic transformations effectively. These include 90°<211> symmetric tilt boundaries that acted as a favourable site for martensite formation while 90^0<211> twist boundaries did not. In the vicinity of grain boundaries, some martensite variants with the habit plane almost parallel to the grain boundary were preferentially formed from amongst 24 possible habit plane variants. The equivalent variants were adjoined at the tilt boundary to maintain the compatibility of the transformation strains across the boundary, resulting in an increase in the martensite-start temperature. These authors have defined this type of nucleation as “cooperative nucleation (CN)”. They have estimated the difference in M_s temperatures for different tilt angles in the vicinity of the grain boundaries as 50K. A grain boundary may reduce the strain energy for the nucleation of martensite. In particular, the symmetric tilt boundary 180^0<211> demonstrated the highest M_s temperature. It suppresses the growth of embryos into martensite (the self-accommodation of a group of variants), since the compatibility requirements are maintained at the boundary and result in higher M_s temperatures and more effective CN.

Many researchers have succeeded in explaining various phenomena or crystallographic features of phase transformations using Eshelby’s inclusion theory [33]. According to this theory, the elastic strain energy due to martensitic transformation may be calculated from the shape strain matrix as follows: The shape strain matrix must be first converted to the symmetric matrix $\varepsilon_{ij}{}^{T}$, which is given by

$$\varepsilon_{ij}{}^{T} = \frac{S_{ij} + S_{ji}}{2} - \delta_{ij} \ , \qquad (2.11)$$

where δ_{ij} is the Kronecker delta [33]. δ_{ij} =1 for i = j and δ_{ij} = 0 for i≠j. The strain energy $U_{0,}$ generated by the shape change of ε_{ij} in an elastic medium, is given by:

$$U_0 = \int_0^{\varepsilon_{ij}} \sigma_{ij} d\varepsilon_{ij} \qquad (2.12)$$

Since Hooke’s law is applicable in an elastically isotropic matrix, the elastic strain energy can be expressed in terms of the strain components as follows:

$$U_0 = \frac{\nu G_M}{1-2\nu}\left(\varepsilon_{xx} + \varepsilon_{yy} + \varepsilon_{zz}\right)^2 + G_M\left(\varepsilon_{xx}{}^2 + \varepsilon_{yy}{}^2 + \varepsilon_{zz}{}^2\right) + 2G_M\left(\gamma_{xy}{}^2 + \varepsilon_{yz}{}^2 + \varepsilon_{xz}{}^2\right) \qquad (2.13)$$

where G_M is the shear modulus and ν is Poisson’s ratio. When a martensite plate nucleates independently in a single crystal, the strain energy U_0 is calculated to be about 1500 J/mol.[34].

Borgenstam and Hillert [35] presented a very good summary on the thermodynamic theory of the martensitic transformation in Fe-X systems. The following paragraph is based on their work and on the general observation by Nishiyama [36]. Johansson [37] was the first to publish in 1937 a thermodynamic analysis of the α and γ phases in the Fe-C system. He discussed the martensitic transformation, presuming that martensite cannot form at that temperature where α and γ have the same Gibbs free energy, but it requires further undercooling for the necessary driving force. He proposed that this extra driving force results from the Carbon atoms within martensite being "frozen" into the positions inherited from the parent γ, and he believed that those positions would give a higher free energy as well as a lower entropy than in α with its random distribution of the Carbon atoms. Zener [38] instead assumed that martensite, which is tetragonal at higher Carbon contents because of the non-random positions of the Carbon atoms, would have a lower free energy because of the Carbon atoms collaborating and thus minimising the strain energy caused by the presence of these atoms in interstitial sites of insufficient size. He even proposed that there is a temperature-composition region where the tetragonal martensite with the non-random distribution of Carbon atoms would have a lower Gibbs free energy than α with a random distribution. He developed a simple theory of ordering and by minimizing the Gibbs free energy, it was possible to predict the degree of order at equilibrium. When evaluating the driving force for the martensitic transformation he assumed that martensite would have those equilibrium ordered properties. Fisher [19] made a more thorough analysis of the Gibbs energy of the ordered α phase by evaluating the driving force for martensite formation and determined values for the Zener's ordering driving force ΔG^* and ordering parameter Z as presented earlier in this paragraph. Many evaluations of the driving force for martensite formation have been published over the years with most of them taking Zener ordering into account.

It should be emphasized that the idea of Carbon atoms inheriting their positions from the parent γ is based on the assumption that the rate of transformation is so high that there is not enough time for Carbon atoms to redistribute by diffusion during the actual transformation. It seems that this could apply to the edgewise growth of plate martensite but possibly not to the growth of lath martensite. If this is so, then the equilibrium degree of order should be used for lath martensite. Furthermore, at very high growth rates there is not even time for the reaction heat to diffuse away and the temperature will be higher at the γ / α interface than in the rest of the system [39].

After these results [19, 35, 36, 37, 39] the driving force for the formation of plate martensite may have a constant value of about 2100 J/mol. For lath martensite it may vary linearly with the formation temperature, possibly from 500 J/mol at $800\,^0C$ to 2100 at $250\,^0C$.

Another uncertainty in the description of the Gibbs free energy of the α phase is the effect of Carbon on the ferromagnetic transition in the α phase. The analysis of the properties of the α phase made by most researchers is made with the assumption that the magnetic properties are not affected by Carbon. Earlier, Nishiyama [36] had already voiced his reservation on the validity of the thermodynamic theories of the martensitic transformation. He stated that in the current thermodynamic theories on the growth of a martensite nucleus, the interfacial and internal chemical energies are considered to be dominant, as in the case of crystallization in a liquid. In addition because of the solid medium, the strain energy of the transformation is also taken into account. These theories, however, assume thermal equilibrium and ignore the microstructural and crystallographic characteristics of the martensitic transformation. He, therefore, felt that such theories are not reasonable and it would be better to rather construct a thermodynamic theory that takes microscopic structures into consideration.

2.2.9. Kinetics of the martensitic transformation

The nucleation of martensite during cooling is believed to take place at structural imperfections in the parent phase. These pre-existing embryos (defects) are stimulated to grow into martensite crystals at different degrees of undercooling below the M_s temperature as they have different energy barriers to activation. Growth can, however, be very fast. Each nucleation event directly leads to the formation of a typical volume of the new phase. Thus, the volume fraction of martensite varies only with the degree of undercooling, which expresses the athermal character of the transformation. Koistinen and Marburger [40] have postulated that the evolution of martensite formation in a sample that is initially fully austenitic, may be described by:

$$f = 1 - e^{C_1(Ms - T)} \qquad (2.14)$$

where f is the volume fraction of martensite in the sample at temperature T below M_s, and C_1 is a constant. This volume fraction is defined as the volume of martensite divided by the volume of austenite that exists in the sample prior to the formation of martensite. Magee [41] derived the following empirical equation from first principles, assuming that in a temperature interval dT, the incremental number dN of new martensite crystals (plates or laths) that form per unit volume of austenite is proportional to the increase in driving force $\Delta G^{\gamma \to \alpha'}$ due to the temperature decrease dT:

$$\frac{dN}{dT} = -C_2 \frac{d\left(\Delta G^{\gamma \to \alpha'}\right)}{dT} \qquad (\Delta G^{\gamma \to \alpha'} < 0) \qquad (2.15)$$

where C_2 is a positive constant expressing the proportionality between the increase in driving force and the consequent increase in density of activated nucleation sites. The change in the volume fraction of martensite corresponding to the temperature decrease dT is then given by:

$$\frac{df}{dT} = \Omega(1 - f)\frac{dN}{dT} \qquad (2.16)$$

where $(1 - f)$ is the volume fraction of austenite available for further transformation and Ω is the average volume of martensite per newly formed crystal. Combining these two equations, yields:

$$\frac{df}{dT} = -\Omega(1 - f)C_2 \frac{d\left(\Delta G^{\gamma \to \alpha'}\right)}{dT} \qquad (2.17)$$

Assuming that Ω, C_2, and $\frac{d\left(\Delta G^{\gamma\to\alpha'}\right)}{dT}$ are constant over the extent of the transformation and integrating from M_s (f = 0) to T gives:

$$\ln(1-f) = \Omega C_2 \frac{d\left(\Delta G^{\gamma\to\alpha'}\right)}{dT}(Ms - T) \qquad (2.18)$$

This equation is equivalent to equation (2.14) with the positive parameter C_1 expressed by:

$$C_1 = -\Omega C_2 \frac{d\left(\Delta G^{\gamma\to\alpha'}\right)}{dT} \qquad (2.19)$$

Thus $\ln(1-f)$ is expected to vary linearly with T when the nucleation and growth of the martensite crystal in a sample obey the characteristics as proposed by Magee. The assumption that Ω is a constant is in contradiction with the Fisher model [42], which assumes that Ω decreases strongly as the transformation progresses. Van Bohemen et al [43] have fitted their experimental data to the Koistinen and Marburger equation for the following steels:

Table (2.9). Chemical composition of steels used in Van Bohemen's study [43]

Steel	C	Si	Mn	P	S	Cr	Cu	Ni
C60	0.6	0.39	0.50	0.020	0.04	0.23	0.21	0.07
C70	0.7	0.37	0.68	0.027	0.04	0.29	0.22	0.16
C80	0.8	0.41	0.61	0.012	0.05	0.28	0.23	0.15

They have found the following values for the fitting parameters of the kinetic equation:

Table (2.10). Fitting parameters for the kinetics of the martensitic transformation

Steel	Ms (^0C)	$C_1(K^{-1})$	$d\Delta G^{\gamma\to\alpha'}/dT(J/mol^0C)$	ΩC_2 (mol/kJ)	$f_A(-)$
C60	282	0.067	7.2	9.3	0.90
C70	248	0.055	7.0	7.9	0.95
C80	211	0.046	6.9	6.7	1.00

2.2.10. Crystallography and morphology of martensite, general considerations and definition of martensite

In optical microscopy one may distinguish between two kinds of martensite: lath and plate types. Lath martensite is usually formed at low alloy contents (or at high M_S) and plate martensite at high alloy contents (or low M_S) and a mixture of the two types occurs in between. At higher magnifications with transmission electron microscopy it appears that lath martensite is a highly dislocated structure and it probably has formed through slip. The midrib of plate martensite is heavily twinned and it probably has formed by a twinning mechanism. The outer part of a martensite plate is often dislocation-rich and without twins and sometimes it resembles lath martensite in optical microscopy.

A martensitic transformation is a phase transformation that occurs by cooperative atomic movements.

That a given structure is produced by a martensitic transformation can be confirmed by the presence of the diffusionless character, the surface relief, and the presence of many lattice defects. Such characteristics are, therefore, criteria for the definition of martensite [36]. Martensite may have many other characteristics, which though suggesting the presence of martensite, are not necessarily proof in themselves that a martensitic transformation has occurred. For example, high hardness was believed a necessary property of martensite at the time when the word "martensite" was first adopted but it is no longer regarded as a good criterion. Equally, the rapidity of the transformation does not necessarily lead to martensite. Though in most steels the time of formation of an α' crystal is of the order of 10^{-7} seconds, the growth is so slow that the process in some alloys may be followed under an optical microscope [36]. The existence of a habit plane and orientation relationship with the parent phase is a necessary consequence of the coherency of a martensitic transformation; although in turn it is not a sufficient criterion, because coherent precipitates that are definitely not classified as martensite also have such characteristics.

A number of types of martensite have been observed in nonferrous alloys. In Carbon and low alloy steels with M_s temperatures well above room temperature, the complete suppression of Carbon diffusion during quenching is virtually impossible to attain. In the lowest Carbon steels with high M_s temperatures the Carbon mobility is sufficient to even cause epsilon carbide ($Fe_{2.4}C$) precipitation in the martensite during quenching to room temperature, a process referred to as autotempering [60]. A more common manifestation of Carbon diffusion in martensite during quenching is its segregation to dislocations and lath boundaries. Speich [51] has presented indirect evidence based on electrical resistivity measurements, for the segregation of Carbon atoms in Iron – Carbon martensite. He reasoned that the *lower slope* in the change in resistivity curve for martensitic structures containing less than 0.2% C, corresponds to complete segregation of the Carbon to dislocations, leaving the ferrite free of the scattering centres due to carbon trapped in octahedral interstitial sites. The *higher slope* in the change in the resistivity curve in martensitic microstructures in steels containing more than 0.2% C was attributed to the scattering by carbon atoms randomly distributed in octahedral sites of the martensite. The measurement of increasing tetragonality of Fe – C martensite crystals with increasing Carbon concentration by X – ray diffraction [61] certainly verifies that a significant fraction of Carbon atoms are retained in octahedral sites in untempered higher Carbon steels. Direct evidence for Carbon atom segregation to dislocations during quenching and room temperature aging of martensite has been obtained by Smith and his colleagues [62] with field ion / atom – probe microscopy. They confirmed Speich's conclusion that almost 90% of the Carbon atoms in a 0.18%C martensite are segregated to dislocations. Mader and Krauss [63] showed that packet martensite consists of dislocated laths (α') which form in steels when the M_s transition temperature is above $350\,^0C$. This temperature is strongly dependent on the steel's composition, especially its Carbon content. McMahon and Thomas [64] showed that the dislocated structures at martensitic lath boundaries (α') were in fact thin microlayers of retained austenite. The identification of such thin layers of retained austenite requires diffraction analysis through electron microscopy. This interlath austenite was revealed by the authors through high resolution lattice imaging electron microscopy from which it was suggested that there was considerable Carbon enrichment at the α'/γ interfaces, i.e. also suggesting Carbon movement. Heat treatments of α'/γ phase mixtures in the range 300 to $500\,^0C$ result in the austenite decomposing to interlath carbides. The structure becomes similar to lower bainite, causing embrittlement in directions transverse with respect to prior austenite.

Liu and Dunne [65] investigated the nature of the terminating interfaces of the twin volumes in Cu-14%Al-3.4%Ni twinned martensite, using Atomic Force Microscopy. Although twin relief was generally evident in the random sections they have examined, well-defined interfacial facets corresponding to the terminating twin volumes were not observed. Instead, side-plates extending beyond the habit plane were common, being associated with the smaller of the twin volumes. They noted that the twin plane is close to the habit plane and its extension ahead of the general interface with its own twinned substructure, is probably related to the plate growth mechanism. From the observed difference in side-plate extensions between thermal and stress-induced plates they suggest that growth occurs by the motion of only one interface in providing strain accommodation of the applied stress, whereas for thermal martensite the growth is constrained by the surrounding matrix and the stresses imposed by transformation shear and a volumetric change. Moreover fine twins on a system other than the primary twinning system were also observed for the thermal martensite in their investigation.

2.2.10.1. Habit plane

Christian [44] noticed that the habit plane is usually one of three types:

- planar, irrational and semi-coherent, separating a single-crystal parent from a slipped and/or faulted single-crystal product;
- planar, irrational and separating a single-crystal parent from a twinned product; or
- curved and thus macrospically displaced from the “true” habit plane, because of interfacial steps.

The martensite interface is observed to be glissile, at least for the forward transformation, and it is implied that either:

- planar sections migrate as a unit, consisting of twin-parent volumes or surface dislocations; or
- steps consecutively sweep across the whole interface.

Christian [45] concluded that the invariant plane strain condition might only be met for “unconstrained” single interface transformations. In polycrystalline austenite, local constraints such as coherency strains could induce the operation of a more complex lattice invariant shear, giving significant habit plane variations. Kennon and Dunne [46] explored the suggestion by Christian , in the case of $\gamma_1^{'}\left(2H\right)$ plates in a cubed-shaped single crystal Cu-Al-Ni alloy. After accurate tilt and habit plane trace measurements with an estimated experimental error in the habit plane normal of less than $\pm 1^0$, they concluded that even in the case of unconstrained transformation, a real variability in the habit plane normal could occur. A close examination of the interface of $\gamma_1^{'}$ martensite by the authors indicated that variations in transformation twin width are not uncommon, resulting in changes in the local average interface plane. The habit plane can curve to accommodate minor localised constraints and any atomic matching across the interfacial twin facet must be high. This observation has been confirmed recently in the case of a {225} martensite transformation in Fe-Cr-C alloy by Lin et al. [47].

Tadaki and Shimizu [48] suggested that the temperature dependence of the lattice parameters of the austenite and the difference between that of austenite and martensite must mean that the crystallography of the transformation will change with the actual temperature of formation of the martensite during the quenching. A continuous spectrum of habit planes is, therefore, possibly to be expected over the transformation temperature range as a function of order and temperature. Dunne and Kennon [49] concluded from the systematic type of habit plane variation, that there is clearly a scatter which is not accounted for by the theory and which is a characteristic feature of the martensitic transformation. Moreover, habit plane "flexibility" is likely to be a characteristic feature of martensite plates.

Given the plane and direction of the lattice invariant shear, the lattice correspondence between the parent and martensite and the pure strain, the crystallographic theory predicts the habit plane on the basis that it is exactly invariant. However, Dunne and Kennon [49], noticed that the invariance may only be local because of localised plastic and/or elastic constraints, leading to macroscopic habit plane measurements which may differ significantly from the predicted plane. Local changes in the invariant shear will occur with strains created by the plate itself or by prior transformation. Accommodating slip or faulting can occur in the parent phase or in the martensite, influencing the form of the moving interface. On the basis of their analysis of habit plane scatter, Dunne and Kennon [49] concluded that the response to the question: "how regular is the habit plane?" must be: "not very". Moreover the variability should be regarded as a characteristic feature of the transformation rather than an anomaly. As the literature shows, good correspondence between measured and predicted habit planes is usually restricted to precisely controlled conditions in which limited transformation occurs in a coarse grained or a single crystal parent phase. In other circumstances and particularly for transformations involving a large volume change, considerable habit plane variability should be expected.

Morito et al [50], have examined the morphology and crystallography of lath martensite in Fe-C alloys with different Carbon contents such as 0.0026, 0.18, 0.38 and 0.61 mass %C by means of optical microscopy, by SEM and by TEM. Their main findings were: as the carbon content increased from 0.0026% to 0.61%, the block and packet size of the martensite units decreased; the orientation relationship between austenite and martensite was close to the Kurdjumov-Sachs relationship and some laths seemed to have nearly the Nishiyama relationship; twenty-four variants in the K-S relationship were suggested as presented in Table (2.11).

In low Carbon alloys (typically 0.0026%C – 0.38%C), martensite packets consisted of well-developed parallel blocks with three blocks (with different orientations) in each packet. Each block consisted of laths of two specific K-S variant groups (called a "sub-block") which were misoriented by small angles of about 10°; and in high Carbon alloys (>0.61% C), packets consisted of fine blocks whose width were a few microns. Blocks consisted of laths with a single variant and six blocks with different orientations existed in a packet.

In martensitic Fe-C alloys and low-alloy Carbon steels with above-room temperature M_s temperatures, Krauss [51] observed that it was impossible to prevent Carbon diffusion during quenching, and strengthening of martensite becomes dependent on static and dynamic strain aging due to Carbon atom interaction with dislocation substructures. The substructure of the martensitic matrix appears to be the dominant strengthening component in these steels.

Table (2.11). Variants in K-S relationship [50]

Variant N_0	**Plane parallel**	**Direction parallel** $[\gamma]//[\alpha']$	**Rotation from variant 1 Axis (indexed by martensite)**	**Angle [deg.]**
V1	$(111)_{\gamma}$ //$(011)_{\alpha'}$	[-1 0 1] // [-1 –1 –1]	-	-
V2		[-1 0 1] // [-1 1 -1]	[0.5774 – 0.5774 0.5774]	60.00
V3		[0 1 –1] // [-1 –1 -1]	[0.0000 – 0.7071 – 0.7071]	60.00
V4		[0 1 –1] // [-1 1 –1]	[0.0000 0.7071 0.7071]	10.53
V5		[1 –1 0] // [-1 –1 1]	[0.0000 0.7071 0.7071]	60.00
V6		[1 –1 0] // [-1 1 -1]	[0.0000 – 0.7071 – 0.7071]	49.47
V7		[1 0 –1] // [-1 –1 1]	[-0.5774 – 0.5774 0.5774]	49.47
V8		[1 0 –1] // [-1 1 –1]	[0.5774 – 0.5774 0.5774]	10.53
V9	$(1\text{-}11)_{\gamma}$ //$(011)_{\alpha'}$	[-1 –1 0] // [-1 –1 1]	[-0.1862 0.7666 0.6145]	50.51
V10		[-1 –1 0] // [-1 1 -1]	[-0.4904 –0.4625 0.7387	50.51
V11		[0 1 1] // [-1 –1 1]	[0.3543 –0.9329 –0.0650	14.88
V12		[0 1 1] // [-1 1 -1]	[0.3568 –0.7136 0.6029]	57.21
V13		[0 –1 1] // [-1 –1 1]	[0.9329 0.3543 0.0650]	14.88
V14		[0 –1 1] // [-1 1 -1]	[-0.7387 0.4625 –0.4904]	50.51
V15	$(\text{-}111)_{\gamma}$ //$(011)_{\alpha'}$	[-1 0 –1] // [-1 –1 1]	[-0.2461 –0.6278 –0.7384]	57.21
V16		[-1 0 –1] // [-1 1 -1]	[0.6589 0.6589 0.3628]	20.61
V17		[1 1 0] // [-1 –1 1]	[-0.6589 0.3628 –0.6589]	51.73
V18		[1 1 0] // [-1 1 -1]	[-0.3022 –0.6255 –0.7193]	47.11
V19		[-1 1 0] // [-1 –1 1]	[-0.6145 0.1862 –0.7666]	50.51
V20		[-1 1 0] // [-1 1 -1]	[-0.3568 –0.6029 –0.7136]	57.21
V21	$(11\text{-}1)_{\gamma}$ //$(011)_{\alpha'}$	[0 –1 –1] // [-1 –1 1]	[0.9551 0.0000 –0.2962]	20.61
V22		[0 –1 –1] // [--1 1 -1]	[-0.7193 0.3022 –0.6255]	47.11
V23		[1 0 1] // [-1 –1 1]	[-0.7384 –0.2461 0.6278]	57.21
V24		[1 0 1] // [-1 1 -1]	[0.9121 0.4100 0.0000]	21.06

Lath martensite forms in low and medium-Carbon steels and consists of parallel arrays or stacks of board- or lath-shaped crystals. In these steels most of the crystals in a parallel group have the same crystal orientation and the parallel groups are referred to as blocks [52]. As Carbon concentration increases, the parallel or almost parallel crystals in a group, termed packets, may have different orientations and variants of $\{557\}_A$ habit planes around a given $\{111\}_A$ plane [53-54]. Plate martensite crystals form in non-parallel arrays and are characterized by irrational habit planes, including $\{3\ 10\ 15\}_A$, $\{2\ 2\ 5\}_A$ and $\{259\}_A$ [55]. The low M_s temperatures, in high Fe-C alloys and steels, cause the lath martensite crystals to form at temperatures where the lattice invariant deformation is accomplished by twinning and limited dislocation motion occurs.

The morphology of the martensite affects the deformation and strengthening of the microstructure in a number of ways. In lath martensites, the block and packet structures, because of the largely common crystallographic orientation of the parallel laths within the blocks and packets, become the effective grain structures, which control deformation. Similarly, because of common $\{1\ 0\ 0\}_m$ cleavage planes in the parallel laths in blocks and packets of martensite, the size of cleavage facets which produce brittle transgranular fracture is directly related to the packet size [56-57]. Also the morphology of the retained austenite within lath and plate martensites determines whether the austenite will mechanically transform by stress- or strain-induced mechanisms [58]. The non-parallel formation of plate-shaped martensite crystals often results in intraplate microcracking due to the impingement of the plates during quenching [54].

2.2.10.2 Theory of the martensitic transformation

A number of crystallographic and thermodynamic theories have been proposed to explain the transformation mechanisms in martensite formation. In the current thermodynamic theories on the growth of the martensite nucleus, the interfacial and internal chemical energies are considered to be dominant, as in the case of the crystallization in a liquid. In addition in solids, the strain energy of the transformation is also taken into account. Thermodynamic theories assume thermal equilibrium and ignore the microstructural and crystallographic characteristics of the martensitic transformation [36]. The Bowles and Mackenzie model [in 36], one of the phenomenological theories, predicts the crystallographic features such as the habit plane, the strain and the orientation relationships between parent austenite and product martensite. Kelly [59] recently demonstrated that, when applied in a rigorous fashion, the Infinitesimal Deformation (ID) approach is exactly equivalent to the Phenomenological Theory of the Martensitic Transformation (PTMT). The disadvantages of the PTMT are its computational cost and its complexity that makes it less understandable than the physical concepts of the minimization of the strain energy following the well-known Eshelby analysis used in the ID approach.

2.2.11. The Bowles – Mackenzie model [in 36]

2.2.11.1. Lattice parameters and tetragonality of the martensite.

Lattice parameters of martensite and retained austenite can be measured by X-ray diffraction with good accuracy. Cheng et al. [66] noticed a significant redistribution of Carbon atoms and a disappearance of the tetragonality of a 5.1at.%C martensitic steel at room temperature during aging times of less than 50 hours. Carbon atoms segregated to lattice imperfections and also transfer from a/b-type octahedral interstices to c-type interstices, thereby decreasing the c_m parameter at room temperature.

Lyssak and co-workers [67] found that the tetragonality of the martensite is abnormally small for Mn steels. Moreover, there are several alloy systems in which the tetragonality of martensite containing Carbon does not obey the well-known experimental equation:

$$c/a = 1 + 0.046p$$

where p is the mass percentage of carbon in the steel.

Kajiwara and Kikuchi [68] made a very extensive and systematic study on the martensite tetragonality in Fe-Ni-C alloys, and found that the tetragonality is quite dependent on the mode of the lattice invariant deformation in the martensite. Uehara et al. [68] have investigated the tetragonality of martensite in high Carbon- Iron alloys containing some Aluminium. From their study it appears that the tetragonality is enhanced by Aluminium and Nickel additions that stop Carbon atoms from moving out of octahedral sites to tetrahedral sites during quenching (auto-tempering). They have measured the tetragonality in martensite containing 2 mass %C and up to 6 mass %Ni using XRD equipment fitted with a cooling unit. Their measurements were done at temperatures as low as 90K.

2.2.11.2. The principal strain.

After measuring the lattice parameters of the parent austenite and the product martensite, the Bowles and Mackenzie (BM) model for predicting the transformation characteristics may be applied as follows:

The principal strains in the Bain distortion denoted by η_i (eta), are represented by:

$$\eta_1 = \sqrt{2}\, a_M / a_\gamma \qquad \text{(2.20a)} \qquad \text{along x-1}$$

$$\eta_2 = \sqrt{2}\, a_M / a_\gamma = \eta_1 \qquad \text{(2.20b)} \qquad \text{along x-2}$$

$$\eta_3 = c_M / a_\gamma \qquad \text{(2.20c)} \qquad \text{along x-3}$$

A unit sphere representing the austenite crystal $x_1{}^2 + x_2{}^2 + x_3{}^2 = 1$ transforms to an ellipsoid $\frac{x_1{}^2}{\eta_1{}^2} + \frac{x_2{}^2}{\eta_2{}^2} + \frac{x_3{}^2}{\eta_3{}^2} = 1$ due to the Bain distortion.

The cones of unextended lines are found from the equation:

$$\left(\frac{1}{\eta_1{}^2} - 1\right) x_1{}^2 + \left(\frac{1}{\eta_2{}^2} - 1\right) x_2{}^2 + \left(\frac{1}{\eta_3{}^2} - 1\right) x_3{}^2 = 0 . \qquad (2.21)$$

The semi-apex angle Φ' of the cone is obtained from the value of $\frac{x_2}{x_3}$ when $x_1 = 0$:

$$\tan(\Phi') = \left(\frac{x_2}{x_3}\right)_{x=0_1} = \left(\frac{1-\eta_3{}^2}{\eta_1{}^2 - 1}\right)^{\frac{1}{2}} \left(\frac{\eta_1}{\eta_3}\right). \qquad (2.22)$$

Φ' gives the positions of the unextended lines after transformation. The initial cone of the unextended lines can be determined by considering a hypothetical inverse transformation, such as α' to γ transformation, i.e. a unit sphere representing the martensite crystal transforms to an ellipsoid representing the austenite.

$$\eta_1{}^2 x_1{}^2 + \eta_2{}^2 x_2{}^2 + \eta_3{}^2 x_3{}^2 = 1 \qquad (2.23)$$

the semi-axes of which are $\frac{1}{\eta_1}$, $\frac{1}{\eta_2}$, $\frac{1}{\eta_3}$. Therefore, it is seen that the equation:

$$(\eta_1{}^2 - 1) x_1{}^2 + (\eta_2{}^2 - 1) x_2{}^2 + (\eta_3{}^2 - 1) x_3{}^2 = 0 \qquad (2.24)$$

represents the locus of all vectors that are unchanged in magnitude due to the hypothetical inverse transformation. The locus is nothing else but the initial cone of the unextended lines. The semiapex angle Φ of the initial cone is calculated from:

$$\tan(\Phi) = \left(\frac{x_2}{x_3}\right)_{x=0_1} = \left(\frac{1-\eta_3{}^2}{\eta_1{}^2 - 1}\right)^{\frac{1}{2}} \qquad (2.25)$$

2.2.11.3. Calculation of invariant lines and normal

A plane normal is defined as a vector whose direction is parallel to the normal of the plane and whose magnitude is proportional to the inverse of the interplanar distance. This vector is simply a reciprocal lattice vector. Then a unit sphere (formed by the plane normal) in the austenite lattice transforms to an ellipsoid, whose semi-axes are:

$$\frac{1}{\eta_1},\ \frac{1}{\eta_2},\ \frac{1}{\eta_3}.$$

The intersection of the ellipsoid with the unit sphere forms a circle, and a cone passing through the circle gives the final position of the plane normal which is unchanged in magnitude. Such a normal is termed an *unextended normal*.

An unextended normal and an unextended line that are also unchanged in direction are termed an *invariant normal* and an *invariant line*, respectively.

Consider x-1 or x-2 is a unit vector parallel to the invariant line. The Bain distortion allows x_i also to transform through the equivalence:

$$\underline{x}_i = Bx_i. \qquad (2.26)$$

Because x_i is unchanged in length, $x_i' x_i = 1$ holds. In addition, $p_2' x_i = 0$ because the shear plane p_2' of the complementary shear must involve three equations for x_i.

Assuming: $p_2' = \left(1/\sqrt{2}\right)\!.(101)$ (2.27)

one obtains the following three equations for x_i:

$$x_1^2 + x_2^2 + x_3^2 = 1 \qquad \text{equivalent to } P_1 = R\left(BPB^{-1}\right)B = RBP \qquad (2.28a)$$

$$\eta_1^2 x_1^2 + \eta_2^2 x_2^2 + \eta_3^2 x_3^2 = 1 \quad \text{equivalent to } P_1 = I + d_1 p_1' \qquad (2.28b)$$

$$x_1 + x_3 = 0$$

From these equations, two solutions for x_i are obtained: x_{i1} and x_{i2}.

Let a unit normal $n_i' \left(n_1, n_2, n_3\right)$ be the invariant normal. The Bain distortion then causes n_i' to transform to $\underline{n}_i' = n_i' B^{-1}$. As the $\underline{n}_i'$ is unchanged in length, $\underline{n}_i' \underline{n}_i = n_i' B^{-2} n_i$. In addition, $n_i' d_2 = 0$ because the plane with normal n_i' does contain the shear direction d_2. Assuming that d_2 is parallel to $\left[\bar{1}\ \ 0\ \ 1\right]$, one obtains the following three equations for n_i':

$$n_1^2 + n_2^2 + n_3^2 = 1$$

$$\frac{n_1^2}{\eta_1^2} + \frac{n_2^2}{\eta_2^2} + \frac{n_3^2}{\eta_3^2} = 1 \qquad (2.29)$$

$$-n_1 + n_3 = 0$$

From these equations two solutions for n_i' are derived, viz. n_{i1}' and n_{i2}'

Four combinations of x_i and n_i' are possible. From these four, one combination will be taken for numerical calculations.

2.2.11.4. The Bain distortion

The Bain distortion is represented by the matrix B:

$$B = \begin{bmatrix} \eta_1 & 0 & 0 \\ 0 & \eta_2 & 0 \\ 0 & 0 & \eta_3 \end{bmatrix} \qquad (2.30)$$

$$\underline{x}_i = Bx_i$$

Now p_2' transforms to $p_2' B^{-1}$ due to the Bain distortion. Considering the normalized $\underline{p}_2'$, one finds

$$\underline{p}_2' = p_2' B^{-1} / \left(p_2' B^{-2} p_2\right)^{1/2} \qquad (2.31)$$

$\underline{x}_i$ is seen to lie in the plane with normal $\underline{p}_2'$, because $\underline{p}_2' . \underline{x}_i$ =0

2.2.11.5 Calculation of the invariant line strain S

The invariant line strain S can be calculated if the rotation matrix is known, with which both $\underline{x}_i$ and $\underline{n}_i$' rotate back to the initial positions, x_i and n_i'. Such a rotation matrix can be obtained in principle by solving two equations, $R_0 \underline{x}_i = x_i$ and $\underline{n}_i' R_0^{-1} = n_i'$, and using the properties of an orthogonal matrix. But in practice, solving these equations is not necessarily easy. A more convenient method is used to obtain the invariant line strain as follows:

The first step is to obtain a rotation matrix that transforms $\underline{x}_i$ to x_i and the second is to obtain a rotation matrix that leaves x_i unchanged and transforms $\underline{n}_i$' to n_i'. The former matrix can be expressed as the product of a rotation matrix R_1, whose elements in the first column coincide with the components of x_i, by another rotation matrix R_2', whose elements in the first row coincide with the components of $\underline{x}_i$. Though the other elements of the rotation matrices, R_1 and R_2', are arbitrary, their three-component vectors must satisfy the orthogonal conditions. As component vectors satisfying these conditions, p_2 and $\underline{p}_2$ will be chosen for R_1 and R_2 respectively. Then one obtains:

$$R_1 = (x_i, p_2, u) \ ,$$

where $u = x_i$ x p_2

$$R_2 = (\underline{x}_i, \underline{p}_2, v),$$

where $v = x_i$ x $\underline{p}_2$

$R_1 \times R_2{}'$ is a rotation matrix that makes $\underline{x_i}$ rotate back to x_i. In other words, the matrix defined by $S_{(0)} = R_1 \times R_2' \times B$ has x_1 as an invariant line. In order to obtain a rotation matrix that makes the $\underline{n}_1$ transform to $\underline{n}_1{}'$ and x_1 remain unchanged, it is convenient to convert the basis to a new i basis $(i_1 \; i_2 \; i_3)$ defined by three orthogonal vectors x_1, p_2 and u.

In the i basis $S_{(0)} = R_1 \times R_2' \times B$ can be rewritten as $(iS_{(0)}i) = R_2' \times B \times R_1$.
Then, the invariant line strain S referred to the i basis (iSi) is obtained by adding a rotation of β around x_1; that is,

$$[1 \quad 0 \quad 0, 0 \quad \cos\beta \quad -\sin\beta, 0 \quad \sin\beta \quad \cos\beta] \times R_2' B R_1 = (iSi)$$

$$\begin{bmatrix} 1 & 0 & 0 \\ 0 & \cos\beta & -\sin\beta \\ 0 & \sin\beta & \cos\beta \end{bmatrix} R_2{}' B R_1 \equiv (iSi) \qquad (2.32)$$

The value of β must be chosen so that $n_i{}'$ remains unchanged after it is operated on by (iSi). When $n_i{}'$ is referred to the I basis, that is,

$$n_{1i} = n_1{}' R_1$$
$$iS_0 i = R_2{}' B R_1$$
$$(n_i{}'; i) = n_i{}' R_1 \qquad (2.33)$$

The following equation must hold:

$$(n_i{}'; i)(iSi) = (n_i{}'; i) \qquad (2.34)$$

From these equations β can be determined. That is substituting equations (2.32) and (2.33) into (2.34).

$$Q = \begin{bmatrix} 1 & 0 & 0 \\ 0 & \cos\beta & -\sin\beta \\ 0 & \sin\beta & \cos\beta \end{bmatrix}$$

$$(iSi) = Q R_2{}'^{*} B R_1 = \begin{bmatrix} 1 & 0 & 0 \\ 0 & \cos\beta & -\sin\beta \\ 0 & \sin\beta & \cos\beta \end{bmatrix} R_2{}'^{*} \begin{bmatrix} \eta_1 & 0 & 0 \\ 0 & \eta_2 & 0 \\ 0 & 0 & \eta_3 \end{bmatrix} R_1 \qquad (2.35)$$

The shape strain matrix is then given by:

$$S = R_1(iSi)R_1{}' \qquad (2.36)$$

2.2.11.6. Calculation of the total shape change P_1 and the complementary shear P_2

The invariant plane normal $p_1{}'$ in the shape deformation is parallel to $p_2{}'S^{-1} - p_2{}'$. The normalised vector is $p_1{}'$ and D is parallel to $p_1{}'$. The Displacement Vector d_1 of the shape deformation is equal to:

$$(Sd_2 - d_2)/(p_1{}'d_2). \qquad (2.37)$$

where y is an arbitrary vector lying in the plane with normal $p_1{}'$.
Then, choosing y to be the cross product $[1 \quad 0 \quad 0]$ x p_1:

$$d_2 = (y - yS^{-1})/(p_2{}'y') \qquad (2.38)$$

Thus, d_1 is not a unit vector. From the normalisation factor for this vector, the magnitude of the shape deformation can be obtained:

$$m_1 = norm(d_1) \qquad (2.39)$$

From the normalisation factor for d_2, the magnitude m_2 and the shear angle α of the complementary shear can be obtained through:

$$\begin{aligned} &\lambda_1 = \eta_1 \\ &\lambda_3 = 1 \\ &\lambda_2 = \eta_1.\eta_3 \\ &s = \left[(\lambda_1{}^2 - 1)(1 - \lambda_2{}^2)\right]^{1/2} \qquad (2.40) \\ &m_2 = s/(\lambda_1\lambda_2) \\ &\alpha = a\tan(m_2/2) \end{aligned}$$

2.2.11.7. Calculation of the orientation relationship

2.2.11.7.1 Kurdjumov – Sachs

The total shape change P_1 associated with the transformation is equal to SP. Since P is not accompanied by any change of crystal orientation, the orientation relationship is determined only by S. According to the Bain correspondence, $(1 \quad 1 \quad 1)_f$ and $[\bar{1} \quad 0 \quad 1]_f$ in the austenite lattice correspond to $(0 \quad 1 \quad 1)_b$ and $[\bar{1} \quad \bar{1} \quad 1]_b$, respectively in the martensite lattice. The $(1 \quad 1 \quad 1)_f$ plane should be transformed by S to $J = [1 \quad 1 \quad 1]$. The $(1 \quad 1 \quad 1)_f$ plane should be transformed by S to $(1/\sqrt{3})(1 \quad 1 \quad 1)S^{-1}$. The unit normal of the transformed $(1 \quad 1 \quad 1)_f$ plane is u_1. u_1 should be a unit vector parallel to the normal of the $(0 \quad 1 \quad 1)_b$ plane.

Therefore, the scalar product of the normal of the $(0\ \ 1\ \ 1)_b$ plane and that of the original $(1\ \ 1\ \ 1)_f$ plane is the cosine of the angle between $(1\ \ 1\ \ 1)_f$ and $(0\ \ 1\ \ 1)_b$. Next, $[\bar{1}\ \ 0\ \ 1]_f$ is transformed by S to $S[\bar{1}\ \ 0\ \ 1]_f$. By normalizing this, we obtain a unit vector parallel to $[\bar{1}\ \ \bar{1}\ \ 1]_b$. From the scalar product of this unit vector with that of $[\bar{1}\ \ 0\ \ 1]_f$, the angle between $[\bar{1}\ \ 0\ \ 1]_f$ and $[\bar{1}\ \ \bar{1}\ \ 1]_b$ is obtained. The non-parallelism indicates that the K-S relation does not hold exactly.

2.2.11.7.2. Nishiyama Wasserman

Use similar calculations regarding the $[\bar{1}\ \ \bar{1}\ \ 2]_f$ direction and the corresponding $[0\ \ \bar{1}\ \ 1]_b$ direction.

2.3. Tempered martensite and its mechanical properties

Generally mechanical properties of a material are determinable (at least in principle), if its microstructure is known in detail. The crystal structure and the chemical composition of the phases in the microstructure are important factors for the mechanical, physical, and chemical properties. Volume fraction, shape, arrangement, and orientation of microstructural constituents are less important for the chemical properties, where constituents can be compared (e.g. in their corrosion resistance). In some cases, such as intercrystalline corrosion or high temperature corrosion, the phase boundaries and the chemical composition of the surrounding matrix must be taken into account. Volume fraction, shape, arrangement, and phase orientation in a microstructure have a greater influence, however, on the physical and mechanical properties. In the different microstructures, the strengthening mechanisms in steels – strengthening by solid solution, dislocations, second phase particles and grain size – are superimposed. Additional effects arise from the arrangement of second phases.

2.3.1 Effect of Carbon additions

In steels, the Carbon content of the alloy will have a significant effect on the hardness of martensite. At too high a value of Carbon, retained austenite will appear and the macro-hardness of the alloy will decrease once more. It appears that the hardness of martensite is a linear function of the square root of the Carbon content. These results are a summary of a large number of investigations [72,73] that also include low alloy steels where the tensile strength of a martensitic steel obeys the following equation:

$$\sigma_M = \sigma_M^0 + K_M \sqrt{C_M}$$

where σ_M^0 and K_M are constants and C_M is the mass percent of Carbon in the steel. This relationship is, of course, only valid if the alloy contains 100% martensite. If this is not the case, then a weighting factor needs to be introduced. Such a relationship is of particular use in martensitic/austenitic dual phase steels.

2.3.2 Effect of Sulphur and Manganese content

There is abundant [74], evidence that reducing the inclusion volume fraction by lowering Sulphur levels to the minimum possible, will improve the upper shelf fracture energy and the impact toughness of the steel. In some cases such data have been interpreted in terms of sulphide spacing and shape and their impact has been primarily the motivation in the production of cleaner steels with very low Sulphur levels. Today, Ultra High Strength steels can be produced with Sulphur levels of the order of 0.003wt %S, or even lower. The Rice and Johnson model [in 74] suggests that the upper shelf fracture toughness of ultra high strength steels should scale as the square root of the sulphide spacing.

Implicit in the second approach to the design of ultra high strength steels is the assumption that appropriate modifications to the microstructure by changes in composition, heat treatment or both, can be found which will improve the toughness of the steel. Empirical knowledge has been gained which suggests that the microstructural features that influence the toughness, include prior austenite grain size, martensite packet size, the amount, morphology and mechanical stability of retained austenite, the size, spacing, shape and coherency of particles precipitated upon tempering, as well as the relative amounts of dislocated and plate-shaped martensite. The proposed model of Garrison [in 74] suggests that at the point of fracture initiation the crack tip opening displacement will scale as the product of two terms – one being the sulphide spacing and the other a measure of localised ductility lacking in the Rice and Johnson model. The data to date suggest that it is through this measure of localised ductility that the microstructure influences the toughness of the steel. This implies that two distinct alloy design methodologies are possible, one to maximise the sulphide spacing and the other to maximise the localised ductility through control of the microstructure.

The critical crack tip opening displacement, δ_{IC} , can be related to the fracture toughness, through the equations:

$$\delta_{IC} = d_n \frac{J_{IC}}{\sigma_0} \qquad (2..41)$$

$$J_{IC} = \frac{K_{IC}{}^2}{E'} \qquad (2.42)$$

$E' = E$ for plane stress conditions and $E' = \dfrac{E}{\left(1-\nu^2\right)}$ for plane strain conditions

where E is Young's modulus, σ_0 is the average of the yield strength and ultimate tensile strength, ν is Poisson's ratio, and d_n is a function of the yield strain, K_{IC} is the fracture toughness, J_{IC} is the area specific energy for crack propagation, and whether plane stress or plane strain conditions are assumed. The plane strain fracture toughness should scale E' as:

$$K_{IC} \approx \left\{ \frac{X_0 (R_V / R_I) \sigma_0 E}{d_n} \right\}^{1/2} \qquad (2.43)$$

This approach predicts the same dependence on X_0, the primary particle spacing, as the Rice and Johnson model, but (R_V / R_l) introduces a measure of the ductility lacking in that model. R_l is the radius of primary particles assumed to be spherical sulphide and R_V is the void radius. This model has been applied to several ultra high strength steels for which the primary particles are spherical sulphides. The average three-dimensional nearest neighbour distance between sulphides, X_0, is been calculated from [74]:

$$\frac{X_0}{R_0} = 0.89 f^{-1/3} \qquad (2.44)$$

where f is the sulphide volume fraction and R_0 the average sulphide radius.

From formulas (2.41) to (2.44) there appears to be an excellent correlation between δ_{IC} and the quantity $X_0 (R_V / R_l)\big|_{R_0}$. However, the factors which determine $(R_V / R_l)\big|_{R_0}$ are not really known. According to the model, $(R_V / R_l)\big|_{R_0}$ will continue to increase in accordance with the stress-strain history until the voids nucleated at sulphides coalesce through processes of void sheet coalescence, strain localisation or both. There is clear evidence that the microstructure can influence $(R_V / R_l)\big|_{R_0}$. However, a number of other factors could also influence this parameter. Presumably these include the yield strength and work hardening capacity as both influence flow localisation. In addition, while manganese sulphides are believed to be weakly bound to the matrix, it is possible that the nucleation strains as well as spatial and size distributions of the sulphides could influence $(R_V / R_l)\big|_{R_0}$. The influence of microstructure on $(R_V / R_l)\big|_{R_0}$ is most clearly illustrated by considering the effect of tempering on the toughness. From the equation $\frac{X_0}{R_0} = 0.89 f^{-1/3}$, X_0 can be increased by increasing R_0, the average sulphide radius, or by reducing the sulphide volume fraction f, which in effect reduces the sulphur content. While X_0 can be increased by reducing f, the fracture toughness will scale as $f^{-1/6}$ if R_0 remains unchanged. However, if R_0 is increased without changing f, the fracture toughness will scale as $R_0^{1/2}$.

The strong dependence of fracture toughness on R_0 suggests that by increasing the average sulphide size – that is, by replacing a dispersion of fine closely spaced sulphides by larger more widely spaced sulphides – significant improvements in toughness can be realised. Even if Sulphur levels are reduced to very low levels ($\cong 0.001 wt\%$ S), it should be possible to achieve further improvements in toughness by increasing X_0 through R_0. At a sulphide spacing of about $10\,\mu m$, low alloy quenched and tempered steels can achieve a fracture toughness of 115 MPa(m)$^{1/2}$ at a yield strength of about 1700 MPa [74]. Significant further improvements in toughness of such steels will require sulphide spacing of the order of 20 – 30 μm. The only way sufficiently large sulphide spacing can be obtained is by reducing sulphide volume fractions to the minimum level possible and then increasing the average size.

Therefore, the application of this methodology for improving toughness reduces to the problem of maximising, for a given sulphide volume fraction, the average size.
The methods utilised in achieving this goal will depend on the nature of the sulphides present in the steel. If sulphides are Manganese sulphides then it is suggested that maximum sulphide size, and hence spacing, can be achieved by integrated application of three strategies. The first is the control of sulphide shape and size in the as – cast condition with the goal being equiaxed sulphides of the largest possible size. The second is to utilise forging techniques, which minimize elongation of the sulphides in the as-cast structures. The third is to coarsen the sulphide distribution after forging [74].

On solidification, three primary sulphide morphologies are observed [74]. Type I sulphides are spherical and are favoured by high Oxygen and low Carbon levels. Type II sulphides are often dendritic, rosette-like or fan-like in form, and are favoured by low Oxygen levels. Type III sulphides are faceted equiaxed particles and are favoured by low Oxygen levels in combination with high Carbon levels, Silicon additions and Aluminium additions. There is also an influence of Sulphur content on sulphide type, with type III sulphides favoured as the Sulphur content is reduced. Cooling rate on solidification can influence the sulphide type. Type II sulphides are favoured over both type I and type III sulphides as the cooling rate is increased. It is agreed [74] that type II sulphides form as a result of the eutectic reaction $L \rightarrow Fe + MnS$. Type III sulphides, because of their faceted form, are believed to precipitate as a solid in the interdendritic liquid. However, Type III sulphides seem to be more uniformly distributed than type II sulphides [74]. This could be attributed to their precipitation in the liquid at higher temperatures than Type II sulphides and their entrapment by growing dendrites. The most useful compositions should be those, which promote Type III sulphides.

There have been numerous studies [74] of the effects of temperature and extent of deformation during hot rolling on the shape and morphology of manganese sulphides. During hot rolling the rod-like type II sulphides become aligned parallel to the rolling direction and type I and type III sulphides become elongated plates, lengthening primarily parallel to the rolling direction. The extent of this elongation is minimised by rolling at the highest possible temperatures. In general it has been found that type III sulphides are more plastic than type I sulphides and elongate during rolling to a greater extent [74]. This has been attributed to the higher Oxygen content of type I sulphides. However, upset and cross forging could alter this simple description. Rolling would orient the rod-like Type II sulphides parallel to the rolling direction and elongate Type III sulphides in the direction of rolling. However, upset and cross forging could break up the Type II sulphides and possibly preserve the equiaxed nature of the Type III sulphides. In that case, after upset and cross forging, the sulphides precipitated as Type II and Type III, would now consist of small broken fragments and larger equiaxed particles respectively.

2.3.3. Effect of alloying elements

Tanino and co-workers [26] have shown that Mo moderately increases the yield strength of martensitic steels, probably due to its large atomic size, whereas the addition of Mn results in a slight decrease in yield strength. Schramm et al. [2] reported that both Mn and Mo increase the stacking fault energy of the austenite matrix, although Mn is generally considered to stabilize the γ- phase by lowering the stacking fault energy of the austenite.

Carbon is considered to increase the stacking fault energy of the austenite matrix [73]. The strengthening of the austenite matrix will require a larger driving force for its decomposition to martensite, giving rise to a decrease in M_s temperature. Silicon has an incredibly small solubility in cementite. Therefore, increasing the Silicon concentration of a steel to a value greater that about 1.5 wt%Si ensures the absence of cementite in upper bainite [75]. Interlath cementite in bainite is responsible for initiating fracture in high-strength steels. Its absence is, therefore, expected to make the microstructure more resistant to cleavage failure and void formation.

The ductile films of austenite, which usually are intimately dispersed between the plates of martensite, have a blunting effect on crack propagation. They further add to the toughness by increasing the energy of fracture as the austenite is induced to transform to martensite under the influence of the stress field of a propagating crack. This is the TRIP effect, or transformation induced plasticity effect.

2.3.4. Ageing of Iron – Carbon martensite at room temperature

The details of Carbon partitioning during or after displacive or martensitic transformation are still somewhat controversial. In martensite, the displacive transformation is usually believed to occur without diffusion of Carbon or interstitials [41], and thus the body – centred martensite phase can be substantially saturated with Carbon. Subsequent Carbon partitioning between martensite and retained austenite is not considered because the temperature is too low for substantial amounts of diffusion to occur after quenching, and because Carbon supersaturation is usually eliminated by competing processes, e.g. carbide precipitation during tempering [59]. There is, however, evidence that Carbon partitioning from martensite to retained austenite does occur to thin interlath films during cooling [26] or by isothermal holding in a Si-containing steel after transformation [76].

Carbon partitioning is one means of stabilizing austenite against further transformation at lower temperatures, and is likely to be especially important in these steels containing alloying additions (e.g. Silicon) that suppress formation of Iron carbides [77].

2.3.5. Low temperature tempering of Martensite

Generally, quenching and tempering are well-established means to produce strengthening in steel, which can be achieved mainly due to the precipitation of a fine dispersion of alloy carbides during tempering at elevated temperatures [72]. Known for forming the highest level of strength in steel, the martensite structure is rarely used in an untempered condition because a large number of internal stresses associated with the transformation cause the material to be lacking in ductility [2,78]. However, low-temperature tempering is sufficient to reduce these stresses considerably without changing the basic features of the martensite structure. Therefore, from the commercial point of view, the study of martensitic steels has to include that of steels tempered in the range of 200-250^0C. However, apart from the effect of tempering temperature, the strength of the martensitic structure is dominated by the Carbon content and volume fraction of martensite and, therefore, is affected indirectly by the M_s and the M_f temperatures [75].

The mechanical behaviour of a quenched-and-tempered steel depends strongly on its microstructure. Thus, the study of the effects of the microstructure and dislocation substructure of a steel on its strength, ductility and fracture characteristics is of great importance from the viewpoint of both theory and practice. The so-called "first stage" of tempering (T1) is associated with the appearance of a metastable and coherent ε transition carbide, which precipitates uniformly throughout the martensite phase. Although the precipitation of the transition carbide proceeds within a few minutes in the temperature range of 100 to $200^{o}C$, precipitation of ε carbides has been detected at temperatures as low as room temperature after several months of aging [78]. Tempering well into the T1 temperature range leads to a dispersion of coarse particles in a matrix of low-Carbon martensite. Above $200^{o}C$ the transition carbide is replaced by the more stable Fe_3C and at higher temperatures by the M_3C carbide if substitutional carbide forming alloying elements are present in the steel. This implies diffusion of substitutional alloying elements at the higher temperatures. If the steel is tempered below $200^{o}C$ the transformation to cementite would necessitate several months to become effective [78]. The precipitation of cementite marks the third stage of tempering.

2.3.5.1. Structure and Morphology of the Stage 1 Carbide

In his early X-ray investigation, Jack [in 72] found that the Stage 1 carbide in high-Carbon martensite possessed hexagonal symmetry and he called this phase epsilon carbide (ε carbide). Jack's proposed orientation relationship between ε carbide and low-carbon martensite:

$$(0001)_{\varepsilon} // (011)_{\alpha}$$

and

$$(10\bar{1}1)_{\varepsilon} // (101)_{\alpha}$$

was confirmed by Wells [in 72] more than 20 years ago and has also been found in numerous other selected-area electron-diffraction studies. Unable to identify the positions of the Carbon atoms in the ε structure, Jack suggested that the ε carbide might exhibit a range of compositions from Fe_2C to Fe_3C. Later calculations based on dilatometry results [78, 79] placed the composition at $Fe_{2.4}C$. The APFIM results of Chang [in 78] on an Fe-15%Ni-1%C martensite tempered at $130^{0}C$, indicate a composition of about 20 to 25 at%C. This is close to the M_3C stochiometry, but considerably less than the 33 at% C required for an M_2C carbide. Detailed electron-diffraction investigations of Fe-C and Fe-Ni-C martensites by Hirotsu et al. [in 72] indicated that Carbon atoms may be ordered in the transition carbide, reducing the symmetry from hexagonal to orthorhombic. They referred to the ordered phase as eta carbide (η carbide) to distinguish it from Jack's hexagonal carbide. Taylor [in 72] has suggested that the η carbide can be regarded as a derivative of the ε carbide structure, and that it may be more appropriate to refer to the ordered carbide as "$\varepsilon^{'}$", thereby recognizing its structural similarity to Jack's ε carbide.

A variety of morphologies have been reported for the Stage 1 carbide. Early TEM investigations of Fe-Ni-C martensitic steels [in 72] reported a plate-like carbide with a $\{100\}_{\alpha}$ habit plane. Later work on Fe-Mn-C [in 72] alloys concluded that the carbides were rodlike in shape along $\langle 100 \rangle_{\alpha}$. Other studies of Fe-Ni-C and Fe-Si-C alloys found the carbide particles to be rodlike, but with the long axis nearly parallel to $\langle 211 \rangle_{\alpha}$. To complicate this issue further, several studies employing dark-field electron microscopy [72] indicated that what appeared to be rodlike carbides were actually composed of arrays of much smaller particles. The disparity among these observations suggests that alloy composition might exert an important influence on the actual carbide morphology.

2.3.5.2 Nucleation and Growth of the Stage 1 Carbide

For many years, Stage 1 carbide precipitation was regarded as a homogeneous process occurring by classical nucleation and growth in a single-phase matrix. However, results on martensite ageing [72] show that a decomposition process precedes the precipitation of T1 carbides, opening up the possibility that structural features of aged martensite influence the mechanism of subsequent Stage 1 carbide nucleation. Nakamura et al. [in 72] have suggested that stage 1 carbides emerge directly from the modulated structure associated with the prior A stage of tempering below room temperature. Nakamura et al., based on their high-resolution TEM imaging results on an Fe-1.5%C alloy, concluded that the Iron-atom displacements produced by interstitial Carbon atoms favour nucleation in the high-Carbon product of the modulated structure. Although the actual mechanism by which Stage 1 carbide nucleation occurs is not yet firmly established, the above results indicate that the nucleation of T1 carbides is heterogeneous, at least in martensites that undergo spinodal decomposition prior to T1 carbide precipitation such as in high Chromium Fe-Cr steels. Macroscopically, precipitation appears to be homogeneous, because the decomposition of virgin martensite occurs uniformly throughout the martensitic phase providing a fine, uniform distribution of sites for subsequent carbide nucleation. New insights into the nature of the growth of the Stage 1 carbide may come from recent results on Fe-Ni-C martensite [72]. What appeared to be stacking faults within platelike carbide particles were observed. These faults appear to represent shearing on the basal plane of the carbide lattice.

In considering the lattice correspondence between ε carbide and the bcc or bct parent phase, Taylor [in 72] demonstrated that the carbide habit plane is macroscopically invariant if a simple shear on the basal plane (representing an internal accommodation deformation mechanism) accompanies the orthorhombic lattice distortion that relates the two structures. Hence, the observed platelike shape of the particles would minimize the strain energy associated with precipitation.

Taylor [in 72] points out that the carbide habit plane and morphology may be composition dependent, inasmuch as the lattice constants (and hence the crystallographic relationship between parent and product phases) are generally a function of alloy composition. This may partly explain the varied carbide morphologies that have been reported. The concept of an invariant-plane strain (IPS) transformation proposed by Taylor has, of course, been widely applied to the diffusionless martensitic reaction in steels. Although the precipitation of T1 carbides is clearly not diffusionless, observations of surface relief produced by Stage 1 tempering on the surfaces of prepolished metallographic specimens [72, 71], indicate that this precipitation has a displacive component. In fact, the net shape strain produced by the bcc $\rightarrow \varepsilon'$-carbide transformation may be responsible for the stress relaxation observed during Stage 1 tempering [72], although other processes such as twinning and detwinning in the martensite phase may also operate. Evidence is accumulating that the IPS mechanism may be at play in reactions that are both displacive and diffusive in nature [72], at least when a lattice correspondence between the parent and product phases can be defined.

2.3.5.3. Kinetics of Stage 1 precipitation

The kinetics of Stage 1 carbide precipitation have been measured in a number of investigations [72]. However, overlap between the A stage (spinodal decomposition of the martensite) and the T1 stage generally complicates the interpretation of the data. Consequently, the rate-controlling mechanism(s) are still not well understood. In general, apparent activation energies in the range of 100 to 150 kJ/mol have been reported [72, 74]. These values are well above the activation energy for Carbon-atom diffusion in body-centred Iron. It has been suggested that carbide precipitation involves the short-circuit diffusion of metal atoms along dislocations, with an activation energy of about 140 kJ/mol. Such diffusion was invoked for the accommodation of growing particles through plastic deformation of the martensitic matrix [77]. However, the proposed IPS transformation suggests that accommodation occurs within the carbide particle, and hence growth would require an intrinsic metal-atom diffusion. Further investigation is required before the factors controlling carbide growth will be completely understood.

2.4. Mechanical properties of tempered martensitic steels

For an alloy steel with the chemical composition;

Elements	**C**	**Si**	**Mn**	**Ni**	**Cr**	**Mo**	**P**	**S**
Wt.(%)	0.39	0.24	0.61	1.46	0.67	0.17	0.021	0.006

Woei-Shyan et al. [78] have found the following main results on the tempering of the martensite:

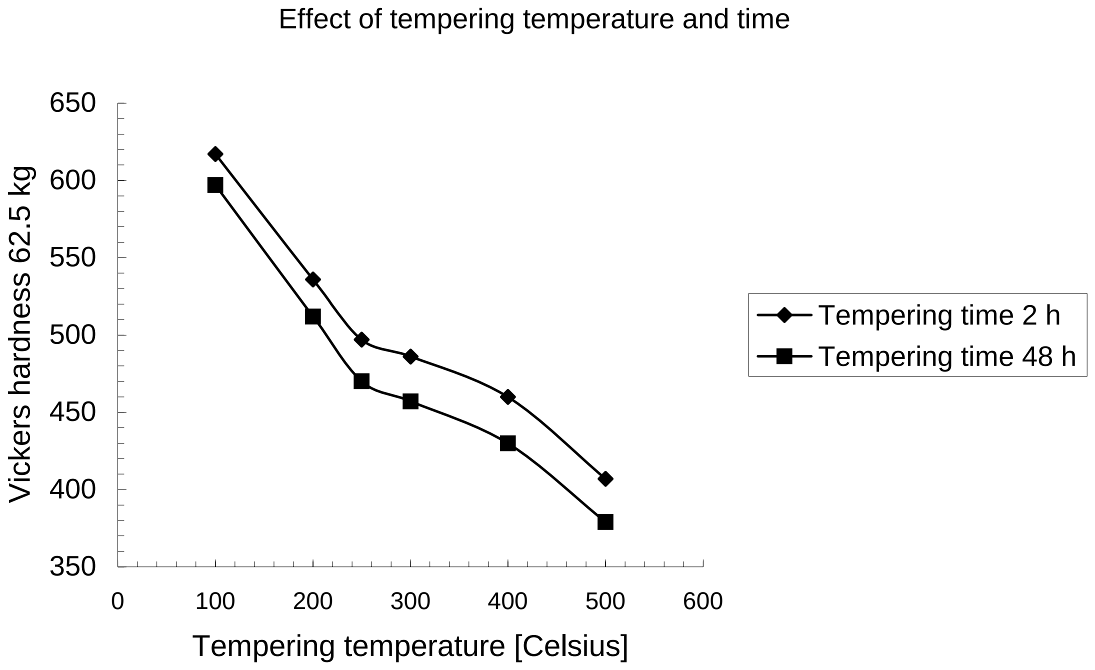

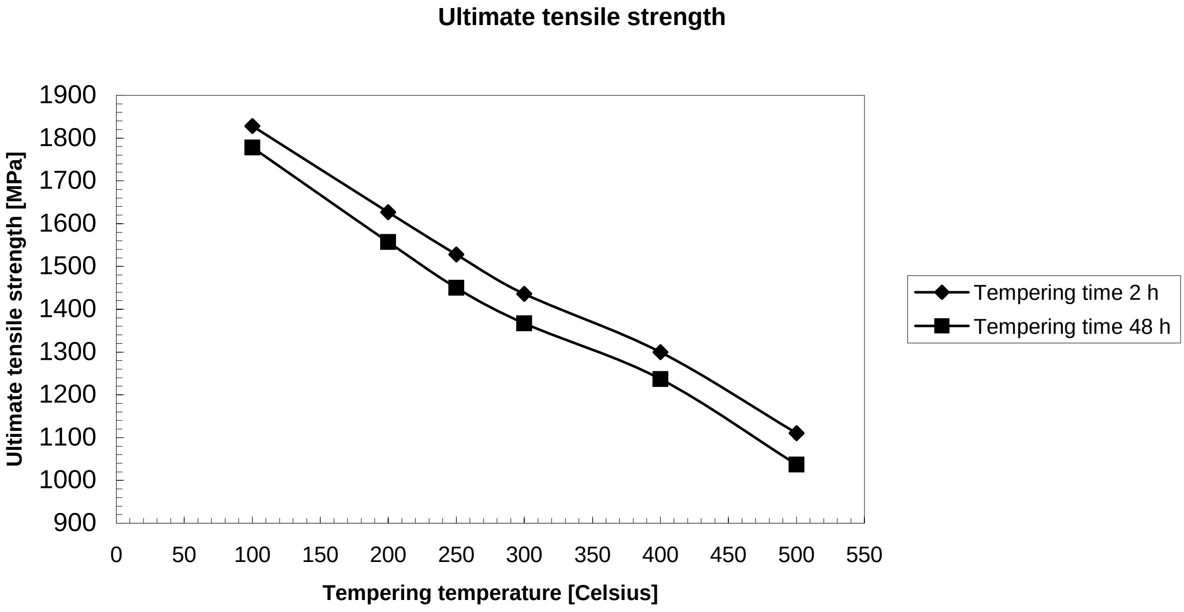

Figure 2.7. Variation of hardness and ultimate tensile strength with the tempering temperature [°C] of a low carbon steel [78]

In the as-quenched condition, the material has the highest level of strength and hardness but its ductility is the lowest, because of the presence of untempered martensite. A large amount of distortion occurs during the formation of the platelets of martensite, which leads to a rapid increase in strength and hardness. The thermal instability of interlath austenite after tempering often leads to the formation of carbide films, which is a fairly general cause of tempered martensite embrittlement [78]. Woei-Shyan et al correlated a loss in toughness after tempering at $300\,^{0}C$ with the retained interlath austenite and the formation of interlath carbide films that are decomposed from the lath boundary retained austenite.

The study of retained austenite films associated with martensite in low alloy steels has assumed new significance, primarily due to its apparent effect on the mechanical properties of quenched and tempered high-strength steels [51]. Retained austenite has been found even in low-alloy steels with high M_S temperatures after fast cooling to $-196\,^{0}C$ [80]. Since such refrigeration fails to give a significant decrease in the amount of retained austenite, chemical or thermal stabilization has been ruled out as the possible reasons for the anomalous stability of the retained austenite films [76]. Azevedo and da Silva [in 74] using Mössbauer spectroscopy, and Bhadeshia [77] using X-ray diffraction, observed no evidence for the chemical stabilization by Carbon enrichment of the austenite. While no such enrichment is expected on the basis of the displacive nature of the martensite transformation, partitioning of Carbon is feasible either during the quench (i.e. after formation of some martensite) or during subsequent tempering [75]. Hence, although no direct evidence is available, the stability of the retained austenite has been attributed to mechanical stabilisation [76].

The propensity for austenite retention has been rationalised in terms of the local inter-martensite crystallography, and it was found that twin-related martensite variants do not favour the retention of austenite. Inter-martensite retained austenite films were most profuse when the adjacent martensite variants were in the same crystallographic orientation [81]. A mechanical stabilisation effect hindered and often prevented transformation to martensite.

Speer and co-workers [95] have recently proposed a thermodynamic model to describe the endpoint of Carbon partitioning between quenched martensite and retained austenite in the absence of carbide formation. This model assumes a stationary α / γ interface, and requires a uniform chemical potential for Carbon (but not for Iron) in the two phases, leading to a metastable equilibrium condition identified as "constrained para-equilibrium" or CPE. In their calculations the authors have shown that the metastable ortho-equilibrium condition between ferrite and austenite cannot be achieved. Consequently they developed a CPE model to predict the endpoint of Carbon partitioning in the presence of a stationary α / γ interface. They have predicted that the austenite inherits most of the Carbon in the steel at constrained para-equilibrium conditions, and the retained austenite can be highly enriched with Carbon in some instances. Applications of CPE partitioning may be considered in steels where carbide formation is suppressed (e.g. with Si, Al, P, or even Ni additions) [75]. They propose the potential for a new "quenching and partitioning" process, or Q&P, where the resulting martensite/austenite mixtures may be substituted for more conventional carbide-free bainitic microstructures such as high-strength TRIP sheet steels or even austempered ductile cast iron.

2.5. The variations of microstructure with tempering temperature and hold time

Woei-Shyan Lee et al. [78] have used TEM investigations to determine the nature of the structural changes and the dislocation distribution after various tempering processes. Since the M_s of their steel was well above room temperature, this has led to autotempering behaviour in the as-quenched structure. Thus, in the case of quenched martensite there are some brief periods in which Carbon atoms can redistribute themselves. Because the stress fields in the lath martensite are situated around individual dislocations and cell walls, certain interstitial lattice sites near to these places, such as defects, provide lower energy positions for Carbon than the normal sites. Such migration can be detected by metallography or by a smaller contribution of Carbon to electrical resistivity or to internal friction, if comparing the Carbon situated in an interstitial site near to a dislocation with that in a "normal" one [82]. Autotempered precipitates were not present in any of the twinned plates but were only resolved in the dislocated laths and untwinned plates formed at lower temperatures, i.e. near to M_f. Tempering involves many different basic processes, such as the precipitation of carbides, the decomposition of retained austenite, and the recovery and recrystallization of the martensite substructure. In the case of Woei-Shyan et al. [78], epsilon carbide ($Fe_{2.4}C$, hcp) was the carbide precipitated when the material was tempered at 200^0C for 2 h. This result confirms fully that of Jack [in 72], but differs from that of Hirotsu et al.[in 72], who found that for martensitic high-Carbon steel, the carbide precipitated during the first stage of tempering is eta-carbide or neta-Fe_2C. The material's microstructure at this temperature is shown in Figure 2.8.1, in which tangles of high-density dislocations and smaller dislocation cells are the two main characteristics in the dislocation structures. Also, epsilon carbide precipitates can be found at the interfaces between the lath martensite.

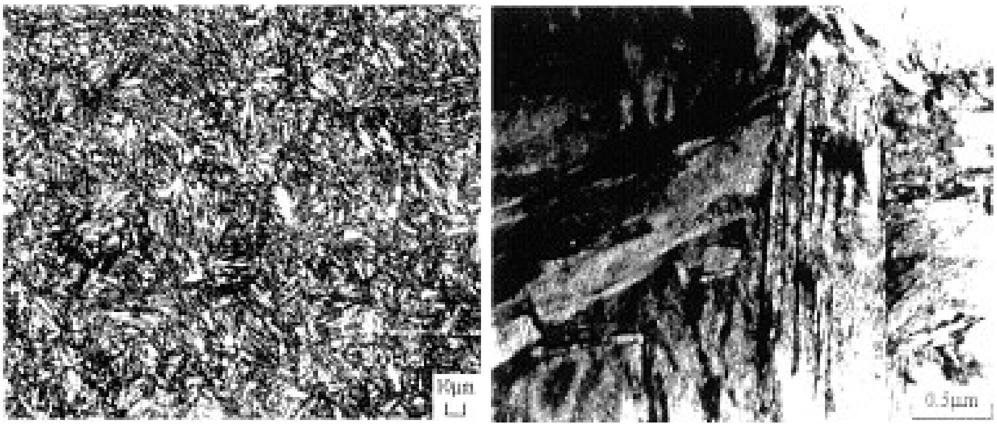

(a) (b)

Figure 2.8.1. (a) Optical micrograph and (b) TEM thin foil of an Fe – 0.2%C specimen quenched in oil (850^{0}C /30minutes) [72].

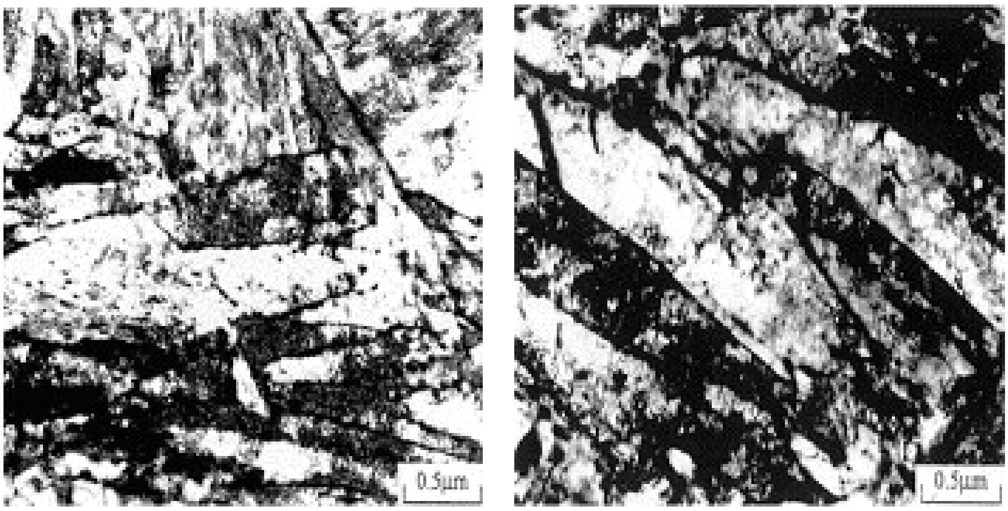

(c) (d)

Figure 2.8.1. (c) TEM micrograph of an Fe – 0.2%C specimen tempered for 2h at 200^{0}C and (d) tempered 48h at 200^{0}C [72].

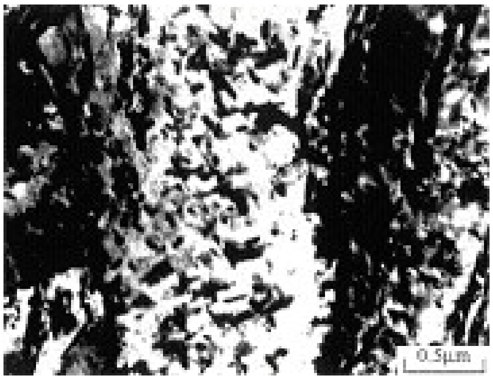

(d)

Figure 2.8.1 (e) TEM micrograph of an Fe – 0.2%C specimen quenched in oil (850^{0}C /30min) and tempered for 2h at 300^{0}C [72].

For the case of material tempered at 200°C for 48 h, the observation by transmission electron microscopy shows that some laths have grown larger. Two operating mechanisms should be involved in lath growth. One is the movement of lath boundaries and the other is the elimination of lath boundaries due to the movement and annihilation of dislocations at the boundaries. In this tempered condition, a high density of dislocations with precipitated carbides on them, are present in most of the laths. These carbides immobilise the dislocations and these cannot form dislocation arrays with a low energy as with small-angle grain boundaries. During tempering of this steel at 300°C for 2h, the nucleation sites of the carbides at low temperatures are frequently martensite lath boundaries and at higher temperatures, ferrite grain boundaries. Pietikainen [85], found similar results than Woei-Shyan and Tzay-Tian Su [78] using a steel with the chemical composition;

Element	**C**	**Si**	**Mn**	**P**	**S**	**Cr**	**Ni**	**Mo**	**V**	**Cu**	**Al**
Content	0.43	0.28	0.70	0.012	0.025	1.054	0.201	0.179	0.007	0.130	0.017

Pietikainen [85] austenitised the Charpy specimens (without notches) and the tensile specimens at $855^{0}C$ for 30 minutes. The specimens were tempered for 1 hr and for 1s in salt baths and the grain size of the austenite was about ASTM No 7. The main results from their study are presented in Figure 2.9. Pietikainen observed that on the fracture surface of the specimens tempered at $200^{0}C$, about 20% of the intergranular fracture face occurred along former austenite grain boundaries. This kind of fracture was near the hinge area of the Charpy specimen. At a tempering temperature of $100^{0}C$ this type of fracture was rare, as also in the case of a tempering temperature of $280^{0}C$ [85]. No tempered martensite embrittlement during the short tempering time is evident in the figure but with some embrittlement appearing after the 1 hour tempering times.

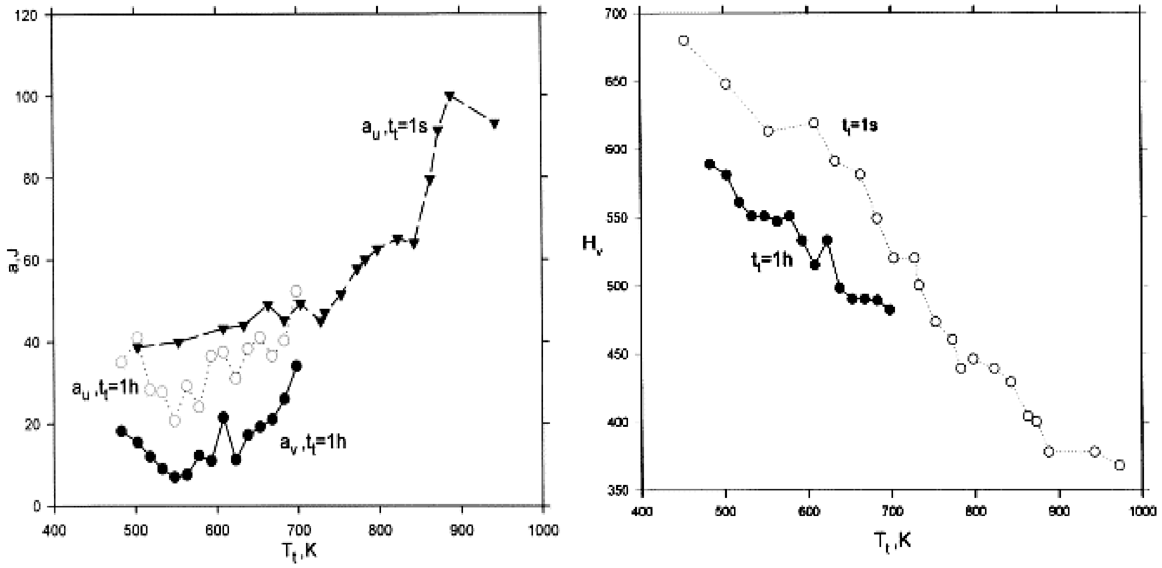

a) b)

Figure 2.9. a) Charpy impact energy U-notch a_u and V-notch a_v , b) Vickers hardness as functions of the tempering temperature [85]

Nakashima and Libsch [86], reported that the Fe_3C particles already become spherical after short tempering times. They were successful in eliminating the TMB in that way.

It seems that this result supports the models in which the plateau with the TMB-valley is connected with the plate-like Fe_3C and not necessarily with the presence of impurities such as As, P, Sb and Sn on austenite grain boundaries. Mechanical instability was considered to be the reason for the tempered martensite embrittlement. Zia-Ebrahimi and Krauss [87] also concluded that TMB was affected by the microstructure and not necessarily by impurities. They also proposed that the localisation of plastic deformation was the reason for the presence of TMB.

2.6. Diffraction patterns of iron carbides

Bimal et al. [88], have investigated the stability of retained austenite in a low Carbon steel subjected to a low temperature ageing treatment. The diffraction patterns of different iron carbides were analysed to characterise the iron carbides precipitated as a function of the tempering temperature. In their study ε-carbide was found to occur in the austenite phase as a result of enrichment by interstitials during isothermal holding.

Decomposition of the austenitic phase commenced at $200\,^0C$. At $300\,^0C$ dislocations were rearranged into parallel arrays. Interfacial dislocations were formed due to the mismatch between the parent austenite and the ferrite product. The ε-carbide gave way to the formation of $\varepsilon'(\eta)$-carbide when the tempering temperature was near and above $400\,^0C$ and the $\varepsilon'(\eta)$-carbide particles formed on dislocations. Tempering at $500\,^0C$ led to the formation of stable cementite. From their study it seems that the shape of the ε-carbides may be a function of the tempering time, although they did not analyse this aspect. The thin foil micrographs and the Selected Area Diffraction Patterns established after their experiments, are illustrated in the following figures 2.10.1 through to 2.10.6.

In their low Carbon steel martensite was seen to undergo degeneration from a planar arrangement of dislocations at $200\,^0C$, as shown in Figure 2.10.1 (d). The tiny particles that decorated these line defects were identified as $\varepsilon -$carbide by the associated $[012]_\alpha$ direction on the SADP. The orientation relationship from the schematic diagram were found as follows:

$$[2110]_\varepsilon // [012]_\alpha$$
$$(0110)_\varepsilon // (200)_\alpha$$
$$(0001)_\varepsilon // (042)_\alpha$$

The early stages in the decomposition of the blocky austenite and the degeneration of the martensite at $200\,^0C$ were also studied.

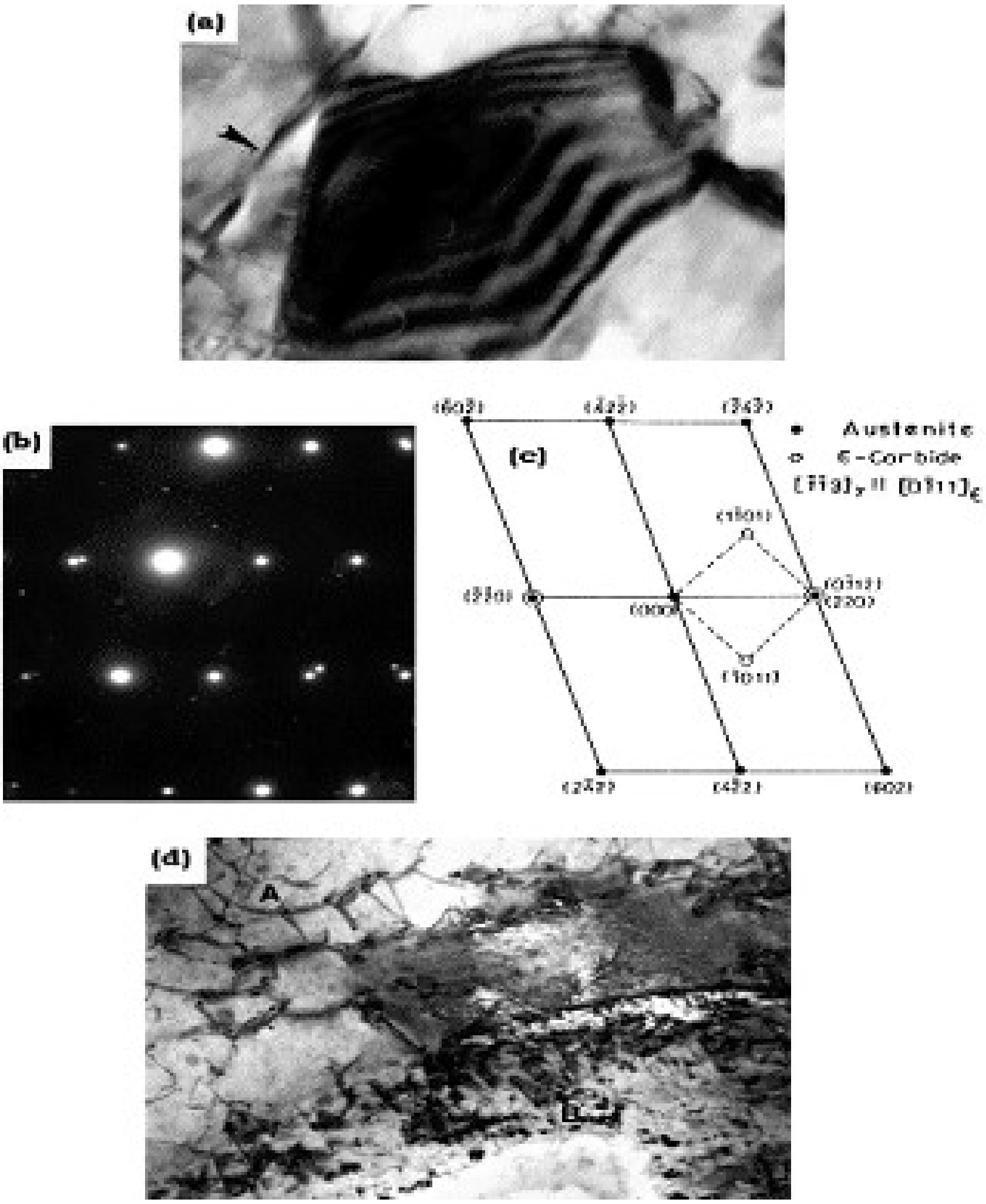

Figure 2.10.1. Transmission electron micrographs of an Fe-0.43%C: a) Bright field electron micrograph revealing blocky nature of retained austenite and the presence of stacking faults as indicated by the arrow. b) Selected area diffraction pattern (SADP) from the same area. c) Schematic representation of the $[113]_{\gamma}$ SADP of Fig. (b) indicating positions of $\varepsilon -$carbide reflections in austenite matrix. d) Bright field image of the same sample showing generation of partials preceding the transformation (region A) and twinning in martensite (region B). After Bimal et al. [88].

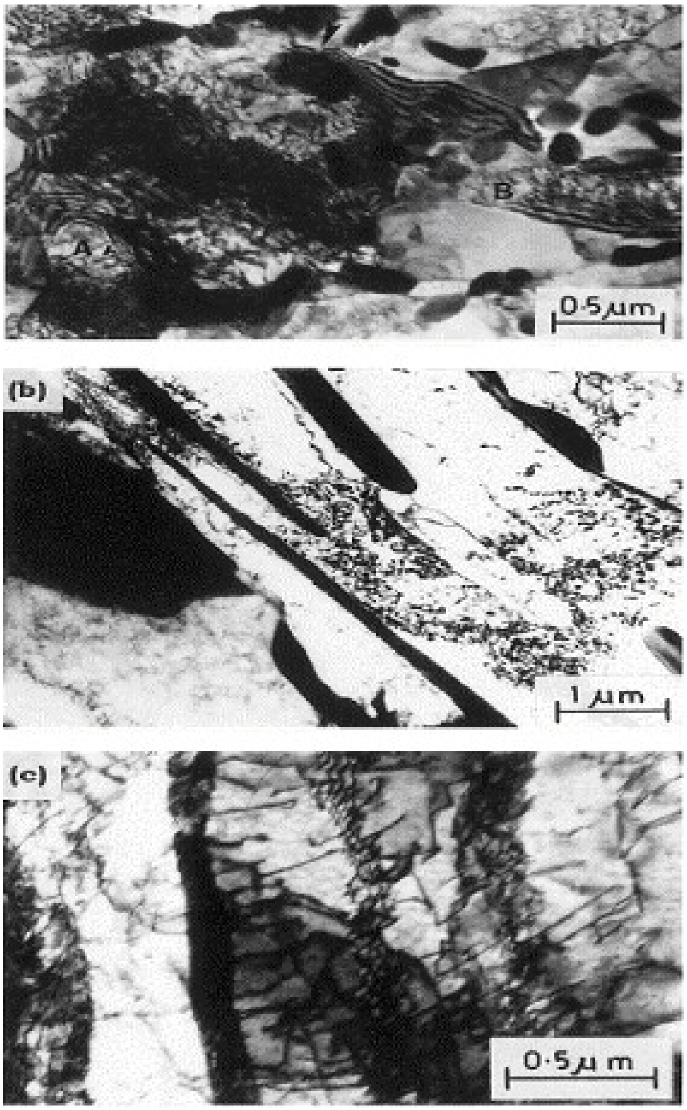

Figure 2.10.2. Bright field electron micrographs from an Fe – 0.43%C sample tempered at $200\,^{0}C$. (a) Early stages in the decomposition of blocky austenite. (b) Film type of austenite in the martensitic regions remain unaffected by tempering. (c) Early stages of degeneration of martensite. After Bimal et al. [88].

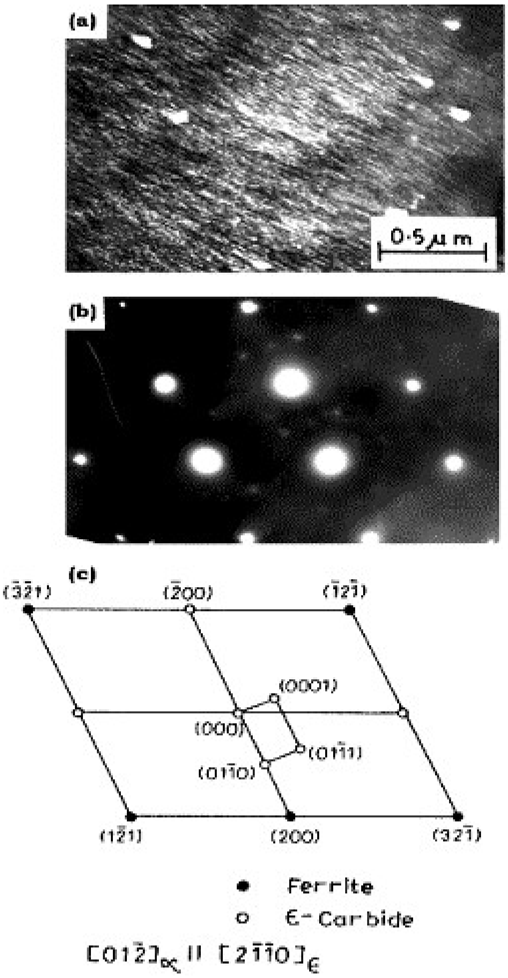

Figure 2.10.3. Transmission electron image from a sample tempered at 300 ^0C. (a) Planar arrays of closely spaced dislocations in ferritic region. Note also the precipitation of fine carbides along dislocations. (b) SADP from the same region. (c) Schematic representation of $[012]_{\alpha}$ SADP of Fig. (b) indicating positions of $\varepsilon-$carbide reflections in ferritic matrix. After Bimal et al. [88].

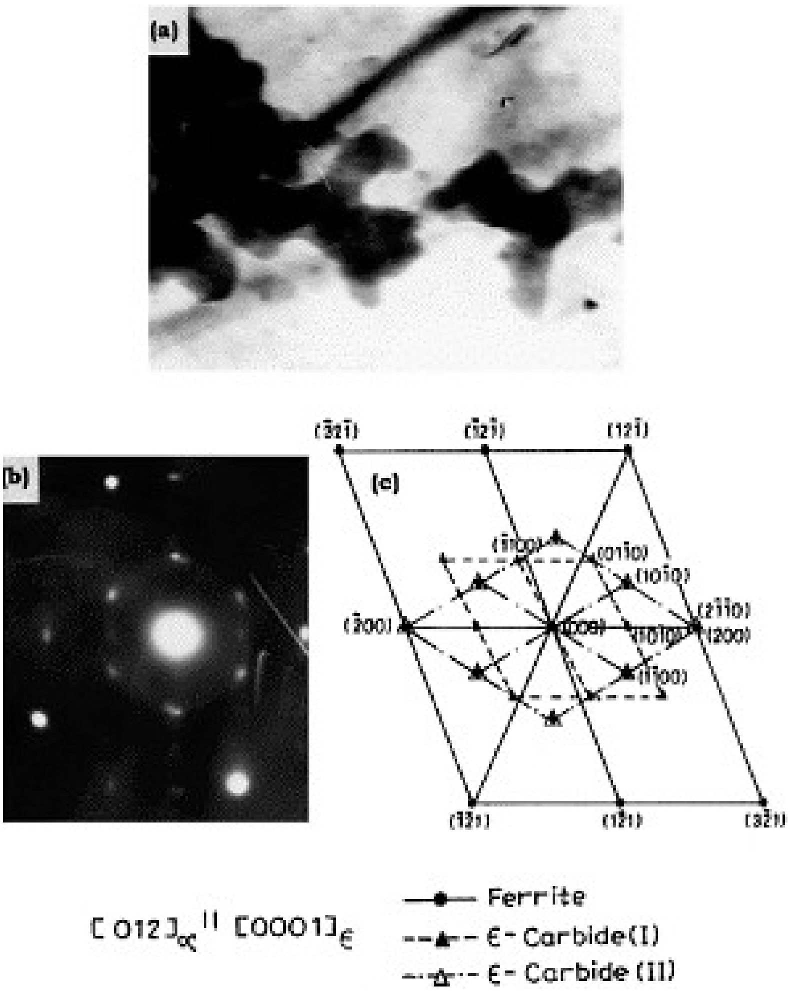

Figure 2.10.4. (a) Bright field electron micrographs showing a three pronged pin-wheel-shaped morphology of $\varepsilon -$carbide precipitate in ferritic matrix. (b) SADP from the same region as in (a). (c) Schematic representation of $[012]_{\alpha}$ of Fig. (b) depicting presence of two domain variants of $\varepsilon -$carbide. After Bimal et al. [88].

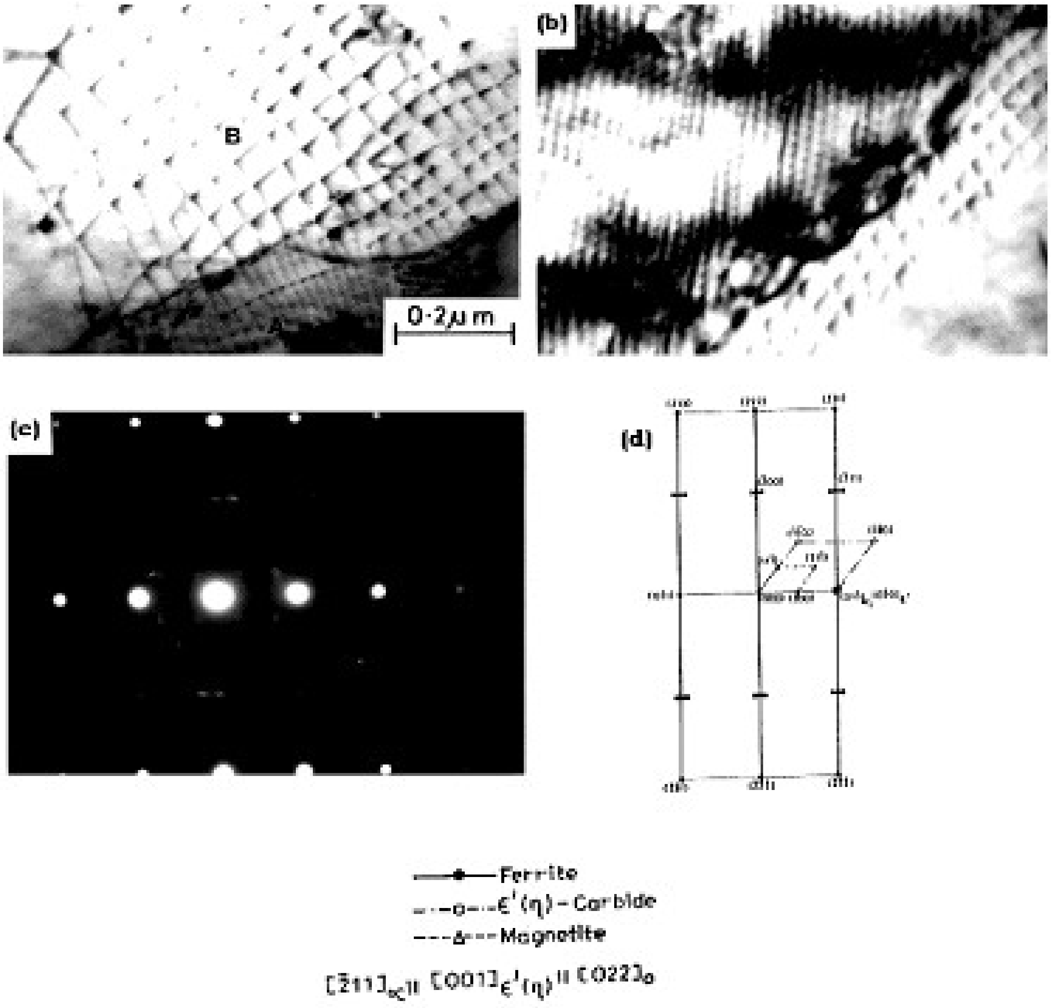

Figure 2.10.5. Transmission electron micrographs from steel sample tempered at $400\,^{0}C$. (a) Bright field showing interfacial structure; (b) precipitation of $\varepsilon'(\eta)$ – carbide along the interfacial dislocation network; (c) SADP from the same region, note the splitting in the $\{200\}_{\alpha}$ and $\{211\}_{\alpha}$ spots; (d) indexed pattern for $[211]_{\alpha}$ indicating locations for $\varepsilon'(\eta)$ – carbide and magnetite reflections. After Bimal et al. [88].

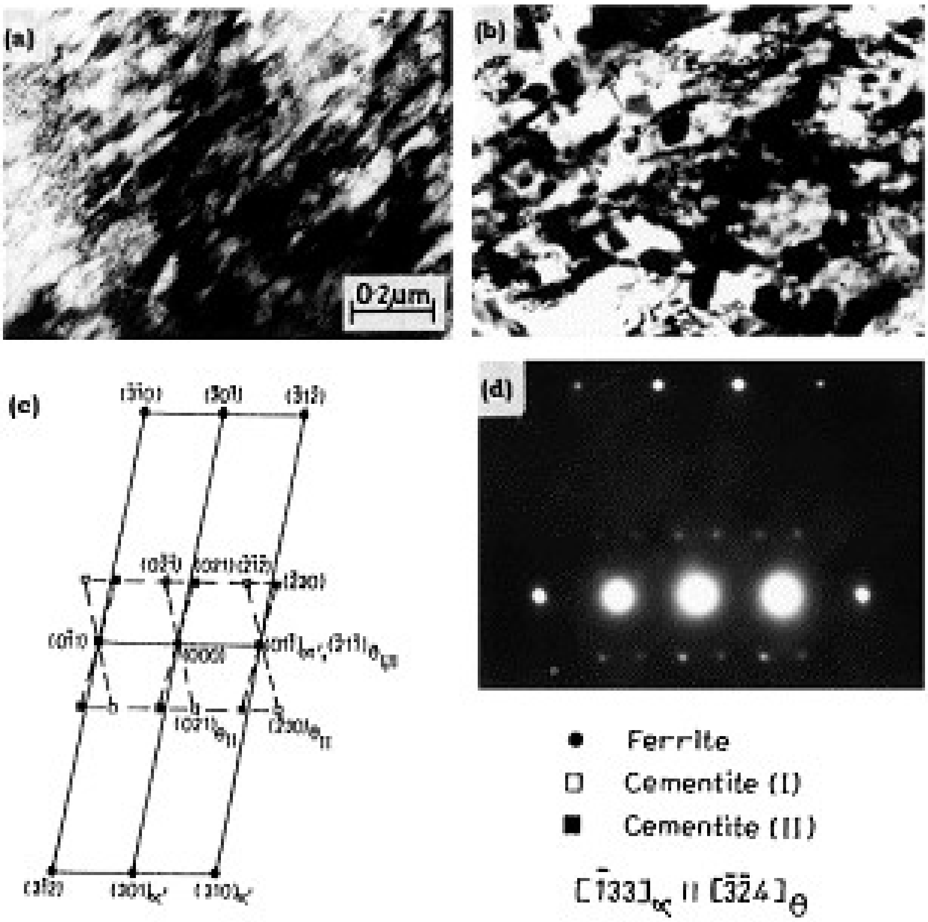

Figure 2.10.6. Transmission electron micrographs from steel sample tempered at 500 ^{0}C . (a) parallel arrays of dislocations in the degenerated martensitic region. (b) Formation of coarse cementite particle in he same specimen. 9c) SADP from the same region as Fig. b. (d) Schematic representation of $[133]_{\alpha}$ SADP of Fig. c showing presence of two variants of cementite precipitates. [88].

Thomson and Miller [89] have investigated the partitioning of substitutional solute elements during the tempering of martensite in Cr and Mo containing steels. They observed no partitioning of Cr, Mo and Mn between cementite and martensite after tempering at 350 ^{0}C for 40 hours. The enrichment of Cr, Mo and Mn in the cementite during prolonged ageing at 450 ^{0}C for 187 hours, before the onset of softening, was the same in both the low and high Carbon alloys, with the interface concentration of solute elements rising slowly towards the equilibrium values. Their results provide further support for the theory that cementite precipitates from supersaturated ferrite via a para-equilibrium displacive transformation mechanism. After prolonged ageing at these higher temperatures, significant enrichment of the cementite with respect to the substitutional alloying elements occurs, with a corresponding depletion in the matrix surrounding the carbide. This enrichment at the cementite/matrix interface was not observed to reach the high levels predicted by equilibrium thermodynamics, as they were found experimentally to be the same in cementite in both a low Carbon and a high Carbon alloy with significantly different equilibrium levels of solute elements. This led the authors to conclude that diffusion of the substitutional solutes through the matrix and within the cementite is the rate-controlling step during the early stages of the enrichment process.

The interface concentrations gradually rise from those dictated by para-equilibrium towards the equilibrium concentrations [89].

Interlath austenite was revealed by high resolution lattice imaging electron microscopy from which it was suggested that there was considerable Carbon enrichment at the $\alpha^{'}/\gamma$ interfaces. Confirmation of this enriched/stabilised interlath austenite was obtained by the powerful atomic resolution method of field atom probe spectroscopy. Heat treatments of $\alpha^{'}/\gamma$ in the range 300 to $500\,^{0}C$ resulted in austenite decomposing to interlath carbides. The structure became similar to lower bainite, causing embrittlement transgranularly with respect to the prior austenite.[89]

2.7. Tensile properties

Martensite tempered at temperatures between 150 and $200\,^{0}C$ is in the temperature range that defines the first stage of tempering. In this temperature range, fine transition carbides, of the order of 2 – 4 nm in size, precipitate within the martensite crystals [90-91]. Many of the Carbon atoms are tied up in the carbide particles and are, therefore, not available for dynamic strain ageing. Also, the higher the Carbon content of the martensite is, the higher the density and closer the spacing of the transition carbides and the transition carbide clusters [92-93]. Reduced lengths of Carbon-free dislocation segments between the transition carbides would require higher stresses for plastic flow according to the work hardening theory of Kuhlmann-Wilsdorf [in 51]. The theory states that the flow stress τ at any given plastic strain, is given by the equation:

$$\tau = \tau_0 + G_M b/\bar{l}$$

where τ_0 is the friction stress, $\bar{l}$ is the instantaneous average of the active dislocation link lengths, and the other terms have their customary meaning.

2.8. Multiple regression as sequential simple regression

Multiple regression analysis is a useful tool to link a large volume of experimental data with an empirical predictive capability. For example in martensitic alloys, a dependent variable such as the M_s temperature can be linked with an arbitrary number of independent variables such as the weight percentages of the alloying elements. The multiple regression approach consists of regressing a dependent variable y (here the M_s temperature) simultaneously with the independent variables $U_0 = 1$ and x (here the weight percentage of an alloying element) .

The error function is given by:

$$e = y - aU_0 - bx$$

The two regression coefficients a and b are found by the solution of the simultaneous equations:

$$a + b\sum x = \sum y$$
$$a\sum N + b\sum x^2 = \sum xy$$

Solving these simultaneous equations by the most efficient method possible, namely either the Gauss method or its equivalent in the form of the Crout method or the m-reduced array method then, in fact, results in the simple regression approach [94]. This consists of three separate simple regressions, each of them not requiring the solution of simultaneous equations. The first is the simple regression of x on U_0 which yields the net variable

$x = \mathrm{x} - \bar{x}$ as the error.

The second is the simple regression of y on U_0 which yields the net variable

$y = \mathrm{Y} - \bar{y}$ as the error.

The third simple regression depends upon the results of the first two, and hence the simple regressions must be carried out in a definite sequence in order to build up the multiple regression [94]. Thus multiple regression may be regarded as a sequential simple regression.

CHAPTER 3. EXPERIMENTAL TECHNIQUES

In this part of the work the variables and the techniques used for analysis are presented and rationalised. The choice of the variables and techniques of analysis is based on the hypothesis made in the paragraph 3.1 of this work and on the scientific and industrial backgrounds presented Chapter 2.

3.1. Hypothesis

3.1.1. How to improve the Hardenability and the Hardness

To obtain a Brinell hardness of at least equal to 600 BHN after tempering, as specified by ARMSCOR and Mittal Steel South Africa, one should consider a Carbon content of the alloy above 0.38%C, which is greater than the specified 0.35%C maximum in the current steels A, B, C and D armour plates. The largest effect on the hardenability of the armour plate should arise from the Manganese content of the steel [3]. A compromise should be considered between the hardenability and the final grain size by considering the fact that the large austenite grain size improves the hardenability, but is detrimental to the impact toughness of the final microstructure. Both the homogenisation temperature and time are important parameters as this determines the dissolution of alloying elements in the austenite from pre-existing carbides. The martensite will present the highest hardness in the as-quenched steel. [3]

3.1.2. How to improve the Toughness of the martensite.

The pure martensitic microstructure will be hard and brittle. To achieve the ballistic requirements, i.e. resistance against spalling, a low- temperature tempering treatment is specified. High-temperature tempering above 400^0C is unacceptable for a high ballistic performance as the softening of the steel is accompanied by a high decrease in the hardness, which should be at about 600 BHN as specified. The final ballistic properties will be strongly dependent on both the tempering temperature and time, as well as on the chemical composition of the steel.

3.1.3. How to improve the resistance to Shock and to Spalling

The largest change in DBTT results from changes to the amount of Carbon and Manganese in the alloy. The transition temperature for V- notch Charpy specimens is raised by about $+4\,^0C$ for each 0.1%C and is lowered by about $-12\ ^0C$ for each 0.1%Mn [74]. Increasing the Carbon content also has a pronounced detrimental effect on the upper shelf impact energy and reduces the weldability of the alloy if that should be considered in manufacturing the armoured vehicle structure. The Mn/C ratio should, therefore, be at least 3:1 for satisfactory notch toughness [2].

3.1.4. How to improve the Tensile Strength

An important development that has resulted in high-strength low-alloy steels with good impact properties is the addition of small amounts of V [73] by causing V_4C_3 precipitates to form during tempering. The dispersion strengthening by this carbide raises the yield strength while at the same time retards grain growth and improves the impact resistance.

3.2. Alloy design

The elements likely to be found in armour steels as well as their potential effects on the microstructure and mechanical properties, are presented in Table (3.1)

Table (3.1). Alloying elements likely to be found in the armour plate steels and their effects on the microstructure and mechanical properties.

Element	Effect	Proposed specification
C	High C content increases the volume fraction of retained austenite after quenching to martensite. Increases the micro-hardness of the martensite	0.38% - 0.45%
Mn	Improves the hardenability of the steel. Weak carbide former.	0.50% - 2.0 %
Mo	Only the metastable Mo_2C provides secondary peak hardening by tempering at about $500\,^0$C. Mo_2C forms by separate nucleation on dislocations. $M_3C \longrightarrow Mo_2C \longrightarrow M_6C$ At 700°C, Mo_2C dissolves and transforms to M_6C. [72, 77] (this will also happen at lower temperatures, such as 600 and 650ºC)	Not applicable in this case 0.6% maximum
Ni	Solid solution hardening. Increases the precipitate/matrix misfit by modifying the lattice spacing of the matrix. Grain refiner, decreases the DBTT. Has a strong effect on decreasing the A_{C1} .	2% - 4.0%
Cr	Cr is effective in retarding the softening from Fe_3C in tempering by forming M_3C. M_7C_3 has little strengthening effect.	1.5 %
Cu	Increases the matrix precipitation of Cu, apparently due to a heterogeneous nucleation mechanism on vacancy-Cu atom combinations [74].	0.3%
Si	Reduces the lattice spacing of the ferritic matrix and increases the precipitate/matrix misfit. Delays the decomposition of the martensite and the precipitation of the transition carbides upon tempering. Increases the corrosion resistance.	1.2% maximum
P	Segregates to grain boundaries	Unwanted in this case and must be reduced to lower than 0.005%P
S	Segregates to grain boundaries	Unwanted.
N	Increases the hardenability, decreases the M_s temperature and forms coarse carbonitrides	Unwanted

To move from the current steels A, B, C and D to the high performance steel armour plates by changes only to the heat treatment parameters, e.g. the solution treatment temperature, the temperature of the last pass in the rolling mill, the cooling rate after rolling, the tempering temperature and time, could be considered as the first approach to the objective.

Changes to the chemical composition of an improved alloy would be considered later if the changes to the thermomechanical parameters are not sufficient for achieving the required properties. It is likely, however, that the harder and tougher armour plate will require a change in composition for achieving its hardness, hardenability as well as its toughness.

3.3. The Heat treatment design

The Grossman hardenability of the current steels A and B alloy is about 33 mm. This is sufficient for producing a fully martensitic microstructure through the entire thickness of a 6 mm thick plate. Nevertheless, the true mass fraction of martensite formed at the centre of the plate will be strongly dependent on the cooling rate and the initial temperature before quenching. The final hardness, toughness and strength will depend on all of the parameters considered at each step of the thermomechanical treatment.

The Carbon equivalent is not a highly accurate parameter for predicting the weldability but it nevertheless allows a first qualitative assessment. For good weldability, the Carbon Equivalent (CE) should be less than 0.6%. Above CE = 0.6%, there is a risk of forming martensite and weld-cracking may occur [2]. For armoured steels, it will certainly be difficult to simultaneously obtain good mechanical properties together with good weldability, because the Carbon content cannot be decreased to lower values without compromising the hardness. The high CE, however, does not mean that welding is impossible. Specific pre- and post-treatment of the steel should be adopted to avoid any damage after welding.

The ballistic performance of these alloys will depend on the ability to form a homogeneous martensitic microstructure throughout the cross section of the plate. The Cr-containing carbide M_3C and the additions of Cr to a ferritic low Carbon steel will delay the onset of overageing or softening considerably [73]. The hardening precipitates should be formed within the matrix or on dislocations, and not on grain boundaries. For this, the driving force for precipitation must be high enough and the precipitates as fine as possible for an effective pinning of dislocations and grain boundaries.

From the above considerations the heat treatment cycle for the armoured steels may comprise:

- Solution treatment for homogenisation at 1050 - 1100 ^0C for 1 hr;
- Hot rolling with the temperature during the last pass in the rolling mill between A_{c3} + 50 to +100 ^0C according to the chemical composition. Using the lowest possible finishing temperature for hot rolling of plates is also beneficial for grain refinement but it can be detrimental to the shape and the surface finish of the plate and of the Manganese sulphide particles [72];
- The degree of the hot work will be between 20% and 30% strain per pass;
- Air-cooling to room temperature;
- Austenitisation at 800 ^0C to 950 ^0C for 1 hour;

- Water-quenching to room temperature;
- Tempering (for stress relief and precipitation) at $150\,^0C$ to $300\,^0C$ for less than 1hour. The particular tempered structure should produce the best combination of strength, resistance to spalling and to localised yielding;
- Air-cooling

3.4. Experimental Variables

To optimise the mechanical properties of the armoured steel plates the following variables have been considered:

1. The chemical composition is considered to be the primary independent variable of the system. It has a determining influence on the martensite start temperature, the volume fraction of retained austenite, the type as well as the thermodynamics, kinetics and the nucleation sites of precipitation during tempering. These factors may determine the mechanical behaviour of the armoured steel plates. Four armoured steels, namely Steel A, Steel B, Steel C and Steel D were used for the preliminary investigation of the effect of the chemical composition on the microstructure, mechanical and ballistic performances. Thereafter nineteen laboratory cast steels with carefully chosen chemical compositions have been tested in two steps. First, steels E through to I, and later after their ballistic testing, Steels J through to W have been tested. The chemical compositions of these twenty-three armoured plate steels are presented in tables (3.2) and (4.3.32).

2. The martensite start temperatures of the steels are strongly dependent on their chemical compositions, but are also functions of the austenitisation temperature and time, which determine the degree of carbide dissolution, the grain size and the grain boundary surface area per unit volume. Moreover the martensite start temperature of the steel determines the morphology of the martensite, either plate or lath martensite, and the volume fraction of retained austenite, which influence the mechanical properties as well as the ballistic performance of the plates. The martensite start temperatures of the twenty-three armoured steels have been measured and an empirical relationship with the chemical composition is proposed for these steels using a multilinear regression method. The surface relief after the martensitic transformation was measured by Atomic Force Microscopy (AFM) and the results are compared between the alloys with low M_s and those with high M_s temperatures. The defect structures in the martensite/retained austenite microstructures are also compared between the different alloys.

3. The austenitisation temperature and time determine the grain size, the degree of carbide dissolution into the matrix and, therefore, the martensite start temperature of the alloys. Four austenitisation temperatures ranging from $800\,^0C$ to $950\,^0C$ were selected for this purpose. The minimum temperature of $800\,^0C$ is based on the measurement of the austenite finish temperature, which was found to be between $739\,^0C$ and $768\,^0C$ for the twenty-three steels. A minimum austenitisation temperature of ($A_f + 50\,^0C$) has been considered which is approximately $800\,^0C$. The maximum of $950\,^0C$ has been chosen to avoid the disadvantages of coarse austenite grains.

4. The Reheat-quench versus Direct-quench (i.e. directly quenched from hot rolling) effect on the ballistic performance has also been investigated. Plates from five alloys were reheated at 900 ^0C before being water quenched. Plates from eight other alloys were directly water quenched after the final hot rolling pass in the laboratory hot rolling mill. The effect of a second reheating of the armoured steel plates for 15 minutes at 850 ^0C after the first ballistic testing have also been investigated on plates from five alloys.

5. The location and shape of the retained austenite in the inter-lath or inter-martensite plate spaces may influence the plastic behaviour of the armoured steel plates. Its effects on the ratio between the yield strength and the ultimate tensile strength of seven alloys have been measured and the effects on the diameter of the deformed regions after the ballistic testing were analysed on eight alloys.

6. The tempering temperature and time may strongly affect the existence and properties of the martensitic armoured steels. The effect of low-temperature tempering treatments on the carbide precipitation behaviour and on the mechanical properties and ballistic performance of the alloys have been analysed. The hardness, the tensile properties, the Charpy V impact energy at -40 ^0C, the precipitation following different tempering conditions, were also compared for the different alloys. The crack formation and the spalling of the plate due to high velocity impacts during the ballistic testing were compared for the different tempering conditions.

7. The lattice parameters of the martensite and the austenite, and their orientation relationships were measured and compared to the predicted values calculated through the phenomenological theory of the martensitic transformation. An approach based on the Bowles and Mackenzie model of the phenomenological theory of the martensite transformation for the calculation of the transformation characteristics and their relationships with the ballistic performances, was examined. A MATLAB script of the BM model is presented for the calculations. The lattice parameters are functions of the chemical composition of the steel and the temperature of the quenching medium. Therefore, they should be considered as dependent variables and their dependencies on the first variables always considered during the analysis.

8. The plate thicknesses through hot rolling have been varied between 4.7 mm and 6.2 mm and the effect of this was compared in terms of radius of the affected region due to the high velocity impact with the fired rounds, the subsequent work hardening and the resistance to cracking and spalling.

Table (3.2): Chemical composition (wt%) of armour steels currently produced or used in RSA and elsewhere in the World

	C	**Mn**	**P**	**S**	**Si**	**Cu**	**Ni**	**Cr**	**Mo**	**V**	**Nb**	**Ti**	***N***
Steel A	0.37	0.52	0.005	0.002	0.754	0.855	3.8	0.318	0.367	0.003	0.001	0.003	
Steel B	0.317	0.855	0.008	0.002	0.176	0.26	2.8	0.79	0.45	0.005	0.001	0.003	0.009
Steel C	0.37	0.684	0.003	0.002	0.241	0.005	1.9	0.48	0.32	0.004	0.001	0.003	0.009
Steel D	0.385	0.55	0.004	0.002	0.768	0.1	1.79	0.14	0.36	0.001	NIL	0.007	

3.5. Plate manufacturing

In addition to the four alloys already available at the start of the investigation, nineteen further chemical compositions were designed for the armoured steel plates to be tested. The main raw material, about 5 kilograms of steel B for each melt, supplied by Mittal Steel South Africa, was melted in an alumina crucible of a vacuum induction furnace under argon with an appropriate addition of high grade ferromanganese to adjust the chemical composition to the target. The melted material was degassed. The alloys were cast into a 45 mm x 70 mm x 230 mm mild steel mould. The final compositions of the cast ingots were verified by spectrometer analysis. The top and bottom of the slabs were cut off to remove the casting defects and the final lengths of the slabs were about 190 mm. The ingots were processed by hot rolling with a 20% strain per pass maximum. The first passes in the rolling mill were with the rolling direction parallel to the 70 mm long side to be elongated up to about 200 mm. The sheet was reheated to 950°C for 20 minutes and hot rolled this time with the rolling direction parallel to the 230 mm long side. This second reduction is referred to as the rolling direction in the next Sections of this work.

The slabs were solution treated for one hour at 1100°C before hot rolling. The temperature of the slab at the last pass in the rolling mill was between 900^0C and 950^0C with a 20% thickness reduction per pass. After reduction to the desired thickness the plates were air-cooled. The final thickness of the plate was considered as a variable in the study of the ballistic performance. The smallest selected thickness was 4.7mm and the highest was 6.2mm. The plate's sizes for ballistic testing after hot rolling were 200 mm to 250 mm wide and 500 to 550 mm in length. Two or three plates were obtained from each of the nineteen chemical compositions. One plate from each alloy was used for the determination of the mechanical properties and a second for the ballistic testing.

3.6. Mechanical testing

The shock between the fired round and the armoured plate is a high strain rate deformation process. The localised temperature within the shock waves of the impacted region may rise by some hundreds of degrees Celsius [18] due to the conversion of a part of the kinetic energy of the fired round into heat. Another fraction of the kinetic energy is adsorbed by the mechanical strain around the impact region and a third fraction is dissipated through the supports of the structure holding the plate.

The interaction between the plate and the fired round is complex, however, and the following mechanical properties have been suggested for predicting the ballistic performance of steel armoured plates [1,2,6,8,12,15,18]:

- the hardness of the steel at room temperature;
- the tensile strength at room temperature;
- the elongation during tensile testing at room temperature; and
- the Charpy impact energy at -40^0C.

These mechanical properties were measured for seven steels selected from amongst the twenty-three steels considered in the study. The hardness measurement, the dilatometer analysis and X-Ray diffraction results were considered as a basis for the selection of the seven steels.

The hardness of the plates after hot rolling and air-cooling was higher than 500 Vickers. They were then annealed and furnace cooled before the manufacture of the specimens for tensile and Charpy V impact testing.

The samples were then austenitised for 20 minutes at 800^0C, 850^0C, 900^0C and 950^0C respectively in an Argon atmosphere to prevent oxidation of the steels. The furnace used was LINDBERG MK-1018 with maximum temperature of 1200^0C. After austenitisation, the samples were water quenched to 20^0C to form the martensite microstructure. Tempering treatments at 150^0C, 180^0C, 200^0C, 250^0C, 300^0C, 350^0C and 400^0C for times from 15 to 60 minutes, were applied to the alloys.

3.6.1. Hardness measurement

Hitherto the hardness was considered as the main mechanical property for armour plate steels. South African specifications suggest the Brinell hardness to be higher than 600 BHN [1] whereas the American specifications [2] suggest the Rockwell C number to be at least between 55 and 60 Rc for armoured plate. The Australian specifications for military and security applications recommend a Brinell hardness between 478 and 578 BHN. [2]

Four techniques have been used for the measurement of the hardness of the steels in the quenched and tempered conditions, and comparisons have been done with the specifications.

Small samples of the hot rolled plates were cut to 15 mm length and 10 mm width. The thickness varied between 4.7 mm and 6.2 mm depending on the thickness of the plate. Samples were austenitised, quenched and tempered as defined previously and the hardness measured. The samples were finely mounted in resin and mechanically polished before the measurement of the hardness.

The Brinell hardnesses were measured in a hydraulic Otto-Wolpe –Werke machine with a 2.5 mm diameter ball at a constant load of 62.5 kg.

Figure 3.1.The tubular furnace
LINDBERG MK-1018 for austenitisation

The Vickers microhardnesses were measured in a microhardness tester of Future-Tech Corporation of Japan with a load of 300g.

Figure 3.2. Microhardness Tester FM F11-1

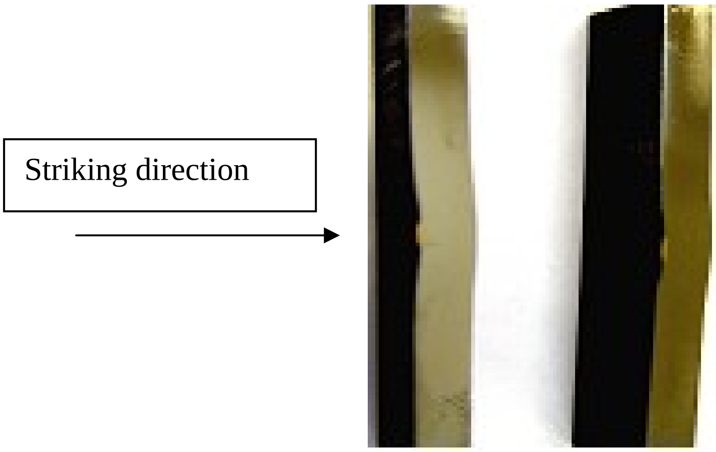

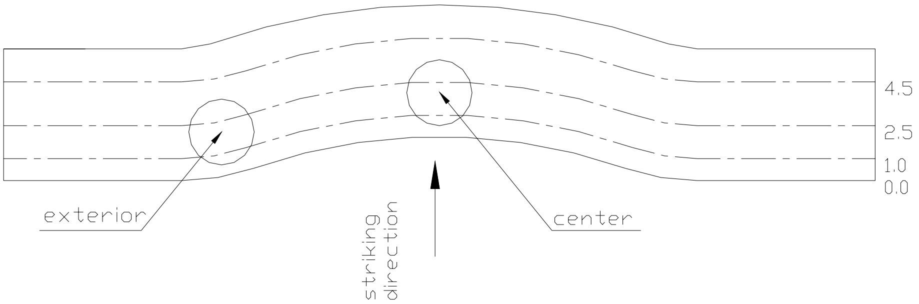

Figure 3.3. (a) Cross sections wire-cut through the ballistic impact-affected regions of steels P and Q. (b) Illustration of the iso-depth lines along which microhardness was measured through the cross sections which were wire cut after ballistic impact.

3.6.2. The tensile strength and elongation

The front surface of the armour plate is subjected to a high rate compressive strain when impacted by a projectile. The rear surface may fail under a high rate tensile stress. Earlier, mention has been made of the localised temperature that rises in the impact region due to shock wave propagation. However, the specifications have been established for ballistic performances using the uniaxial tensile test at room temperature. South African specifications specify the yield strength to be a minimum of 1300 MPa, the tensile strength a minimum of 1700 MPa and the elongation to be more than 7% for good ballistic performance.

The tensile specimens were cut parallel to the rolling direction from the hot-rolled and air-cooled plate for the selected steels. For others, because of a high hardness, an annealing treatment was applied to the plates before the wire cutting of the tensile specimens. The flat tensile specimens had a rectangular cross section calculated according to Barba's law [101] for comparison with the standard specimens.

$$\frac{\sqrt{A_s}}{L_s} = \frac{\sqrt{A_1}}{L_1}$$

where A_s and A_1 are the cross section areas of the standard and the tested specimens respectively and L_s and L_1 their respective gauge lengths. The dimensions of the flat tensile specimens are then:

Table (3.3). Dimensions of the tensile specimens

Total length [mm]	**Gauge length [mm]**	**Accord radius [mm]**	**Width [mm]**	**Thickness [mm]**
100	33	5	6 ± 0.2	6 ± 0.2

The tensile specimens were wire-cut before the heat treatment to avoid the laborious machining of the hard martensite formed after quenching and were austenitised under Argon, quenched and tempered as stated before. The yield strength, the ultimate tensile strength and the elongation were determined using an INSTRON 8500 hydraulic tensile testing machine.

Figure 3.4. Universal testing machine INSTRON 8500

The Yield strength and the Ultimate tensile strength were correlated through the first constraint equation with the optimum of the hardness and the ballistic performances of the armour steel plates. Fractured specimens were analysed under a scanning electron microscope to establish the mechanisms of fracture and the possible role of inclusions.

3.6.3. The Charpy V-notch impact energy

As in the case of the tensile properties, specifications exist for the impact energy of armoured plate steels. Those specifications utilise the results from a Charpy V-notch test that is relatively a slow strain rate phenomenon compared to the high velocity impact during ballistic testing. The more conservative specifications [2] for armour steels recommend a minimum of 27 Joules impact energy at -40^0C on full size Charpy V-notch specimens, which has its axis transverse to the rolling direction. The less conservative specifications [1] fix the minimum at 13 Joules impact energy at -40^0C on full size Charpy V specimens with its length normal to the rolling direction. The Impact energy also provides an indication of the resistance of the steels to brittle fracture and to spalling. The resistance to spalling during the impact is a safety criterion and is also a good indication of the ability of the armour steels to absorb the kinetic energy of the bullets. The Charpy-V impact energy of the sub-sized specimens was, therefore, considered as the second constraint on the hardness and the ballistic performance. The relationship between the impact energy and the heat treatment parameters was used to construct the second constraint equation on the optimum level of hardness on ballistic performance.

Because of the plate thicknesses being less than 10 mm, sub-standard Charpy sized specimens had to be used. These were wire-cut with the following dimensions: 55 x 10 x 5 mm. The notch was 2 mm deep with an angle of 45^0, and the radius of the fillet at the tip was 0.25 mm.

The Charpy V-notch impact energy of the sub-sized specimens quenched and tempered, were measured at -40^0C to construct the second constraint equation on the ballistic performances. Specimens were cooled and kept for 10 minutes at -60^0C in a mixture of ethanol and dry ice. They were then heated to -50^0C by adding controlled amounts of ethanol to the mixture, and were then removed from the cold liquid and tested. The time between the removal from the cold liquid and the impact of the pendulum was estimated to be between four and six seconds. Testing was done on a Charpy impact testing machine from Mohr and Federhaff AG, Germany.

Figure 3.5. The Pendulum Impact Testing Machine

3.6.4. Fracture analysis

The fracture surfaces after tensile and impact testing were analysed in a scanning electron microscope to determine the mode of cleavage and the possible role of inclusions in the fracture mechanism. Freshly fractured surfaces were protected against contamination and analysed in the secondary electron mode on a JEOL JSM-6300. Fracture surfaces (if present), cross sections through the impact region, cracks, micro-cracks and grain boundaries in the impact region after ballistic testing were also analysed in both the backscattered and secondary electron modes in the same SEM equipment.

Figure 3.6. Scanning Electron Microscope JEOL JSM-6300, Model P90E.

3.6.5. Microstructure analysis

The microstructure of the steels is the result of a complex combination of the effects of the chemical composition, the mechanical processing and the heat treatment. The properties that determine the ballistic performance of the armour steel plates, may be attributes of the microstructure. The structure and morphology of the martensite laths or plates, the location and volume fraction of retained austenite, its orientation relationships with the martensite and the precipitation of the cementite have been analysed and their effects on the ballistic performances were established. The combination of the scanning electron microscopy, the transmission electron microscopy, the atomic force microscopy and the X-ray diffraction was necessary to fully characterising the microstructures of these armour steels.

3.6.5.1. Phase analysis and Lattice parameters measurements

X-ray diffraction was used to determine the phases present in the steels and their lattice parameters. The analysis was done on two different groups of samples.

The first group was solution treated for 20 minutes at $900\,^{0}C$ in a tubular furnace under an argon atmosphere, water quenched to $20\,^{0}C$ and then electro polished in a solution of 5% volume perchloric acid and 95% volume of glacial acetic acid before the X-ray diffraction analysis. The second group of 1 mm thick discs of the same steels, was finely polished and then solution treated for 10 minutes at $900\,^{0}C$, under a 10^{-4} torr vacuum in a Theta dilatometer, then quenched to room temperature in Helium gas. The equipment used was from X'Pert PRO PANalytical

Figure 3.7. X-ray diffraction analyser X'Pert PRO PANalytical

3.6.5.2. Morphology of the martensite

The defect structure of the martensitic structure together with the surface relief and the diffusionless character, are proof of the existence of the martensitic transformation. The Bright Field and Dark Field Images from the TEM were analysed to determine the morphology of the plate or lath martensite, and the phases present such as the retained austenite and the cementite. Carbon replicas and thin foils of fifteen armour steels were analysed.

The thin foils were prepared from the 3 mm diameter discs wire-cut as shown in Figure 3.4 in the as-quenched or in the quenched and tempered plates before and after ballistic impact. The discs had an initial 0.6 mm thickness. They were mechanically polished to less than 200 micrometers in thickness before eletropolishing in a solution of 6vol% of perchloric acid and 0.5vol% chromium oxide in glacial acetic acid. The thin foils and the carbon replicas were analysed in a PHILIPS CM 200 TEM equipped with STEM, EDS and an electron beam source of 160 kV.

Figure 3.8. Transmission Electron Microscope PHILIPS CM 200

3.6.6. Transformation surface relief

The surface relief after the martensitic transformation was measured on a nanometre scale using the Atomic Force Microscope Topometrix TMX 2000 "Discoverer". The samples for the atomic force microscopy were prepared from 1 mm thick specimens of the selected steels. They were finely polished on a one micron diamond paste before electropolishing in a solution of 5vol% perchloric acid and 95vol% glacial acetic acid at 0ºC. The polished samples were then austenitised for 10 minutes at $900^{0}C$ under high vacuum in the Theta dilatometer and quenched to room temperature in a flow of Helium gas. The quenched samples were then cleaned in an ultrasonic cell with pure acetone to remove any contamination or dust from the surface.

The very small features such as the size of the twins, the twinning angles and the relative orientation between the plate axis and the twins were measured for these steels. The Fast Fourier Transform implemented by the discrete Fourier transform algorithm was used to analyse the periodicity of the surface relief. The calculations were performed using MATLAB 7.0 software.

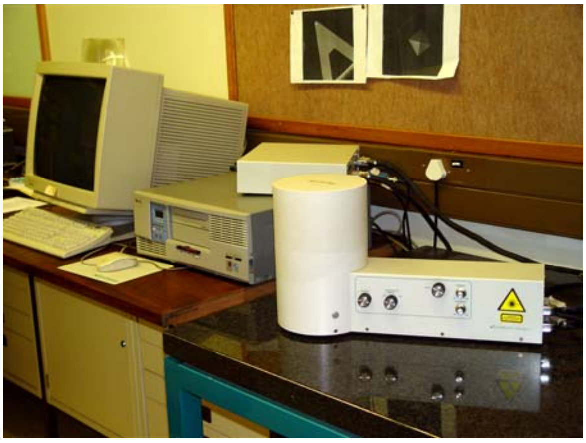

Figure 3.9. Atomic Force Microscope: Topometrix TMX 2000 "Discoverer"

3.7. Martensite start temperatures

The characteristic transformation temperatures during cooling of all twenty-three steels were measured by a dilatometer. The Martensite start temperatures were correlated with the chemical compositions and with the solution treatment temperatures of all 23 steels and an empirical relationship is proposed for estimating the M_s temperature of these armour steels. The M_s temperature was used later as an indirect variable for estimating the volume fraction of retained austenite in the martensitic steel and the orientation relationship between the retained austenite and the martensite. The dependence of the ballistic performances of these armour plate steels on the M_s temperature were also analysed. The autotempering phenomenon was also detected for some of these steels through the dilatometer curves.

The sample preparation for the dilatometer analysis is described in paragraph 3.6.5.1. The equipment used was a THETA 734 Single Silica Push Rod LVDT dilatometer.

Figure 3.10. Dilatometer THETA 734

3.8. Ballistic testing

3.8.1. Specifications for the test

Thirteen armoured steels were tested in a ballistic testing tunnel at Mittal Steel South Africa (Vanderbijlpark) where the temperature and the humidity are controlled as specified, to standardise testing conditions. The testing distance was 30 metres and the obliquity angle was zero degrees. One plate was tested from a distance of only 10 meters. The prescribed velocity range for the R4’s 5.56 mm rounds is 940 ± 10 m/s. An optical testing system assesses the success or failure of the plate by remaining opaque to a light beam.

3.8.2. Analysis after ballistic testing

After ballistic testing optical and scanning electron microscopy analyses were done on the front and rear surfaces of the plates. The impact region was sectioned by wire cutting and a cross section was analysed through optical and scanning electron microscopy for crack analysis. Hardness profiles along three iso-depth lines, respectively at 1.5, 2.5 and 4.5 mm below the front surface of the impact region, were determined. Finally thin foils from the centre and the periphery of the impact region were analysed by TEM and their microstructures compared to the initial martensite before ballistic testing.

CHAPTER 4. RESULTS AND DISCUSSION

4.1. Preliminary results on the steels A and B currently in production in South Africa as well as two imported steels C and D.

4.1.1.Objective

Steel A and B armour plates are currently produced by Mittal Steel (South Africa) and were considered as the reference steels for the development of the advanced armour plate steels for two reasons:

- the materials are known, they meet the ballistic requirements and have already been tested both in ballistic tunnel tests and in combat; and
- Steels C and D are imported and are also used occasionally in South Africa for ballistic protection as substitutes for the Steels A and B.

These four armour steels, therefore, served as benchmark steels for the development of the new advanced performance armour steel RB600. A good understanding of the differences in ballistic performance of these four steels constitutes the basis for the desired improvement. Moreover, the industrial implementation of the metallurgical processes for the manufacture of the new RB600 armour steel, may be economically justified if the processing parameters remain close to those currently applied for the manufacture of steels A and B as armour plate.

4.1.2. Methodology

The specifications for armour steel plate in South Africa are actually formulated in terms of mechanical properties, i.e. hardness, yield strength, tensile strength, elongation of a 50 mm gauge length and assessed by ballistic tests. Amongst these specifications the hardness of the steel is considered to be the main indicator of ballistic performance. This design approach has been considered as an hypothesis in the first step for the characterisation of these steels. The attempt to maximise the hardness of these four armour steels has been established through water quenching of austenitised samples. More investigations based on the chemical compositions, dilatometric analyses, carbon extraction replicas and thin foil transmission electron microscopy have revealed some significant microstructural differences between steels A, B, C and D armour plates.

4.1.3. Results

4.1.3.1. Dilatometric analysis

a) Principle of the determination of the Ac_1 and Ac_3 temperatures

The 2 mm thick samples were slowly heated from room temperature to 900°C at a constant rate of 2°C per minute. The cooling down to room temperature was also done at the same rate. The useful part of the heating curve was then isolated for accurate reading of the A_c temperatures as schematically presented in the following figure:

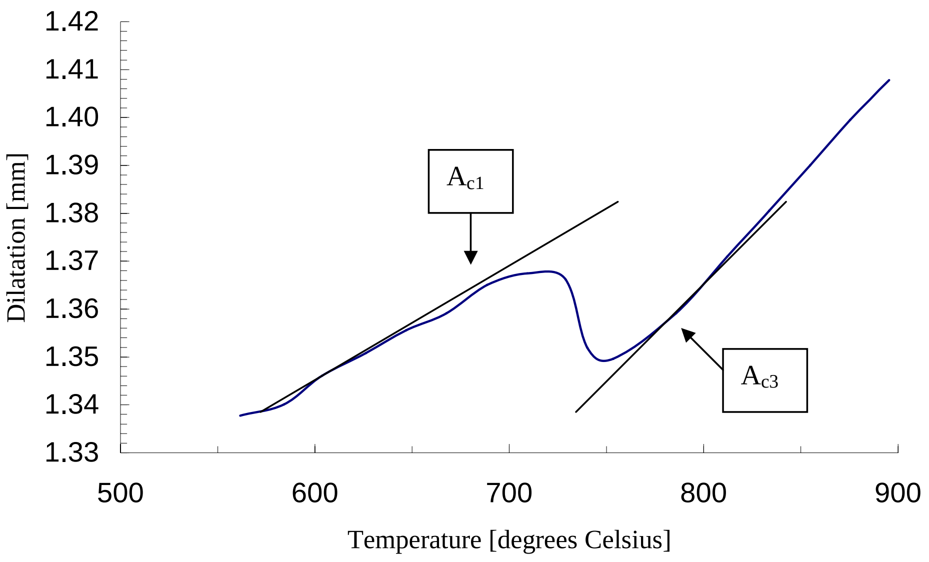

Figure 4.1.1. Illustration of reading off of the A_c temperatures on the heating curve of steel E

b) Principle of the determination of the M_s temperature

The M_S temperatures are read off from faster cooling rate curves. The 2 mm thick samples were heated up to 800°C, 850°C, 900°C or 950°C at a constant rate of 2°C per minute, soaked for 5 minutes and then quenched in a flow of Helium at a cooling rate higher than 200°C per second to form martensite. A typical dilatation curve is presented in figure 4.1.2. The determination of the martensite finish temperature by this technique is not accurate because it is difficult to determine the exact point of contact between the cooling curve and the straight-line tangent. Here the tangent is considered to be parallel to the first part of the heating curve. The measured transformation temperatures, for steel A to D are presented in table (4.1.1)

Table (4.1.1). Transformation temperatures measured by dilatometric analysis

	Ac_1 **[°C]**	Ac_3 **[°C]**	**M_s [°C]**
Steel A	698	758	285
Steel B	704	764	253
Steel C	702	742	241
Steel D	694	748	243

From these results the minimum austenitisation temperature was determined by adding 50°C (at least) to the Ac_3 temperatures, leading to about 800°C as a minimum.

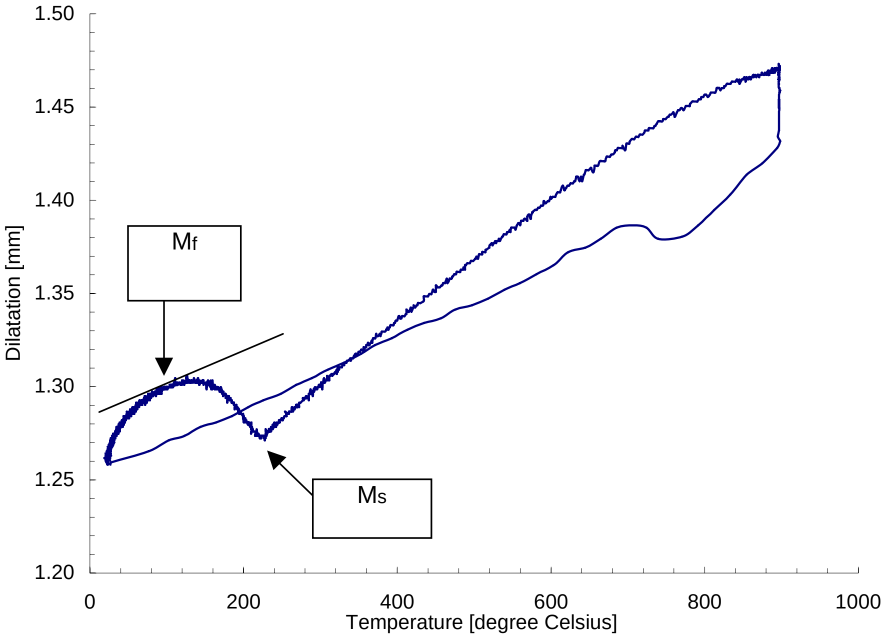

Figure 4.1.2. Determination of the M_s and M_f temperatures

4.1.3.2 . Quenching and tempering of Steel B

The average hardness of 8.5 mm thick steel A and that for 30 mm thick steel B armour plates after quenching and tempering, were found to be 520 VHN and 390 VHN respectively. The hardness profiles of both steels A and B produced lower hardnesses than the specified range of 640 VHN to 750 VHN, or a minimum of 600 BHN as specified for the RB600 armour steel to be developed.

Samples of Steel B were austenitised at 800°C, 850°C, 900°C and 950°C for 20 minutes, quenched into brine and then tempered at low temperatures varying between 170°C and 250°C. This ideal quench was used to determine the maximum hardness achievable for this steel. The initial material was received in 30 mm thick plates with a hardness of 378 VHN to 400 VHN. The highest hardness value obtained after the above ideal quench was 543 VHN, i.e. well below the specified minimum.

These results are plotted in Figure 4.1.3. At low tempering temperatures of between 170°C and 200°C**,** the effect of the tempering treatment on the hardness is more pronounced within the first hour. The hardness is very sensitive to the tempering temperature for a given tempering time.

Table (4.1.2). Hardness values of Steel B after austenitisation at 850°C, water-quenched and low-temperature tempering

	Vickers hardness after tempering at these temperatures		
Tempering time [hr]	170°C	200°C	250°C
0	543	543	543
0.5	540	500	481
1	520	502	481
4	502	508	473
11	511	484	436
24	499	481	449

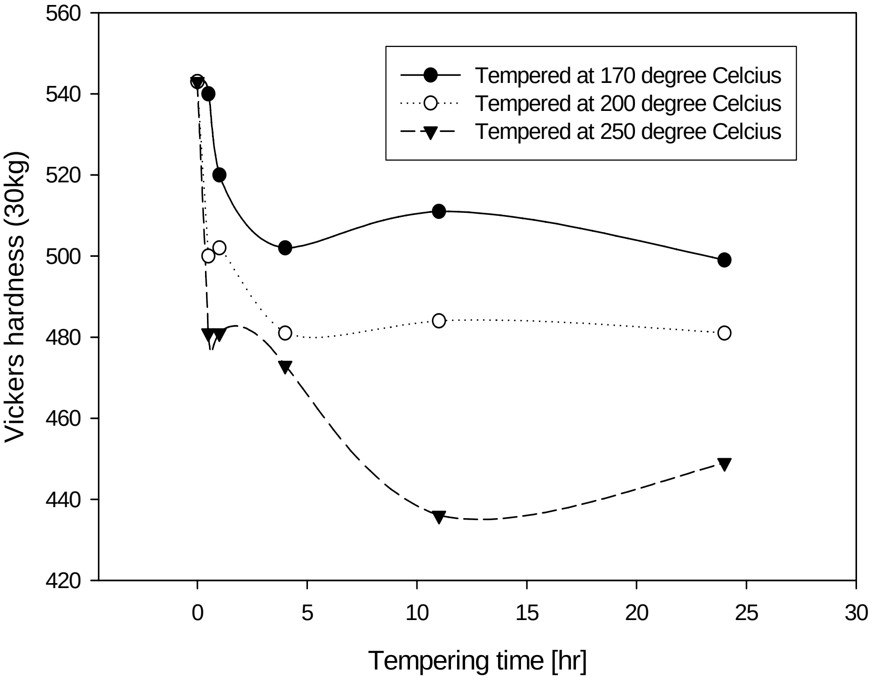

Figure 4.1.3. Vickers hardness of Steel B after austenitisation at 850°C for 20 minutes, water-quenching and tempering

An increase in the austenitisation temperature to 900°C or to 950°C does not alter this general behaviour, but rather determines the highest hardness achievable as shown in Figure 4.1.4. After austenitisation at 900°C and water-quenching, the Vickers hardness of steel B is slightly higher than the one obtained after austenitisation at 850°C**,** but the corresponding decrease in hardness during tempering is faster as shown in Table (4.1.3).

The austenitisation treatment at 950°C for 20 minutes produced a lower hardness in the as-quenched condition. The maximum Vickers hardness obtained for Steel B, was only 454 VHN in this case. That is almost equal to the hardness in the as-received condition.

Table (4.1.3). Vickers hardness of Steel B after austenitisation at 900°C, water-quenching and tempering

Time [hr]	**VHN hardness after tempering at these temperatures**		
	170°C	**200°C**	**250°C**
0	557	557	557
0.5	527	508	429
1	517	465	429
4	481	467	462
11	454	454	459
24	454	454	462

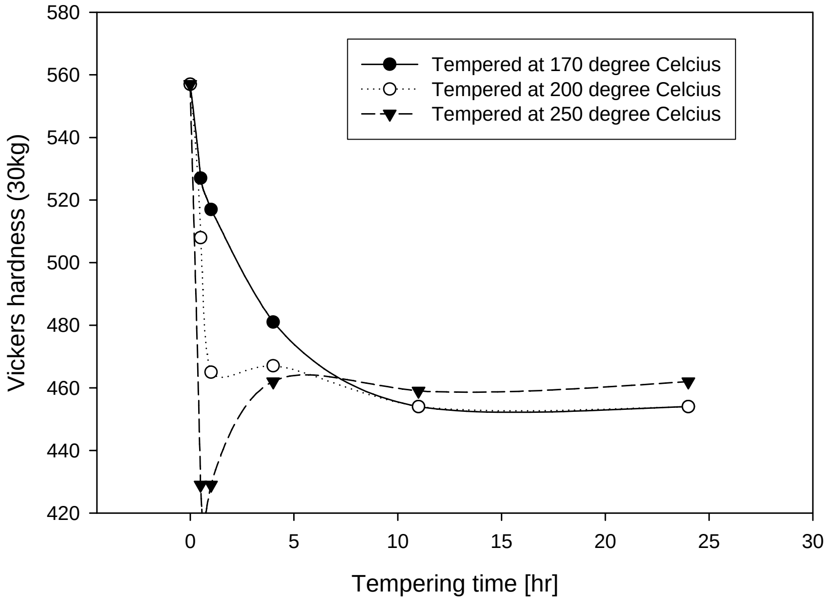

Figure 4.1.4. Vickers hardness number of steel B austenitised at 900°C for 20 minutes, water-quenched and tempered.

Carbon extraction replica transmission electron microscopy of the as-received steel B, revealed a significant volume fraction of coarse carbides formed on ferrite grain boundaries. The semi-quantitative analysis of the carbide particles by X-ray diffraction showed that these coarse particles contain Iron, Chromium, Manganese and Vanadium, whereas the finer particles contain mainly Titanium and Vanadium with less Chromium, Manganese and Iron. The coarse carbide particles formed consistently during the tempering of the 30 mm thick plates of steel B at 590°C. The Titanium particles were inherited from the steel making process and would necessitate a very high solution temperature (and for a long time) to dissolve before quenching. This will cause grain growth with its detrimental effect on the subsequent toughness of the armour plate. Therefore, from a direct comparison of the locally produced steel B with the imported steel C, it appears that the Titanium and Vanadium should be reduced to the lowest level in these steels, and the tempering temperature should be low to prevent diffusion of the alloying elements and the subsequent formation of the corresponding carbide. To avoid excessive grain growth, however, in a Ti-free steel, the austenitisation times should be kept as short as possible.

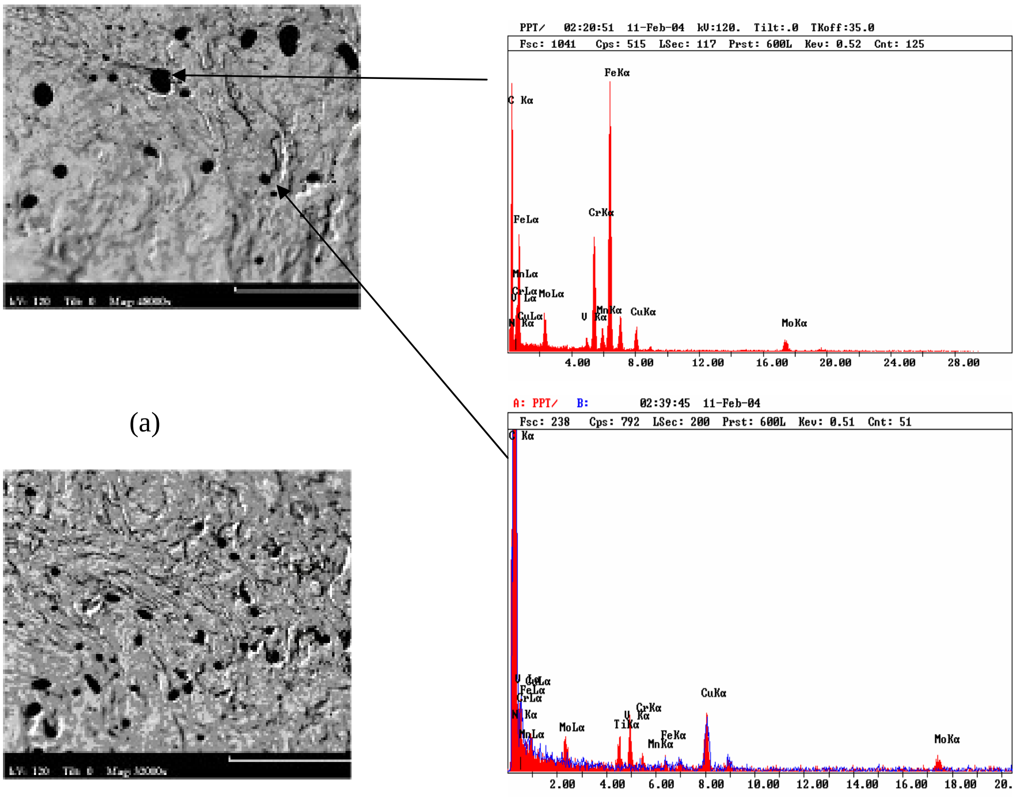

(a)

(b)

Figure 4.1.5. (a), (b) Carbon extraction replica transmission electron microscopy of a 30 mm steel B armour plate austenitised at 910°C , water quenched and tempered at 590°C for 38 minutes (label scale length = 10 microns)

4.1.3.3. Dilatometric analysis, quenching and tempering of steel C

From the experience at Mittal Steel (South Africa), the imported steel C has superior ballistic properties than the locally produced steel B. The hypothesis of the existence of a relationship between the microstructure and the ballistic performance of an armour steel, suggests that the difference in ballistic performance between these two steels may be established from their differences in microstructures.

The mechanical properties and microstructure of steel C have, therefore, been used as the minimum requirement for the new RB600 armour steel. The specifications for the steel C are given in Table (4.1.3).

Table (4.1.4). Specifications for steel C

	BHN	**$YS_{0.2\%}$ [MPa]**	**UTS [MPa]**	**Charpy impact energy at-40^0C[Joule]**	**Minimum elongation [%] on a 50 mm gauge length**
Steel C (specification)	570 – 640	1500	2000	12	5
Steel C (actual)	573 – 632	1400	2000	18	6

The transformation temperatures of steel C were determined by dilatometry and are reported in Table (4.1.1). A typical slow heating curve of steel C is shown in Figure 4.1.6(a), and the fast cooling curve for the determination of its M_S is shown in Figure 4.1.6(b).

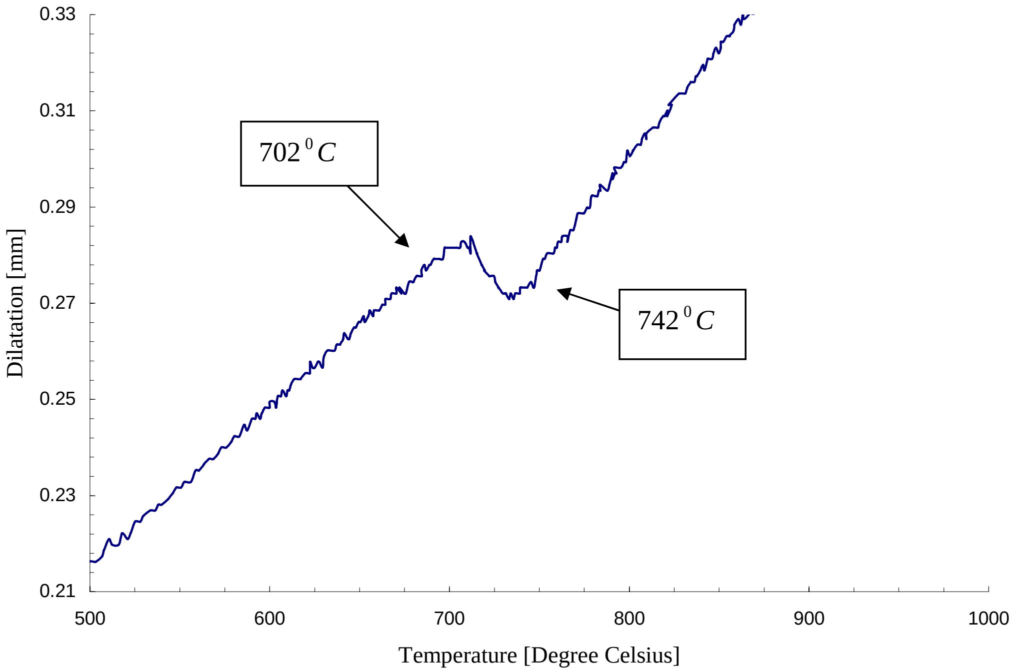

Figure 4.1.6(a): Slow heating curve of Steel C showing it's A_c transformation temperatures

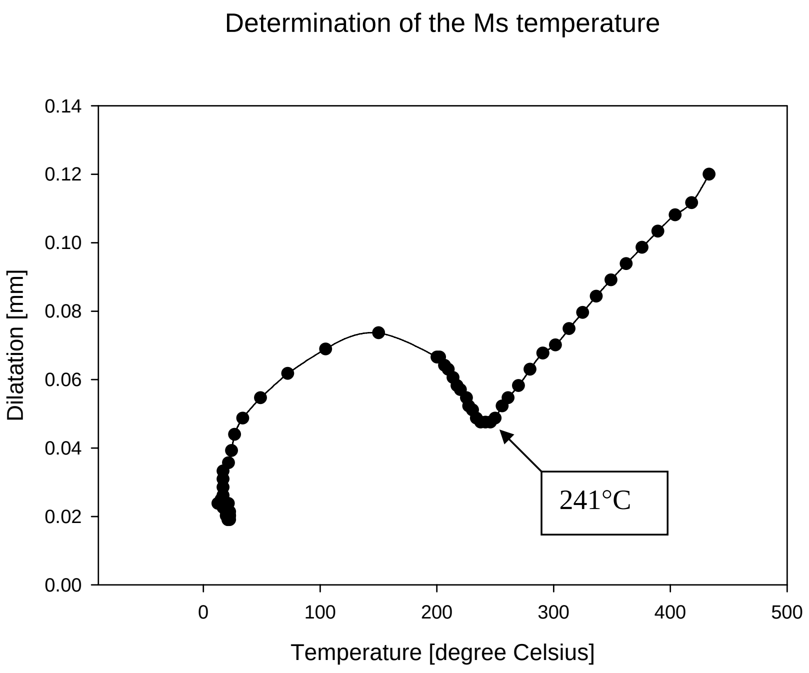

Figure 4.1.6(b) Fast cooling curve of steel C and reading off of the M_s temperature.

4.1.3.3.1. Hardness of steel C

The measurements of the Vickers hardness along four traverse lines crossing the 6.7 mm thick plate of steel C, are given in Table (4.1.5).

Table (4.1.5). Hardness profile of the 6.7 mm armour steel C plate

Depth from the surface [mm]	**VHN 30[kg/mm^2]**			
	Cross-line 1	**Cross-line 2**	**Cross-line 3**	**Cross-line 4**
0.5	652	648	618	639
1.5	680	661	657	666
2.5	631	635	644	637
3.5	614	622	644	627
4.5	635	626	652	638
5.5	648	626	622	632
Average	643	636	640	640
Std dev%	3	2	2	2

Steel C produced a Vickers hardness of 640 VHN with a standard deviation of 3%. Steel C is, therefore, harder than steel B. It also appears that steel C has a more consistent hardness through its cross section, which suggests the presence of a harder homogeneous microstructure. Nevertheless the hardness profile shows a relative maximum at about 1.5 mm below the outer surface and a relative minimum at a depth of about 3.5 mm on each of the four cross - lines.

This hardness profile indicates a relatively harder microstructure near the outer surface than near the inner surface, probably due to a difference in cooling rate on either side during the quench. The outer surface would, therefore, present a higher resistance to penetration in a ballistic test while the inner surface would be more resistant to spallation. Within the first 0.4mm depth from the outer surface, the Vickers micro hardness drops below 446 HV, probably due to some decarburisation during austenitisation. Near the other surface the micro hardness remains above 600 HV. This surface will, therefore, be better as the outer surface of the protective structure.

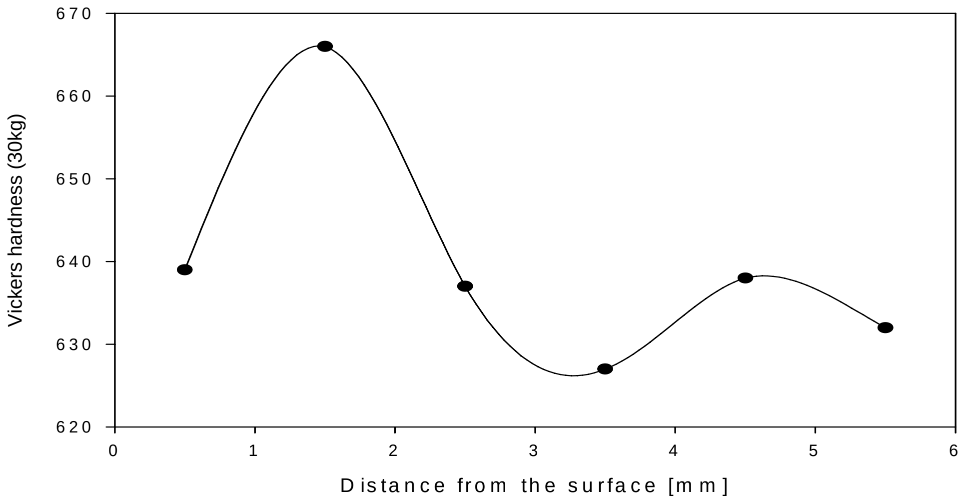

Figure 4.1.7. Transverse average hardness profile of Steel C

To explain the transverse hardness profile, two hypotheses were made. The first hypothesis is a possible segregation and a non-uniform distribution of alloying elements along the four hardness cross-lines. A cross-line semi-quantitative analysis with the scanning electron microscope did not reveal any major or measurable segregation of the main alloying elements, as may be seen in Figure 4.1.8, where the approximated weight percentages of the alloying elements determined by X-ray diffraction may be read off from the y-axis.

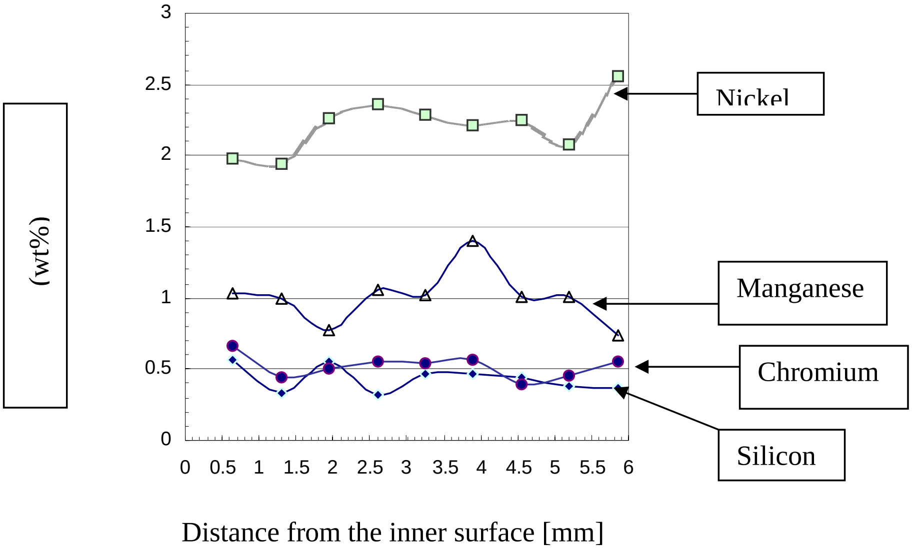

Figure.4.1.8. Alloying element distribution along a cross-line of Steel

The second hypothesis that was tested, is a possible fine precipitation of some carbides on grain boundaries during cooling after hot-rolling or during the tempering treatment. Such a precipitation can lead to some degree of depletion in Carbon within some areas. The assessment of this hypothesis is presented in the next section in Figure 4.1.10, by means of carbon extraction replica transmission electron microscopy.

.

4.1.3.3.2. Microstructure of steel C

The microstructure of steel C consists of a fine-grained martensite as shown Figure 4.1.9, by scanning electron microscopy. The resolution of optical microscopy was not enough to resolve this fine microstructure and, therefore, backscatter scanning electron microscopy was used for this purpose. Through the use of this SEM technique, it was not possible to confirm the presence of bainite in the martensitic microstructure. The grain size of steel C, as measured by SEM, varies between 8 and 10 micrometers. The grain boundaries and the precipitates were unresolvable because of their small sizes of less than 2 micrometers.

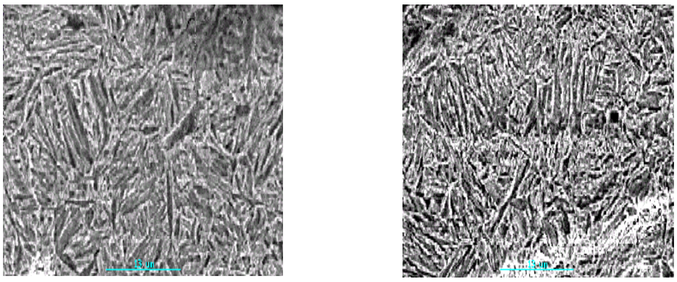

(a) (b)

Figure. 4.1.9. Microstructure of the 6.7 mm thick Steel C plate. Scanning electron micrographs at (a) 2.5 mm and (b) 3.5 mm depth into the plate.

The microstructure of this steel is a fine and homogeneous martensite throughout the cross section of the 6.7 mm plate. This fine microstructure may partially explain the higher hardness, combined with the higher toughness of steel C compared to steel B since it is well known that the microstructure predetermines the mechanical properties as assumed in the table below.

Table (4.1.6). Relationships in microstructure – mechanical properties

	Properties	**Controlling parameters**
Martensite	High hardness, high strength	Carbon and Manganese contents, austenitisation temperature and time, quench rate
Fine microstructure	highly defected substructure, retained austenite, fine precipitates	Nickel content, austenitisation temperature, cooling rate
Homogeneity	No stress raisers, high impact energy	Sulphur, Copper and Silicon contents, austenitisation temperature, cooling rate, tempering parameters

Figure 4.1.10 reveals no coarse carbide particles through carbon extraction replica transmission electron microscopy of sections taken at different depths below the outer surface. Contrary to steel B, the grain boundaries of steel C are without any carbides. Its matrix has finely dispersed particles of Titanium carbides and Titanium nitrides and these contain less Chromium and Manganese as in Steel B. There was also no measurable coarsening of the fine Titanium carbide and nitride particles during the tempering treatment, as was observed in steel B. A lower-temperature tempering for a shorter time of steel C may be the reason of the observed no coarsening of those particles.

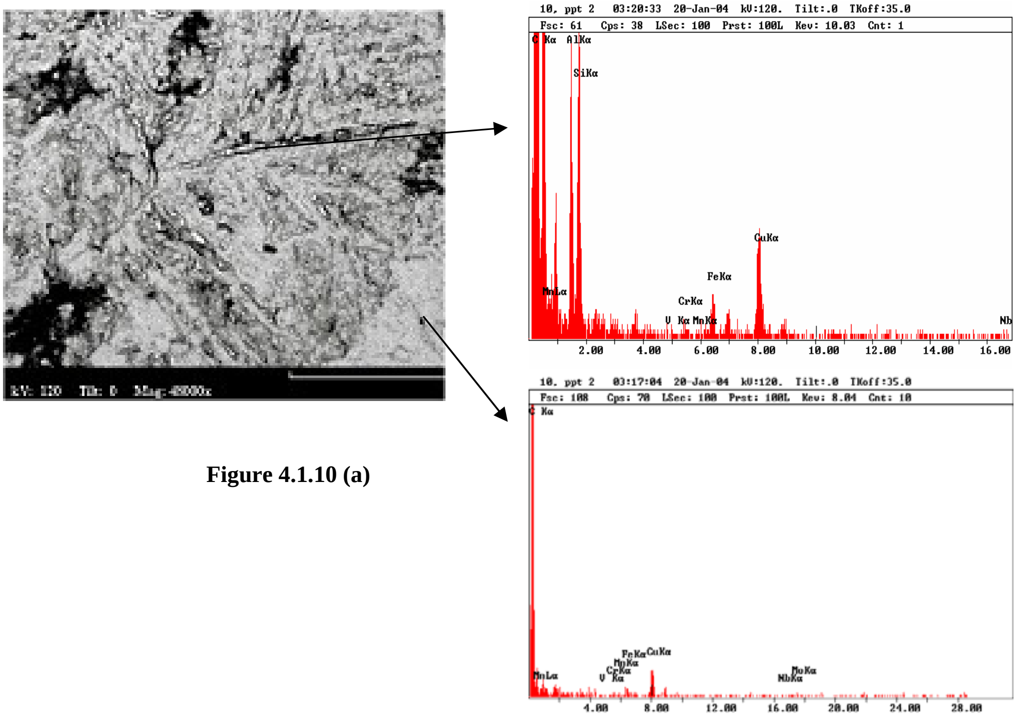

Figure 4.1.10 (a)

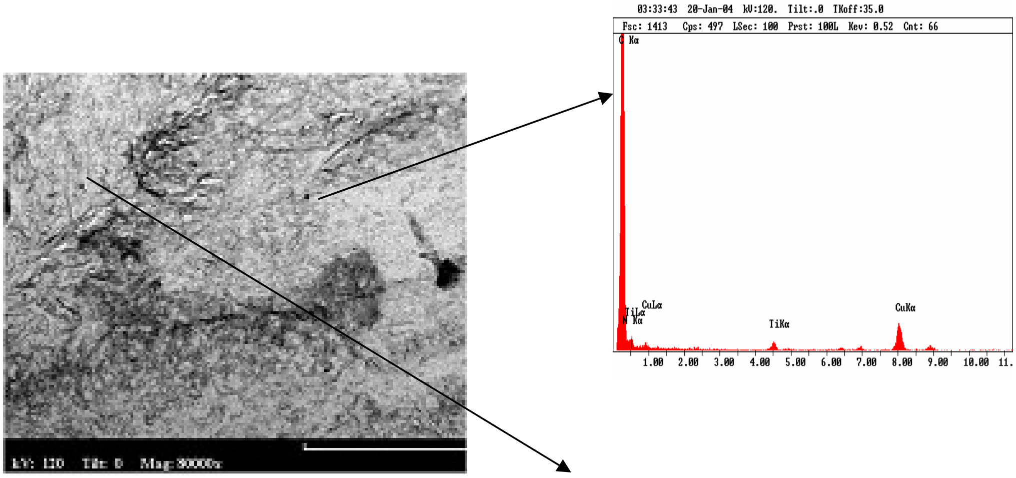

Figure 4.1.10 (b)

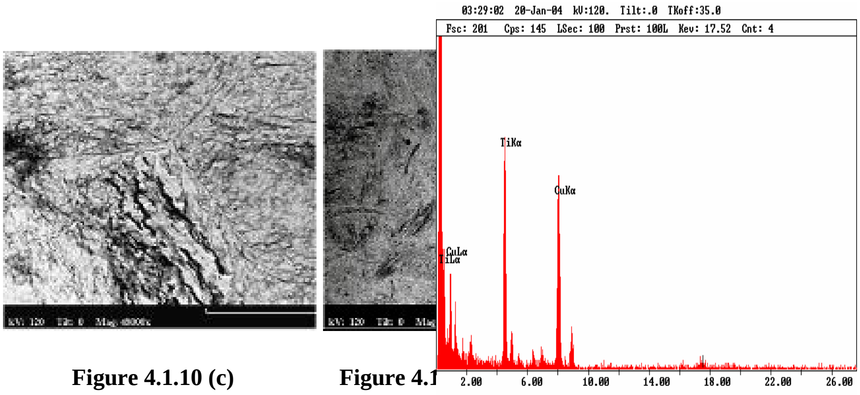

Figure 4.1.10 (c) **Figure 4.1**

Figure 4.1.10. Carbon extraction replica transmission electron micrographs and dark field images showing very fine carbides and nitrides within the matrix
(a): TEM carbon extraction replica at a depth of 0.5 to 1.5 mm from the surface;
(b) and (c): TEM extraction carbon replicas at a depth of 1.5 to 2.5 mm from the surface showing precipitate-free grain boundaries and small Titanium carbides and nitrides within the matrix.
(d): TEM extraction carbon replica at a depth of 3.5 to 4.5 mm from the surface revealing more fine particles than at depths of 1.5 mm and at 2.5 mm from the surface. (label scale length = 10 microns)

Thin foil transmission electron microscopy of Steel C in the as-received condition and an optical micrograph of a sample after a high-temperature tempering at 600°C for 30 seconds, are presented in figures 4.1.11 (a), 4.1.11 (b) and 4.1.12.

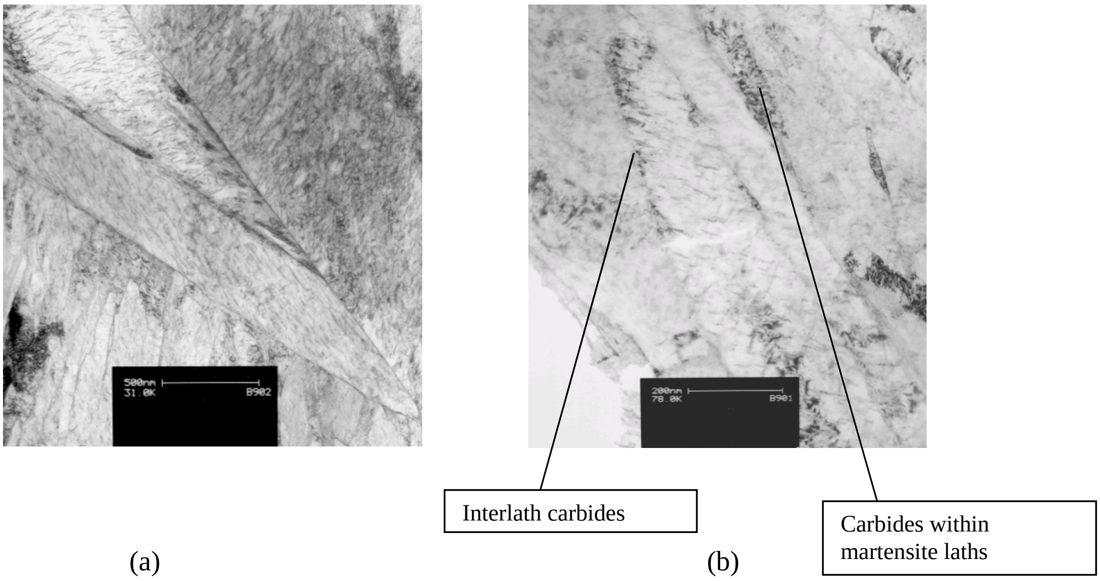

(a) (b)

Figure 4.1.11. Thin foil transmission electron microscopy of Steel C in the as-received condition.

Figure 4.1.11 (a) and (b) show fine elongated carbides within the martensite laths of Steel C and slightly round carbide particles on and near the lath interfaces. The optical micrograph of the sample tempered at 600°C presents a microstructure composed of ferrite and coarse carbide particles, with a lower hardness.

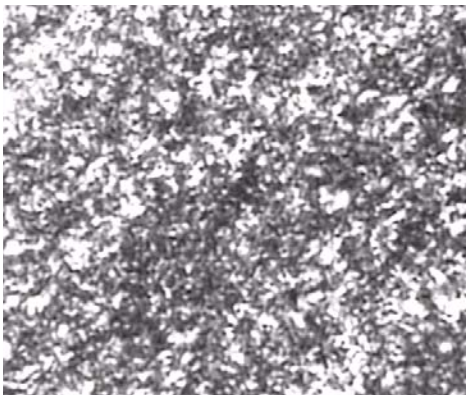

Figure 4.1.12. Optical micrograph of the Steel C after tempering 30 seconds at 600°C (magnification x1000).

Tempering of Steel C at 600°C for 30 seconds already softened the material to a hardness well below the specification. The hardness values of Steel C corresponding to the microstructures in figure 4.1.11 and figure 4.1.12 are compared in table 4.1.7.

Table (4.1.7). Vickers hardness of Steel C as-received and after tempering at 600°C.

	Figure No.	**Vickers hardness**
As-received	4.1.10 (a) and 4.1.10 (b)	640
850°C for 20 minutes		652
900°C for 20 minutes		661
Tempered at 600 ^{0}C for 30 seconds	4.1.11	446

The hardness values of Steel C after austenitisation at 850°C and 900°C followed by water-quenching to room temperature, are slightly higher than in the as-received condition, as shown in Table 4.1.7. The difference in Vickers hardness between the austenitised and then water quenched sample, and the as-received Steel C armour plate, is about 20 VHN units, confirming the presence of a low-temperature tempering applied to this steel, contrary to the high-temperature-tempering applied to Steel B. After tempering at 600°C for 30 seconds, the martensitic microstructure is completely transformed into a structure consisting of ferrite and carbides have also formed, as shown in figure 4.1.11. This structure had a hardness of only 446 VHN, far below the specified range for Steel C which is 660 to 720 VHN or 580 BHN to 640 BHN.

Simulation of water quenching of a 6 mm and a 8 mm plate of Steel C, was performed in the THETA dilatometer using a flow of Helium as coolant.
This was done to assess the efficiency of the industrial quenching process. After this simulation the Vickers hardness varied between 661 VHN and 671 VHN, which is in the same range of the Vickers hardness obtained after water quenching and higher by 30 units than the hardness of the as-received 6.7 mm Steel C armour plate. This again confirms the effectiveness of a low-temperature tempering treatment for a short time as was apparently applied in the case of Steel C armour plate. Figure 4.1.13 presents the three simulation curves superimposed on six experimental cooling curves of water quenching in the Mittal plant of steel bars and plates. The legend attached to the curves may be read as: 13B8P WQ designates the cooling curve for a 13 mm bar or a 8 mm plate, water-quenched to room temperature.

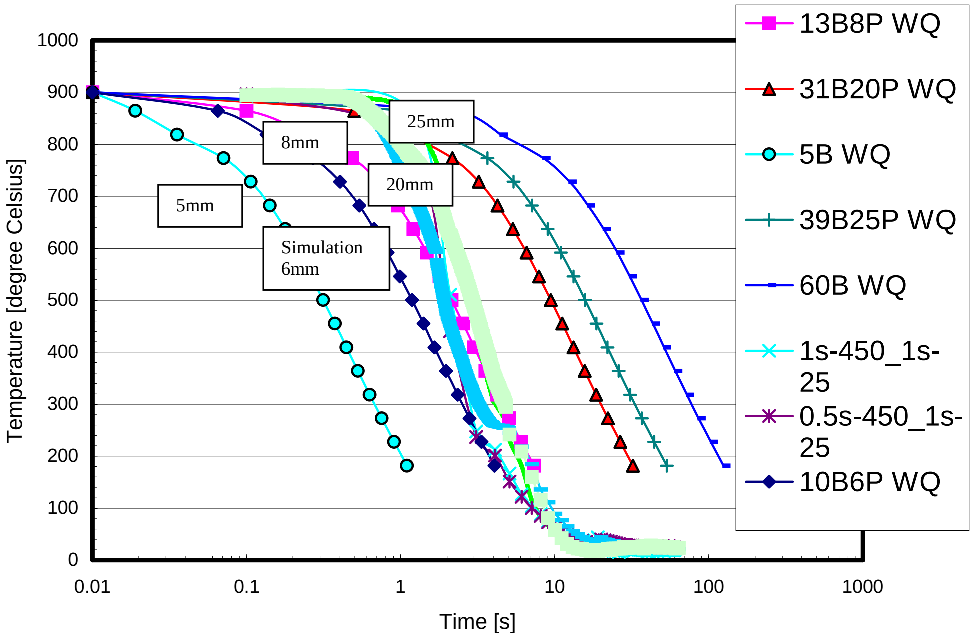

Figure 4.1.13. Three simulation curves of the water quenching of Steel C plates superimposed on 6 experimental cooling curves of industrial water quenching of plate steels in the Mittal plant.

The simulation samples were austenitised at 900°C for 10 minutes before being quenched in a flow of Helium according to the three simulation curves in °C versus time (in seconds) above.

4.2. Proposed design for an advanced RB600 armour plate

From these experiments it appears that the highest achievable hardness with steel B under the specified conditions, is 557 VHN. This hardness is reached through austenitisation at 900°C for 20 minutes and a water-quench to room temperature. The relatively low Carbon content of 0.3%C is the main barrier to the improvement in hardness of Steel B to values up to 640 VHN or 600 BHN after quenching, as required by the specification. Extraction carbon replica transmission electron microscopy has revealed that the high-temperature tempering at 590°C for more than 38 minutes (as was applied to Steel B armour plates) led to the precipitation of coarse carbides and to undesirable heterogeneities in the microstructure that alter the ballistic performance negatively. The coarse carbide particles are potential stress-raisers and reduce the nominal stress for effective resistance to impact loading. A low-temperature tempering should be considered to avoid this effect. Moreover, preliminary experiments have also shown that the hardness decreases by 10% to 25% of its initial value in the as-quenched condition when a low-temperature tempering between 170°C and 250°C is applied to both steel B and C armour plates.

A good armour martensitic steel should, therefore, have a fine and homogeneous microstructure consisting of a low temperature tempered martensite. Furthermore, such material must be clean with neither inclusions nor carbide precipitates on grain boundaries.

The following hypotheses have, therefore, been formulated for the development of an advanced armour plate steel with a superior ballistic performance:

1. to slightly increase the hardness and the strength of the martensitic steel through a moderate increase of the Carbon content to between 0.38%C and 0.43%C;
2. to prevent quench-cracking in the plates by adding Manganese in the range of 0.8 % to 2 %Mn;
3. to prevent or to delay the precipitation of cementite or any M_3C precipitates by adding Silicon and Chromium within the range of 0.4 % to 1.5 %;
4. to austenitise between 80°C 0 and 950°C for less than 60 minutes to prevent austenite grain growth;
5. to temper the armour plate below 250°C for less than 60 minutes for the necessary reduction of quench residual stresses for an increase of the toughness of the martensitic microstructure;
6. the Sulphur content should ideally be kept below 0.005%S to prevent the formation of Manganese sulphide particles that may act as stress raisers; and
7. the Titanium and Niobium contents should ideally be kept lower than 0.005%.

These seven hypotheses formed the basis for designing the first five high-performance armour steels. In practice, however, slight deviations from some of these “ideal” limits were found in some of the experimental alloys. These slight deviations appeared, however, not to be critical to the main hypotheses by which the alloy’s compositions were selected. The optimisation of their mechanical properties, microstructures and their ballistic performances are presented in the next paragraph.

4.3. Optimisation of the mechanical properties.

4.3.1. The optimisation problem

Until now, the hardness of armour plate was considered to be the decisive criterion in predicting the ballistic performance of the steel as it is supposed to indicate the ability of the target to withstand the impact of the projectile. Other design specifications for ballistic steels are based on the true strength to fracture and the resistance to spallation upon high velocity and hypervelocity impact that induces a high strain rate in the target. It appears that one possible approach in designing an advanced performance armour steel, defined here as RB600, would consist of a constrained optimisation problem of the hardness, the objective function, with two constraint functions, i.e. the tensile strength and the impact energy. Another design philosophy would specify an optimum constrained minimum of the objective function defined by the ratio YS/UTS of the candidate armour steel with two constraint functions, namely the Charpy impact energy at -40°C and the tensile strength at room temperature which is an indication of the true fracture strength of these steel.

It may be shown that the ratio YS/UTS is proportional to $(n)^n$, where n is the Hollomon work hardening exponent, by the relationship $\frac{YS_{(0.2)}}{UTS} = \left(\frac{e \times 0.2}{n}\right)^n$. The Hollomon work hardening exponent n, defines the ability of the material to resist instability in strain as found in the localisation of plastic deformation. The function $\frac{YS_{(0.2)}}{UTS}$, therefore, may define the objective function that must be minimised to meet the ballistic requirements, because this ratio decreases when n increases as $n < 1$.

It was noted in Chapter 2 that adiabatic conditions prevail in the impacted region during ballistic testing and the localised temperature may exceed 700°C, which is far above the testing temperature at which the mechanical properties are commonly measured for ballistic materials. At 700°C, phase transformations may occur that modify the microstructure and the mechanical properties of the armour steels. It is, therefore, necessary to finally assess the ballistic performance of the armour steels by ballistic testing to assure conformation with the requirement for military and security standards. The analysis of the localised microstructures of the armour steels before and after ballistic testing will, therefore, become a vital tool for understanding the relationship between the microstructures, the mechanical properties and the ballistic performance. The following methodology was, therefore, followed in the design of the advanced RB600 armour plate steel:

- design the first five alloys and their heat treatment based on the industrial and metallurgical understanding of the current armour steels B and C;
- solve the constrained optimisation problem of the mechanical properties in terms of four *independent variables*; viz. the austenitisation temperature, the tempering temperature, the tempering time and the chemical composition and one *dependent variable*, the martensite start temperature;
- predict the ballistic performance of the armour steels using three different criteria based on the hardness, the Ballistic Performance Index (BPI) [6], (quoted in paragraph 2.2.4), and the ratio YS/UTS;

- perform the ballistic testing according to the ARMSCOR specification for military applications and assess the validity of the specification;
- analyse the microstructures and other features of the martensitic steels;
- understand and explain the metallurgical reasons for the high as well as the low performances; and
- redesign a range of new alloys and their heat treatment parameters and repeat steps 3 to 6 of the above methodology scheme.

4.3.2 The chemical composition

Based on the hypothesis formulated in section 2.8 and the conclusion after the orientation tests in section 4.2, five steels, namely, steels E, F, G, H and I whose chemical compositions are given in Table (4.3.1), were vacuum melted in 5 kg casts each, hot rolled, heat treated and tested mechanically as well as ballistically. The tensile tests were performed at room temperature whereas the Charpy-V impact energy of the sub-sized specimens (due to limitations on the plate thicknesses) was measured at -40°C. The hot rolled plates were austenitised for 20 minutes at different temperatures and tempered for different times up to two hours, also at different temperatures, as described in section 4.3.3.

Table (4.3.1): Chemical compositions (wt%) of the first five high performance armour steels

	C	**Mn**	**P**	**S**	**Si**	**Cu**	**Ni**	**Cr**	**Mo**	**V**	**Nb**	**Ti**	**N**
Steel E	0.39	1.22	0.008	0.003	0.21	0.10	2.99	1.49	0.5	0.006	0.002	0.003	0.0049
Steel F	0.39	0.65	0.017	0.009	0.8	0.23	2.8	0.22	0.24	0.003	0.006	0.01	0.0051
Steel G	0.37	0.40	0.016	0.011	0.43	0.33	2.3	0.24	0.3	0.006	0.006	0.009	
Steel H	0.37	1.15	0.015	0.011	1.06	0.14	3.8	0.52	0.43	0.008	0.008	0.007	0.0036
Steel I	0.34	0.39	0.019	0.012	0.40	0.32	2.43	0.27	0.37	0.009	0.009	0.008	

The martensite start temperatures of these steels were measured by dilatometry as described previously and are given in Table (4.3.2). The volume fractions of retained austenite in the respective alloys were determined by quantitative X-ray diffraction.

Table (4.3.2): Measured M_S temperatures [°C] and volume fractions of retained austenite after quenching of steels E through to steel I

	Designation of the Steel				
	Steel E	**Steel F**	**Steel G**	**Steel H**	**Steel I**
Ms temperature [°C]	196	255	271	210	309
Volume fraction of the retained austenite [%]	5	0.6	0.5	4	0.5

4.3.3. The heat treatment cycle

Tensile specimens and sub-sized Charpy specimens, whose dimensions are presented in paragraphs 3.6.2 and 3.6.3 respectively, were austenitised at temperatures ranging between 800°C and 950°C for 20 minutes, before being water-quenched to room temperature and tempered at relatively low temperatures between 150°C and 400°C for various times between 0 and 120 minutes. The low-temperature tempering treatment was motivated by the constraint on the hardness requirement which, as specified by ARMSCOR and Mittal Steel South Africa for the high performance armour steels, should be as high as 600 HBN or 640 VHN, and also by the abrupt drop of hardness to values lower than 450 VHN observed on steels B and C when tempered above 200°C. However, to capture the effects of this softening behaviour, the effect of the tempering temperature on the mechanical properties was, therefore, studied over quite a large range, i.e. from room temperature to 400°C. Moreover, the effect of the heat treatment parameters on the ratio YS/UTS was analysed.

4.3.4. Variation of the mechanical properties

The variation of the yield strength to ultimate tensile strength ratio YS/UTS, the ultimate tensile strength and the Charpy impact energy of steels E through to I as a function of the austenitisation temperature and the tempering temperature, are first presented. This will be followed by a comparative analysis taking into account the differences in the martensite start temperatures of the candidate advanced performance armour steels. The optimisation problem is stated for each steel in terms of the objective function that needs to be minimised and two constraints. The three equations were determined for each of the five steels E through to I by surface fitting using EXCEL 2000 software. The three-dimensional plots of the surfaces and the projections of the isolines for the two-dimensional mapping of the optimum regions were performed using MATLAB 7.0.

From the experimental data it was observed that third degree polynomials could fit the results within the experimental ranges of the austenitisation temperature and the tempering temperature, with good accuracy. This led to the general mathematical expression of the surfaces representing the properties as follows:

- The austenitisation and tempering temperatures require normalisation to allow the computation and to provide the minimum rounding errors. It was found to be better to work with values within the same numerical range, i.e. –1 to +2 rather than using two different ranges for the austenitisation temperatures and the tempering temperatures. The normalised tempering temperature T_{tn} is defined, here, as follows:

$$T_{tn} = \frac{(T_t - T_{tm})}{(T_{tm} - 25)} \qquad (4.1)$$

where T_t is the actual tempering temperature in degrees Celsius, T_{tm} is a mean tempering temperature from $T_{tm} = \frac{25+300}{2}$ =162.5°C. Exactly how this normalised temperature is defined is not too important for the purposes of this study as the same trends will be found using a different normalisation definition.

- The normalised austenitisation temperature T_{an} is defined, here, as follows:

$$T_{an} = \frac{T_a - T_{am}}{T_{am} - 850} \qquad (4.2)$$

where T_a is the actual austenitisation temperature in degrees Celsius and T_{am} is the mean austenitisation temperature from $T_{am} = \frac{800+950}{2}$ =875°C.

- The particular mechanical property (MP) is then fitted by the surface fitting equation:

$$MP(T_{an},T_{tn}) = a(T_{an}) \times T_{tn}^{3} + b(T_{an}) \times T_{tn}^{2} + c(T_{an}) \times T_{tn} + d \qquad (4.3)$$

where the fitting parameters a, b, c and d are polynomials in T_{an} and are of the general form:

$$p = A \times T_{an}^{3} + B \times T_{an}^{2} + C \times T_{an} + D \qquad (4.4)$$

where A, B, C and D are constant real parameters.

- Combining equations (4.3) and (4.4) gives a sixth order non-linear equation in the normalised temperatures T_{an} and T_{tn}:

$$MP(T_{an},T_{tn}) = (A_1 \times T_{an}^{3} + B_1 \times T_{an}^{2} + C_1 \times T_{an} + D) \times t_{tn}^{3} + (A_2 \times T_{an}^{3} + B_2 \times T_{an}^{2} + C_2 \times T_{an} + D_2) \times t_{tn}^{2} + \\ (A_3 \times T_{an}^{3} + B_3 \times T_{an}^{2} + C_3 \times T_{an} + D) \times t_{tn} + (A_4 \times T_{an}^{3} + B_4 \times T_{an}^{2} + C_4 \times T_{an} + D_4) \qquad (4.5)$$

Equation 4.5 is the mathematical presentation of the particular mechanical property to be considered in the optimisation problem. The optimisation techniques currently used apply to the optimisation of quadratic non-linear problems. It then becomes necessary in the present case to graphically solve the problem using two-dimensional projections of contours of equal height (i.e. iso-lines) to visualise the optimum regions in the normalised (T_{an}, T_{tn}) planes.

4.3.4.1 Mechanical properties of Steel E

a) Fitting function for the UTS

The results from the measurements of the ultimate tensile strength of steel E are presented in Table (4.3.3).

Table (4.3.3). Ultimate tensile strength of steel E (MPa)

		Ultimate tensile strength in MPa as a function of the austenitisation temperature [°C]			
Tempering temperature[°C]	**Normalised tempering temperature T_{tn}**	**800°C**	**850°C**	**900°C**	**950°C**
25°C	-1	1202	1456	1400	1436
150°C	-0.09091	1956	1767	1580	1524
200°C	0.272727	1935	1846	1472	1535
250°C	0.636364	1874	1609	1326	1484
300°C	1	1800	1320	1308	1317
350°C	1.363636	1553	1265	1173	1115
400°C	1.727273	1532	1202	1076	995

The surface fitting is done in two steps and the first one gives the estimate of the parameters required in Equation (4.3) at different austenitisation temperatures. The results of these calculations and the correlation coefficient R^2 for steel E are tabled below:

Table (4.3.4): The fitting parameters and the correlation coefficients in equation (4.3) for the ultimate tensile strength of steel E

Austenitisation temperature	**Normalised austenitisation temperature**	**Fitting parameters in equation (4.3)**				**Correlation coefficient**
		a	**b**	**c**	**d**	
800°C	-1	158.3	-488.26	112.67	1961.2	0.984
850°C	-0.33333	184.05	-410.62	-209.35	1832.6	0.939
900°C	0.333333	79.271	-201.67	-148.29	1537.3	0.965
950°C	1	12.683	-177.44	-67.755	1553	0.978

It appears that the parameters a, b, c and d are some function of the austenitisation temperature. The second step of the surface fitting process consists of determining the variation of each of these parameters in Table (4.3.4) with the normalised austenitisation temperature. The results of the calculations are tabled as follows:

Table (4.3.5): The fitting parameters and the correlation factors in equation (4.4) for the ultimate tensile strength of steel E.

	Parameters in equation (4.4)				**Correlation coefficients**
	A	**B**	**C**	**D**	
a	94.905	-51.94	-167.71	137.43	1
b	-177.77	-30.043	333.18	-302.81	1
c	-204.53	226.44	114.32	-203.98	1
d	268.71	81.169	-472.81	1675.9	1

The variation of the ultimate tensile strength of steel E with the normalised austenitisation and tempering temperatures may then be represented mathematically by the function:

$$UTS=\left(94.905T_{sn}^{3}-51.94T_{an}^{2}-167.71T_{an}+137.43\right)\times T_{tn}^{3}+\left(-177.77T_{an}^{3}-30.043T_{an}^{2}+333.18T_{an}-302.81\right)\times T_{tn}^{2}$$
$$+\left(-204.53T_{an}^{3}+226.44T_{an}^{2}+114.32T_{an}-203.98\right)\times T_{tn}+\left(268.71T_{an}^{3}+81.169T_{an}^{2}-472.81T_{an}+1875.9\right)$$

(4.6)

b) Fitting function for the ratio YS/UTS

The determination of the function expressing the variable YS/UTS for steel E, also as a function of the austenitisation and tempering temperatures, is done by the same two-step process above that was used for the surface fitting of the ultimate tensile strength.

The results on the YS/UTS ratios from the tensile tests at room temperature on steel E are given in the Table (4.3.6). The calculated surface fitting parameters to be considered in Equations (4.3) and (4.4) for the YS/UTS ratio are shown in Tables (4.3.7) and (4.3.8).

Table (4.3.6): The YS/UTS ratio of steel E at room temperature, as a function of the austenitisation and tempering temperatures

		YS/UTS ratio as a function of the austenitisation temperature			
Tempering temperature	**Normalised tempering temperature**	**800°C**	**850°C**	**900°C**	**950°C**
25°C	-1	0.47	0.46	0.44	0.42
150°C	-0.09091	0.50	0.47	0.44	0.43
200°C	0.272727	0.53	0.49	0.45	0.46
250°C	0.636364	0.57	0.51	0.49	0.51
300°C	1	0.61	0.53	0.53	0.55
350°C	1.363636	0.64	0.55	0.57	0.59
400°C	1.727273	0.66	0.57	0.61	0.64

Table (4.3.7) The fitting parameters and the correlation coefficients in equation (4.3) for the ratio YS/UTS of steel E

		Parameters in equation (4.3)			
Austenitisation temperature	**Normalised austenitisation temperature**	**a**	**b**	**c**	**Correlation coefficient**
800°C	-1	0.0159	0.0632	0.5167	0.98
850°C	-0.33333	0.0098	0.0336	0.4816	0.997
900°C	0.333333	0.033	0.043	0.4444	0.993
950°C	1	0.0291	0.0635	0.4464	0.991

Table (4.3.8) : The fitting parameters and the correlation factors in equation (4.4) for the ratio YS/UTS of the steel E.

	Parameters in equation (4.4)				**Correlation coefficients**
	A	B	C	D	
a	-0.0317	0.0012	0.0383	0.0213	1
b	-0.0157	0.0282	0.0158	0.0352	1
c	0.0232	0.0209	-0.0584	0.4607	1

The variation of the YS/UTS ratio with the austenitisation and the tempering temperatures is then described by the function introducing the normalised temperatures T_{an} and T_{tn} expressed in Equation (4.7):

$$\frac{YS}{TS} = \left(-0.0317T_{an}^{3} + 0.0012T_{an}^{2} + 0.0383T_{an} + 0.0213\right) \times T_{tn}^{2} + \left(-0.0157T_{an}^{3} + 0.0282T_{an}^{2} + 0.0158T_{an} + 0.0352\right) \times T_{tn}$$
$$+ \left(0.0232T_{an}^{3} + 0.0209T_{an}^{2} - 0.0584T_{an} + 0.4607\right) \qquad (4.7)$$

c) Fitting function for the Charpy impact energy

Equation (4.7) is the objective function that needs to be minimised for steel E. Equation (4.6) is the first constraint on the system while the second constraint is taken from the Charpy impact energy of the sub-sized specimens tested at -40°C.

The fitting surface is obtained from the experimental values of the Charpy impact energy presented in Table (4.3.9). The fitting parameters for Equations (4.3) and (4.4) obtained by regression analysis, are given in Tables (4.3.10) and (4.3.11) respectively.

Table (4.3.9): Charpy impact energy (in Joules) of steel E (of the sub-sized specimens) tested at -40°C, as a function of both the austenitisation and the tempering temperatures

		Charpy impact energy (J) as a function of the austenitisation temperature			
Tempering temperature	**Normalised tempering temperature**	**800°C**	**850°C**	**900°C**	**950°C**
25°C	-1	6.9	5.9	4.9	4.9
150°C	-0.09091	7.9	6.9	5.9	4.9
200°C	0.272727	8.9	7.9	7.9	6.9
250°C	0.636364	10.8	8.9	7.9	6.9
300°C	1	12.8	9.8	8.9	7.9
350°C	1.363636	13.8	11.8	9.8	7.888
400°C	1.727273	13.8	12.8	11.8	10.8

Table (4.3.10: Fitting parameters of the Charpy impact energy of steel E, in Equation (4.3)

		Fitting parameters in (4.3)				
Austenitisation temperature	**Normalised austenitisation temperature**	**a**	**b**	**c**	**d**	**Correlation coefficients**
800°C	-1	-1.3036	1.8385	4.1496	7.946	0.995
850°C	-0.33333	-0.1717	0.925	2.2822	7.1079	0.995
900°C	0.333333	0.2342	0.2435	1.7912	6.648	0.97
950°C	1	0.293	0.4097	1.0982	5.808	0.906

Table (4.3.11): Fitting parameters of the Charpy impact energy of steel E, in Equation (4.4)

	Fitting parameters in (4.4)				**Correlation coefficients**
	A	**B**	**C**	**D**	
a	0.2131	-0.6036	0.5825	0.0983	1
b	0.3463	0.6073	-1.0607	0.5168	1
c	-0.8878	0.6606	-0.6379	1.9633	1
d	-0.4265	-0.0011	-0.6425	6.8781	1

The mathematical expression that fits the experimental Charpy impact energy may be written as:

$$
\begin{aligned}
CIE(-40^0C) = {} & \left(0.2131T_{an}^{\ 3} - 0.6036T_{an}^{\ 2} + 0.5825T_{an} + 0.0983\right) \times T_{tn}^{\ 3} + \left(0.3463T_{an}^{\ 3} + 0.6073T_{an}^{\ 2} - 1.0607T_{an} + 0.5168\right) \times T_{tn}^{\ 2} \\
& + \left(-0.8878T_{an}^{\ 3} + 0.6606T_{an}^{\ 2} - 0.6379T_{an} + 1.9633\right) \times T_{an} + \left(-0.4262T_{an}^{\ 3} - 0.0011T_{an}^{\ 2} - 0.6425T_{an} + 6.8781\right)
\end{aligned}
\tag{4.8}
$$

Equation (4.8) is the second constraint of the system to be optimised.

Overall fitting

The optimisation problem may be written in classical form as follows:

$$\begin{aligned} YS/UTS &\leq r_0 \\ UTS &\geq \Sigma_0 \\ CIE(\text{-}40°\mathrm{C}) &\geq IE_0 \end{aligned} \tag{4.9}$$

where r_0 is the boundary in the YS/UTS ratio yet to be determined after ballistic testing, Σ_0 is the current limit in UTS specified by ARMSCOR and is equal to 1700 MPa. The validity of this limit will be re-assessed later after the ballistic testing. CIE_0 is the minimum Charpy impact energy that indicates the resistance against spallation when the armour steel is impacted by a high velocity projectile at sub-zero temperatures. The ARMSCOR specification fixes this minimum at 13 Joules for full size Charpy specimen tested at -40°C. The optimisation problem represented in Equation (4.9) is shown graphically in Figure (4.3.1). From Tables (4.3.3), (4.3.6) and (4.3.9), it appears that a three-dimensional plot of the three functions that compose the system within the same axes, will require a scaling factor for visualisation of the problem. This is due to the fact that the absolute values of the YS/UTS ratio are very small compared to the ultimate tensile strength. A scaling factor of 2000 is, therefore, applied to the YS/UTS ratio and one of 100 to the Charpy impact energy function $CIE(\text{-}40°\mathrm{C})$ before plotting. The effect of the scaling factors is only a translation of the fitting surfaces from lower to high values, but will still display the trends as before**.** The objective function YS/UTS is represented by the surface in between the ultimate tensile strength surface on top and the Charpy impact energy surface on the bottom. The feasible region as well as the optimum region are visualised by the use of the contours of equal values of the properties.

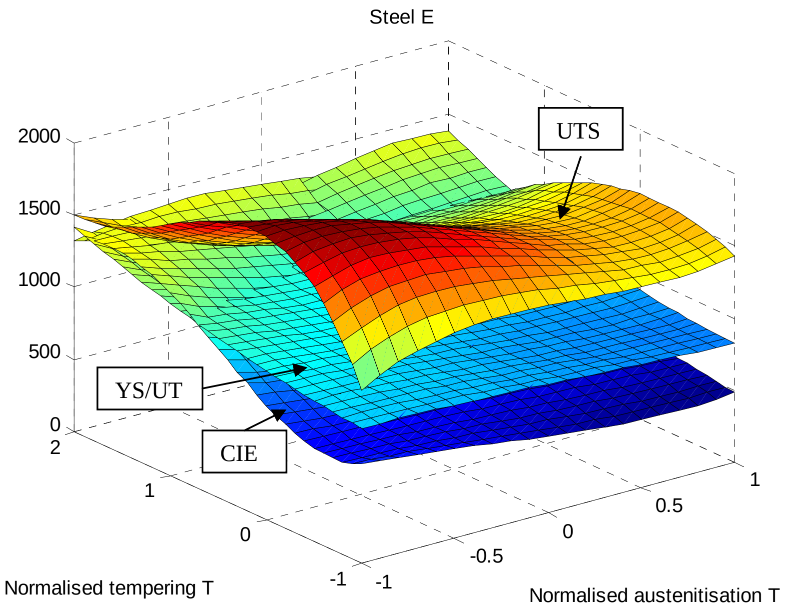

Figure 4.3.1(a): Three-dimensional representation of the YS/UTS objective function (surface in the middle), the UTS (upper surface) and the Charpy impact energy (lower surface)

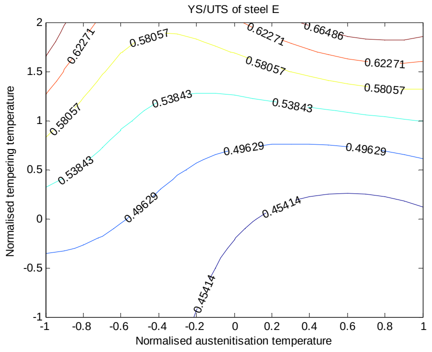

Figure 4.3.1(b): Contours of constant YS/UTS ratio for steel E

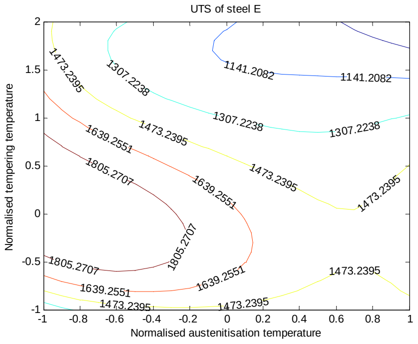

Figure 4.3.1(c): Contours of constant tensile strength (in MPa) of steel E

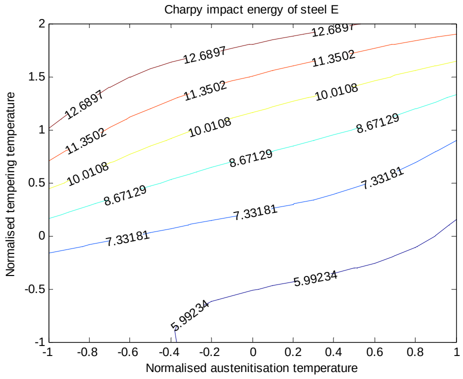

Figure 4.3.1(d): Contours of constant Charpy impact energy (in Joules) at -40°C for Steel E

From Figure 4.3.1(b), it appears that the optimum region for the YS/UTS ratio corresponds to the region of medium to high normalised austenitisation temperatures which lie between the normalised values of –0.6 to 1, or actually between 830°C and 950°C; together with low values of the normalised tempering temperatures, lying between the normalised values of –1 and 0.4, or actually lower than 217°C.

From Figure 4.3.1(c), it appears that a tensile strength larger than 1700 MPa is obtained for steel E when the normalised austenitisation temperature is lower than –0.1 or lower than actually 867°C and the normalised tempering temperature lies between the normalised values of –0.5 and 1, or actually between 95°C and 300°C. If the tempering temperature is lower than 95°C, the tensile strength would become difficult to determine because of the brittle behaviour of steel E in this condition. From Figure 4.3.1(d) a Charpy impact energy at -40°C that is higher than the specified 13 Joules, is obtained for the normalised temperatures between –1 and 0.2 or lower than the actual 890°C and the normalised tempering temperature is above 0.9 or actually 286°C. The summary of this discussion is presented in Table (4.3.12).

Table (4.3.12). Heat treatment conditions predicted to be favourable to the ballistic properties for steel E.

	Favourable conditions	
Property	**Austenitisation temperature**	**Tempering temperature**
Low YS/TS	830°C to 950°C	< 217°C
High UTS	< 867°C	95°C to 300°C
CIE(-40°C)	< 890°C	> 286°C

The optimum heat treatment region for steel E may be fixed in a first approach, at an austenitisation temperature between 830ºC and 900ºC. It is more difficult to find a compromise concerning the tempering temperature between the YS/UTS ratio and the Charpy impact energy at -40°C, as can be seen from the third column in Table (4.3.12). Predominance has been given to the ratio YS/UTS according to the design methodology chosen in Section 4.3.1; and the optimum tempering temperature is, therefore, fixed at below 200°C for steel E.

The hardness of steel E varies with both the austenitisation temperature and the tempering temperature. The results on the Vickers hardness of this steel are given in Table (4.3.13). The regression analysis and the surface fitting were developed following the same scheme as proposed earlier in this Chapter. It is to be noted that the hardness of steel E decreases very fast to values as low as 450 VHN when the tempering temperature is above 200°C. That would be very low compared to the value of 650VHN specified by ARMSCOR and Mittal Steel South Africa for their advanced performance armour steels.

Table (4.3.13): Variation of the Vickers hardness of Steel E with the austenitisation temperature and the tempering temperature.

	Vickers hardness as a function of the austenitisation temperature [^{0}C]			
Tempering temperature °C	**800°C**	**850°C**	**900°C**	**950°C**
25°C	560	590	630	620
150°C	550	545	550	610
200°C	490	450	450	545
250°C	460	422	430	520
300°C	440	415	420	500

The fitting parameters for the corresponding Equations (4.3) and (4.4) are contained in Tables (4.3.14) and (4.3.15) respectively.

Table (4.3.14): Fitting parameters for the Vickers hardness of Steel E, in Equation (4.3)

		Fitting parameters for (4.3)				
Austenitisation temperature	**Normalised austenitisation temperature**	**a**	**b**	**c**	**d**	**Correlation coefficients**
800°C	-1	75.755	-33.953	-135.13	534.8	0.992
850°C	-0.33333	44.411	-14.824	-116.57	532.79	0.998
900°C	0.333333	29	8.5389	-113.52	537.12	0.997
950°C	1	79.519	-32.044	-138.65	593.22	0.985

Table (4.3.15): Fitting parameters for the Vickers hardness of steel E, in Equation (4.4)

	Fitting parameters for (4.4)				**Correlation coefficients**
	A	**B**	**C**	**D**	
a	28.123	46.048	-26.241	31.589	1
b	-38.351	-33.588	39.306	0.5894	1
c	0	-24.576	-1.1265	-112.31	0.983
d	0	32.687	26.939	531.32	0.96

The variation of the Vickers hardness with the austenitisation temperature and with the tempering temperature is then written in terms of the normalised temperatures as follows:

$$HV = \left(28.123T_{an}{}^{3} + 46.048T_{an} - 26.241T_{an} + 31.589\right)\times T_{tn}{}^{3} + \left(-38.351T_{an}{}^{3} - 33.588T_{an}{}^{2} + 39.306T_{an} + 0.5894\right)$$
$$\times T_{tn}{}^{2} + \left(-24.576T_{an}{}^{2} - 1.1265T_{an} - 112.31\right)\times T_{tn} + \left(32.687T_{an}{}^{2} + 26.939T_{an} + 531.32\right) \qquad (4.10)$$

The surface representing the Vickers hardness is presented in Figure 4.3.2(a), together with the plane for a hardness of 650VHN as specified by ARMSCOR and Mittal Steel South Africa. The plane for 550VHN is also shown in the same figure.

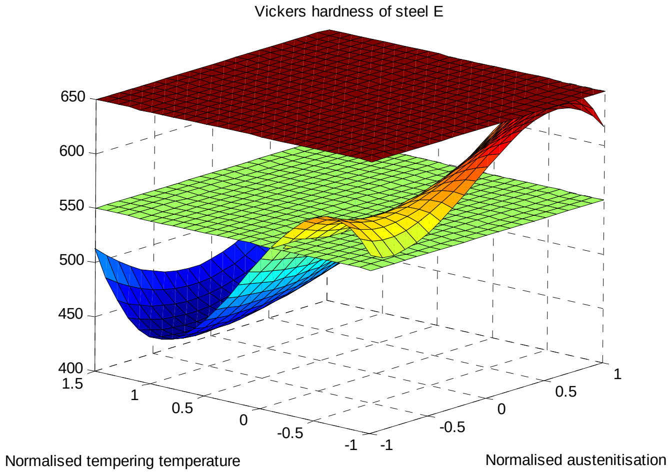

Figure 4.3.2(a): Variation of the Vickers hardness of steel E with the normalised austenitisation and tempering temperatures. The surface corresponding to the specified 650 VHN is shown together with one for 550 VHN.

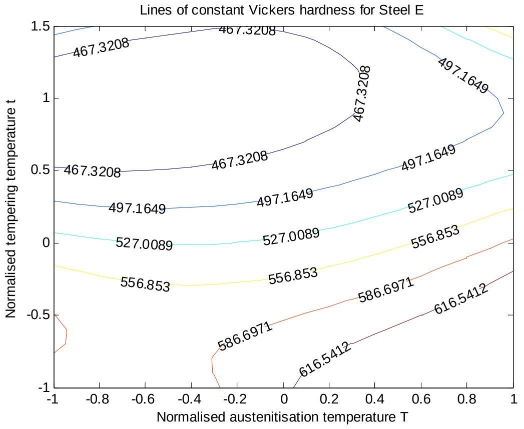

Figure 4.3.2(b): Lines of constant hardness corresponding to Figure 4.3.2.a.

The hardness of steel E in the quenched condition, is relatively constant when the austenitisation temperature is increased between 800°C and 900°C. Above this austenitisation temperature range, for instance at 950°C, however, the maximum hardness that was attained increased. This increase in hardness is mainly due to two factors; firstly the solid solution hardening of the parent austenite due to the increased dissolution of some carbides when the austenitisation temperature was increased and secondly, to a subsequent decrease in the M_S temperature leading to a harder untempered martensite with a greater amount of Carbon in solution.

At 950°C grain growth of the austenite may also become significant. The decrease in the martensite start temperature may, however, lead to an increase in the volume fraction of retained austenite and impose a limit on the increase in the average hardness of the steel. The grain size of steel E after austenitisation for 20 minutes, as determined by the line intercept method using the line scanning function of the scanning electron microscope, increased from $7.0 \pm 0.8\,\mu m$ when the austenitisation temperature was 850°C, to $10 \pm 0.8\,\mu m$ when the austenitisation temperature was 950°C.

It is to be noted in Table (4.3.12) that the higher tensile strength was achieved when the austenitisation temperature was below 867°C and it dropped again above this austenitisation temperature. This effect may also be related to grain growth and the increase in the volume fraction of the retained austenite. Therefore, it appears that both the tensile strength and the hardness increase with an increase in the austenitisation temperature, but the upper limit in the tensile strength occurs earlier than for the hardness. This apparent "disjunction" between the maximum hardness and UTS at a low austenitisation temperature for the former and at a high austenitisation temperature for the latter, may be related to the presence of retained austenite after a high austenitisation temperature which affects the different mechanical processes of hardness and tensile testing differently (due to different strain rates). A secondary effect may also arise from an increase in grain size at high austenitisation temperatures although this effect is probably relatively small due to a small increase in grain size from 7 to 10 μm.

The rate of decrease in hardness of steel E upon low-temperature tempering, appears to be slower when the austenitisation temperature is lower within the range from 800°C to 900°C**.** This trend indicates that at higher austenitisation temperatures the amount of Carbon dissolved into the parent austenite is high, which leads to a higher activity of Carbon in the martensite upon tempering. The sudden change of slope of the hardness curves in Figure 4.3.2(a) suggests the existence of two different mechanisms by which the martensite is softened within the considered tempering temperature range. The first softening mechanism is active below 150°C and the second mechanism, leading to a sharp drop in hardness, becomes active upon tempering between 200°C and 250°C. Tempering this armour steel between 200°C and 250°C leads to the coarsening of the metastable transition ε-carbides or η-carbides previously formed below 150°C and to their transformation into cementite.

The elongation upon tensile testing at room temperature increases when the tempering temperature is increased and it decreases when the austenitisation temperature is increased.

Table (4.3.16): Elongation of the 33 mm gauge length of steel E that was austenitised at 850°C and at 900°C respectively, water-quenched and tempered for 60 minutes.

	Tensile elongation (%) after austenitisation at these temperatures	
Tempering temperature	**850°C**	**900°C**
Water quenched	0.3	0.3
150°C	4.5	3.5
200°C	7	4.5
250°C	8.5	5.8
300°C	8.5	6.5

4.3.4.2. Mechanical properties of steel F

The optimisation problem for the candidate armour Steel F was established in the same manner than was done for steel E. The fitting parameters and final equations are given in Appendix A2 and only the graphical presentation is given here.

The optimum region for the predicted ballistic performance of this steel is discussed later in comparison with the optimum region for its mechanical properties.

Table (4.3.17): The yield strength to the tensile strength ratio of steel F.

		YS/UTS ratios as a function of the austenitisation temperature			
Tempering temperature	**Normalised tempering temperature**	**800°C**	**850°C**	**900°C**	**950°C**
25°C	-1	0.51	0.49	0.46	0.44
150°C	-0.09	0.53	0.51	0.47	0.47
200°C	0.27	0.53	0.53	0.51	0.49
250°C	0.64	0.57	0.54	0.53	0.51
300°C	1	0.61	0.59	0.57	0.55
350°C	1.36	0.66	0.65	0.60	0.59
400°C	1.73	0.71	0.67	0.61	0.60

The first constraint equation is derived from the measured tensile strength of steel F at room temperature and these are presented in Table (4.3.18). The corresponding fitting parameters are presented in Tables A2.1(c) and A2.1(d) of Appendix A2, which leads to the mathematical expression of the fitting surface A2.Eq1(b).

Table (4.3.18): Room temperature tensile strength in MPa of steel F.

		Ultimate tensile strength (MPa) as a function of the austenitisation temperature			
Tempering temperature	**Normalised tempering temperature**	**800°C**	**850°C**	**900°C**	**950°C**
25°C	-1	1624	1934	2246	1901
150°C	-0.09	2154	2277	2375	1998
200°C	0.27	2131	2364	2280	2010
250°C	0.64	2064	2103	2054	1954
300°C	1	1982	1784	1882	1770
350°C	1.36	1710	1724	1623	1548
400°C	1.73	1687	1654	1516	1415

The second constraint is derived from the Charpy impact energy of the sub-sized specimens of steel F measured at –40°C. The results in Joules are contained in Table (4.3.19) and the fitting parameters in Tables A2.1(e) and A2.1(f) from which the regression equation may be derived.

Table (4.3.19): The Charpy impact energy at –40°C of the sub-sized specimen of steel F

		Charpy impact energy (Joules) as a function of the austenitisation temperature			
Tempering temperature	**Normalised tempering temperature**	**800°C**	**850°C**	**900°C**	**950°C**
25°C	-1	9.0	7.7	6.4	6.4
150°C	-0.09	10.3	9.0	7.7	6.4
200°C	0.27	11.5	10.3	10.3	9.0
250°C	0.64	14.1	11.5	10.3	9.0
300°C	1	16.7	12.8	11.5	10.3
350°C	1.36	17.9	15.4	12.8	10.3
400°C	1.73	17.9	16.7	15.4	14.1

The optimisation problem for steel F is written in terms of the objective function A2.1(a) and the constraint equations A2.1(b) and A2.1(c) given in Appendix 2. The fitting surfaces for steel F are graphically represented in Figure 4.3.4(a). The same scaling factors as were applied to steel E were also applied here. The optimum regions for the mechanical properties are visualised in two-dimensional plots of the iso-lines in the plane (T_{an}, T_{tn}).

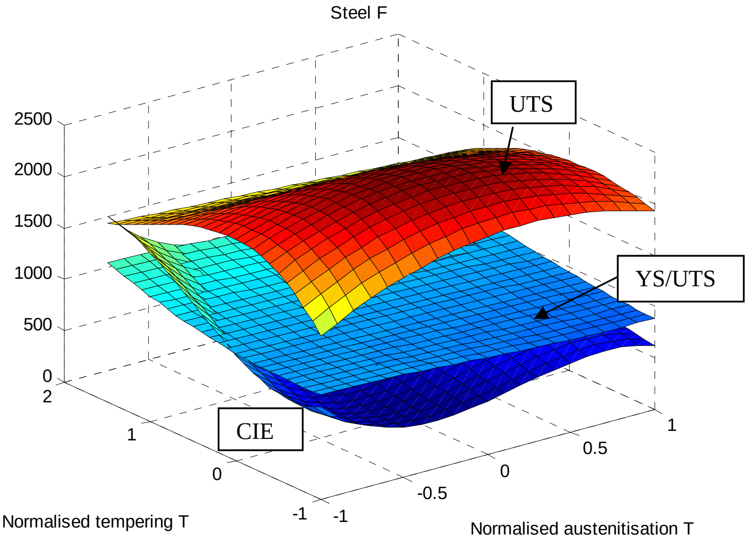

Figure 4.3.4(a): Three-dimensional representation of the optimisation problem for steel F showing the surface of the ultimate tensile strength at room temperature (upper surface), the Charpy impact energy at –40ºC (lower surface) and the objective function of the YS/UTS ratio in the middle.

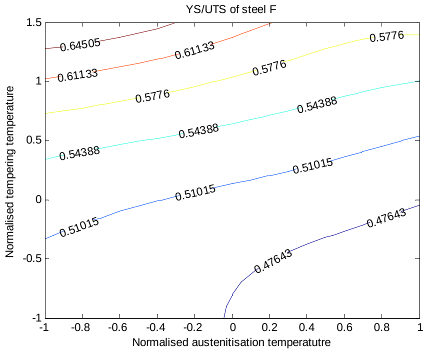

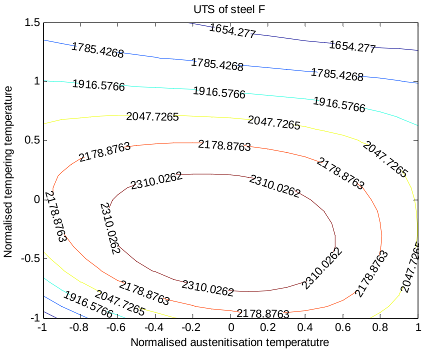

Figure 4.3.4(b): Iso-lines of the objective function YS/UTS of steel F

Figure 4.3.4(c): Iso-lines of the ultimate tensile strength of steel F

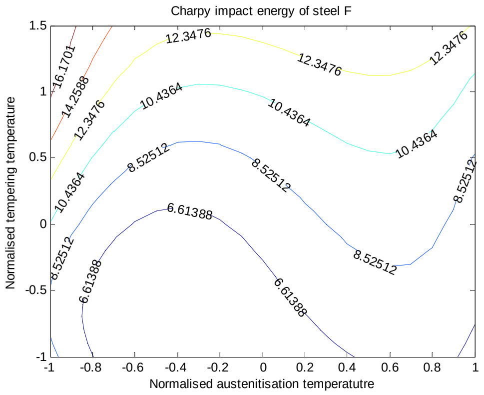

Figure 4.3.4(d): Iso-lines of the Charpy impact energy of the sub-sized specimens of steel F measured at -40°C

Figure 4.3.4(b) shows that the lower YS/UTS ratio for steel F is achieved with low normalised tempering temperatures between –1 and 0, or actually lower than 163°C. This limit is lower than the 200°C found in the case of steel E. Steels E and F have the same Carbon content of 0.39%C but have two different martensite start temperatures, which are 196°C and 255°C respectively. This difference is due to the differences in their Manganese and Chromium contents. The morphology of the martensite in these two steels is compared in section 4.4.3 through thin foil transmission electron microscopy. The tensile strength of steel F is very high compared to steel E and is also high compared to the limit specified by ARMSCOR and Mittal Steel. The tensile strength of steel F was found to be higher than 1700 MPa throughout the entire range of austenitisation and tempering temperatures used here, as shown in Figure 4.3.4(c). Steel F also has tensile elongations larger than 11% when tempered at 200°C. This steel also has the highest hardness in the as-quenched condition and also after tempering below 200°C. The Vickers hardnesses are above 720 VHN or 640 BHN. Finally it also has a higher YS/UTS ratio than steel E. More details on the comparison between these two armour steels will be given in section 4.4 after the ballistic testing and in Section (4.5) after transmission electron microscopy and atomic force microscopy.

4.3.4.3. Mechanical properties of steel G

Steel G has a lower Manganese and Chromium contents than both steels E and F. The martensite start temperature of steel G was measured as 271°C. The volume fraction of retained austenite in this steel was lower than the detection limit of the X-ray diffraction technique used in this study. The optimisation problem for steel G follows the same scheme than for steels E and F. The objective function YS/UTS ratio is derived from the results of the tensile tests at room temperature and is presented in Table (4.3.20). The similar regression analysis produced the fitting parameters in Tables A2.2(a) and A2.2(b) in Appendix 2 after which the mathematical expression of the objective function may be found.

Table (4.3.20): The yield strength to ultimate tensile strength ratio of steel G

		YS/UTS ratio as function of the austenitisation temperature			
Tempering temperature	**Normalised tempering temperature**	**800°C**	**850°C**	**900°C**	**950°C**
25°C	-1	0.66	0.61	0.49	0.46
150°C	-0.09	0.67	0.68	0.51	0.49
200°C	0.27	0.68	0.67	0.53	0.53
250°C	0.64	0.72	0.77	0.57	0.57
300°C	1	0.76	0.71	0.61	0.61
350°C	1.36	0.79	0.74	0.66	0.66
400°C	1.73	0.83	0.76	0.69	0.64

The first constraint on the system is the tensile strength and its variation with the austenitisation and tempering temperatures is presented in Table (4.3.21). The surface fitting parameters are again calculated in two steps. The first analysis produced the parameters for Equation (4.3) and the second produced the parameters for Equation (4.4). These parameters are presented in Tables A2.2(c) and A2.2(d) in Appendix 2. As may be observed, the parameters in Table A2.2(c) are some function of the austenitisation temperature. Hence they are fitted to third degree polynomials to obtain the final parameters A, B, C and D in Table A2.2(d).

Table (4.3.21). Measured tensile strength in MPa for steel G.

		Ultimate tensile strength in MPa as a function of the austenitisation temperature			
Tempering temperature	**Normalised tempering temperature**	**800°C**	**850°C**	**900°C**	**950°C**
25°C	-1	1324	1934	2120	1901
150°C	-0.09	2252	2171	2193	2089
200°C	0.27	2061	2020	1932	1926
250°C	0.63	1872	1790	1833	1750
300°C	1	1643	1631	1753	1565
350°C	1.36	1597	1594	1584	1488
400°C	1.72	1335	1326	1340	1298

The second constraint is defined by the Charpy impact energy at -40°C. The measured impact energy values in Joules, are tabulated as follows:

Table (4.3.22): Charpy impact energy in Joules measured at –40°C on sub-sized specimens of steel G

		Charpy impact energy (in Joules) as a function of the austenitisation temperature			
Tempering temperature	**Normalised tempering temperature**	**800°C**	**850°C**	**900°C**	**950°C**
25°C	-1	9.9	8.9	9.9	9.9
150°C	-0.09	17.7	14.8	16.8	13.8
200°C	0.27	18.7	15.8	16.8	15.3
250°C	0.64	18.7	16.8	17.7	15.8
300°C	1	17.7	16.8	17.7	16.3
350°C	1.36	17.7	17.3	18.2	16.8
400°C	1.73	17.7	16.3	17.7	15.8

From the results in Table (4.3.22), the fitting parameters for the Equations (4.3) and (4.4) are calculated and tabulated in Tables A2.2(e) and A2.2(f) respectively, in Appendix 2. The fitting parameters in Table A2.2(e) are again some function of the austenitisation temperature. The second regression analysis becomes necessary and gives the fitting parameters in Table A2.2(f). The second constraint of the system is written after the parameters in Table A2.2(f) and is mathematically presented in Equation A2.Eq2(c) in Appendix 2.The optimisation problem is then written in the classical form using the objective function to be minimised given by Equation A2.Eq2(a) and the two inequality constraints given by the Equations A2.Eq2(b) and A2.Eq2(c) in Appendix 2, as described in Equation (4.9). The three-dimensional representation of the system is shown in Figure 4.3.5(a). The same scaling factors applied in the two previous cases are also applied here for the same reasons. The corresponding two-dimensional representations in the (T_{an}, T_{tn}) planes are shown in Figures 4.3.5(b) through to 4.3.5(d).

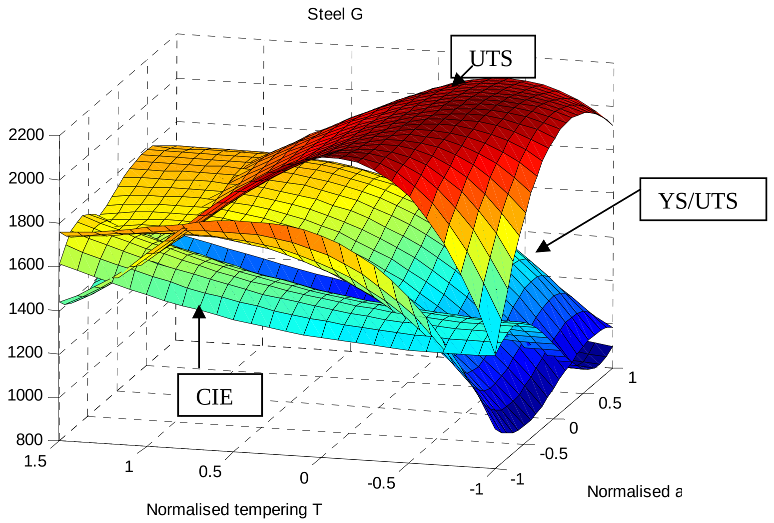

Figure 4.3.5(a): Three-dimensional representation of the objective function and the constraints in the case of steel G.

Deleted:

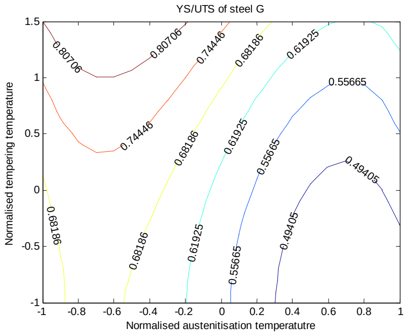

Figure 4.3.5(b): The yield strength to ultimate tensile strength ratio of the Steel G
temperature

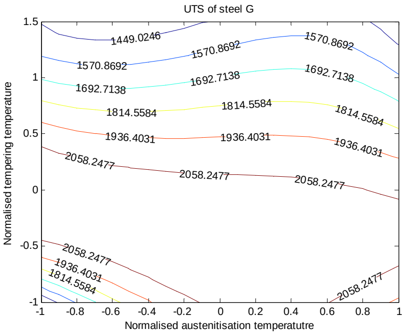

Figure 4.3.5(c): Iso-lines of the ultimate tensile strength in MPa of steel G measured at room

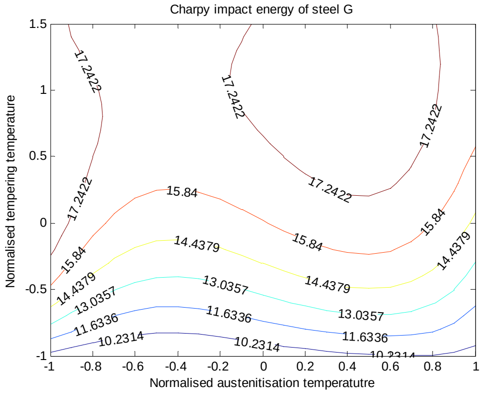

Figure 4.3.5(d): Iso-lines of the Charpy impact energy of the sub-sized specimens of steel G measured at -40°C

Some similarity of steel G to steel F may be noticed. The YS/UTS ratios are higher than in the case of steel E. The tensile strength is also higher than the specified 1700 MPa throughout the entire range of the austenitisation and tempering temperatures. The Charpy impact energy at –40°C is also higher than the specified 13 Joules throughout the entire range of the heat treatment parameters. Some resemblances are then expected between the microstructures of steel G and steel F that differ from steel E. Their martensite start temperatures are both above 250°C and no retained austenite was detected by X-ray diffraction. The ultimate tensile strength of steel G is slightly lower than for steel F but remains higher than 1700 MPa when the normalised tempering temperature does not exceed the normalised value of 1 or actually 300°C.

4.3.4.4. Mechanical properties of steel H

Steel H has the same Carbon content than steel G but has a lower martensite start temperature of 210°C, which is below 250°C. X-ray diffraction detected 4% volume fraction of retained austenite in the quenched specimens. The YS/UTS ratio of this steel as a function of the austenitisation and tempering temperatures is given in Table 4.3.23. The regression analysis allowed the determination of the fitting parameters presented in Tables A2.3(a) and A2.3(b) in Appendix 2.

Table (4.3.23): The yield strength to ultimate tensile strength ratio of steel H

		YS/UTS ratio of steel H as a function of the austenitisation temperature			
Tempering temperature	**Normalised tempering temperature**	**800°C**	**850°C**	**900°C**	**950°C**
25°C	-1	0.46	0.44	0.44	0.43
150°C	-0.09	0.47	0.46	0.46	0.44
200°C	0.27	0.50	0.47	0.47	0.45
250°C	0.64	0.55	0.53	0.49	0.46
300°C	1	0.59	0.57	0.53	0.49
350°C	1.36	0.57	0.61	0.55	0.51
400°C	1.73	0.66	0.61	0.57	0.53

The function describing the variation of the YS/UTS ratio is noted as Equation A2.Eq3(a) in the same appendix. The constraint equation on the ultimate tensile strength is derived from the experimental measurements in Table (4.3.24) from which the fitting surface is determined. The surface fitting parameters are given Tables A2.3(c) and A2.3(d).

Table (4.3.24): The ultimate tensile strength in MPa of steel H.

		The ultimate tensile strength (in MPa) of steel H as function of the austenitisation temperature			
Tempering temperature	**Normalised tempering temperature**	**800°C**	**850°C**	**900°C**	**950°C**
25°C	-1	1415	1543	1118	822
150°C	-0.09	1905	1806	2146	1816
200°C	0.27	2020	1942	2146	1862
250°C	0.64	1902	1909	1955	1830
300°C	1	1929	1724	1894	1770
350°C	1.36	1713	1704	1698	1566
400°C	1.73	1603	1615	1678	1521

The mathematical expression of the tensile strength in MPa is written using the parameters in Table A2.3(d) and has the form given in Equation A2.Eq3(b) in Appendix 2. The second constraint is defined by the Charpy impact energy measured at -40°C and is derived from the experimental results reported in Table (4.3.25).

The surface fitting parameters obtained by regression analysis are contained in Tables A2.3(e) and A2.3(f) (Appendix 2). The equation for the Charpy impact energy surface is written in terms of the normalised temperature as Equation A2.Eq3(c). The second constraint equation is written in terms of the normalised temperatures using the parameters determined in Table A2.3(f) (Appendix 2) and is noted as Equation A2.Eq3(c).

Table (4.3.25): The Charpy impact energy in Joules of the sub-sized specimens of steel H measured at -40°C

		Charpy impact energy (in Joules) of steel H as function of the austenitisation temperature			
Tempering temperature	**Normalised tempering temperature**	**800°C**	**850°C**	**900°C**	**950°C**
25°C	-1	7.5	8	6	6.5
150°C	-0.09	19	14.5	18	12
200°C	0.27	19	15	17	14
250°C	0.64	19	13.5	17	14
300°C	1	15	10	12	11
350°C	1.36	13	8	8	8
400°C	1.73	10	7.5	8	7

The optimisation problem for the properties of steel H is stated in the classical form described in Equation (4.9) using the objective function of Equation A2.Eq3(a) and the constraint functions of Equations A2.Eq3(b) and A2.Eq3(c). The three-dimensional representation of the system is shown in Figure 4.3.6(a).

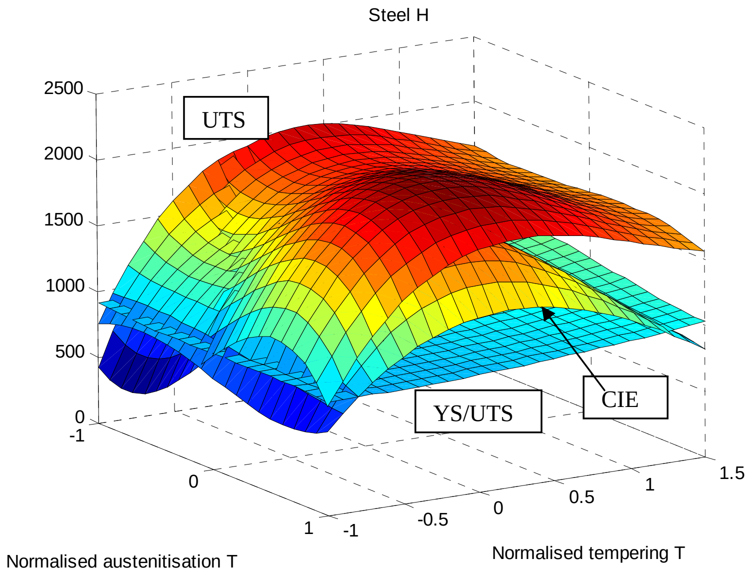

Figure 4.3.6(a): Three-dimensional representation of the optimisation problem for steel H showing the ultimate tensile strength surface(upper surface), the Charpy impact energy surface in the middle and the YS/UTS ratio in the bottom (bottom surface).

The same scaling factors than in the previous figures have been applied here. The corresponding iso-lines in the planes (T_{an}, T_{tn}) are shown in Figures 4.3.6(b) through to 4.3.6(d).

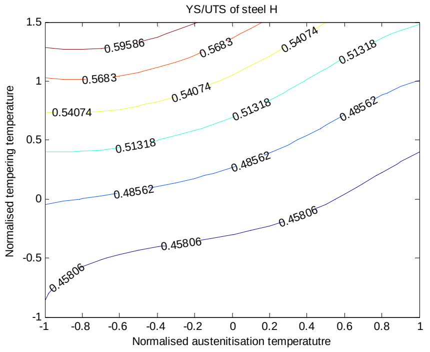

Figure 4.3.6(b): Iso-lines of the YS/UTS ratio in the plane (T_{an}, T_{tn})

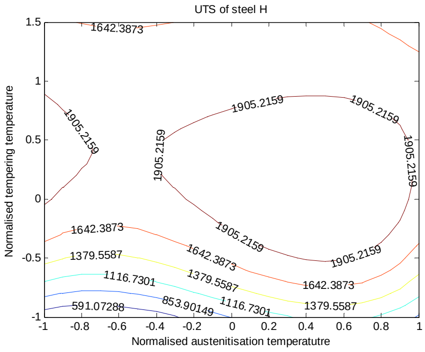

Figure 4.3.6(c): Iso-lines of the ultimate tensile strength (in MPa) of steel H in the plane (T_{an}, T_{tn})

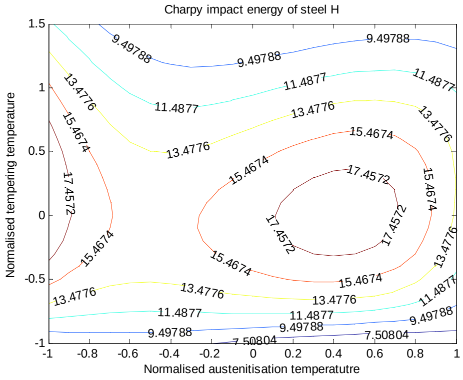

Figure 4.3.6(d): Iso-lines of the Charpy impact energy (in Joules) at –40°C of steel H

Steel H has intermediate values of the YS/UTS ratio, lying between steel E on one side and steels F and G on the other side. Like steel E it presents a brittle behaviour in the untempered condition, where it is difficult to measure the ultimate tensile strength. The tensile strength of this steel has also intermediate values between the two groups of steels previously identified. It remains close and above the specified 1700 MPa after tempering at 350°C for the entire range of the austenitisation temperature. The Vickers hardness of steel H also remains above 550 VHN after tempering at 300°C for one hour. The resistance to tempering of this steel is due to its high Silicon content. It is well known that Silicon delays the transformation of the transition ε - carbide to cementite during tempering.

4.3.4.5. Mechanical properties of steel I

The martensite start temperature of steel I measured by dilatometry was found to be 309°C, which is higher than the martensite temperatures of the other four steels. The volume fraction of retained austenite in the quenched condition was lower than the detection limit of the X-ray diffraction technique used for the analysis. The results of the measurement of the YS/UTS ratio of this steel are shown in Table (4.3.26). It may be observed that steel I presents the highest values of the YS/UTS ratio of all of the five steels considered up to here.

The YS/UTS ratio of steel I in the quenched condition is in the same range than that of steels E and H after low-temperature tempering. The relatively high values of this ratio for steel I may be caused by auto-tempering during the quenching of this steel, in view of its relatively high M_s temperature.

Table (4.3.26): The YS/UTS ratio of steel I

		YS/UTS ratio as a function of the austenitisation temperature			
Tempering temperature	**Normalised tempering temperature**	**800°C**	**850°C**	**900°C**	**950°C**
25°C	-1	0.66	0.62	0.6	0.62
150°C	-0.09	0.70	0.71	0.61	0.61
200°C	0.27	0.74	0.74	0.63	0.63
250°C	0.64	0.78	0.74	0.63	0.62
300°C	1	0.80	0.78	0.64	0.64
350°C	1.36	0.83	0.77	0.66	0.64
400°C	1.73	0.83	0.81	0.71	0.66

The objective function describing the YS/UTS ratio is written in terms of the normalised temperature using the fitting parameters in Table A2.4(b) in Appendix 2 and is noted as Equation A2.Eq4(a). The constraints on the system are derived from the results of the tensile tests and the Charpy impact tests. Table (4.3.27) contains the results of the ultimate tensile strength measurements. The fitting parameters for the ultimate tensile strength surface of this steel are presented in Tables A2.4(c) and A2.4(d) of Appendix 2.

Table (4.3.27): The ultimate tensile strength (in MPa) of steel I

		Ultimate tensile strength (in MPa) as a function of the austenitisation temperature			
Tempering temperature	**Normalised tempering temperature**	**800°C**	**850°C**	**900°C**	**950°C**
25°C	-1	2100	1954	1948	1543
150°C	-0.09	2040	1920	1900	1755
200°C	0.27	1842	1751	1763	1649
250°C	0.64	1714	1675	1623	1588
300°C	1	1515	1446	1485	1452
350°C	1.36	1447	1453	1434	1327
400°C	1.73	1312	1261	1284	1187

The mathematical equation describing the tensile strength of steel I is then derived from the parameters in Table A2.4(d) (Appendix 2) and noted as Equation A2.Eq4(b). The second constraint is derived from the measured vales of the Charpy impact energy at -40°C using the experimental values in Table 4.3.28.

Table (4.3.28): Charpy impact energy of the sub-sized specimens of steel I at -40°C

		Charpy impact energy as a function of the austenitisation temperature			
Tempering temperature	**Normalised tempering temperature**	**800°C**	**850°C**	**900°C**	**950°C**
Ally 25°C	-1	16	17	17	17
150°C	-0.09	18	19	19	19
200°C	0.27	19	19	20	20
250°C	0.64	18	19	20	19
300°C	1	18	19	19	20
350°C	1.36	19	19	19	21
400°C	1.73	18	20	20	21

The equation representing the Charpy impact energy of the sub-sized specimens of steel I measured at -40°C, is finally derived from the parameters contained in Table A2.4(f) and noted as Equation A2.Eq4(c). The optimisation problem is stated in classical form by substituting the objective function in Equation A2.Eq4(a) and the constraint functions in Equations A2.Eq4(b) and A2.Eq4(c) in the system defined in Equation (4.9). The three-dimensional representation of this system, using the previous chosen scaling factors, is presented in Figure 4.3.7(a).

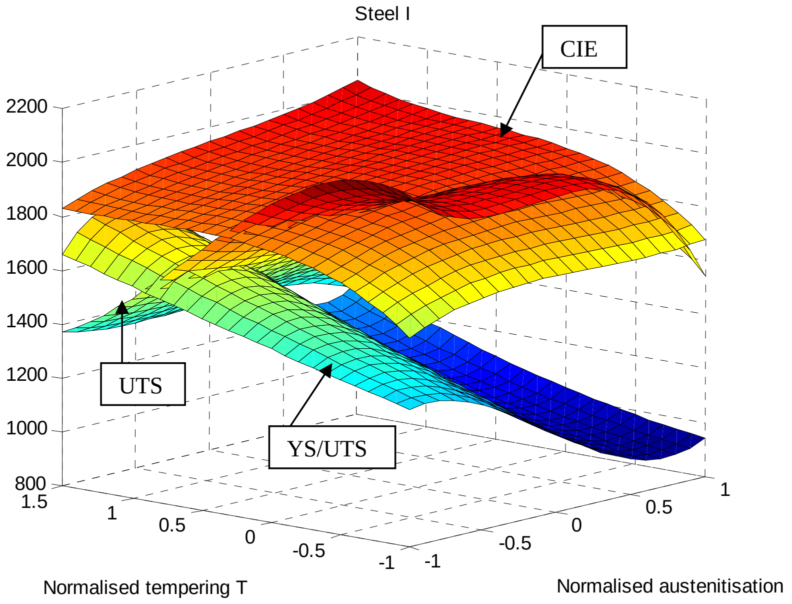

Figure 4.3.7(a): Three-dimensional representation of the optimisation system for steel I.

From Figure 4.3.7(a), it may be observed that the surface representing the Charpy impact energy of steel I is at high levels and it remains high throughout the entire range of heat treatment parameters considered.

However the ultimate tensile strength surface drops to levels lower than 1700 MPa when the tempering temperature is higher than 200°C. The corresponding iso-lines are shown in Figures 4.3.7(b) through to 4.3.7(d).

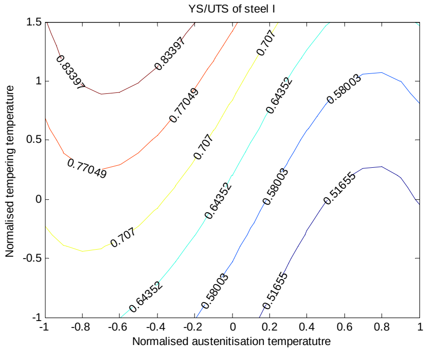

Figure 4.3.7(b): Iso-lines of the yield strength to ultimate tensile strength ratio of steel I

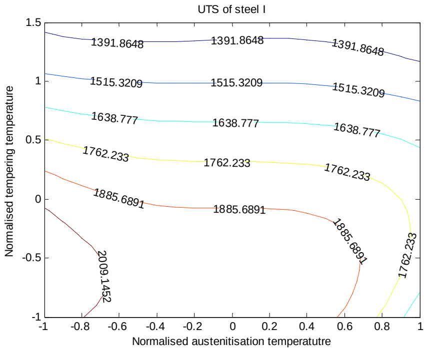

Figure 4.3.7(c): Iso-lines of the tensile strength of steel I.

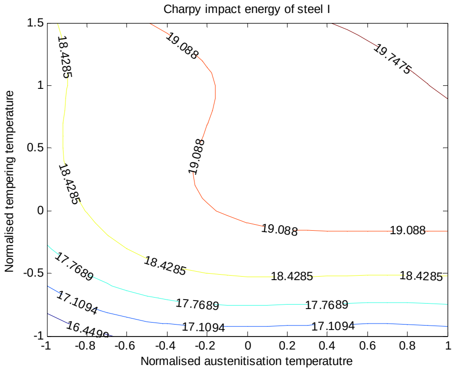

Figure 4.3.7(d): Iso-lines of the Charpy impact energy of steel I measured at -40°C

4.3.5. General observations on the mechanical properties of steels E through to I.

From the results of the measurements presented in Section 4.3.4, it appears that the five armour steels considered may be classified following their martensite start temperatures. Three groups of armour steels may be defined. The first group of armour steels, comprising steel E and steel H, have relatively low martensite start temperatures, lower than 210°C. The second group comprises steels F and G which has martensite start temperatures near to 250°C. The third group comprises steel I which has martensite start temperatures near to 300°C. The YS/UTS ratios of these steels are plotted for graphical comparison in Figure 4.3.8.

Table (4.3.29). Groups of armour steels classified according to the martensite start temperatures for the austenitisation temperatures comprised in the range from 800°C to 950°C.

Group	Armour steel	Martensite start temperature	YS/UTS
1	E	196°C	< 0.6
	H	210°C	
2	F	255°C	0.65 to 0.75
	G	271°C	
3	I	309°C	> 0.70

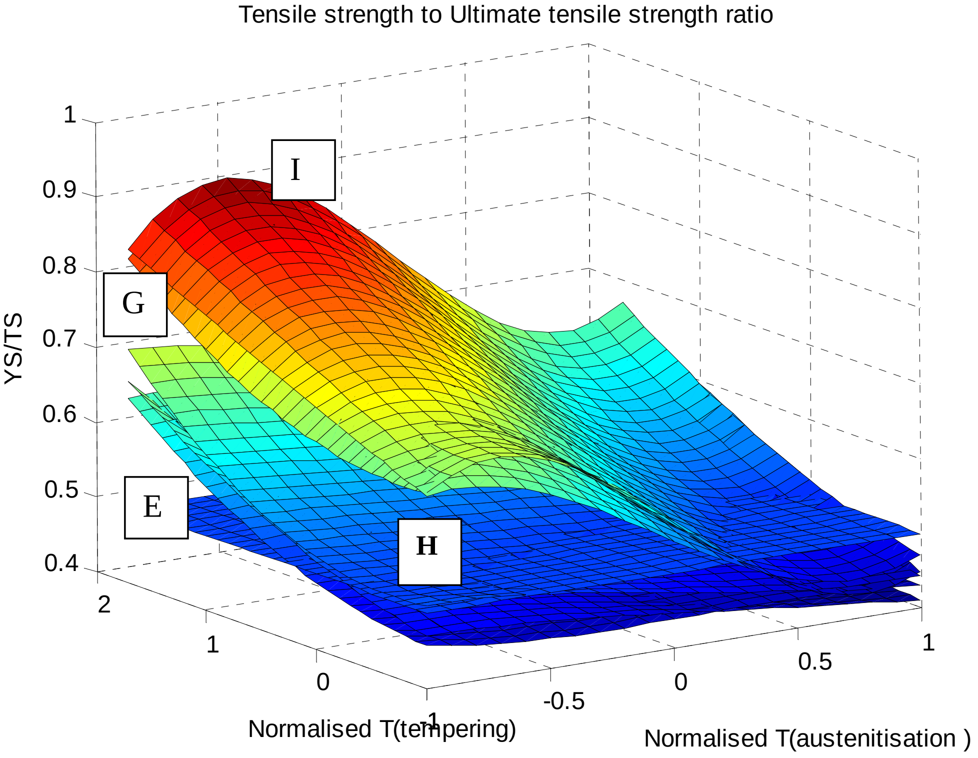

Figure 4.3.8: Showing the comparison of the levels of the yield strength to ultimate tensile strength ratio surfaces of the steels E through to I. Steel I and steel G on top, steel E, steel F and steel H on the bottom. The plane of YS/UTS=0.5 is also shown.

From this figure it may be observed that high martensite start temperatures lead to high values of the YS/UTS ratio in the quenched as well as in the tempered conditions for these five armour steels. The YS/UTS ratio increases with an increase in the tempering temperature. The high values of this ratio in the cases of high martensite temperatures, is probably a consequence of auto-tempering during quenching. However, this ratio decreases with an increase in the austenitisation temperature which leads to grain growth and an increase in the volume fraction of retained austenite because of the lower martensite start temperature. The volume fraction of retained austenite in the armour steels becomes the main factor determining the YS/UTS ratio. This ratio is lower in the conditions corresponding to a higher volume fraction of retained austenite in these armour steels. This is the case for the two armour steels E and H in the first class.

The tensile strength of steel E (group 1) and steel F (group 2) are compared in Figure 4.3.9, where the plane of 1700 MPa is also shown. The gap in the tensile strength between these two groups of armour steels is large. It was noted earlier that the steels A (M_s =285°C), B (M_S = 253°C), C (M_S =241°C) and D (M_S =265°C) are currently in production by Mittal Steel and others and are already utilised in military and security applications. The specifications for these ballistic purposes are stated in terms of the yield strength that should be higher than 1500 MPa and the tensile strength, that should be higher than 1700 MPa. These two strength limits will lead to values of the YS/UTS ratio close to 0.88 and will lead to the occurrence of localised yielding during impact. Experience within the industry has found that steel C has a better ballistic performance than the other three for plate thickness between 8.5 mm up to 30 mm. In the current assessment methodology, steel A, steel B and steel D may, therefore, be classified into the second class, whereas steel C belongs to the transition between the first class and the group 2 of armour steels as previously defined from their martensite start temperatures.

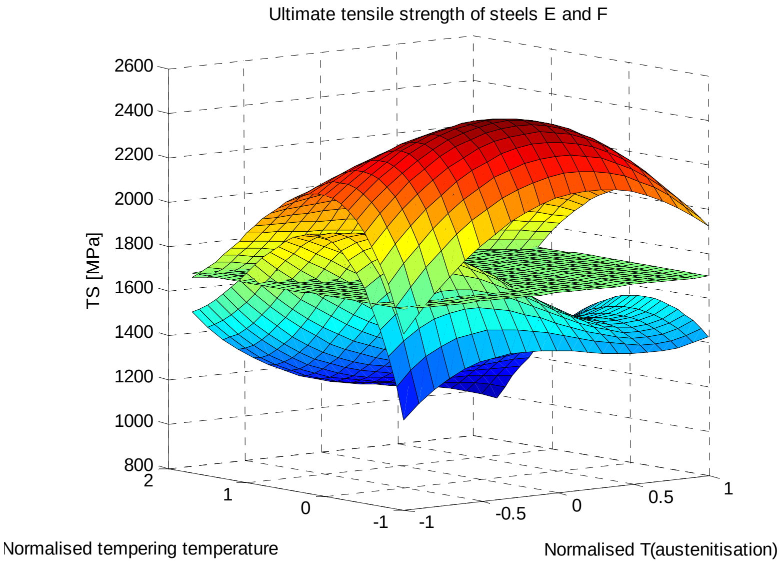

Figure 4.3.9: Comparison of the ultimate tensile strength between steel E (group 1) in the lower surface, steel F (group 2) in the upper surface and the specified plane of 1700 MPa.

The armour steels in group 3 (high martensite start temperatures) have an intermediate tensile strength between those in the first and in the second groups. The same observation is valid for their hardnesses. Hence the second group of armour steels is currently produced for military applications based on the design philosophy that would link the ballistic performance to the hardness and the tensile strength of these steels. Earlier in Chapter 2 mention was made of a new approach in the definition of the Ballistic Performance Index where the hardness of the armour steel is no longer an important determinant. Rather the tensile strength is considered to be important as it compares well to the true fracture strength during high-velocity impact. In the present study the YS/UTS ratio is also considered in predicting the ballistic performance of the armour steels and comparison is made between the three modes of predicting the ballistic performances using (i) the hardness of the plates, (ii) their ballistic performance index BPI, or (iii) their YS/UTS ratio.

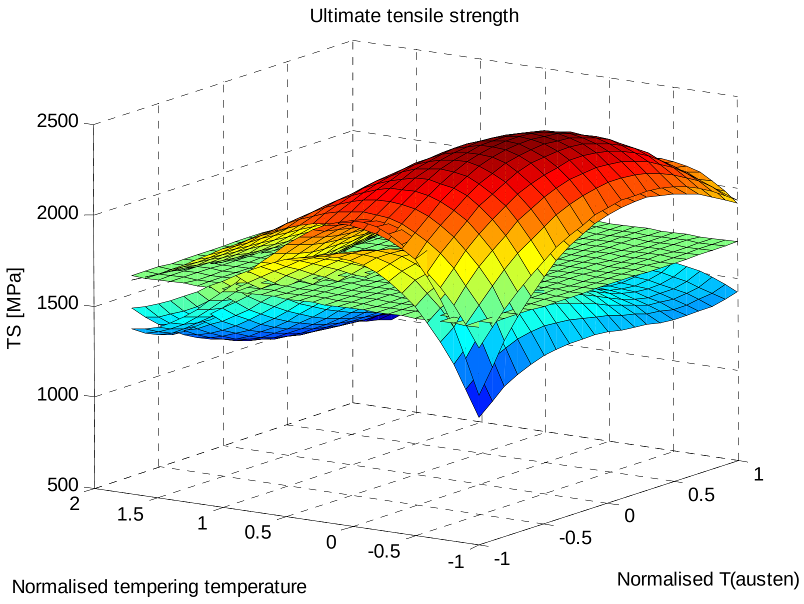

Figure 4.3.20: Comparison between the tensile strength of steels E, F and I showing the intermediate level of the strength of steel I (group 3) between that of steel F (group 2) in the upper surface and steel E (group 1) in the lower surface. The plane of 1700 MPa is also shown.

The Charpy impact energy at -40°C of steels E, F, G and I are compared in Figure 4.3.21, where it may be observed that steel I (group 3) has the highest impact energy (upper surface) throughout the entire range of the austenitisation and tempering temperatures, whereas steel E and steel H (group 1) have the lowest impact energy (lower surfaces) throughout the entire range of the austenitisation and tempering temperatures considered in this study. Steel F (group 2) has a fairly intermediate level of Charpy impact energy. It also appears from Figure 4.21 that the Charpy impact energy of the sub-sized specimens of the armour steels measured at –40°C, increases when the martensite start temperature of the armour steel is higher.

The fracture surfaces after the tensile tests at room temperature and the Charpy impact tests at -40°C of these three classes of armour steels, as classified according to their martensite temperatures, are compared in Section 4.3.6. The effect of Silicon, Chromium and Manganese contents in their resistance to low-temperature tempering, are also analysed. The effect of the shape and the size of the Manganese sulphide particles on the fracture mode of these armour steels is particularly examined.

4.3.6. Fracture analysis after the Charpy impact and the tensile tests.

4.3.6.1. Group 1 armour steels

The fractured surfaces of the Charpy specimens of steels E (0.003%S, 1.22%Mn) and H (0.011%S, 1.15%Mn) whose martensite start temperatures are respectively 196°C and 210°C, were analysed by secondary electron scanning electron microscopy. Two areas were considered in each fractured surface, firstly, where only the shear lips were analysed for the sake of the mechanism by which the fracture was initialised, and secondly, the unstable propagation of the crack that occurred throughout the cross-section of the specimen.

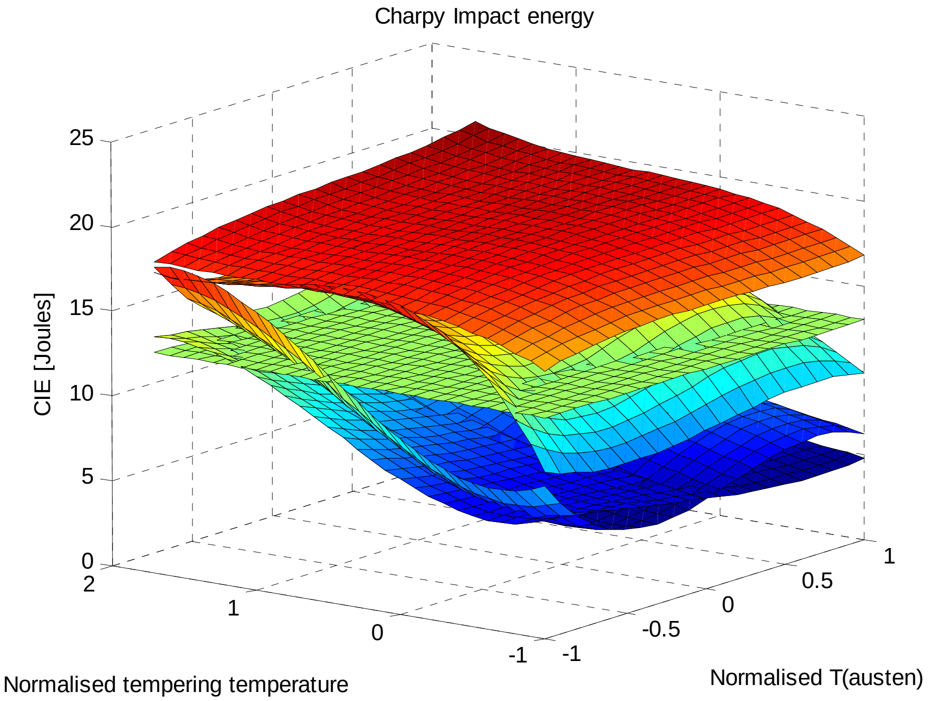

Figure 4.3.21. Comparison between the Charpy impact energy of the sub-sized specimens of steel E (lower surface), steel H (second lower surface), steel G (second upper surface) and steel I (upper surface). The plane of the specified 13 Joules is also shown.

The first area was generally near the standard notch of the Charpy specimen while the second area was situated within the fracture face at a position below the notch and very near to the area of contact with the striking edge of the pendulum. The Charpy impact energy of the sub-sized specimens, measured at -40°C, allowed the selection of the three tempering temperatures for steel H, as shown in Figure 4.3.22. The Charpy impact energy of these two steels remains lower than the specified 13 Joules in the untempered condition and also when tempered at temperatures lower than 200°C. It exceeds 13 Joules, however, when the steels E and H are tempered at temperatures between 200 and 300°C and decreases again when the tempering temperature is higher than 300°C. The untempered Charpy specimens and those tempered at 200°C and at 300°C for 20 minutes and for 60 minutes, were selected for observation in the scanning electron microscope.

From Figure 4.3.22 it appears that the armour plates in the group 1 (low martensite start temperatures) fractured by a brittle inter-granular mechanism in the untempered condition during the test at -40°C. The former austenite grain size is the operating grain size during the fracture. This behaviour is more noticeable in the shear lips formed near to the notch in the specimens (Figure 4.3.22(a-1)) than in the shear lips near the impact point

(Figure 4.3.22(a-2)) where fracture rather occurs by a compound mechanism involving an inter-granular and a trans-granular mechanism. The specimens tempered at 200°C again show a more brittle behaviour near to the notch (Figure 4.3.22(b-1)) than near to the impact point (Figure 4.3.22(b-)2). Tempering at 200°C slightly improved the toughness of these armour steels and increased their Charpy impact energy to 12 Joules. Dimples were formed in areas near the faces close to the impact area away from the notch. At the same time the effect of Manganese sulphide particles becomes observable (craters on the bottom of Figure 4.3.22(b-2)). Tempering at 250°C led to values of the impact energy between 13 Joules and 18 Joules for steels E and H. The fracture of these Charpy specimens became ductile with small dimples formed near the notch (Figure 4.3.22(c-1)) as well as near the impact area away from notch. The size of the plastically deformed regions around the Manganese sulphide particles became larger as may be observed in the Figure 4.3.22(c-2). The decrease in the Charpy impact energy of the specimens upon tempering above 300°C is partially attributed to the detrimental effect of the Manganese sulphide particles in a relatively soft martensite when the tempering temperature exceeds 200°C.

The brittle inter-granular fracture near the notch of the Charpy specimens may be explained by the stress concentration effect of the notch that introduces local stresses higher than the nominal stress far from the notch during the impact test.

Tempering produces carbides and removes the Carbon from solid solution in the martensite and it is this that lowers the hardness and increases the toughness. However the detrimental effect of the Manganese sulphide particles plays a role in the fracture mechanism of these steels and imposes a limit to their increase in toughness with fracture cavities of up to 7 μm that were formed. The shape of the Manganese sulphide particles has a strong effect on the stress concentration effect during impact and tensile loading as will be shown later in this paragraph. The shape is important but of equal importance here is the very low adhesion between the ferrite matrix and MnS particles. Specifically, upon tempering above 250°C the softening of the martensite promotes the decohesion around the elongated Manganese sulphide particles. Cavities of diameters larger than 16 μm were formed upon unstable shearing of the areas around the Manganese sulphide particles as illustrated in Figure 4.3.22(c-2). The Charpy impact energy of these armour steels becomes once again lower upon tempering at 400°C.

Backscattered scanning electron microscopy of the untempered and the specimen tempered at 400°C for 60 minutes, show the advanced decomposition of the martensite into ferrite and cementite in between the plates previously formed upon quenching. A high magnification is necessary to observe this advanced decomposition of the martensite as shown in Figures 4.3.23(a-1) to 4.3.23(b-2). At a low magnification of about 1700X the shape of the martensite plates seems unaltered upon tempering at 400°C (Figure 4.3.23(b-1)) compared to the untempered condition (Figure 4.3.23(a-1)). But a higher magnification of about 20000X reveals the decomposition of the martensite whereas in the untempered condition backscattered electron microscopy does not reveal the presence of any cementite (Figure4.3.23(a-2)).

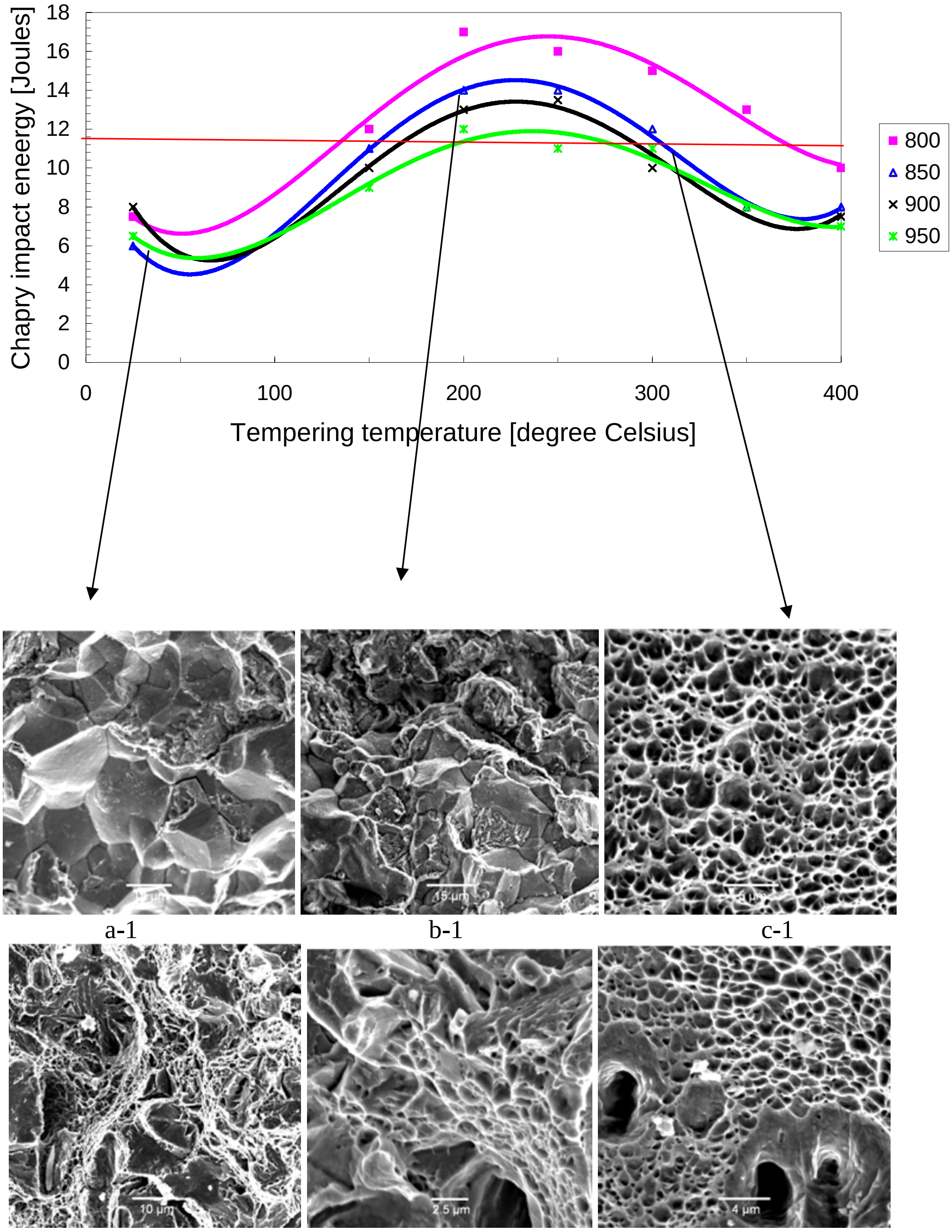

a-1 b-1 c-1

a-2 b-2 c-2

Figure 4.3.22. Secondary electron scanning electron micrographs of the fractured Charpy specimens of steel H after testing at -40°C, showing the evolution of the operating mode during the fracture as a function of the tempering temperature and the effect of the notch.

Fig. 4.3.22(a-1) and (a-2): SEM fractograph of steel H austenitised at $850\,^{0}C$, quenched in water showing a brittle inter-granular fracture near the notch (Figure a-1), and a quasi cleavage fracture near the incidence site of the specimen in direct contact with the striking edge of the pendulum.

Fig. 4.3.22(b-1) and (b-2): SEM fractograph of steel H austenitised at $850\,^{0}C$, quenched in water and tempered at $200\,^{0}C$, showing brittle fracture near to the notch and a more ductile fracture near the impact area away from the notch. Cavities were formed around the MnS particles.

Fig. 4.3.22(c-1) and (c-2): SEM fractograph of steel H austenitised at $850\,^{0}C$, quenched in water and tempered at $300\,^{0}C$, showing ductile fracture near the notch as well as near the impact area away from the notch. Small equi-axed dimples and large cavities had formed around the MnS particles.

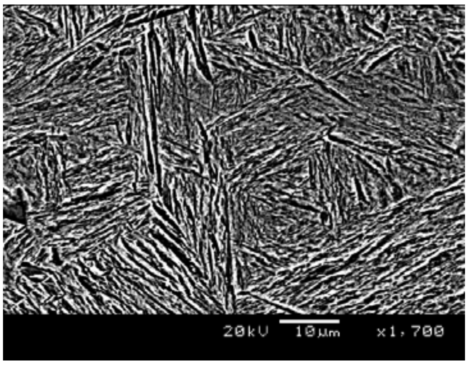

Figure 4.3.23(a-1): SEM of untempered and polished sample of the steel H at 1700 magnification

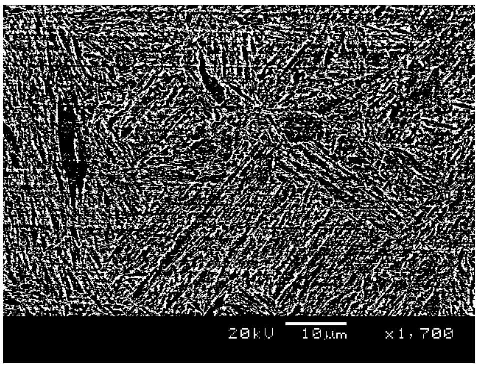

Figure 4.3.23(b-1): SEM of polished sample of steel H tempered at 400°C (× 1700 magnification)

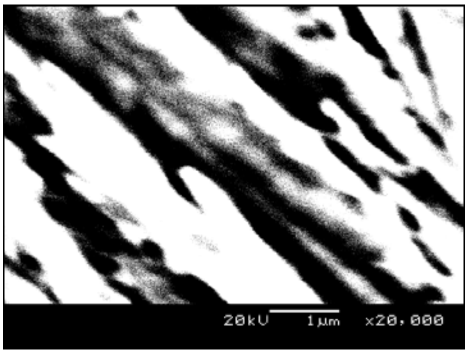

Figure 4.3.23(a-2): SEM of untempered and polished sample of steel H at 20000 magnification

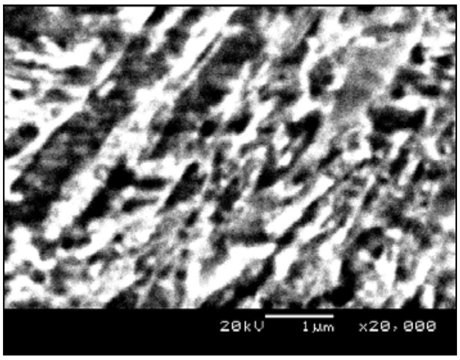

Figure 4.3.23(b-2): SEM of polished sample of steel H tempered at 400°C (× 20000 magnification)

The presence of the cementite and the Manganese sulphide is, therefore, prejudicial to the resistance against impact loading despite the presence of the soft ferrite. The shear lips of the tensile specimens have also been examined in secondary electron scanning electron microscopy. The brittle behaviour of the armour steels in the untempered condition makes it very difficult for the determination of the tensile properties. Figure 4.3.24 shows the fracture surface under tensile stress of steel H in the quenched and untempered condition. It confirms that the brittle behaviour in the case of a low strain rate axial loading is less severe than one under impact loading as was illustrated in the Figures 4.3.22(a-1) and

4.3.22(a-2). The fracture surface of the untempered tensile specimens presents features of brittle fracture by decohesion of the grains as can be seen in Figure 4.3.24. Cavities of 2.5 μm are formed around the spherical inclusions of Manganese sulphide. The elongated plate-like inclusions of Manganese sulphide increases the size of the cavities to more than 12 μm that are formed during the tensile test and are shown in Figure 4.3.25 . This phenomenon may by explained by the occurrence of localised high stresses around the inclusions of the Manganese sulphide plates and consequently it leads to a decrease of the nominal ultimate tensile strength of the armour steel upon tempering. The other reason for this decrease of the ultimate strength is the decomposition of the martensite itself and the formation of coarse cementite.

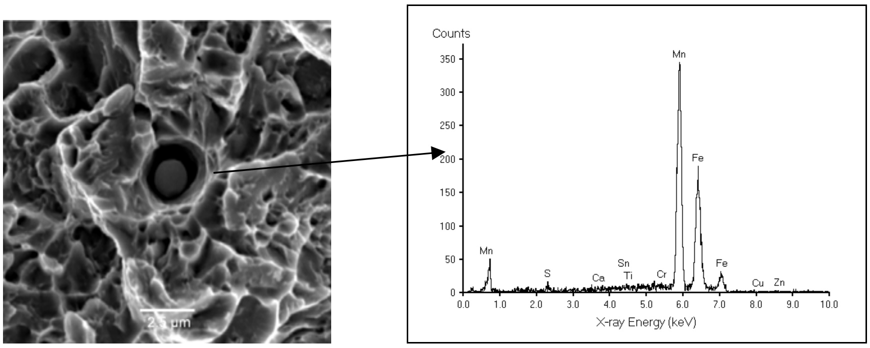

Figure 4.3.24: Secondary electron scanning microscopy of the shear lips of steel H in the quenched and untempered condition, showing spherical inclusions of MnS after tensile test.

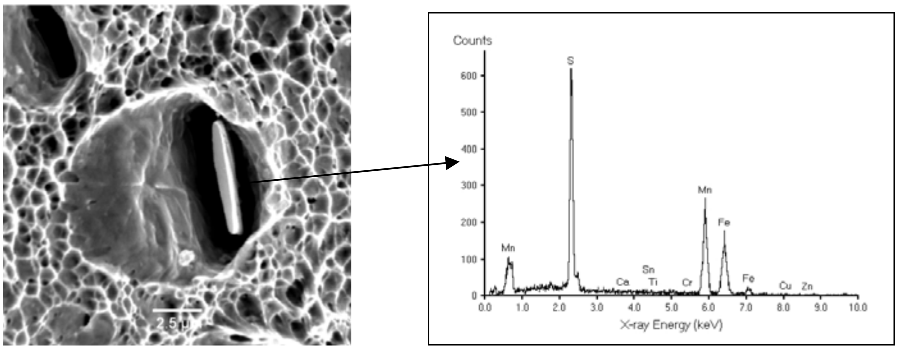

Figure 4.3.25: An elongated plate-like inclusion of Manganese sulphide, observed after the tensile test of steel H tempered at 150 ^{0}C, showing large cavities around the inclusions of the MnS.

4.3.6.2 Group 2 armour steels

The sub-sized Charpy specimens of steel F (0.009%S, 0.65%Mn) whose martensite start temperature is 255°C, have shown the same brittle behaviour in the untempered condition as was the case with the steels E and H but with a slightly higher impact energy. Besides the mentioned reasons of the brittle behaviour in the untempered condition, other inclusions such as the Calcium-Aluminium compounds inherited from the casting process also act as stress raisers and, therefore, act as crack initiators in the hard untempered martensite during the tensile test. The initiation of such cracks is illustrated in Figure 4.3.26. For steel F also the effect of the Manganese sulphide inclusions becomes observable and large cavities were formed around this type of inclusion that weakens the armour steel when the tensile or the Charpy specimens are tempered at temperatures above 200°C, as illustrated in Figure 4.3.27.

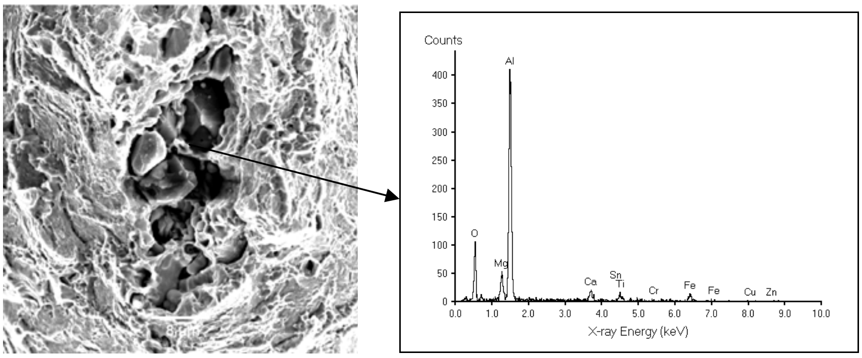

Figure 4.3.26: Crack initiation near an inclusion of a Calcium-Aluminium-Oxygen compound in the tensile specimen of steel F.

The comparison between the fracture appearances of the shear lips in the untempered and the tempered conditions in steel F also showed a transition from brittle to ductile fracture when the specimens were tempered at 200°C.

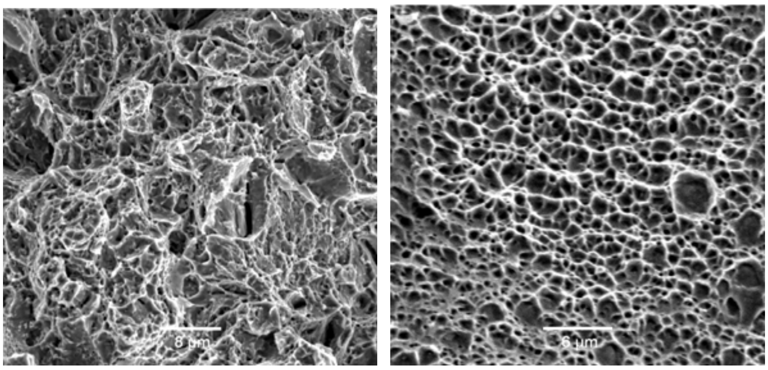

Fig. 27(a) Fig. 27(b)

Fig 4.3.27. Secondary electron scanning microscopy of Steel F after tensile testing at room temperature (a) austenitised at 900 ^{0}C and water quenched, (b) austenitised at 900 ^{0}C, water quenched and tempered at 200 ^{0}C, showing dimples that indicate ductile fracture during the tensile test.

The mechanical properties of steel F in the above mentioned conditions are shown in Table (4.3.30).

Table (4.3.30): Mechanical properties of the steel F austenitised at 900°C for 1 hr, in the quenched condition and after tempering at 200°C.

	UTS [MPa]	**Elongation A_f %**	**Impact energy at $-40\,^0C$ [J]**
Austenitised and quenched	2246	4	7
Austenitised, quenched and tempered at 200°C	2280	9	12

The ultimate tensile strength and the elongation of steel F (M_S = 255°C), containing 0.6% volume fraction of retained austenite is very high compared to that of steels E (M_S = 196°C, 5% retained austenite) and H (M_S = 210°C, 4% retained austenite) in the same conditions. The impact energy of steels F and H are comparable. It has been mentioned previously that the tensile properties were very difficult to determine in the untempered condition in the case of steels E and H because of their brittle behaviour. The intermediate martensite start temperature of the Group 2 armour steels led to the highest ultimate tensile strength and hardness but it did not improve the impact energy compared to the armour steels of Group 1.

4.3.6.3. Group 3 armour steels

The fracture of steel I (0.012%S, 0.39%Mn) whose martensite start temperature was 309°C, was ductile with formation of dimples within the grains under tensile stress, as shown in Figure 4.3.28. The auto-tempering of the martensite laths increases the elongation to fracture to 11% of this armour steel. The same goes for the impact energy that supersedes 16 Joules in all the conditions. On the other hand, the ultimate tensile strength decreases from 2000 MPa to values below 1300 MPa due to the auto-tempering and the tempering effects.

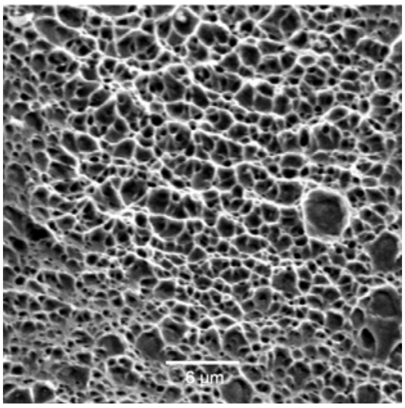

Figure 4.3.28: Typical surface fracture appearance of steel I under tensile stress austenitised 30 min at 850°C and tempered at 150°C for 1 hr

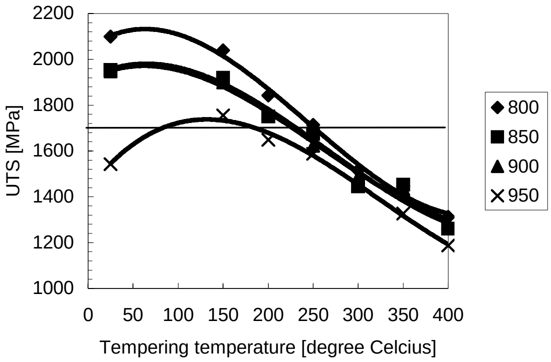

Figure 4.3.29: Ultimate tensile strength of steel F. austenitised for 30 min at the given temperatures and tempered for 1 hr.

4.3.6.4 General observations

The surface appearance of the fractured faces after the tensile and impact testing showed significant differences between the specimens that produced higher and those that produced lower mechanical properties, as observed in secondary electron scanning electron microscopy. The surface appearances were analysed on the shear lips where the fracture initiated before the unstable propagation of the cracks through the cross section.

The brittle fracture of steels E and H indicates that they cannot be used in the untempered condition because of the risk of spallation if impacted by high velocity projectiles. The tempering treatment at temperatures ranging between 150°C and 250°C has increased the ability of the armour steels of Group 1 and 2 to undergo ductile plastic deformation at room temperature and at sub-zero temperatures. The secondary electron scanning electron microscopy also showed that the tempering treatment enhanced the negative effect of the Manganese sulphide particles. Inclusions of Manganese sulphide were not observed in steel E that contains only 0.003% Sulphur. The notch in Charpy testing enhanced the brittle behaviour and inter-granular fracture of the untempered armour steels in Group 1. All potential stress raisers should therefore be avoided in the manufacturing of armour plates.

Any inclusions have negative effects on both the strength and the resistance to impact loading. Other workers [71] have observed the influence of the shape, the distribution and the size of the Manganese sulphide particles on the strength of steels. In this study two types of inclusions, namely Manganese sulphide and the Calcium-Aluminium-Oxygen compounds have been identified in the fractured surfaces.

The tensile strength, the elongation and the resistance to impact loading may then be improved by developing cleaner steels without Sulphur and inclusions or by lowering the volume fraction of the Manganese sulphide. For improving the toughness of these steels, it is then suggested that the control of Manganese sulphide shape and size in the as-cast condition be introduced with the goal of equi-axed sulphide particles of the largest possible size to increase their interspacing throughout the matrix. A small interspacing between the Manganese sulphide inclusions will be negative as illustrated in Figure 4.3.30.
The most useful compositions should be those, which promote equi-axed sulphide particles (Type III). Type III sulphides are faceted equi-axed particles and are favoured by low oxygen levels in combination with high Carbon levels, and are promoted by Silicon and Aluminium additions. There is also an effect of Sulphur content on sulphide type, with type III sulphides favoured as the sulphur content is reduced.

The cooling rate upon solidification can also influence the sulphide type. Type II sulphides (rosette-like or fan-like) are favoured over both Type I (spherical) and type III sulphides as the cooling rate is increased.

The second type of inclusions seen in these fractured surfaces, are the coarse particles of a Calcium-Aluminium-Oxygen compound inherited from the steel-making process. Secondary electron scanning electron microscopy has shown that micro-cracks within the hard martensitic armour steel, are initiated near and around these type of inclusions before they propagate toward the surface of the tensile specimen. Therefore, they act as stress raisers and participate in the reduction of the nominal tensile strength of the armour steels.

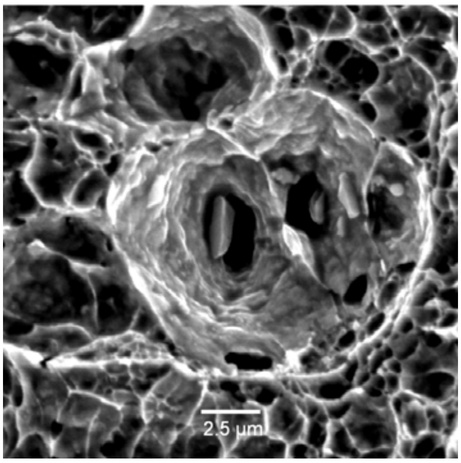

Figure 4.3.30: Effect of the small interspacing between inclusions of MnS in steel F

4.3.7. Martensite start temperatures of the armour steels.

Measurements of the martensite start temperatures of steels E through to W whose chemical compositions are given in Tables 4.3.31 and 4.3.32, were done using dilatometry. The measured values have been compared to values calculated using two different formulas published in the literature. The scatter between the measured and the calculated values using these two formulas have suggested the determination of another multi-linear approximation for the prediction of the martensite start temperatures for these armour steels.

The main hypothesis made for this estimate is the dependence of the M_S temperature on the chemical composition. The predicted values of the martensite start temperature were calculated from the following formulas:

- After Stevens and Haynes [73] based on 59 steels without considering any interaction parameters between alloying elements themselves:

$$M_s\left({}^0C\right) = 539 - 423C - 30.4Mn - 17.7Ni - 12.1Cr - 7.5Mo - 7.5Si + 10Co \quad (4.12)$$

- After Wang et al [73] based on 157 steels and considering interaction parameters between alloying elements using an Artificial Neural Network analysis (ANN):

$$\begin{aligned} M_s\left({}^0C\right) = {} & 540 - 584W_C - 23.1W_{Si} - 117.7W_{Mn} - 42.5W_{Cr} - 49W_{Mo} - 62.5W_{C-Si} + \\ & 178.3W_{C-Mn} - 10.0_{C-Cr} + 52.5W_{C-Mo} + 117.2W_{Si-Mn} + 50.9W_{Si-Cr} - 142.2W_{Si-Mo} - \\ & 129.2W_{Mn-Cr} - 9.7W_{Mn-Mo} + 69.9W_{Cr-Mo} \end{aligned} \quad (4.13)$$

Table (4.3.31): Chemical composition (wt%) of the steels tested for the development of advanced performance steel armour plates

	C	**Mn**	**P**	**S**	**Si**	**Cu**	**Ni**	**Cr**	**Mo**	**V**	**Nb**	**Ti**	**N**
Steel E	0.39	1.22	0.008	0.003	0.21	0.102	2.99	1.49	0.5	0.006	0.002	0.003	0.0049
Steel F	0.39	0.65	0.017	0.009	0.8	0.23	2.8	0.22	0.24	0.003	0.006	0.01	0.0051
Steel G	0.37	0.40	0.016	0.011	0.43	0.33	2.3	0.24	0.3	0.006	0.006	0.009	
Steel H	0.37	1.15	0.015	0.011	1.06	0.14	3.8	0.52	0.43	0.008	0.008	0.007	0.0036
Steel I	0.34	0.39	0.019	0.012	0.40	0.32	2.43	0.27	0.37	0.009	0.009	0.008	
Steel J	0.30	0.48	0.018	0.012	0.35	0.12	1.4	0.48	0.19	0.01	0.01	0.015	0.0059
Steel K	0.3	0.65	0.016	0.017	0.75	0.11	2.83	0.84	0.45	0.01	0.01	0.01	
Steel L	0.30	0.97	0.018	0.013	0.93	0.12	4.1	0.83	0.69	0.005	0.008	0.012	
Steel M	0.43	1.21	0.018	0.012	0.76	0.13	4.34	1.52	0.44	0.005	0.01	0.01	0.0049
Steel N	0.42	0.63	0.016	0.014	0.5	0.11	2.8	0.52	0.28	0.005	0.007	0.012	
Steel O	0.42	0.44	0.018	0.013	0.49	0.12	2.53	0.51	0.28	0.005	0.007	0.012	
Steel P	0.43	1.87	0.019	0.011	1.37	0.18	4.20	1.64	0.61	<0.005	<0.005	<0.005	
Steel Q	0.40	1.81	0.012	0.005	1.43	0.15	3.55	1.63	0.57	<0.005	<0.005	<0.005	
Steel R	0.39	1.56	0.011	0.005	1.03	0.16	3.83	0.94	0.6	<0.005	<0.005	<0.005	
Steel S	0.39	1.57	0.011	0.005	1.03	0.16	3.7	0.92	0.59	<0.005	<0.005	<0.005	
Steel T	0.39	1.59	0.012	0.006	0.45	0.16	3.66	1.41	0.61	<0.005	<0.005	<0.005	
Steel U	0.40	1.57	0.012	0.005	0.45	0.16	3.84	1.46	0.63	<0.005	<0.005	<0.005	
Steel V	0.40	2.08	0.01	0.008	0.98	0.17	3.76	1.00	0.57	<0.005	<0.005	<0.005	
Steel W	0.43	2.11	0.01	0.007	0.98	0.16	3.78	0.99	0.61	<0.005	<0.005	<0.005	

Table (4.3.32): Martensite start temperatures [°C] of the steels A through to O measured by dilatometry.

Steel	**A**	**B**	**C**	**D**	**E**	**F**	**G**	**H**
M_S [°C]	285	253	241	243	196	255	271	210
Steel	**I**	**J**	**K**	**L**	**M**	**N**	**O**	**P**
M_S [°C]	309	305	318	252	175	241	218	115
Steel	**Q**	**R**	**S**	**T**	**U**	**V**	**W**	
M_S [°C]	178	170	182	184	170	145	130	

Linear regression based on M_s measurements of these 23 armour steels without considering any interaction parameters between alloying elements showed that it is difficult to fit all the experimental data on the martensite start temperature with the chemical composition using one equation. The formula proposed by Wang gives good approximations only when the M_s of the armour steel is higher than 200°C. Above 0.40%C the differences from the measured values of M_s become larger than 100°C. The following approach was then suggested in this study for the estimation of the martensite start temperature of the steels with chemical compositions in the range considered.

$$M_S\left({}^0C\right) = 548 - 590C - 35Mn - 18Ni - 14Cr - 9.5Mo - 12Si \qquad (4.14)$$

Formula (4.14) proposed in this work for the estimate of the martensite start temperature of the armour steels, is based on measured values within the range of chemical compositions of interest for ballistic performance steels. The chemical compositions of these steels are well within the specified ranges for the previous formulas (4.12) and (4.13), which makes the comparison between them valid.

4.3.7.1 Determination of the relationship between the chemical composition and the martensite start temperature proposed in formula (4.14)

After measuring the martensite start temperatures of the first 15 armour steels (Steels A through to O) their martensite start temperatures were fitted through multi-linear regression of the martensite start temperatures to the chemical compositions. The validity of each fitting was verified with the eight remaining steels. The three best fittings were considered in the prediction of the martensite start temperatures of the steels P through to W and the final equation was assessed through a comparison between the predicted and the measured values.

Table (4.3.34) Measured martensite start temperatures of six armour steels

Name of the steel	Martensite start temperature [°C]
B	253
G	271
H	210
I	309
J	306
K	318

The most likely elements in these steels to affect the M_s temperature are Carbon, Manganese, Silicon, Nickel, Chromium and Molybdenum. The hypothesis of the chemical composition dependency of the martensite start temperature of the steels may be expressed, without interaction parameters, as:

$$M_S\left[{}^0C\right] = 539 + a \times W_C + b \times W_{Mn} + c \times W_{Si} + d \times W_{Ni} + e \times W_{Cr} + f \times W_{Mo} \qquad (4.15)$$

where a, b, c, d, e and f are six regression parameter to be determined and W_C, W_{Mn}, W_{Si}, etc. are the mass percentages of the alloying elements in the armour steels. The experimental values of the martensite start temperatures and the chemical compositions of the six steels were introduced into Equation (4.15). Therefore, a system of six equations with six unknowns, viz. the regression parameters, was developed. The corresponding matrix representation for the martensite start temperatures measured after austenitisation at 900°C, therefore, was:

$$\begin{bmatrix} -286 \\ -268 \\ -329 \\ -230 \\ -233 \\ -221 \end{bmatrix} = \begin{bmatrix} 0.317 & 0.855 & 0.176 & 3.8 & 0.318 & 0.367 \\ 0.37 & 0.40 & 0.43 & 2.8 & 0.24 & 0.3 \\ 0.37 & 1.15 & 1.06 & 3.8 & 0.52 & 0.43 \\ 0.34 & 0.39 & 0.40 & 2.43 & 0.27 & 0.37 \\ 0.3 & 0.48 & 0.35 & 1.4 & 0.48 & 0.19 \\ 0.30 & 0.65 & 0.75 & 2.83 & 0.84 & 0.45 \\ 0.30 & 0.97 & 0.93 & 4.1 & 0.83 & 0.69 \end{bmatrix} \times \begin{bmatrix} a \\ b \\ c \\ d \\ e \\ f \end{bmatrix} \tag{4.16}$$

The solution of the above system using the method of the inverse matrix, gives the regression factor vector:

$$\begin{bmatrix} -719 & -197 & 9.83 & 64 & 96 & -325 \end{bmatrix} \tag{4.17}$$

The components of the vector in Equation (4.17) are the coefficients to be averaged to obtain the coefficients in Equation (4.14). One should expect a dependence of these coefficients on the austenitisation temperature and time because of differing degrees of dissolution of alloy carbides; hence the martensite start temperature itself should be a tribute of the austenitisation parameters.

The graphical comparison between the measured and the predicted values using the three formulas for the 23 steels are compared in Figure 4.3.31. From Figure 4.3.31 it appears that the published Equation (4.12) leads to systematically higher estimates of the martensite start temperatures than the measured values. For the armour steels whose martensite start temperatures are between 200°C and 318°C, the formulas (4.13): published) and (4.14): proposed) give comparable results close to the experimental values. But at martensite start temperatures lower than 200°C the published formula (4.13) deviates from the experimental values whereas the proposed formula (4.14) still gives good agreement between measured and predicted values. However, at low martensite start temperatures the formula (4.14) also results in larger differences between the experimental and the predicted values. This suggests that the effects of the alloying elements on the martensite start temperatures of these steels is not necessarily linear. Moreover, the predictive models of the martensite start temperature should possibly be defined for either the low (plate martensite) or the high martensite start temperatures (lath martensite).

A single model that uses the estimates of martensite transformation temperatures for both plate and lath martensite may deviate at one end of the temperature scale. Secondly, Nitrogen (that has not been included in this analysis) may also modify the magnitudes and the signs of the regression coefficients in these formulas substantially. The standard deviation is 52°C for the published formula (4.12), 34°C for the published formula (4.13) and only 19°C for the proposed formula (4.14).

Table 4.3.34. Measured and estimated values of the martensite start temperatures of 23 armour steels

	Martensite start temperature {°C]			
Steel designation	**Measured**	**(Eq 4.14 proposed in this study**	**Wang**	**Stevens**
A	285	218	266	287
B	253	255	241	315
C	241	251	261	318
D	243	247	268	318
E	196	185	117	261
F	255	221	271	294
G	271	254	289	321
H	210	189	212	263
I	309	271	298	331
J	306	308	315	363
K	318	264	259	323
L	259	225	213	288
M	175	131	110	216
N	241	203	237	280
O	218	215	247	291
P	115	100	35	191
Q	178	131	58	217
R	170	155	128	235
S	182	158	129	238
T	184	158	84	236
U	170	148	78	228
V	145	132	78	216
W	130	112	73	215

Theories on the chemical composition dependency of the martensite start temperature of steels, stipulates that the substitutional elements Mo, Mn, Ni, Cr and Si have different effects on the proof stress of the austenite matrix due to differences in the misfit strain and the chemical bond energies.

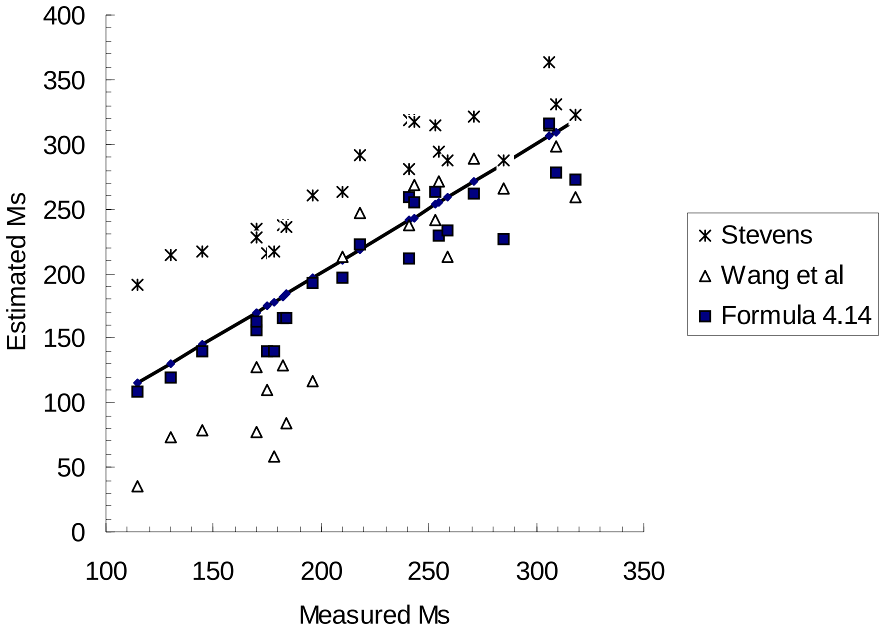

Figure 4.3.31: Comparison between the measured and the predicted martensite start temperatures for the 23 experimental alloy steels. The predictions were from the published empirical formulas (4.12), (4.13) and the proposed empirical formula (4.14) for armour steels is also shown. The diagonal represents the measured values

The strengthening of the austenite matrix will require a larger driving force for its decomposition into martensite since the transformation front has to move through a hardened matrix, giving rise to a decrease in the martensite start temperature. However, Schramm and Reed [21] reported that both Mn and Mo increase the stacking fault energy of the austenite matrix, although most substitutional elements are generally considered to lower the stacking fault energy of the austenite matrix, allowing stacking faults to separate further making cross slip of screw dislocations more difficult.

A least squares fitting applied to the above three formulas for the 23 armour steels of this study, gives the following values that show a better agreement between the measured martensite start temperatures and the predicted values using formula (4.14).

Table (4.3.35): Sum of squared differences between measured and calculated values of the M_s for the 23 steels (steel A through to W)

Sum of the squared differences		
Formula (4.12)	**Formula (4.13)**	**Formula (4.14)**
72651	70670	13578

Stevens (formula 4.12) reported that Cobalt increases the martensite temperature and Aluminium may have the same effect. The monotonic decrease of the martensite start temperature with the alloying element content should then be considered as a particular case and not as a rule. The multiplying factors are strongly dependent on the chemical composition ranges, the austenitisation temperature and the technique used for the measurement. The acoustic technique, for example, detects the formation of the very first plates of martensite and generally gives higher values of the martensite start temperature whereas optical metallography is less sensitive and gives lower values of the M_S. In turn, the multiplying factor in a predictive formula will also change.

4.3.7.2 Effect of the austenitisation temperature on the M_s temperature

The effect of the austenitisation temperature on the martensite start temperature was analysed for seven armour steels selected from the twenty-three experimental steels. The martensite start temperatures of the steels E, F,G, H, J, M and N are presented in Table 4.3.36 for four different austenitisation temperatures.

Table (4.3.36): Martensite temperatures of seven steels as a function of the austenitisation temperature

	Martensite start temperature [°C]						
Austenitisation temperature	**Steel E**	**Steel F**	**Steel G**	**Steel H**	**Steel J**	**Steel M**	**Steel N**
800°C	193	244	278	202	299	187	241
850°C	189	244	275	205	305	176	239
900°C	196	255	282	210	308	175	238
950°C	187	248	271	193	293	169	233

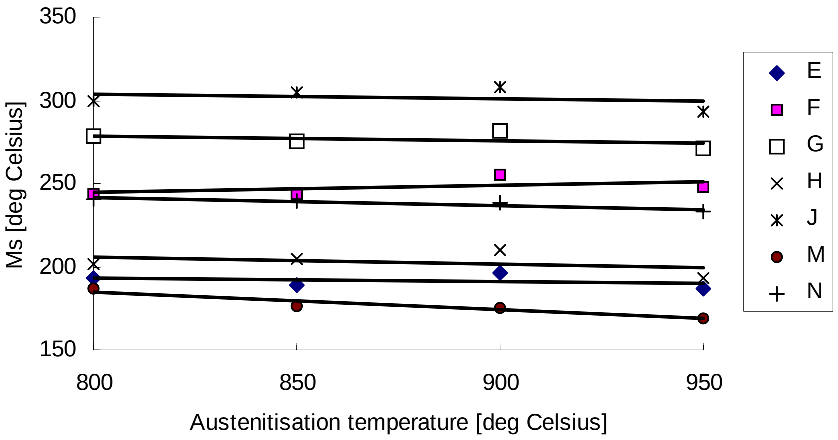

Figure 4.3.32: Effect of the austenitisation temperature on the M_s of seven armour steels

The martensite start temperatures of these armour steels appear to slightly decrease when the austenitisation temperature is increased from 800°C to 950°C. The increase in the austenitisation temperature has many consequences, i.e. greater dissolution of carbides, solid solution hardening of the parent austenite and grain growth and all of these may modify the thermodynamic as well as the kinetic characteristics of the transformation. Greater dissolution of the carbides changes the chemical composition of the matrix and, hence, the chemical driving force for the transformation to martensite. It also increases the solid solution hardening of the parent austenite, which affects the movement of the transformation front through the austenite.

4.3.7.3. Steel composition considerations

From the preceding paragraphs it may be concluded that the following chemical composition factors are to be noted in designing an improved armour steel:

a. Carbon is the main element determining the hardness of the martensite. A hardness higher than 500 VHN may be obtained when the Carbon content of the armour steel is above 0.37 wt%C as established in Sections 4.1 and 4.2.

b. It appears that the Silicon content of the steel has a strong effect on the stability of the martensite upon tempering as shown in Table (4.3.37) for five armour steels from this study. Silicon delays the softening of the martensite during tempering to higher temperature.

Table (4.3.37): Silicon content and the temperature of softening of the martensite in five experimental steels

Steel	Si	Cr	Ms	Temperature of start in decrease in mechanical properties
E	0.21	1.49	196°C	200°C
F	0.8	0.22	255°C	250°C
G	0.43	0.24	271°C	150°C
H	1.06	0.52	212°C	300°C
I	0.40	0.27	309°C	200°C

Silicon increases the stability of the martensite by reducing the chemical activity of carbon [75, 77, 80]. Silicon becomes effective in delaying the decomposition of the martensite in the range between 0.5 wt% to 1.0 %C. The combined effect of Silicon and Chromium presents a maximum effect at 1.5 wt%(Si+Cr). In these steels the martensite remains stable in an "untempered" condition below 150°C. Further Silicon additions may increase this temperature up to 300°C.

c. The fractographs of the shear lips from the Charpy and tensile tests have shown a detrimental effect of elongated particles of MnS under impact as well as under tensile stress. Sulphur should therefore be kept below 0.003 wt%S for these steels. The shape of the MnS particles is strongly dependent on the Oxygen content of the solidifying steel. A lower Oxygen content will favour the less detrimental equi-axed shape.

d. The samples austenitised at 900°C, quenched in water at room temperature and then polished electrolytically in a 5% percholric acid and 95% glacial acetic acid solution were analysed by XRD for a semi quantitative analysis of the retained austenite.

e. The ideal alloy should be Titanium-, Niobium- and Aluminium-free to avoid the risk of cracking initiation near the coarse inclusions or precipitates.

For the steels with 0.37%C to 0.39%C and 0.5 %Si to 1.0%Si, the tempering heat treatment should be kept below 200°C to achieve both hardness (500– 600 VHN) and tensile strength between 1300 and 2200 MPa. Tempering above 250°C is not acceptable because of the lower hardness that results. In these conditions the impact energy of the sub-sized specimens at -40°C is in the range 10 to 18 Joules.

f. The martensite start temperature of the armour steels may be approximated with acceptable accuracy using the formula (4.14)

4.4. Results of the ballistic testing (First series)

4.4.1. Ballistic report

The first series of ballistic testing was done on five plates of which two of steel E, one of steel F, one of steel G and one of steel H and their results are reported in Table 4.4.37. The second plate of steel E was tested from a firing distance of only ten meters which is significantly less than the specified thirty meters. The plates that were considered to have passed the ballistic test, had to resist penetration after at least five shots. The parameters and effect of each shot was recorded. No light should be visible through the impacted region for the shot as having been resisted and the test to be considered as having passed. The 5.56 mm projectiles used for the ballistic testing are presented in Figure 4.4.33.

Ball High Pressure Tracer SS109

Figure 4.4.33: 5.56 mm rounds fired by a R4 during the ballistic test (first series)

The mechanical properties of the first series of five armour steel plates mentioned above, are as follows:

Table (4.4.37): Properties of the plates austenitised at 900°C for 1 hr and tempered at 180°C for 1 hr before the first series of ballistic testing

	Thickness [mm]	**Vickers Hardness**	**YS [MPa]**	**UTS [MPa]**	**YS/UTS**	**Retained austenite [%]**	**Elongation [%]**	**Impact energy at –40 [Joules]**	**Martensite start temperature [°C]**
Steel E	6.2	578	880	1780	0.50	6	4	10	196°C
Steel F	6.2	610	1500	2200	0.68	0.6	8	14	255°C
Steel G	6.1	475	1500	2000	0.75	0.6	12	17	271°C
Steel H	6.1	565	1100	1897	0.58	4	6	14	210°C

In the above table the Charpy impact energy was measured on the sub-sized specimens of $5 \times 10 \times 55$ mm. The comparison of the ballistic performances of these plates is shown in the next Section and the validity of the prediction models discussed.

Typical images of the plates after ballistic testing are presented in Figure 4.4.34. The visual analysis of the rear face of the plate of steel E in Figure 4.4.34(b) does not show any sign of deformation due to the ballistic impact. This observation led to decreasing the firing distance to ten meters for the second plate of steel E. This observation was also instrumental in redesigning the alloys in the next series for the advanced performance armour plates.

Table 4.4.38: Ballistic report (first series)

Plate designation		**Firing Distance (Meter)**	**Firing Angle (°)**	**Hardness Vickers**	**Measured projectile velocity (m/s)**	**Ballistic performance**
Name	**Thickness [mm]**					
Steel E	6.2	30	0	578	943	Passed well
					951	Passed well
					956	Passed well
					952	Passed well
					987	Passed well
Steel E	6.2	10	0	578	-	Passed well
					-	Passed well
					-	Passed well
					-	Clean Penetration
					-	Clean Penetration
Steel F	6.2	30	0	610	954	Clean Penetration
					942	Clean Penetration
					957	Clean Penetration
					944	Passed well
					952	Passed well
Steel G	6.1	30	0	475	948	Clean Penetration
					955	Clean Penetration
					947	Clean Penetration
					933	Clean Penetration
					948	Clean Penetration
Steel H	6.1	30	0	535	1013	Passed well
					951	Bulge + Crack + No light penetration
					947	Passed well
					956	Passed well
					940	Passed well

4.4.34(a): Front face of steel E

4.4.34(b): Rear face of steel E

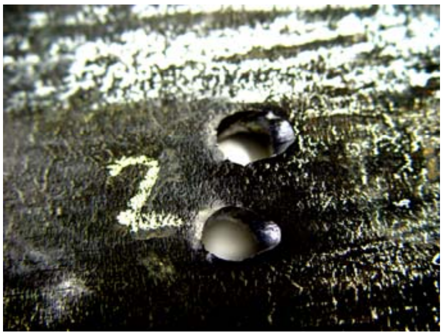

4.4.34(c:). Front of Steel F plate after firing

Figure 4.4.34: (a) and (b) Front and rear faces of the plate of steel E showing good resistance to the ballistic impact after being fired from 30 meters. 4.4.34(c) : Front face of the plate of steel F showing the clear penetration holes and the elevated contours at the edges of the penetration due to the compressive stresses in the incidence region.

4.4.2. Comparison with the ballistic performance specifications

In the following sub-sections, results of the first series of ballistic testing, reported in Table 4.4.38 are compared to the prediction using two different criteria, one reported in the literature and one specified by ARMSCOR and Mittal Steel (South Africa); and a third improved criterion from this study is proposed.

4.4.2.1. The Ballistic Performance Index (BPI).

The Ballistic Performance Index introduced by Srivathsa and Ramakrishnan [6,7] has been defined in Sub-section 2.2.4. Although the knowledge of the relationship between the mechanical properties and the ballistic performance of steels is still lacking, the BPI constitutes an attempt to quantify and to be able to compare such performance for two armour materials. The BPI does not consider the hardness as a determining factor for the ballistic performance. This is totally different for the specification used by Mittal Steel (South Africa) where the high hardness of the steel plate is the major criterion in predicting the resistance to ballistic impact.

The BPI of the steels E, F, G and H calculated according to the above-mentioned model are shown in Table 4.4.39. For this calculation a minimum muzzle velocity of 940 m/s is considered. The Young's modulus of the steels is assumed to equal 200 GPa and the density equal to 7800 kg/m^3.The reductions in area after tensile testing were respectively 6%, 11%, 20% and 8% for these four steels.

Table 4.4.39: The ballistic Performance Index of the steels E, F, G and H

	Steel E	Steel F	Steel G	Steel H
BPI	3.7	3.9	4.6	4.5

It is concluded from this table that the BPIs of these four steels are very close but with a tendency to higher values for the steels with higher strength, which is contradictory to the experimental observation on these four steels.

The formula for the BPI has the value of taking into account the effect of the reduction in area on the ballistic performance. It shows the tendency for localised yielding in steels with a large reduction in area that leads to poor ballistic performance. The formula of the BPI also demonstrates the decrease in ballistic performance when the velocity of the fired round increases. In the case of these four steels the BPI is multiplied by 3 to 4 when the velocity of the round is reduced from 940 to 400 m/s. But the BPI still seems to predict a higher performance for steels that have a higher strength which the authors themselves disproved from their experience and is also contradictory to the ballistic results of this study in Table (4.4.39).

The assessment of performance by ballistic testing remains indispensable and confirms the current observation that a clear relationship between the mechanical properties and the ballistic performance is still lacking. The Ballistic Performance Index should then possibly be considered only as a qualitative indication of ballistic performance and may be used for the comparative selection between different armour materials only when the BPIs are different by more than a margin or a ratio yet to be determined.

4.4.2.2. The Mittal Steel (South Africa) specifications

From the current specifications for military applications of armour steels, Mittal Steel (South Africa) has determined the specification limits for the advanced performance armour steel to be developed in this study, as follows [1]:

- the hardness is the main factor determining the ballistic performance and should be higher than 600 BHN, that is equivalent to 640 VHN;
- the Charpy impact energy of the full size specimen at -40°C should be higher than 13 Joules;
- the yield strength of the steel should be higher than 1500 MPa;
- the ultimate tensile strength should be higher than 2000 MPa; and
- the minimum elongation of a 50 mm gauge is fixed at 6%.

According to this specification the prediction of the ballistic performance is favourable for steel F only. However, the result from the ballistic testing is uncertain because the plate of this steel resisted two shots well but three others penetrated the plate. On the other hand steels E and H passed the ballistic test well despite the lower hardness and tensile properties than specified. Steel G satisfied all the aspects of the specification except the main one, i.e. the hardness, and it failed the ballistic test. One should conclude then that the high yield strength, the high tensile strength, the high elongation and the high impact energy of steel G did not play a decisive role in resisting high velocity impacts.

4.4.3. Differences in the microstructures between steels E, F, G, H and I

This paragraph aims to define a *direct relationship* between the microstructure and the ballistic performance instead of to seek an *indirect relationship* via the mechanical properties. The microstructures and the phases present in these four armour steels before ballistic testing were analysed in thin foil transmission electron microscopy, in atomic force microscopy and X-ray diffraction. The X-ray diffraction allowed the determination of the volume fraction of the retained austenite as well as the lattice parameters of both the martensite and the retained austenite. In this paragraph the differences in microstructures and phases are considered and used to explain directly the observed differences in ballistic performance of the above steels. Further characterisation of the martensite will be done in Chapter 6.

The measured volume fraction of the retained austenite in these five steels and their martensite start temperatures were found to be:

Table (4.4.40): % Retained austenite in steels E, F, G, H and I after water quenching from 900°C

	Steel E	Steel F	Steel G	Steel H	Steel I
Retained austenite [%volume]	6	0.6	0.5	2	0.5
Martensite start temperature	196	255	271	210	309

The detection limit for retained austenite of the X-ray equipment used is generally less than 2% volume fraction, below which the volume fraction may not be quantified accurately. From Table (4.4.40) it may be seen that the 6 mm armour plates of the Group 1 alloys contains detectable amounts of retained austenite and these steels have passed the ballistic test while those with non-detectable retained austenite failed the test.

It may also be observed from Table (4.4.37) that steels E and H have values of the yield strength to ultimate tensile strength ratio smaller than 0.6. The low value of the YS/UTS ratio indicates a resistance against localised yielding; in other words, it indicates the ability of the material to dissipate the impact energy transversally to the incidence direction of the fired round in the plate . This property increases the volume of the material interacting with the fired round, offering better resistance to perforation. The elongation during uniaxial tensile testing also indicates the tendency for localised yielding of the steel when impacted. It should be kept lower than 7%, which is contrary to the specification used by Mittal Steel (South Africa).

The different types of morphologies of the martensite in these five steels are shown in the following figures where they are arranged in order of increasing martensite start temperature.

The untempered steels E and H contain twinned martensite and nodular particles of retained austenite (RA), as shown in Figures 4.4.35(a) and (b). The size of the RA nodules allow their detection by X-ray diffraction analysis. The twins run across the entire width of the martensite plates. No traces of auto-tempering were observed throughout the thin foils under 18000 to 43000 magnification. Steels F and G on the other hand contain lath martensite with high dislocation densities within the laths. They also contain thin films of retained austenite along the lath inter-faces, as shown in the dark field thin foil electron micrograph in Figures 4.4.35(c) and (d). The volume fraction of retained austenite in these two steels was estimated to be less then 0.6%. The bright field transmission electron micrographs of the quenched specimens of steels F and G also contain areas with fine carbides along the lath inter-faces. In these steels with intermediate martensite start temperatures, auto-tempering due to the relatively rapid diffusion of the Carbon atoms and the subsequent formation of fine cementite particles, could not be avoided during the quenching. This observation was also mentioned earlier by Krauss [51] for steels of which the martensite start temperatures are well above room temperature.

Figure 4.4.35(e) is a thin foil bright field image of steel I of which the martensite start temperature is relatively high, i.e. 309°C. The martensite in this steel consisted of large laths which were less dislocated, possibly due to enhanced annealing of the dislocations and the large plastic accommodation across the reaction front during the martensitic transformation at this high temperature. The laths are large and contain large areas with fine cementite particles that are not confined to the lath interfaces as was the case in steels F and G. This microstructure of steel I presented the lowest hardness, the highest impact energy and the largest elongation among the five steels discussed here. The tensile properties of steel I were also measurable in the quenched condition that was not the case for steels E and H.

From the morphology, M_s temperatures, Silicon contents of these steels and the evidence obtained in indexing some SADPs of these steels (see later in Section 6.4) as well as the fact that these dark field micrographs were obtained from untempered steels and hence could only possess very minor quantities of autotempered carbides in the high-M_s temperature steels, it is concluded that the dark field micrographs in Figure 4.4.35 do represent the retained austenite.

The surface relief of these five steels after quenching and analysed in simple contact atomic force microscopy shows, likewise, as in transmission electron microscopy, a change in the morphology from the sheared twinned martensite to the dislocated and the plastically accommodated lath martensite as the martensite start temperature increased. The Figures 4.4.36(a) through to (d) present the surface relief evolution for these five steels, once more arranged by increasing martensite start temperatures. These measurements to analyse the characterisation of the twinned and the lath martensite with respect to their surface relief, are presented in Chapter 6. Olson [58] reported that the morphology of the retained austenite within laths or plates, determines whether the austenite will transform by a stress- or strain-induced mechanism to martensite.

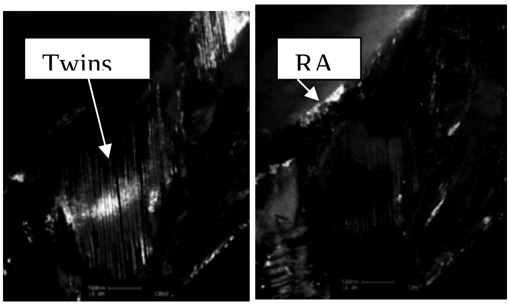

Figure 4.4.35(a): Steel E, M_S=196°C

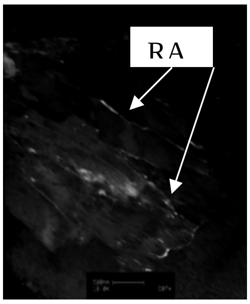

Figure 4.4.35(b): Steel H, M_S=210°C

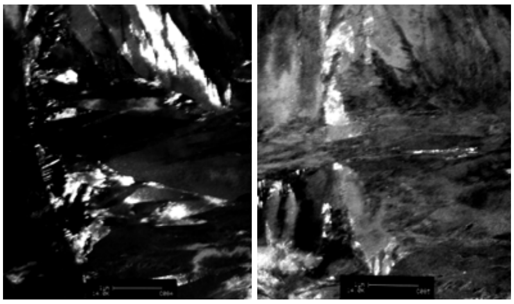

Figure 4.4.35(c): Steel F, M_S=255°C (label 500 nm)

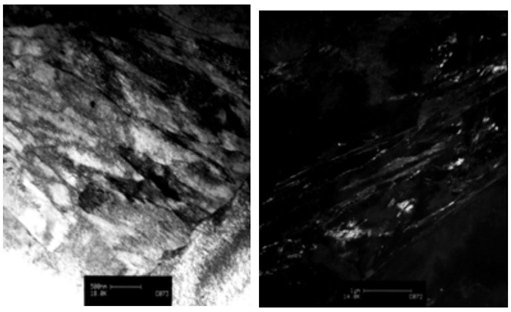

Figure 4.4.35(d): Steel G, M_S=271°C

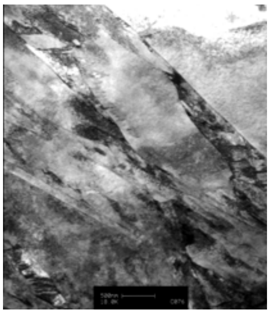

Figure 4.4.35(e): Steel I, M_S=309°C (label 500 nm)

Figure 4.4.35: Thin foil transmission electron micrographs (x 10000, label 500 nm) showing the morphology of the martensite and retained austenite in steels E through to I after water quenching from 900°C.

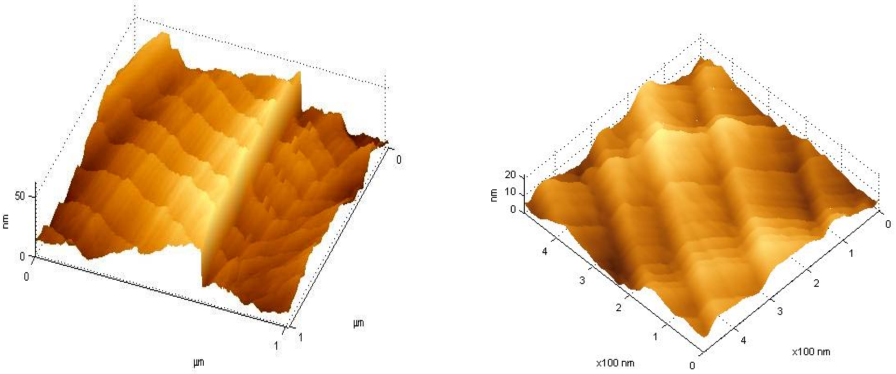

Figure 4.4.36(a): Steel E, M_S = 196°C, twinned martensite

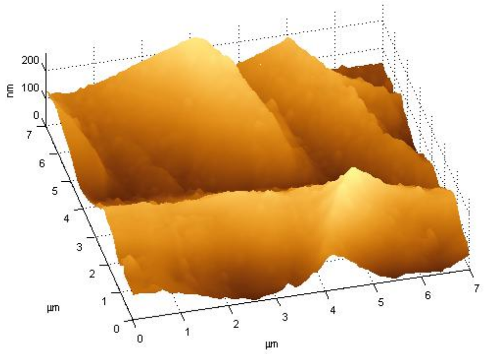

Figure 4.4.36(b): Steel H, M_S = 210°C, sharp edges and regular N-shaped surface of twinned martensite without sheared micro-twins

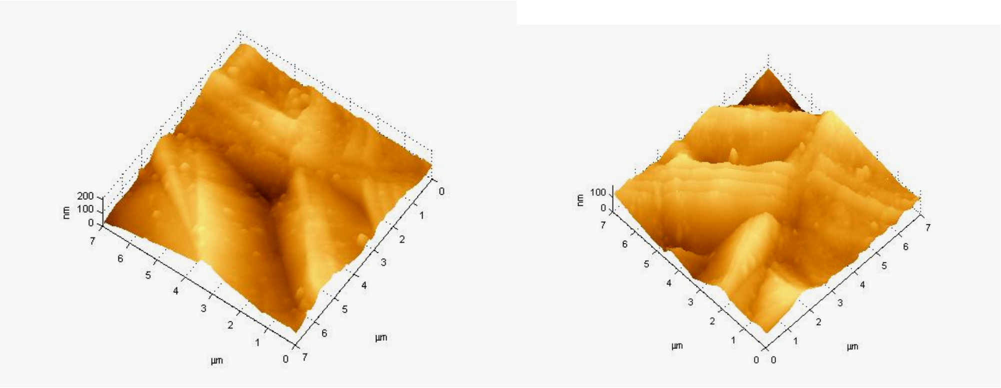

Figure 4.4.36(c): Steel F, M_S = 255°C, lath martensite with rounded edges

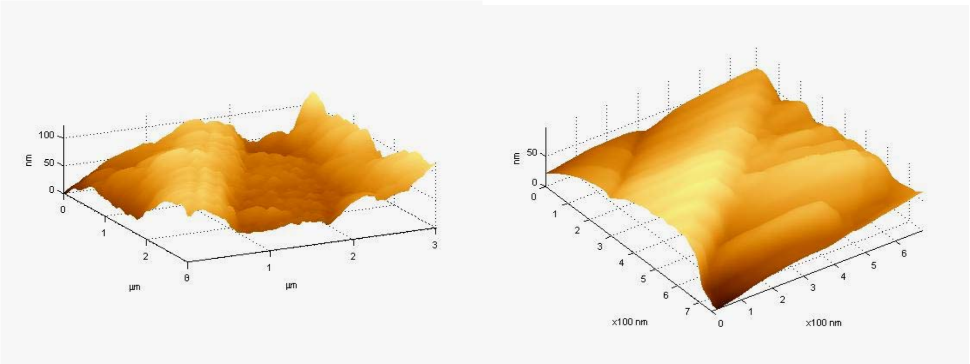

Figure 4.4.36(d): Steel G, M_S = 271°C, background of lath martensite that contains some twins

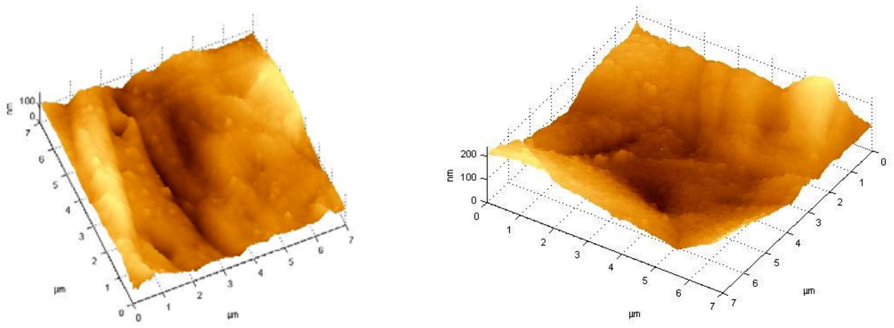

Figure 4.4.36(e): Steel I, M_S = 309°C, lath martensite. Surface showing plastic strain accommodation

Figure 4.4.36: Atomic force microscopy of the surface relief of steels E to I.

Figure 4.4.36 demonstrates that atomic force microscopy is a useful complementary technique that may be used in characterising the martensite. It does suffer from two deficiencies however. (1) The relief of peaks of the martensite plates formed at high M_s temperatures, may be blunted somewhat through rapid surface diffusion of atoms before reaching room temperature where the relief measurements are actually carried out. (2) The martensite formed at a free surface is only partially restrained whereas that formed within the volume of the microstructure is fully hydrostatically restrained. This difference may place some question marks on conclusions derived from surface relief measurements.

Surface relief measurements nevertheless constitute a complementary contribution to a study of the internal details revealed by the thin foil transmission electron microscopy. Indeed Figure 4.4.36(a) demonstrates the formation of martensite with micro-twins within the plate martensite. This mechanism of formation is one of those predicted by the crystallographic theory of the martensitic transformation. The amplitude of the plastic strain accommodation during the martensitic transformation increases as the martensite start temperature increases. The mechanism of formation of the martensite seems to be a shear when the martensite start temperature is lower than 210°C as shown in Figure 4.36(b). For the martensite start temperatures of 255°C and 271°C, the twinned martensite was formed as plate martensite with their shape no longer regular with sharp edges as was the case in Figures 4.4.36(a) and 4.36(b). These irregular shapes may be related to a significant rotation of the habit plane during the martensitic transformation, although the possibility of surface diffusion may also have made some contribution. This observation on the rotation of the habit plane is in good agreement with the earlier conclusions in the literature by Mou and Aaronson [21] on a change in the mechanism of martensite formation and the coexistence of both lath and plate martensite when the martensite start temperature is about 250°C.

The data reported in Table (2.7) show that the two types of martensite may be formed together in a wide range of martensite start temperatures ranging from 200°C to 390°C. In this range of martensite start temperatures both the shear mechanism and the plastic accommodation of the deformation strain by slip and rotation of the habit plane are operative. This combined mechanism produces irregular N-shaped profiles that indicate irregular habit planes and is in agreement with the conclusion by Kennon and Dunne [46, 49] about the flexibility of the habit plane that is likely to be a characteristic feature of the plate martensite not accounted for by the crystallographic theories. Tadaki and Shimizu [48] also suggested that the formation of a continuous spectrum of habit planes should be expected based on their measurements of the variation of the lattice parameters of the martensite and the retained austenite as a function of the actual temperature of formation. The topology of the surface of steel I, in Figure 4.36(e), of which the martensite start temperature was 309°C, can be interpreted that the plastic strain accommodation results from the slip of dislocations.

4.4.4. Differences in microstructure between steels E, F, G, H in the tempered condition before ballistic testing

Thin foil transmission electron micrographs of the tempered armour steels E , F, G and H before ballistic testing, are compared in Figures 4.4.37(a) through to 4.4.37(d). The steel plates were tempered at 180°C for one hour. Fine elongated strings of carbides were found to have precipitated within steels E and H respectively, as shown in Figures 4.4.37(a) and 4.4.37(b). These two steels passed the ballistic testing well. On the other hand, coarse carbides have precipitated within the laths and on the lath interfaces of steels F and G that gave poor ballistic performances.

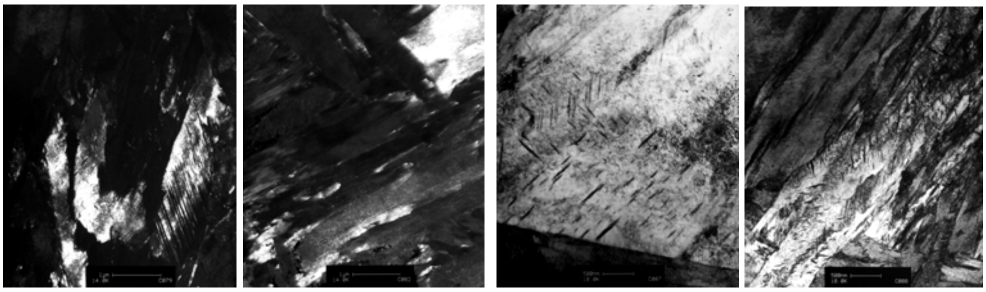

4.4.37(a) 4.4.37(b) 4.4.37(c) 4.4.37(d)

Figure 4.37: Thin foil transmission electron microscopy of the steels E (4.4.37(a)), steel F (4.4.37(b)), steel F (4.4.37(c)) and steel H (4.4.37(d)) after tempering at 180°C (label scale = 500 nm).

A high ballistic performance requires a microstructure consisting of twinned martensite with some retained austenite without coarse carbides. The precipitation of cementite may be controlled by the chemical composition of the armour steel and by the tempering temperature.

Steels E and H that gave good ballistic performances after tempering at 180°C for one hour, were then tempered at a higher temperature of 350°C for 1 hour with a view to determine the maximum tempering temperature that does not lead to the precipitation of the coarse cementite which is detrimental to the resistance to high velocity impact during ballistic testing. The thin foil micrographs in Figure 4.4.38 show large strings of cementite that had formed along the plate interfaces of steel E, shown in Figure 4.4.38(a) while steel H had formed noticeably less of these coarse strings of carbides during tempering at 350°C.

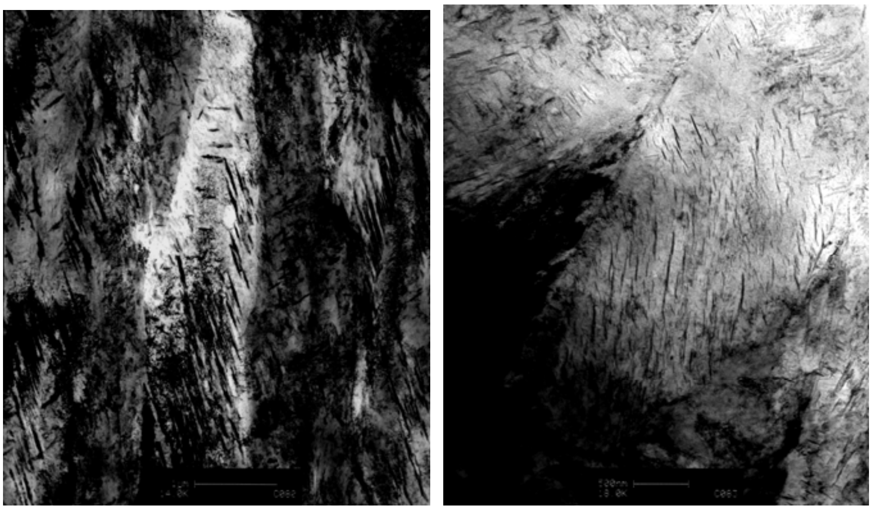

4.38(a): Steel E **4.38(b):** Steel H

Figure 4.4.38: Bright field thin foil transmission electron micrographs (x18000) of steels E and H after tempering at 350°C (label scale = 500 nm).

The retardation in formation of cementite during tempering of steel H may be attributed to its higher Silicon content of 1.06%, compared to the lower Silicon content of steel E of 0.21%Si. Silicon is well known for its effect on delaying the formation of cementite from supersaturated metastable martensite.

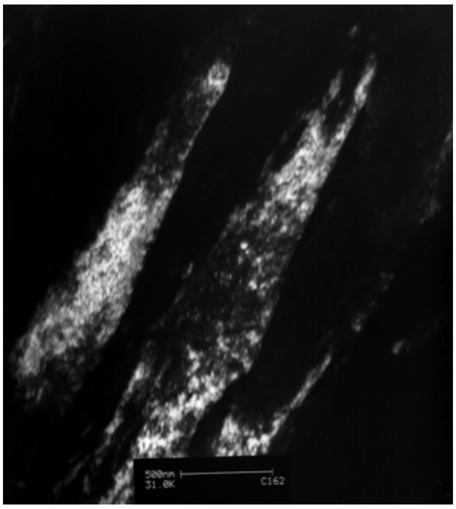

Figure 4.39: Thin foil TEM DF of steel E tempered at 400°C showing the cementite precipitated within the plates

Figure 4.4.40: Bright field thin foil transmission electron microscopy of steel H tempered at 300°C showing the cementite

Figure 4.4.41: Bright field thin foil transmission electron microscopy of steel E tempered at 400°C showing large strings of the cementite.

4.4.2.3. Proposition to redefine the specification of armour plate steels

Considering that neither the high hardness nor the higher levels of mechanical properties (yield strength, ultimate tensile strength, impact energy, % elongation) appear to be accurate criteria for predicting the ballistic performance of armour steels, an alternative design methodology is proposed. Those new design criteria are based on the results of this study of ballistic testing, the mechanical properties and the microstructure of the martensite.

This design approach is developed by also considering the volume fraction of retained austenite, the ratio of yield strength to ultimate tensile strength and the martensite start temperature of the five plate armour steels tested. The new proposal is derived from Tables 4.4.37 and 4.4.38 in which the steels E and H of the Group 1 armour steels, gave superior ballistic results, whereas steel G of Group 3 gave poor ballistic results and steel F of Group 2 gave intermediate ballistic results.

The new specifications should, therefore, rather prescribe the following:

- the volume fraction of retained austenite in the martensitic steel should be between 2% and 7%;
- the ratio of yield strength to ultimate tensile strength should be less than 0.6;
- the martensite start temperature should ideally be comprised in the range from 130°C to 220°C. The martensite start temperature may be determined by dilatometric analysis or predicted (with an error of ± 30°C) using the empirical Formula (4.14) derived from this study;
- the chemical composition should be close to that of steels E and H, i.e. 0.39%C, 1.2%Mn, 0.8%Si, 1.5%Cr, 0.5%Mo, 2.5%Ni.
- The austenitisation temperature between 850 and 950 for 30 minutes to one hour
- The tempering treatment at temperatures lower than 250 for 15 minutes to 1 hour

CHAPTER 5. IMPROVEMENT IN THE BALLISTIC PERFORMANCE

5.1 Approach methodology

The results of the first series of ballistic tests and the recommendations formulated in Chapter 4 constitute the basis for the ballistic improvement in steels E and H and the development of the chemical compositions for the further eight advanced performance armour steels P through to W and their appropriate heat treatment. The thickness range of the plates to be tested was reduced from 6 mm to between 4.5 and 5.2 mm in order to introduce a further safety factor in the maximum protection of the cockpit and the passenger cell with 6 mm thick armour plate. The volume fraction of the retained austenite in the plate martensite is considered to be the main factor determining the ratio of the yield strength to ultimate tensile strength (YS/UTS) of the armour steels and their resistance to localised yielding and perforation during a ballistic impact.

The morphology of the martensite and the volume fraction of the retained austenite after water quenching of the steels are *inter alia* functions of the martensite start temperature, which in turn, is a function of the chemical composition and the austenitising conditions. The latter effect provides effective dissolution of the carbides into the austenite matrix, which modifies its chemical composition and thus its chemical driving force for the martensitic transformation. Moreover the grain size of the parent austenite that grows with increasing austenitisation temperature and time, determines the total volume of the grain boundaries where the heterogeneous nucleation of the martensite can initiate. Consequently, the following reverse procedure was adopted in determining the chemical composition of the further eight advanced performance armour steels:

- The retained austenite (RA) located in the plate inter-faces was more effective in reducing the ratio YS/UTS than the RA located in the lath inter-faces. The optimum range of the volume fraction of retained austenite for an advanced ballistic performance was estimated at between 2% to 7%;

- The martensite start temperature of the advanced armour steels should, therefore, be lower then 210°C to enhance the formation of plate martensite over lath martensite;

- Using the proposed formula in Equation (4.14), the chemical compositions within the range specified in Section 4.4.2.3 to obtain eight suitable compositions, was found with predicted martensite start temperatures ranging from 100°C to 200°C within a ±30°C error. The chemical compositions of the eight steels P through to W were thus determined through this procedure;

- The steels were produced in a vacuum melting furnace, Calcium treated and degassed and cast into 5 kg ingots before being solution treated at 1050°C for one hour, hot rolled to thicknesses of 4.5 ± 0.2 or to 5.2 ± 0.2 mm, directly quenched into water at room temperature and lastly tempered at 180°C or at 250°C for 20 minutes;

- Samples for thin foil transmission electron microscopy before the ballistic testing and those for the determination of the martensite start temperature, were cut from these plates;

- The ballistic testing was performed and samples are cut from the impact regions for the X-ray diffraction analysis of the retained austenite, for the scanning electron microscopy of the cracks and for the thin foil transmission electron microscopy. The micro-hardness profiles across the impact region were also determined;

- Differences between the microstructures before and after the ballistic impact are explained;

- A revised specification, comprising the chemical composition range, the heat treatment and the mechanical properties for the high performance 6 mm steel armour plates is then formulated.

The chemical compositions of the steels P through to W, as determined by the above procedure, are given in Table (4.3.32). The martensite start temperatures after austenitisation determined by dilatometric analysis and those calculated, are included in Table (5.1). The volume fraction of the retained austenite before the ballistic test, determined by X-ray diffraction is also included in the same table.

Table (5.1): Martensite start temperatures and volume fraction of retained austenite in the tempered steels P through to W before ballistic testing

	Martensite start temperatures °C		**Volume fraction of retained austenite**	**Vickers hardness**
Designation of the armour steel	**Measured**	**Calculated using the formula (4.27)**	**%**	**VHN (30kg)**
P	115	63	6	580
Q	178	63	4	615
R	170	141	3	610
S	182	141	3	510
T	184	172	0.6	578
U	170	164	2	510
V	145	150	5.3	595
W	130	140	6	565

The volume fraction of retained austenite was determined within a 0.5% standard deviation.

5.2. Ballistic report

Plates of these eight armour steels were tested in the same ballistic conditions than those of the earlier steels E, F, G and H. The results of this second series of ballistic testing are reported in Table (5.2).

The steel T was the only that did not pass the ballistic test despite its higher hardness and thickness. Typical photographs of the front and of the rear faces of the plates that passed the test well from this second series of ballistic testing are shown in Figure 5.1.

Table (5.2): Ballistic report of the steels P through to W

Plate	Plate thickness	Firing distance (Meter)	Firing angle (°)	Hardness (VHN)	Projectile Velocity (m/s)	Ballistic performance
					933	Passed well
					928	Passed well
Steel P	4.7	30	0	580	931	Passed well
					955	Passed well
					952	Passed well
					947	Passed well
					943	Passed well
Steel Q	4.9	30	0	615	937	Passed well
					948	Passed well
					938	Passed well
					947	Passed well
					939	Passed well
Steel R	5.1	30	0	610	946	Passed well
					935	Passed well
					947	Passed well
					942	Passed well
					940	Passed well
Steel S	5.2	30	0	578	947	Passed well
					942	Passed well
					952	Passed well
					944	Failed Clean Penetration
					945	Failed Clean Penetration
Steel T	5.4	30	0	610	945	Failed Clean Penetration
					945	Failed Clean Penetration
					935	Failed Clean Penetration
					941	Failed Clean Penetration
					939	Passed well
					941	Passed well
Steel U	4.9	30	0	578	951	Passed well
					951	Passed well
					961	Passed well
					938	Passed well
					947	Passed well
Steel V	5.1	30	0	595	947	Passed well
					948	Passed well
					952	Passed well
					952	Passed well

Table 5.2 Continued

					942	Passed well
					935	Passed well
Steel W	4.8	30	0	565	941	Passed well
					941	Passed well
					931	Passed well

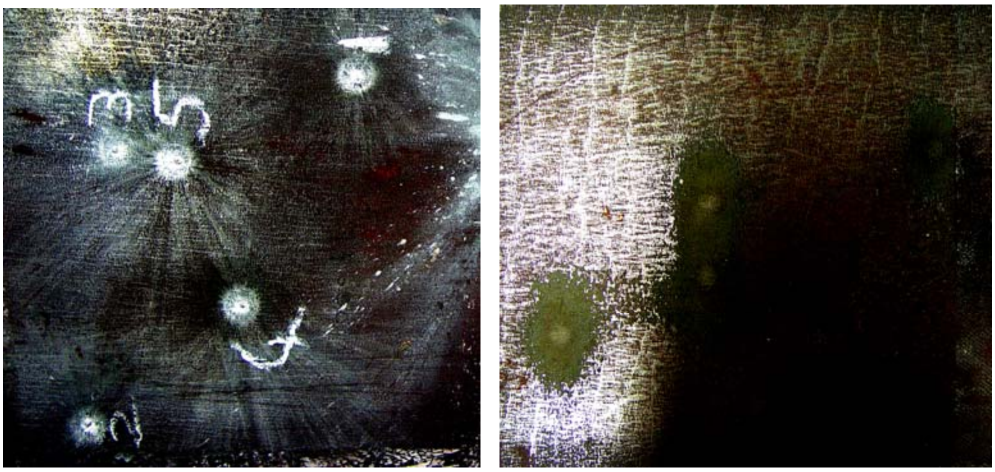

(a) Image of the front face of steel Q plate **(b)** Image of the rear face of steel Q plate

Figure 5.1: Photographs of the impact regions of the 4.9 mm steel Q plate that passed the ballistic testing

It is concluded from Table (5.2) that only steel T, containing the lowest volume fraction of retained austenite of about 0.6% did not pass the ballistic test.

5.3 The Ballistic Parameters

Visual observation of the areas affected by the ballistic impact revealed three concentric domains around the incidence point of the fired round in the armour plate. These three domains may also be observed around the penetration hole in plate T that failed the test. The size of these domains indicates the resistance to localised yielding of the armour plate. The existence of these three domains in the perforated plate of steel T that failed the ballistic test, may be explained by the relatively high velocity of the “slower” plastic wave that follows the precursor “faster” elastic wave compared to the longitudinal movement of the fired round through the thickness of the plate.

The inner domain, zone 1, that may be seen from the rear face in Figure 5.1(b), is penetrated more into the plate and had almost the same diameter in all eight plates, irrespective of whether the plate passed or failed the test. The thickness of the plates and the volume fraction of retained austenite in these steels seemed to have very little effect on the diameter of this inner zone 1. The diameter of the intermediate domain, zone 2, on the other hand differed while the diameter of the outer domain, zone 3, differed significantly.

The zones 2 and 3 are distinguishable on the front face as shown in Figure 5.1(a). The diameters of these three circular domains within the ballistic impact-affected areas are given in Table (5.3) for these eight steels.

Table (5.3): Diameters of the three concentric zones within the ballistic impact affected areas of the armour plates tested

	Thickness of the plate [mm]	**Volume fraction of retained austenite [%]**	**Diameter zone 1 [mm]**	**Diameter zone 2 [mm]**	**Diameter zone 3 [mm]**	**Ballistic parameter BP**
Steel P	4.7	6	13	26	54	0.0546
Steel Q	4.9	4	12	24	46	0.0298
Steel R	5.1	2	13	28	48	0.0061
Steel S	5.2	3	12	27	44	0.0165
Steel T	5.4	0.6	7	8	24	0.0027
Steel U	5.1	2	13	28	40	0.0061
Steel V	5.1	5.3	13	26	50	0.0323
Steel W	4.8	6	12	30	56	0.0494

The differences between these diameters as well as their variations are shown by plotting their values versus a ballistic parameter, defined as follows:

$$\mathrm{BP} = \frac{\mathrm{RA}(\%)}{\mathrm{EXP}(\delta)} \qquad (5.1)$$

where RA is the volume fraction of retained austenite and δ is the thickness of the steel plate in millimeters. The choice of this expression for the BP parameter is based, firstly on the proportional lowering of the ratio of YS/UTS by the retained austenite and secondly, on the increase of the effective penetrating weight when the thickness of the plate increases because of the direct transmission of the linear momentum to the cylinder of material ahead of the fired round within the plate. Figure 5.2 is a graphic presentation of the diameters of the three zones as functions of the ballistic parameter BP.

More ballistic testing is necessary before determining an accurate mathematical description of the diameters of the three zones in terms of the ballistic parameter BP. Nevertheless, the general shape of the curves in Figure 5.2 may suggest that within the range of the experimental parameters used, including the impact velocity, the firing angle, the volume fraction of the retained austenite and the thickness for the martensitic steel armour plates, the optimum ballistic performance is realised for values of the ballistic parameter BP between 0.0180 and 0.060.

The ballistic performance may decrease again at higher values of the parameter, whose limit is yet to be determined experimentally, because of a too high volume fraction of retained austenite or because of a too low thickness of the steel plate. The minimum hardness and the minimum thickness requirement of the armour steels should then be determined and the feasible region for the ballistic application redefined.

The ballistic parameter BP of the steels P through to W calculated as defined by Equation (5.1) are shown in Table (5.3). Plotting the measured diameters of the three concentric zones 1, 2 and 3 also shown in Table (5.3), produces the following Figure 5.2.

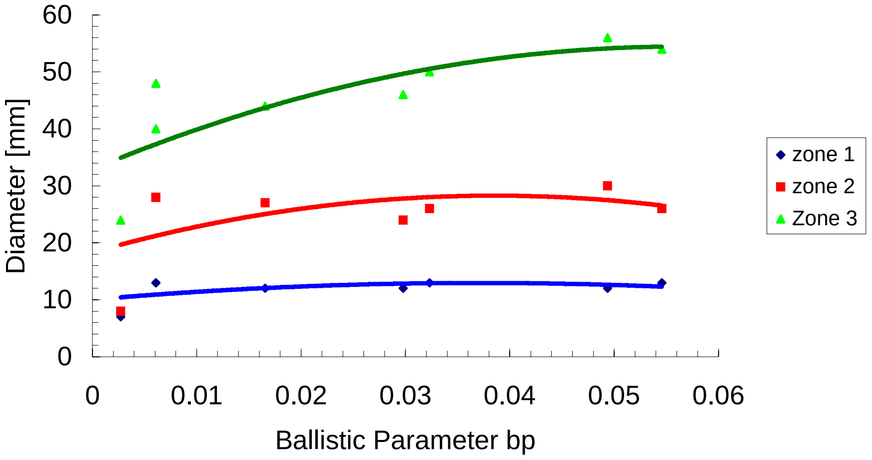

Figure 5.2: Variation of the diameters of the concentric zones 1, 2 and 3 within the ballistic impact affected domains as functions of the BP parameter.

The material in zone 1 is heated up to high temperatures during the impact as suggested by the scanning electron microscopy of the surface of the armour plates that are covered by the molten lead from the fired rounds. The temperature and pressure within these zones was high enough to cause welding of the copper and the lead from the fired round to the steel plates. The effect of the temperature rise on the microstructure within these zones was examined through thin foil electron microscopy after the ballistic testing by cutting specific localised 3 mm discs from these zones with a spark erosion wire cutting machine.

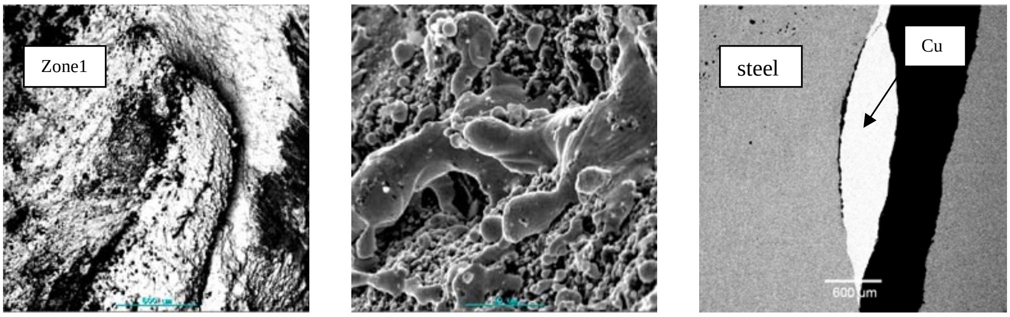

5.3(a) **5.3(b)** **5.3(c)**

Formatted

Figure 5.3: Secondary electron scanning electron microscopy of zone 1's front face of steel plate R covered with molten lead form the fired round (Figures 5.3 (a) and 5.3(b), label mark: 500µm). A polished cross section of zone 1 showing the copper from the fired round welded to the plates (figure 5.3(c)).

Figure 5.3(a) also illustrates the wavelike separation of the material within zone 1 by being dragged into the plate thickness. This illustrates the known theory, which predicts that at high strain rates and high temperatures the solid steel behaves like a dynamic liquid. Scanning electron microscopy of the cross-section of some impact regions revealed the presence of a tri-dimensional crack, the so-called Hopkinson sphere [5], formed where the compressive elastic wave was reflected from the outer edges of the plate. This composed an additional interference wave together with the slow compressive plastic wave, which produced a tensile stress higher than the true fracture stress of the armour steel. Closer observation of the crack demonstrates that the crack was composed of micro-cracks propagating along the grain boundaries outwards from the impact sphere. Figure 5.4 shows a typical cross section cut from one of the plates after ballistic testing.

Figure 5.4: Cross section throughout the affected impact region showing the copper from the round attached on to the front face of a 4.8 mm steel W plate. The bending of the plate in the affected impact region is also observable.

Figure 5.5 shows the tri–dimensional crack and the dynamic micro-cracks along the grain boundaries within the cross-section of the impact region. The surfaces in Figures 5.5(a) and 5.5(b) were not etched whereas the one in Figure 5.5(c) was etched.

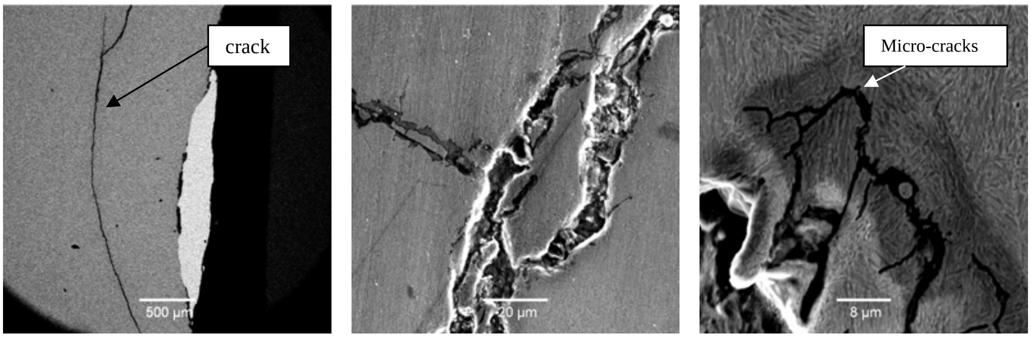

5.5(a) 5.5(b) 5.5(c)

Figure 5.5: Backscatter scanning electron microscopy of the Hopkinson sphere and the micro-cracks formed dynamically within the tensile region

The micro-cracks along the grain boundaries demonstrate the significance of the grain boundary properties on its ballistic performance of an armour steel. Clean grain boundaries without segregated particles or precipitates will have a higher cohesion strength and, therefore, a better resistance against the pull-out of grains due to the high tensile stress that occurs near to the spherical crack. The micro-crack substructures were encountered within the cross sections of steel R that passed the ballistic test and also in the plate of steel T that failed the ballistic test. These two steels were similar in their lower volume fraction of retained austenite. This observation may confirm that the retained austenite also arrests the propagation of the micro-cracks initiated in the region where high tensile stress waves are formed during the ballistic impact. The literature reports levels of tensile stress as high as 28 GPa [16, 17, 18] that may develop in the steel armour plate during the ballistic impact before fracture.

The untempered armour steels U and V also complied with the requirement of the specifications for ballistic performance but they also had macro-cracks and some parts were actually broken-off from the plate. The broken sections were about fifteen centimetres from the centre of the impact region as shown in Figure 5.6.

Figure 5.6: Untempered armour plate of steel U fractured by impact loading during ballistic testing showing the fracture some centimetres away from the impact points.

This observation agrees with the theory of an additional shock wave interference at a certain distance from the impact point, formed between a precursor “faster” compressive elastic wave reflected as a tensile wave by the edges of the plate and a following “slower” compressive plastic wave. The distance at which interference between the two waves will take place and reach such an amplitude that the true fracture strength of the material at high strain rate is exceeded, depends on the mass and velocity of the fired round as well as the mass, Young’s modulus and the density of the plate.

The relation between stress wave propagation and fracture has been studied for more than a hundred years. B Hopkinson [quoted in 5], in his published paper on “ The Effects of Momentary Stresses in Metals” where he repeated his father’s work, provided an explanation of the rather puzzling phenomenon of spalling or scabbing. It is characteristic of the impact of high-speed projectiles or the detonation of explosive charges in contact with brittle targets. In this phenomenon, which takes place when an impact occurs on one side of a brittle plate, most of the fractures are observed not near the point of impact, but at the opposite free surface of the plate away from the impact region. J. Hopkinson [quoted in 5] in his paper on “ On the Rupture of Iron Wire by blow” had showed that the following surprising results occurred:

- “The effects of two blows, which will break the wire, were not equal when the momentum or the energies were equal, but when the velocity of the mass at impact reached a certain critical value”;
- In his experimental conditions the wire did not break near to the point at which the impact took place but fractured further away.

In this Section the explanation that J. Hopkinson gave in the case of the drop weight impact test, was adapted to the case of a ballistic impact on a steel plate as follows:

1. The tensile stress σ_0 associated with a particle velocity $\overline{V}_0$ is $\rho \overline{V}_0 c_0$, where ρ is the density of the wire. c_0 is the velocity of extension waves in the wire;
2. $c_0 = (E/\rho)^{1/2}$ where E is Young's modulus;
3. The maximum particle velocity $\overline{V}_0$ is equal to the velocity of the fired round and plate system immediately after impact;
4. Then, if the impact is inelastic, $\overline{V}_0 = [2ghM/(M+m)]^{1/2}$, where M is the mass of the fired round and m is the mass of the plate;
5. The falling height h is converted in to the round's velocity V as follows: $h \approx V^2/2g$.
6. Then $\overline{V}_0 = [V^2 M/(M+m)]^{1/2}$;
7. The tensile stress associated with the velocity $\overline{V}_0$ is $\sigma_0 = \rho c_0 V[M/(M+m)]^{1/2}$;
8. The peak stress in the pulse is dependent on V, M and m. The tensile stress after superposition between the reflected pulse and the incident one is $2\sigma_0 = 2\rho c_0 V[M/(M+m)]^{1/2}$;
9. If the tensile strength of the plate is σ, the condition for fracture near the clamping support of the plate is $\sigma = 2\sigma_0$

$$V_F = \frac{\sigma}{2\rho c_0 [M/(M+m)]^{1/2}} \qquad (5.2)$$

where V_f is the minimum velocity of the round at which fracture will occur. The condition for fracture to occur near the top of the plate is $\sigma = \sigma_0$ or:

$$V_F = \frac{\sigma}{\rho c_0 [M/(M+m)]^{1/2}} \qquad (5.3)$$

Taylor [5] has pointed out that the situation is in fact much more complicated than J. Hopkinson had realized, since the pulse produced by the impact has an infinitely long "tail".

The model considered by Taylor can be adapted to the case of ballistic impact as follows:

1. The equation of motion of the fired round and the plate after impact is $M\,dV/dt = A\sigma = A\rho V c_0$, where A is the cross sectional area of the plate and V is the velocity of plate and round at time t. The solution of this equation is:

$$V = \overline{V}_0 \exp[-\rho A c_0 t / M] \qquad (5.4)$$

where $\overline{V}_0$ is the combined velocity at time t=0;

2. Thus, the stress at the clamp holding the plate is given by $\sigma = \rho c_0 V = \rho c_0 \overline{V}_0 \exp(-\rho A c_0 t/M)$ and a sharp-fronted pulse with an exponential decay travels through the plate;

3. The stress at a distance x from the clamp is given by:

$$\sigma(x,t) = \rho c_0 \overline{V}_0 \exp[\rho A/M(x - c_0 t)] \qquad (5.5)$$

4. Equation (5.5) can also be written as:

$$\sigma(x,t) = \rho c_0 \overline{V}_0 \exp[\beta(x - c_0 t)] \qquad (5.5(a))$$

5. These conditions apply for times up to $t = L/c_0$, where L is the distance between the impact point and the point where the wave front reaches the clamping support and the pulse is reflected. Since the plate support is fixed the reflected pulse is one of tension and in the time region $L/c_0 < t < 2L/c_0$ for $0 < x < (2L - c_0 t)$, one has only the tail of the incident pulse, i.e. $\sigma(x,t) = \rho c_0 \overline{V}_0 \exp[\beta(x - c_0 t)]$;
6. For $x > (2L - c_0 t)$, one has the superposition of the reflected tensile pulse and the tail of the incident pulse, i.e.:

$$\sigma = \rho c_0 \overline{V}_0 \{\exp \beta[(2L - x) - c_0 t] + \exp \beta(x - c_0 t)\}. \qquad (5.6)$$

7. Now, the reflected pulse will once again be reflected at the plate support but since the mass is finite, this reflection will result in a change in the velocity of the plate and the round's mass M and after this reflection, there will be three superimposed waves in the plate;
8. The process will continue and can result in stresses greater than the stress of $2\rho \overline{V}_0 c_0$ postulated by J. Hopkinson. The degree to which this value is exceeded depends on a nondimensional parameter α, which is the ratio $M/(L\rho A)$, i.e. the ratio of the mass of the fired round to the mass of the plate. Taylor has shown that this maximum stress is given approximately by the expression:

$$\overline{\sigma} = \rho c_0 \overline{V}_0 \left[1 + \alpha^{-1/2}\right] \qquad (5.7)$$

Thus Taylor predicts $\overline{\sigma} = 4.2\rho c_0 \overline{V}_0$ rather than $\overline{\sigma} = 2\rho c_0 \overline{V}_0$ as postulated by J. Hopkinson and this occurs later than at the third reflection at the plate support. Hammond and Proud [16] recently reported stress values as high as 28 GPa, or a multiplying factor of 12 instead of 4.2 as in the above relation of the maximum tensile stress being reached during a ballistic impact in a 12 mm thick steel plate. The common idea in all of these estimates is that the steel can resist higher tensile stresses dynamically than statically, a conclusion that is supported by the usual strain rate dependence of the flow stress of most metals.

It is possible to design an armoured structure in such a manner that the transmissibility between the plates and the structure-support is higher to allow a controlled fraction of the incident energy to flow into the structure, thereby reducing the amount of energy reflected into the plate. But this solution should be carefully examined in order not to destroy the integrity of the support-structure and its reliability. Another solution may be the lengthening of the transmissibility path such that the elastic as well as the plastic waves are attenuated in such a way that their interference does not induce stresses higher than the true fracture stress of the armour steel during ballistic impact.

The stress distribution within the plate as a function of the time and the distance from the plate-support is presented in Figure 5.7. For this calculation the average mass of the plates is estimated at 4.5kg, the density of the steel is 7800kg/m^3, the mass of the round is 3.5g and the striking velocity is 940m/s. The results of the calculation are presented in Table (5.4).

Table (5.4): Predicted theoretical characteristics of the plate – round system during the ballistic impact, using the model proposed by Taylor [5].

Characteristics				
Velocity of the pressure wave front c_0 [m/s]	**Velocity of the system plate-round V_0 [m/s]**	**Predicted yield strength σ_0 [MPa]**	**Spalling strength S_0 [MPa]**	**Dynamic tensile strength $\sigma_{\max}$ [GPa]**
5063	27.1	1071	1070	38

This model predicts the uniaxial tensile strength to be at about 1071 MPa and the true fracture stress due to dynamic impact loading, at about 38 GPa for these armour steels. The difference between the measured maximum stress reported by Hammond and Proud [16] and others [17, 18] with the predicted value of 38 GPa, may be explained by the neglect of the influence of any existing defects present in the material in the theoretical model. Any such defects will reduce the effective dynamic fracture strength of the steel armour plates according to the well-known principles of elastic fracture mechanics. The analysis of Equation (5.6) shows that the stress distribution throughout the plate is strongly dependent on the time of stress wave travel. The stress distribution in the region between one and two hundred centimetres wave path length from the centre of impact is shown in Figure 5.7. The model predicts a tensile stress of between 11.7 GPa and 13.2 GPa in that region in which the fracture lines are located. This means that the fracture occurs between the fourth and the fifth reflections of the tensile wave from the edges of the plate.

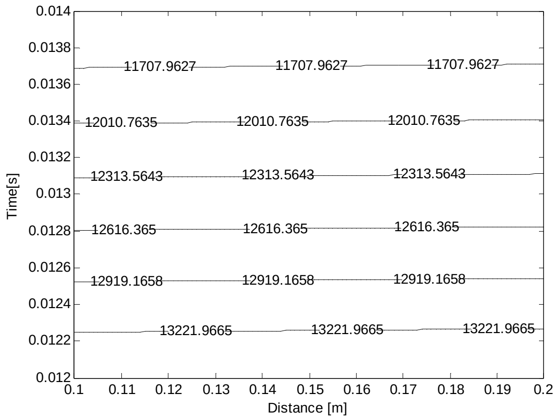

Figure 5.7: Predicted tensile stress distribution within the plates tested in this study due to the ballistic impact, as a function of the time and wave path length measured from the impact point and considering reflection at the top end on Figure 5.6.

5.3. The fracture mechanism due to the high strain rate during ballistic testing of plates of steels P through to W

The shear lips of the fractured surfaces of the untempered steels U and V plates were analysed by secondary electron scanning to identify the mechanism of the crack initiation and its propagation. Two directions of propagation of the cracks were observed throughout the fractured sections. The first three–dimensional crack propagated in a cylindrical surface whose generator lies parallel to the surface of the plate. The second crack propagated in a direction transverse to the surface of the plate and this crack determined the fractured surface. Figure 5.8 shows these three-dimensional cracks near the edges of the untempered steel U plates.

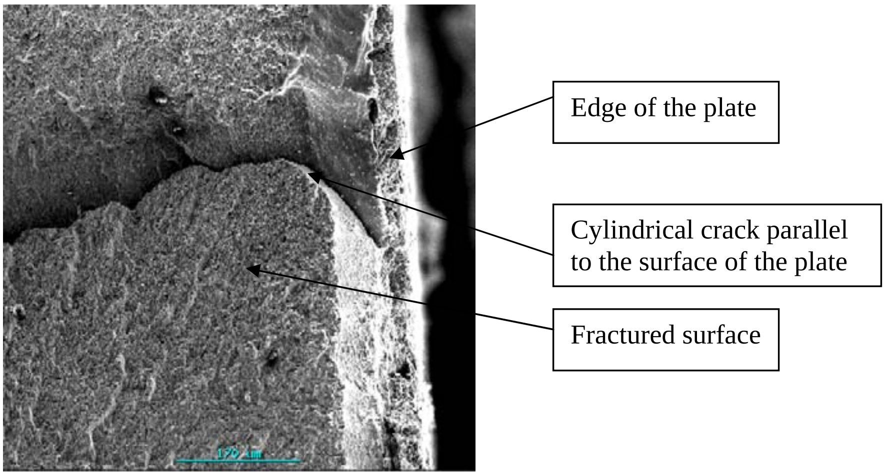

Figure 5.8: Secondary electron scanning microscopy of the shear lips of the fractured surface near the edge of the untempered plate of steel U. Label mark 170µm.

The scanning electron microscopy also revealed shear bands that cross the fractured surfaces of the untempered plates. These bands suggest that the ballistic impact induces cyclic loading in the plates due to the multiple reflections of the tensile stress wave from the edges of the plates. The shapes of the shear bands indicate that the fracture further away from the impact region, initiates near the edge of the plate and propagates cyclically throughout the thickness resulting in complete fracture. Such shear bands are shown in Figure 5.9. The initiation of these cracks near the edge of the plate verifies the earlier proposal of a reflection of the compressive wave as a high stress tensile wave from the edges as proposed by Taylor. The cracks were probably initiated just after the first or the second reflection of the tensile wave from the edge because of the poor mechanical behaviour of the untempered martensite under tensile stress in these plates.

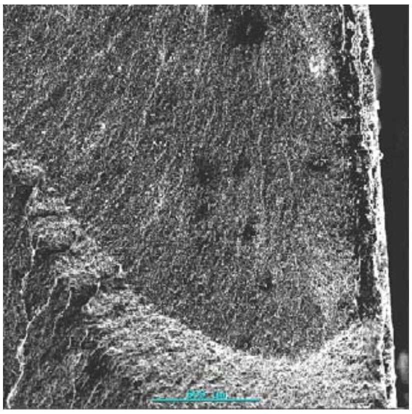

Figure 5.9: Secondary electron scanning microscopy showing the shear bands in the fractured surface of the untempered steel U plate at 12cm far from the impact point. Label mark 500µm.

The shear bands have two different appearances depending on the distance from the initiation point. Near the edge of the plate the shear lips of the broken plate are smooth with very fine dimples as shown in Figure 5.10(a), while a brittle inter-granular fracture of Figure 5.10(b), with blocks of grains being pulled out was observed at about one millimetre depth into the plate, as shown in Figure 5.10(c).

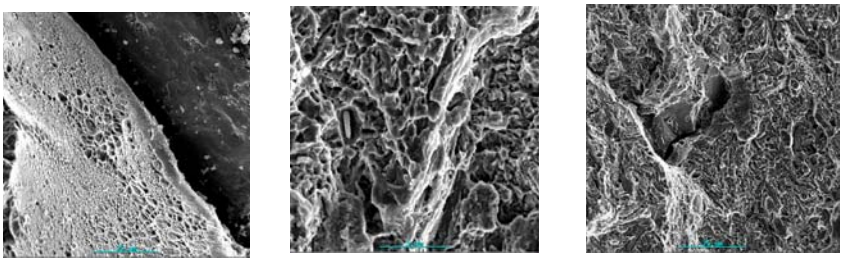

(a) (b) (c)

Figure 5.10: Secondary electron scanning microscopy of the shear lips showing two different modes of fracture in the same fractured surface (a) smooth shear lips with fine dimples observed near the edges of the fractured surface. (b) and (c) brittle fracture away from the edges where unstable propagation of the crack took place. Label mark 2.8µm.

From Figures 5.10(b) and (c) it appears that the grain boundaries may be a low resistance path for the propagation of the tensile stress wave caused by the ballistic impact through the entire thickness of the armour plate.

The ballistic impact excites the natural vibration modes of the plates. The first natural frequency of the armour plate should then be kept higher than the highest excitation frequency of the firing rifle to avoid any synchronisation that will lead to a catastrophic spalling of the plates. The mass, stiffness, damping factors and shape are the main parameters that determine the natural resonant frequencies of the plates. The mass and the length of the plate can easily be controlled and reduced through design so that the first natural frequency is high. The reduction of the mass is possible by manufacturing thinner and smaller plates, as was the entire aim of this study.

The stiffness and the damping factors of the plate depend on the microstructure that is inherited from the chemical composition and the heat treatment applied to the armour plate.
Considering that the microstructure is optimised for the ballistic performance, only the mass and the shape of the plates may practically be changed to take into account the effect of the excitation frequency of the firing rifle.

5.4. Morphology of the martensite and microstructures of the steels P through to W that were tested ballistically

The microstructures of the above mentioned armour steels were analysed before and after the ballistic test to identify any differences between them for the purpose of finding a direct relationship between the microstructure and its ballistic performance. The effect of the strength of the armour plate on the perforation of the plates using different projectile nose shapes has been investigated recently by Dey and Borvik [15]. They found that when a blunt projectile hits the target, the material in front of the projectile accelerates, while the rest of the target is relatively stationary. Hence, the deformation localises in narrow shear bands under adiabatic conditions where the shear strain, shear strain rate and temperature may locally be very high. According to their study [15], these shear bands may either consist of only *deformed* material or *transformed* material depending on the temperature that was reached in this localised area.

Mescheryakov and Divakov [17] have concluded from their investigation into the shock-induced structural transitions and dynamic strength of solids, following from the analysis of peculiarities of high-velocity penetration and also from the analysis of experimental data, that the strength-component of the resistance of solids to penetration (as a complementary factor to the inertial forces) is determined by the resistance to plastic deformation. This means that if the character of the plastic deformation changes, for example, because of a change in the structural mechanism of deformation, the strength-component of the resistance to penetration changes as well. Recent studies based on the measurement of the mechanical properties of armour steels, confirm the need for the understanding of the ballistic performance of these armour plates based on their microstructural behaviour. Hammond and Proud [16], in their work on the pressure-induced ($\alpha - \varepsilon$) phase transformation in low-alloy steels, where they have measured and compared the ballistic performance of lower and upper bainite respectively in terms of the Hugoniot Elastic Limits and spalling strength of these two phases, have concluded:

“ In order to understand why the materials behaved as they did and possibly to predict material properties in the future, it is important to investigate the microstructural response to the different impact conditions. This could take the form of microscopy, X-ray diffraction and hardness testing. Such research may help to establish why the phase transition was not observed in upper bainite and why the Hugoniot Elastic Limits of the two materials are so different”.

They have found the HELs to be 3.5 ± 0.5 GPa and 2 ± 0.5 GPa for the lower and higher bainite respectively. The lower-bainite was found to have a phase transition at 13 ± 0.5 GPa.

The eight plates from Table (5.3) were sectioned after the ballistic tests for different analyses and micro-hardness measurements. X-ray diffraction analysis was done in the cross section of the impact-affected zones (Figure 5.4) to determine the volume fraction of the retained austenite after the ballistic impact.

Table (5.5): Volume fraction of the austenite in the impact-affected regions before and after ballistic testing

	Thickness of the plate [mm]	**Volume fraction of retained austenite before testing [%]**	**Volume fraction of retained austenite after ballistic testing [%]**
Steel P	4.7	6	<0.5
Steel Q	4.9	4	<0.5
Steel R	5.1	2	<0.5
Steel S	5.2	3	<0.5
Steel T	5.4	0.6	<0.5
Steel U	5.1	2	<0.5
Steel V	5.1	5.3	<0.5
Steel W	4.8	6	<0.5

The volume fraction of the retained austenite in the impact-affected regions are systematically lower after the ballistic testing than before, indicating a transformation process.

The Vickers micro-hardness profiles of the same cross-sections of steels P, Q R, T and W were compared to appreciate the significance of the work hardening of the armour steel plate in resisting ballistic perforation. The plates of the steels P, Q, R, T and W were selected on the basis of their initial volume fraction of retained austenite, their plate thickness and the ballistic behaviour. The comparison was then possible firstly, between the armour plates that all had passed the ballistic test and secondly, between those that passed the tests and the plate of steel T that had failed the test. Three lines of measurement were drawn on each cross section of the impact-affected zones. The first line was drawn at one mm depth from the incidence surface and the second one at 2.5 mm and the third one at 4.5 mm depth. The Vickers micro-hardness was measured along each line with the reference zero point for the measurement along a line intersecting the line and the incidence direction of the fired round which is also the longitudinal axis of the deformed volume, shown by the arrow in the figure below.

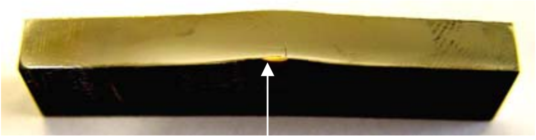

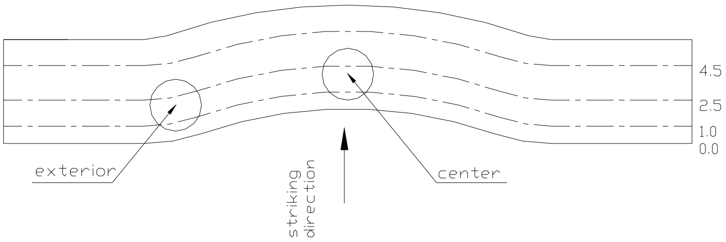

Figure 5.11: Illustration of the principle for the drawing of the iso-depth lines along which the micro-hardness was measured and the positions from where 3mm discs were cut for thin foil TEM. The arrow shows the incidence direction of the fired round.

The measured Vickers micro-hardnesses are given in Table 5.6:

Table (5.6): Vickers micro-hardness throughout the cross section of the deformed zones after the ballistic testing

	Vickers micro-hardness											
Depth from the impacted surface	**Distance from the incidence direction of the fired round[mm]**											
Steel P (4.7mm)	**1**	**2**	**3**	**5**	**7.5**	**10**	**12.5**	**15**	**17.5**	**20**	**25**	
1 mm	639	648	671	671	680	622	622	639	622	622	606	
2.5 mm	594	626	666	652	685	639	626	639	620	606	594	
4.5 mm	710	710	746	705	639	644	644	644	626	622	598	
Steel Q (4.9mm)	**1**	**2**	**3**	**5**	**7.5**	**10**	**12.5**	**15**	**17.5**	**20**	**25**	
1 mm	551	564	568	575	575	579	537	537	537	537	537	
2.5 mm	564	550	564	598	554	543	537	537	530	530	530	
4.5 mm	602	602	602	602	602	561	564	537	530	530	530	
Steel R (5.1mm)	**1**	**2**	**3**	**5**	**7.5**	**10**	**12.5**	**15**	**17.5**	**20**	**25**	
1 mm	496	575	583	590	583	579	571	598	588	583	598	
2.5 mm	626	652	661	631	648	639	598	594	618	598	598	
4.5 mm	661	635	635	690	652	639	639	610	602	586	598	
Steel W (4.8mm))	**1**	**2**	**3**	**5**	**7.5**	**10**	**12.5**	**15**	**17.5**	**20**	**25**	**30**
1 mm	657	666	671	666	657	671	661	666	639	644	614	622
2.5 mm	661	622	648	657	666	648	648	648	648	639	639	626
4.5 mm	661	685	675	675	675	635	630	631	606	614	614	614
Steel T (5.4mm)				**5**	**7.5**	**10**	**12.5**	**15**	**17.5**	**20**	**25**	
1 mm				614	505	481	446	427	422	422	422	
2.5 mm				602	564	523	523	517	517	515	511	
4.5 mm				511	514	499	505	508	505	508	508	

The hardness measurements start at approximately 6 millimetres from the axis of the perforation hole for the plate of the steel T that failed the test. These hardnesses are compared in Figure 5.12.

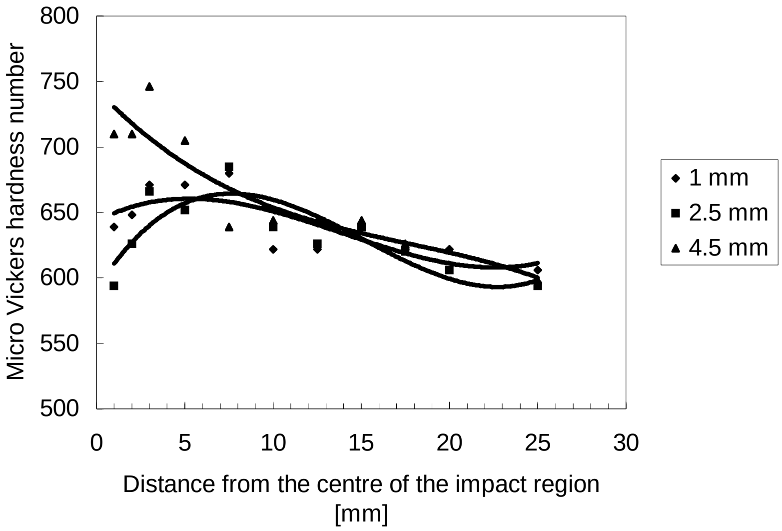

Figure 5.12(a): Vickers micro-hardness profiles throughout the cross section of the deformed zone of the plate of steel P

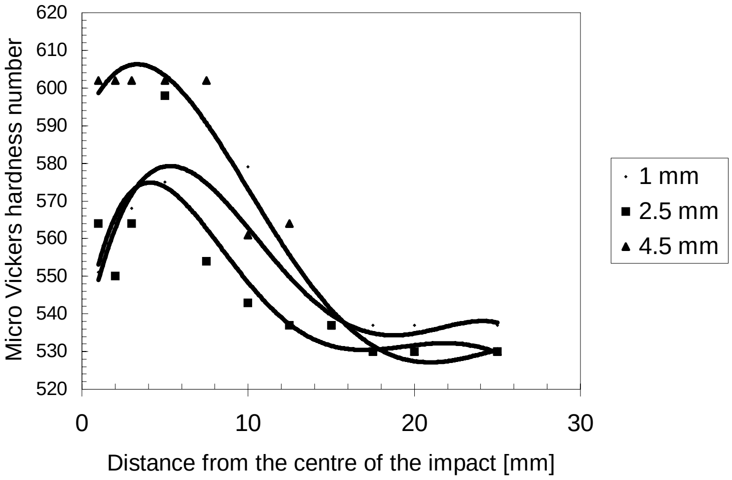

Figure 5.12(b): Vickers micro-hardness profiles throughout the cross section of the deformed zone of the plate of steel Q

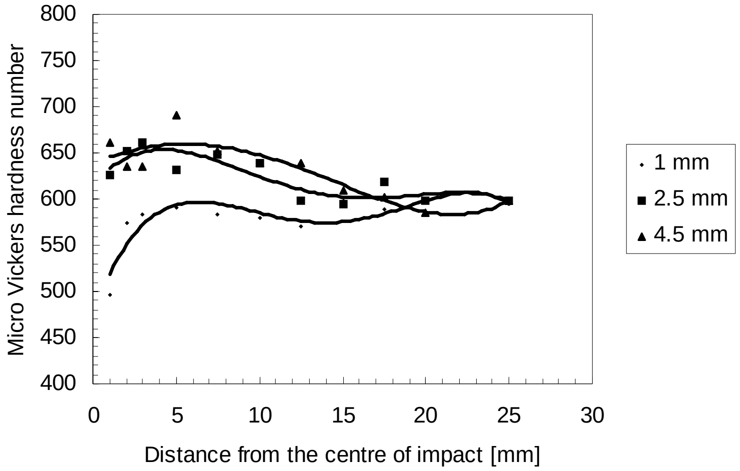

Figure 5.12(c): Vickers micro-hardness profiles throughout the cross section of the deformed zone of the plate of steel R

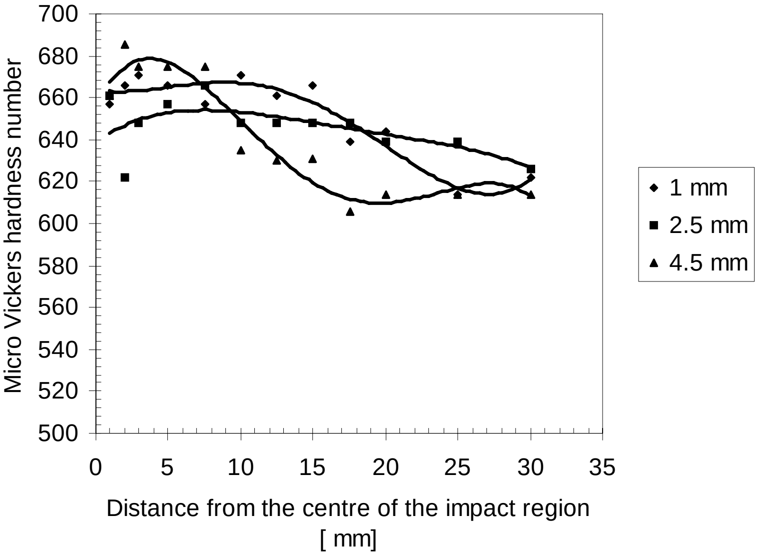

Figure 5.12 (d): Vickers micro-hardness profiles throughout the cross section of the deformed zone of the plate of steel W

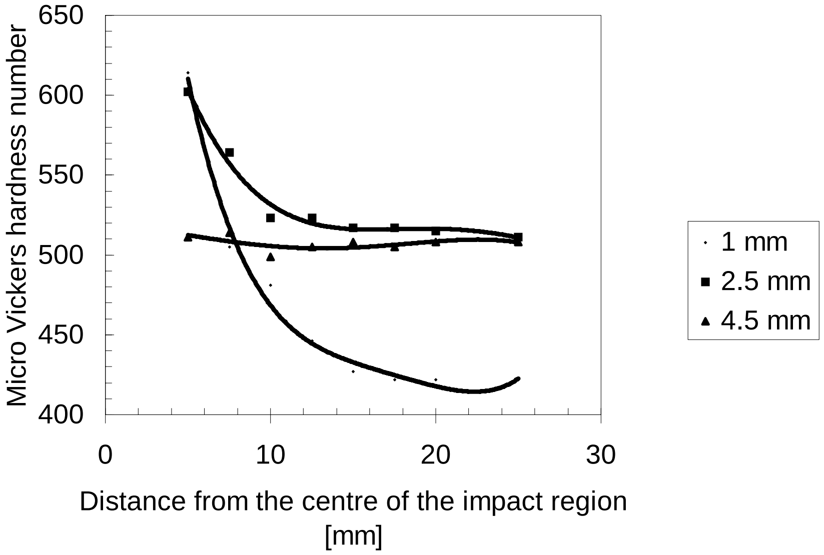

Figure 5.12(e): Vickers micro-hardness profiles throughout the cross section of the deformed zone of the plate of steel T that had failed the test

The following observations can be made:

(i) For the plates that withstood the fired round, the hardnesses near the incidence direction, i.e. in zone 1, are higher for the iso-depth lines situated at 4.5 mm from the incidence surface than for the iso-depth lines situated at 1 and 2.5 mm . For the latter two iso-depth lines the hardness curves have a maximum at about 10 mm from the incidence direction of the fired round while the hardnesses within zone 1 are lower. The Vickers micro-hardness on the iso-depth-lines at 4.5 mm increased by about 100 units for the steels P, Q and W that had a higher volume fraction of retained austenite before the ballistic testing than steel R with only 2% retained austenite and whose hardness increased only by about 50 units.

(ii) The plate of steel R with 2% retained austenite, showed a decrease in hardness along the 1 mm iso-depth line compared to the hardness at 25 mm further away from the impact incidence direction. This is opposite to the tendency in the plates of steels P, Q and W with higher volume fractions of retained austenite.

(iii) The plate of steel T that had failed the test had a higher hardness around the perforation hole for the iso-depth lines at 1 and 2.5 mm and a lower hardness for the iso-depth line at 4.5 mm. This is again opposite to the observation in the non-perforated plates of steels P, Q, R and W. Moreover steel T had softened during the ballistic impact.

Thin foils cut by spark erosion from the same zones were analysed in transmission electron microscopy to examine the differences between these steels and the variation in their hardnesses in the cross section of the same steel.

Three areas were selected on each cross section for the cutting of the thin foils, i.e. the centre of the impacted region (center in Figure 5.11), the circumference of the deformed zone (exterior in Figure 5.11) and the non-deformed area. The bright field and dark field images of these areas are compared below:

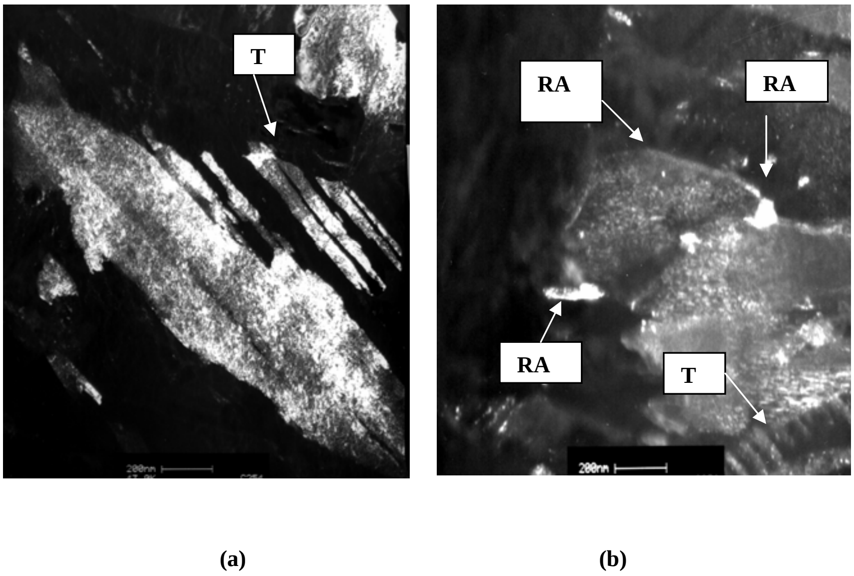

(a) **(b)**

Figure 5.13: Dark field transmission electron microscopy showing the twinned martensite with retained austenite in steel P before the ballistic test.

Two types of shape of the retained austenite were observed in the dark field image in Figure 5.13(b), i.e. a nodular type and an interplate film type along the plate interfaces.

The microstructure of steel Q was close to that of steel P, consisting of twinned martensite with retained austenite along the plate interfaces.

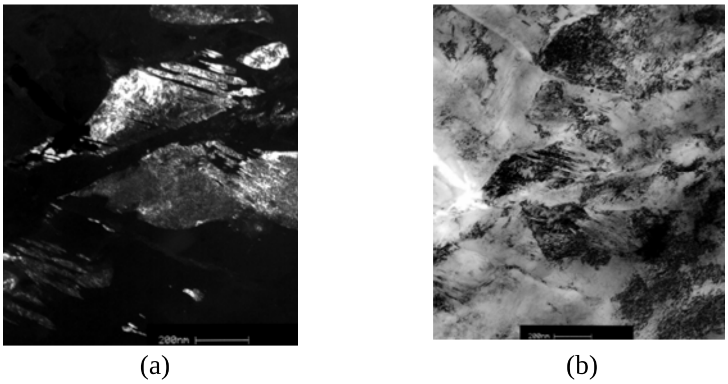

(a) (b)

Figure 5.14: Transmission electron microscopy of steel Q, (a) dark field image and (b) corresponding bright field image of the twinned martensite.

The thin foil images of transmission electron microscopy from the centre of the impact and from the circumference of the deformed region are compared below. At the centre of the impact "new" martensite was formed. Fine carbides were precipitated within the martensite matrix and no twins were observable.

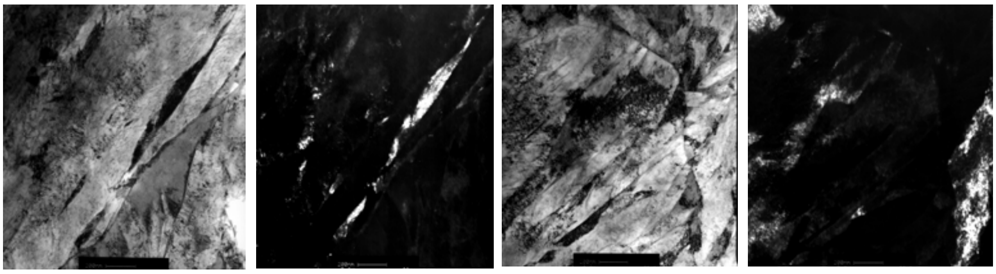

(a) **(b)** **(c)** **(d)**

Figure 5.15: Transmission electron microscopy of the centre of impact of steel Q; (a) and (c) bright field images, (b) and (e) respective corresponding dark field images showing no twins and neither retained austenite after ballistic test. Label mark 200 nm.

The absence of twinned martensite in the "new martensite" could arise from incomplete solution of carbide, diluting the austenite and raising the Ms temperature.
Because reaustenitisation occurs transiently in the impact zone the properties of austenite will be important in energy absorption and ballistic resistance. The kinetics of reaustenitisation will also be composition dependent.

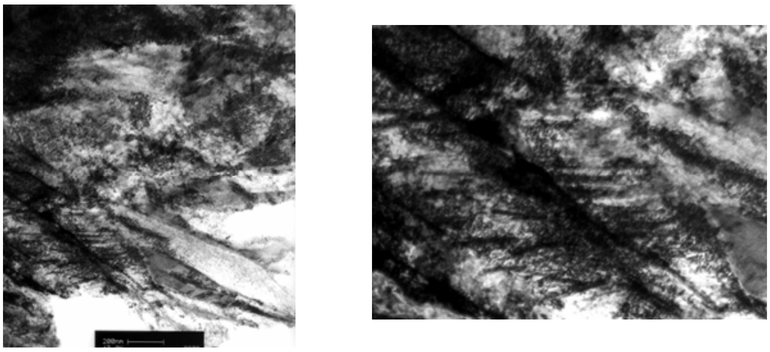

(a) **(b)**

Figure 5.16: (a) and (b) Thin foil dark field images of the circumference of the deformed region showing twinned martensite with dislocation pile-ups at twin interfaces in steel Q. Label mark 200 nm.

At 25mm away from the incidence direction the morphology was a twinned martensite with a large number of dislocations piled up at the twin interfaces. It appears that the twin interfaces are acting as dislocation barriers. This area has a higher Vickers micro-hardness than the centre of the impact area and also higher than the plate before the ballistic test.

The plate of steel R containing 2% retained austenite consisted of twinned martensite as well. At 2% the retained austenite is not easily observable in the dark field thin foil transmission electron microscopy images.

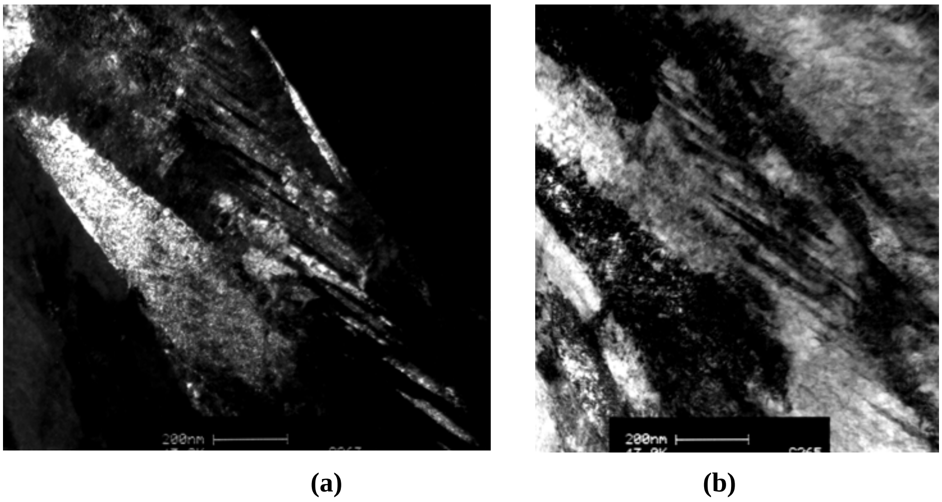

Figure 5.17: (a) Thin foil dark field image and (b) corresponding bright field image of steel R before the ballistic test.

The bright field and dark field images of the centre of the impact area revealed untwinned martensite and the massive formation of fine carbides within the martensite plates and on the plate inter-faces despite its 1.03%Si content which should delay such a transformation.

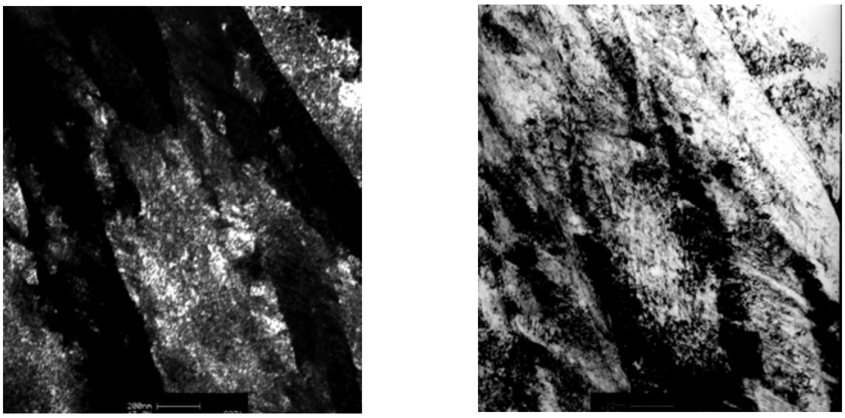

Figure 5.18: Thin foil transmission electron microscopy; (a) dark field and (b) the corresponding bright field image showing the disappearance of the twins and the formation of large aggregates of fine carbides throughout the martensite matrix at the centre of the ballistic impact area on the plate of steel R. Label mark 200 nm.

This formation of carbides may explain the decrease in the micro-hardness observed upon ballistic impact along the iso-depth line at one mm in Figure 5.12(c).

The plate of steel W contains 6% volume fraction of retained austenite and the nodules of retained austenite are located on the plate interfaces.

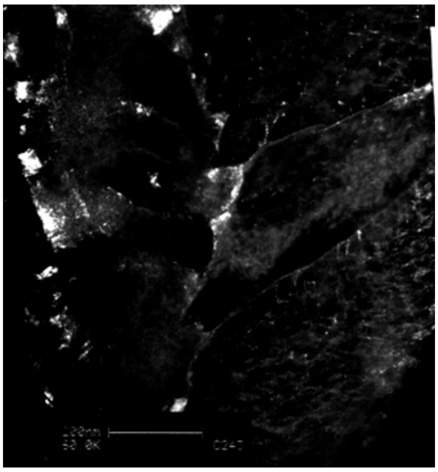

Figure 5.19: Dark field image thin foil transmission electron microscopy of steel W (0.98wt% Si) before the ballistic test. Label mark 200 nm.

Fine carbide particles have precipitated throughout the martensite plates upon tempering at 250°C for 15 minutes before the ballistic test.

Figure 5.20: Thin foil TEM bright field image showing the precipitation of fine carbides in the matrix before the ballistic test of steel W tempered at 250°C for 15 minutes. Label mark 200 nm.

The plate of steel T (the failed one) had the lowest volume fraction of retained austenite of about 0.6%, which is almost equal to the absolute error of detection by the X-ray diffraction equipment used. However, the thin foil transmission electron microscopy revealed elongated films of retained austenite along the lath interfaces. The measured martensite start temperature of steel T was 184°C, which is comparable to those of the other seven steels successfully tested in this second series of ballistic testing. Nevertheless, it is still the highest M_s temperature in this series of steels. The morphology of the martensite before the ballistic testing was coarse laths with coarse cementite.

The cementite may have formed due to auto-tempering during the quenching and then coarsened upon tempering at 180°C. The low Silicon content of 0.4%Si was apparently not enough in this case to delay the formation of coarser cementite. The carbide particles around the perforation hole have coarsened further upon ballistic impact.

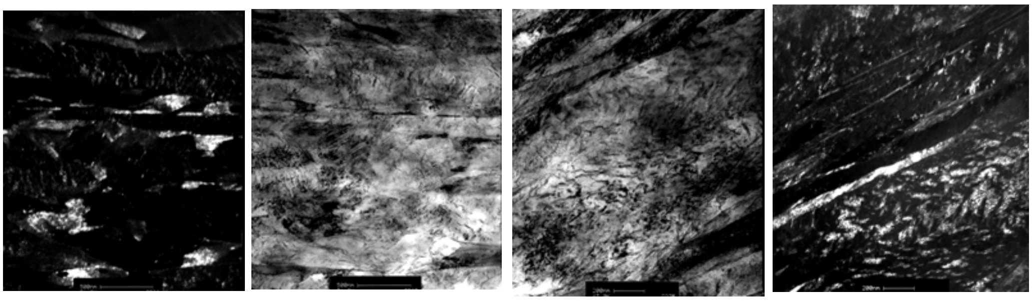

(a) (b) (c) (d)

Figure 5.21: Thin foil transmission electron microscopy of steel T; (a) and (b) dark field and corresponding bright field images before the ballistic test and (c) bright field image and (d) corresponding dark field image after the ballistic test, showing the coarsened carbide particles and the films of retained austenite. Label mark 500 nm.

5.5. General observation

The microstructure of the armour steel has a definite effect on its ballistic performance for plates with a thickness smaller than 6 mm and it is clear that there is a direct relationship between the microstructure and the ballistic performance of martensitic steel armour plates. The ballistic parameter BP, which takes into account the thickness of the plate and the volume fraction of retained austenite contained in the martensitic steel, may be used for predicting the ballistic performance and the following conclusions can be made at this stage.

(i) High ballistic performance may be achieved by combining twinned martensite with retained austenite in the same microstructure;
(ii) Coarse carbide particles are detrimental to the ballistic performance of the armour steels;
(iii) Stress-induced transformations occur inside the shock-affected region upon ballistic impact; and
(iv) The microstructure at the centre of the impact region does not contain any of the initial twins after impact.

The de-twinning process may be explained as follows: Part of the kinetic energy of the fired round is transformed into heat by entropy trapping, which raises the temperature high enough for the twinned martensite to recrystallise and re-austenitise. The new austenite is then quenched by the surrounding material and transforms into new untwinned martensite. This means that there is no memory effect present between the initial state with twinned martensite and the final state without twins. This transformation extends to a large volume around the impact region depending on the amount of retained austenite present in the plate. The kinetic energy of the fired round is then used to:

- heat up the surrounding material and induce the phase transformations; and
- mechanically deform the affected region.

The third part of the energy is transferred to the plate's support structure.

The phase changes during the ballistic impact should be considered in predicting the ballistic performance of a martensitic steel, as the fraction of the kinetic energy consumed by the phase transformation may be very important by resulting in a reduction of the effective energy available for the perforation stage.

The susceptibility of the retained austenite to stress-induced transformation appears to depend on its shape and location within the martensite. The nodular austenite, found when the volume fraction is higher than 2%, gave a stronger TRIP effect than the inter-lath films. This may be due to differences in the mechanical stability upon high strain rate impact of the two types of retained austenite.

Thin foil TEM of the experimental armour steels considered in this study revealed a change of the morphology of the retained austenite from film to nodular when its volume fraction increases. The ballistic performance of the experimental martensitic armour steels also increased as the volume fraction of retained austenite increased in the range from 1% to 6% although an upper limit has not been found within this range.

At too high volume fraction of retained austenite, adverse effects may occur following an excessive softening of the armour plates and the resistance to ballistic perforation. Further studies are needed on a possible upper limit of retained austenite content and to find an explanation on the mechanism by which retained austenite is transformed under impact, or whether a stress-induced or a strain-induced transformation occurs. Furthermore, investigations as to the location, the shape of the retained austenite and their mechanical and thermal susceptibilities will be useful in predicting and simulating the ballistic performance of martensitic armour steels containing some volume fraction of retained austenite.

CHAPTER 6. CHARACTERISATION OF THE MARTENSITIC TRANSFORMATION IN ARMOUR STEELS

6.1. Background

6.1.1 Theories of the martensitic transformation

A number of crystallographic and thermodynamic theories of the martensite transformation and the subsequent modifications to these theories have been briefly presented in Chapter 2. The Phenomenological crystallographic Theories of the Martensitic Transformations (PTMT) are concerned with the relationships that exist between the Bain strain, the invariant shape strain, the rotation and shear processes that comprise the so-called inhomogeneous or complementary strain. The original phenomenological approaches of Wechsler, Lieberman and Read (WLR) [102] and Bowles and Mackenzie (BM) [103] are equivalent. The first theory of WLR derived the shape strain as the result of the rotation R, the Bain distortion B and an inhomogeneous shear. The second theory of BM derived the total strain S which describes the homogeneous lattice strain occurring over a range of a few unit cells as the result of the shape strain and a complementary shear. Bowles and Mackenzie proposed that the complementary shear strain was part of a twinning shear in the martensite. This hypothesis implies that oppositely directed complementary shears could possibly produce twin orientations within a martensite plate, and it is well known that the plates produced in many martensitic transformations are twinned on a very fine scale. The Bowles and Mackenzie model predicts the crystallographic features such as the habit plane, the strain and the orientation relationships between the parent austenite and the product martensite.

The Phenomenological crystallographic Theories of the Martensitic Transformations have been successfully applied to many alloy systems, but as shown by Christian [45], in steels it can only be applied mainly to $\{2 \quad 5 \quad 9\}$ and $\{3 \quad 10 \quad 15\}$-type martensite plates; $\{2 \quad 2 \quad 5\}$ martensite plates and lath martensites have been proven difficult to fit to the theory. The concept of the displacement vector of the lattice deformation was then advanced by Gu et al [71]. They considered two ways to reduce the strain energy, i.e. the self-accommodation between different martensitic variants and plastic accommodation between the parent phase and martensite to explain the formation of $\{5 \quad 7 \quad 5\}$ martensite. Kelly [59] recently demonstrated that, when applied in a rigorous fashion, the Infinitesimal Deformation (ID) approach is exactly equivalent to the Phenomenological crystallographic Theory of the Martensitic Transformation (PTMT). The PTMT assumes the invariability of the habit plane. On the other side many researchers such as Christian [45], Kennon and Dunne [46], Tadaki and Shimizu [48], and Dunne and Kennon [49] have demonstrated that the flexibility of the habit plane is rather a characteristic of the martensite transformation than an exception.

In this study the PTMT model proposed by Bowles and Mackenzie was used for predicting the theoretical features of the martensite and their possible relation with the ballistic performance of the armour steels. The atom force microscopy is then used to find correspondences between the surface relief accompanying the martensitic transformation and the prediction by the Bowles and Mackenzie model of the PTMT. It can be accepted that an internally twinned martensite is mathematically equivalent to one that is internally slipped. That is, algebraically a predeformed austenite followed by the Bain deformation is equivalent to a martensite formed by the Bain mechanism followed by an inhomogeneous shear. When the martensite is not internally twinned, e.g. as in lath martensite, a single correspondence

relation and Bain deformation applies to an entire lath. In general, the reasons for a particular operative substructure (inhomogeneous shear) in a given material are rather obscure[69].
Zhang et al [98] have reported the results of many investigations made on the morphology transition from lenticular to butterfly to lath martensites. Variables reported to influence the martensite morphology include: transformation temperature, quench rate above M_s, chemical composition, dispersion of particles, thermodynamic driving force, austenite defect structure and stacking fault energy and the martensite and austenite strength. Davies and Magee [99] supposed that the morphology differences result from the different habit planes. The lattice invariant shear for the various martensite habit planes are as follows [99]:

$\{2 \quad 5 \quad 9\}$ - twinning in ferrite
$\{2 \quad 2 \quad 5\}$ - slip in austenite and twinning in ferrite
$\{1 \quad 1 \quad 1\}$ - slip in ferrite and austenite

These different habit planes usually correspond to lenticular, butterfly and lath martensites.

6.1.2. Tetragonality of martensite

The tetragonality of martensite in steels containing Carbon and Nitrogen is consistent with the correspondence implied by the Bain strain. Whereas in cubic ferrite the octahedral interstitial sites are occupied at random, in tetragonal martensite there must be a preferred occupancy of sites with only those octahedral sites along the martensite c-axes being filled, so producing the observed tetragonality. It was noticed in Chapter 2 that a significant redistribution of Carbon atoms and a disappearance of the tetragonality of a 5.1at.%C martensitic steel occurred at room temperature during aging times of less than 50 hours [66]. Carbon atoms segregated to lattice imperfections and also transferred from a/b-type octahedral interstices to c-type interstices, thereby decreasing the c_m parameter of the tetragonal martensite at room temperature.

Lyssak et al [67] have found that the tetragonality of the martensite in Manganese steels is abnormally small. Moreover, they have observed that there are several alloy systems in which the tetragonality of martensite containing Carbon, does not obey the well-known experimental equation:

$$c/a = 1 + 0.046\,p$$

where p is the mass percentage of Carbon in the steel. Kajiwara and Kikuchi [68] made a very extensive and systematic study of the martensite tetragonality in Fe-Ni-C alloys and found that the tetragonality is quite dependent on the mode of the lattice invariant deformation in the martensite.

Uehara et al. [69] have investigated the tetragonality of martensite in high Carbon- Iron alloys containing some Aluminium. From their study it appears that the tetragonality is enhanced by Aluminium and Nickel additions that prevent Carbon atoms from moving out of octahedral sites to tetrahedral sites during quenching (auto-tempering).

6.1.3. Techniques used in characterising the martensitic transformation

The features of the martensitic transformation may be determined by combining the determination of the phases present in the microstructure and their lattice parameters by the X-ray diffraction method, with the analysis of the morphologies, the spatial distribution and shapes of the phases determined by Transmission Electron Microscopy. Recently the introduction of Atomic Force Microscopy has brought in new possibilities of investigating the characteristics of the martensitic transformation by analysing the surface relief accompanying the transformation on a nanometric scale.

6.2. Characterisation methodology

(i) The inputs in the Bowles and Mackenzie model used in this study for the characterisation of the martensite are the lattice parameters of the martensite and of the retained austenite measured by X-ray diffraction at room temperature.
(ii) Complementary details on the martensite formation were determined by analysing the surface relief by Atomic Force Microscopy on a nanometric scale;
(iii) Scanning Electron Microscopy was used for analysis on a micrometric scale as complementary to the observation from the Atomic Force Microscopy; and
(iv) Transmission Electron Microscopy was used to determine the morphologies and the location of the phases that are present in the armour steels.

6.3. Characteristics of the martensite formation in the armour steels

6.3.1. Crystallographic characteristics

The volume fraction of the retained austenite and the lattice parameters of both the austenite and the martensite were determined by X-ray diffraction of the specimens austenitised at 900°C and quenched into water at room temperature. The martensite start temperatures were determined by dilatometric analysis. The crystallographic characteristics of the martensite formation were then calculated using the Bowles and Mackenzie model.

It was found from the XRD measurements of the lattice parameters that the martensite in these armour steels, is cubic with a_m approximately equal to c_m or, alternatively, it is possible that the tetragonality was so small that it could not be detected. Samples were double checked on two different XRD machines and were also stored at sub-zero temperatures between the quenching step and the XRD analysis to prevent significant Carbon movement. No tetragonality could be found. The measured lattice parameters and the calculated characteristics of the martensitic transformation in the nineteen armour steels are presented in Table (6.1).

The calculated magnitude of the complementary shear strain varies between 0.24 and 0.30 for these steels. The calculated misorientation from the Kurdjumov-Sachs orientation relationship is less than 1.2°. Nishiyama [36] estimated the limit of application of the calculated Kurdjumov-Sachs orientation relationship using the Bowles and Mackenzie model, to those cases where the calculated misorientation angle between the directions $\left[-1 \quad 0 \quad 1\right]_{\gamma}$ in the austenite and $\left[-1 \quad -1 \quad 1\right]_{m}$ in the martensite are smaller than 4°. According to this prediction the K-S orientation relationship may be applied to the martensite formation in these armour steels. Figure 6.1 illustrates the effect of the martensite start temperature on the scattering from the Kurdjumov-Sachs orientation relationship, on the complementary shear and on the magnitude of the displacement vector. It appears from this figure that the Kurdjumov-Sachs orientation relationship may be present in twinned as well as in lath martensitic armour steels.

Table (6.1). Lattice parameters and features of ferrous martensite in armour steels.

		Inputs								
Name of the armour steel	**Ms temperature [°C]**	a_γ **[nm]**	a_m **[nm]**	**Invariant line normal n**	**Complementary rotation Q**	**Total shape strain for the invariant line S**	**Invariant plane normal p1**	**Magnitude of the complementary shearm2**	**Shear angle [°]**	**Deviation from K-S [°]**
E	196	0.36448	0.2867291	0.4876 0.7243 0.4876	[1.0000 0 0 0 0.9876 -0.1073 0 0.1073 0.9876]	[1.0807 -0.0267 0.0973 0.0512 1.1188 0.0650 -0.1173 -0.1191 0.7667]	0.1984 0.6680 0.7172	0.28	8.19	0.94
F	255	0.36559	0.2863991	0.4769 0.7384 0.4769	[1.0000 0 0 0 0.9869 -0.1098 0 0.1098 0.9869]	[1.0751 -0.0266 0.0941 0.0496 1.1164 0.0659 -0.1109 -0.1194 0.7629]	0.1904 0.6511 0.7347	0.29	8.38	1.06
G	271	0.3683	0.2865805	0.4593 0.7604 0.4593	[1.0000 0 0 0 0.9858 -0.1138 0 0.1138 0.9858]	[1.0663 -0.0268 0.0889 0.0468 1.1122 0.0671 -0.1009 -0.1189 0.7570]	0.1780 0.6244 0.7605	0.30	8.68	1.27
H	210	0.36556	0.2862345	0.4756 0.7400 0.4756	[1.0000 0 0 0 0.9868 -0.1101 0 0.1101 0.9868]	[1.0744 -0.0266 0.0937 0.0494 1.1161 0.0660 -0.1101 -0.1194 0.7624]	0.1895 0.6491 0.7367	0.29	8.40	1.08
I	309	0.368300	0.286643	0.4598 0.7597 0.4598	[1.0000 0 0 0 0.9859 -0.1137 0 0.1137 0.9859]	[1.0666 -0.0268 0.0891 0.0469 1.1123 0.0671 -0.1012 -0.1190 0.7572]	0.1784 0.6253 0.7597	0.30	8.67	1.26
J	306	0.36652	0.2866597	0.4727 0.7438 0.4727	[1.0000 0 0 0 0.9866 -0.1108 0 0.1108 0.9866]	[1.0729 -0.0266 0.0929 0.0489 1.1154 0.0662 -0.1084 -0.1194 0.7614]	0.1874 0.6446 0.7412	0.29	8.45	1.11
K	318	0.36469	0.2864401	0.4835 0.7296 0.4835	[1.0000 0 0 0 0.9873 -0.1082 0 0.1082 0.9873]	[1.0786 -0.0266 0.0961 0.0506 1.1179 0.0654 -0.1148 -0.1193 0.7652]	0.1954 0.6616 0.7240	0.29	8.26	0.98
L	259	0.36475	0.286822	0.4865 0.7257 0.4865	[1.0000 0 0 0 0.9875 -0.1075 0 0.1075 0.9875]	[1.0802 -0.0267 0.0970 0.0510 1.1186 0.0651 -0.1166 -0.1191 0.7663]	0.1976 0.6663 0.7190	0.28	8.21	0.95
N	241	0.36468	0.2863646	0.4829 0.7304 0.4829	[1.0000 0 0 0 0.9873 -0.1084 0 0.1084 0.9873]	[1.0783 -0.0266 0.0959 0.0505 1.1178 0.0654 -0.1145 -0.1193 0.7650]	0.1949 0.6606 0.7250	0.29	8.27	0.99
O	218	0.36569	0.2863932	0.4761 0.7394 0.4761	[1.0000 0 0 0 0.9868 -0.1100 0 0.1100 0.9868]	[1.0747 -0.0266 0.0939 0.0495 1.1162 0.0660 -0.1104 -0.1194 0.7626]	0.1899 0.6499 0.7359	0.29	8.39	1.07
P	115	0.35837	0.285753	0.5211 0.6759 0.5211	[1.0000 0 0 0 0.9904 -0.0990 0 0.0990 0.9904]	[1.1002 -0.0293 0.1077 0.0551 1.1256 0.0618 -0.1392 -0.1146 0.7796]	0.2267 0.7252 0.6502	0.26	7.54	0.57
Q	178	0.35781	0.285086	0.5193 0.6788 0.5193	[1.0000 0 0 0 0.9902 -0.0995 0 0.0995 0.9902]	[1.0991 -0.0290 0.1071 0.0549 1.1252 0.0620 -0.1379 -0.1150 0.7788]	0.2249 0.7218 0.6546	0.26	7.58	0.59
R	170	0.36521	0.285806	0.4742 0.7418 0.4742	[1.0000 0 0 0 0.9867 -0.1104 0 0.1104 0.9867]	[1.0737 -0.0266 0.0933 0.0492 1.1158 0.0661 -0.1093 -0.1194 0.7620]	0.1885 0.6470 0.7388	0.29	8.43	1.09

S	182	0.35792	0.285704	0.5238 0.6718 0.5238	[1.0000 0 0 0 0.9906 -0.0984 0 0.0984 0.9906]	[1.1019 -0.0297 0.1085 0.0554 1.1261 0.0616 -0.1410 -0.1139 0.7807]	0.2292 0.7301 0.6438	0.26	7.49	0.55
T	184	0.36559	0.286066	0.4739 0.7422 0.4739	[1.0000 0 0 0 0.9867 -0.1105 0 0.1105 0.9867]	[1.0735 -0.0266 0.0932 0.0491 1.1157 0.0661 -0.1091 -0.1194 0.7619]	0.1882 0.6465 0.7394	0.29	8.4361	1.10
U	170	0.36486	0.286106	0.4794 0.7351 0.4794	[1.0000 0 0 0 0.9871 -0.1092 0 0.1092 0.9871]	[1.0764 -0.0266 0.0948 0.0500 1.1170 0.0657 -0.1123 -0.1194 0.7638]	0.1923 0.6550 0.7308	0.29	8.34	1.03
V	145	0.3578	0.2853	0.5212 0.6759 0.5212	[1.0000 0 0 0 0.9904 -0.0990 0 0.0990 0.9904]	[1.1002 -0.0293 0.1077 0.0551 1.1256 0.0618 -0.1392 -0.1146 0.7796]	0.2267 0.7252 0.6501	0.26	7.54	0.57
W	130	0.35819	0.285883	0.5235 0.6723 0.5235	[1.0000 0 0 0 0.9906 -0.0984 0 0.0984 0.9906]	[1.1017 -0.0297 0.1084 0.0553 1.1260 0.0616 -0.1408 -0.1140 0.7805]	0.2289 0.7295 0.6446	0.26	7.50	0.55

The higher martensite start temperatures led to larger angles between the directions $\left[-1 \quad 0 \quad 1\right]_\gamma$ and $\left[-1 \quad -1 \quad 1\right]_m$. For values of this angle larger than 4°, an intermediate orientation relationship between that of Kurdjumov-Sachs and Nishiyama-Wasserman may be found [36].

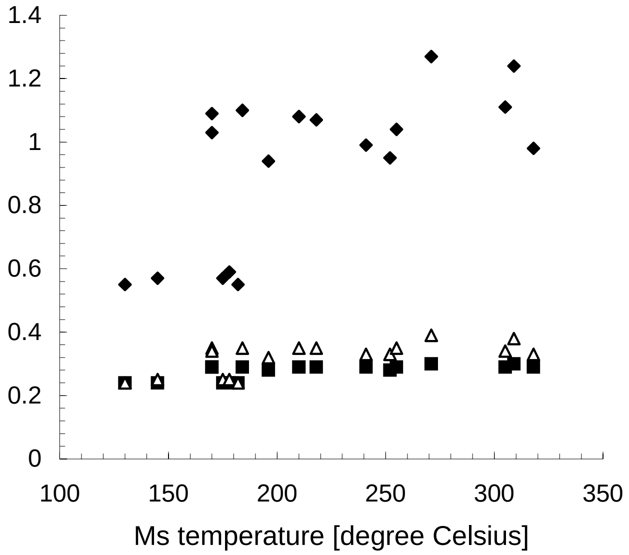

Figure 6.1: Dependence of the martensite formation characteristics on the measured martensite start temperature calculated by the Bowles and Mackenzie model.

The general trends of these characteristics present a plateau for the martensite start temperature within the range 200°C to 250°C. The values of these three characteristics are larger when the martensite start temperatures are higher than 250°C. The plateaux of intermediate constant values of the scattering from the Kurdjumov-Sachs orientation relationship, of the complementary shear strain and of the magnitude of the displacement vector may be explained by the equal probability of formation of the martensite by a slip or by a twinning mechanism in armour steels of which the martensite start temperatures range from 200°C to 250°C, contrary to the other two plateaux where one of the two mechanisms predominate at the expense of the other. The data collected by Morozov and co-workers [21] and presented in Table (2.5), show that many researchers have calculated the various parameters using different thermodynamic models and have predicted a change in the martensite formation mechanism at M_s temperatures between 232°C and 284°C for different Fe-C alloys. The plateaux of the crystallographic characteristics using the Bowles and Mackenzie model as presented in Figure 6.1, are in good agreement with these thermodynamic predictions. The variation in the morphology of the martensite in three armour steels is illustrated in Figure 6.2 for samples of steels H, G and I of which the martensite start temperatures were respectively 210°C, 271°C and 309°C, and that were austenitised at 900°C for 20 minutes in an argon atmosphere and then water-quenched to room temperature. The samples were then polished mechanically and etched for 7 seconds with a 2% Nital solution. In steel G whose martensite start temperature was 210°C, the martensitic structure consisted largely of plates coexisting with large laths.

The lath substructure became slimmer as the martensite start temperature became higher as illustrated in Figures 6.2 (a), (c) and (e) respectively for the three steels.

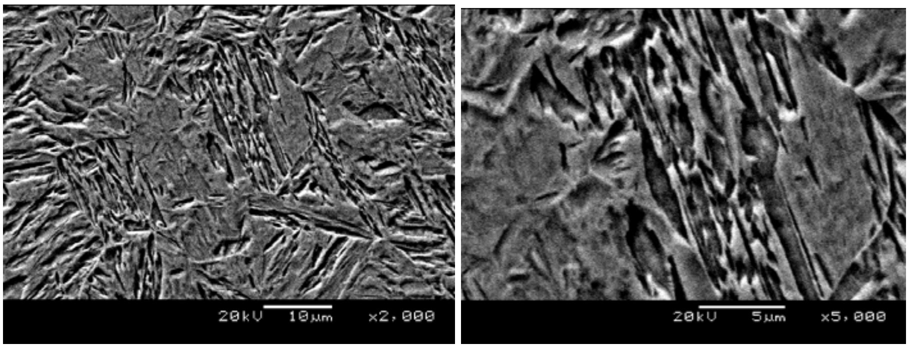

(a) (b)

Figure 6.2 (a) and (b): Backscatter scanning electron microscopy of steel G (M_S = 210°C). (a) x2000 and (b) x5000

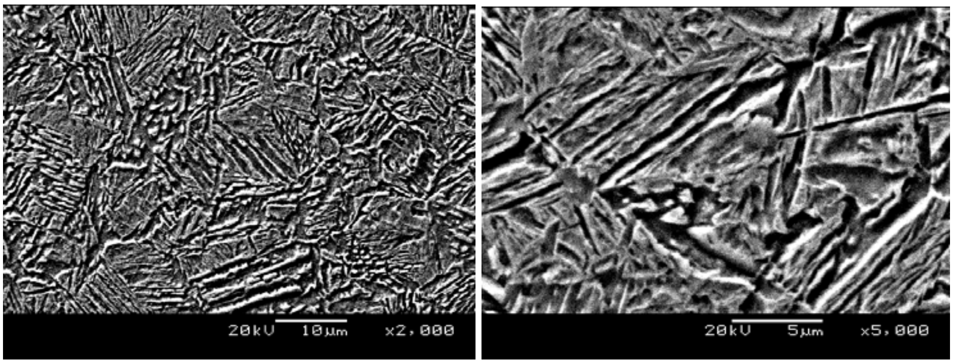

(c) (d)

Figure 6.2 (c) and (d): Backscatter scanning electron microscopy of steel G (M_S = 271°C). (c) x2000 and (d) x5000

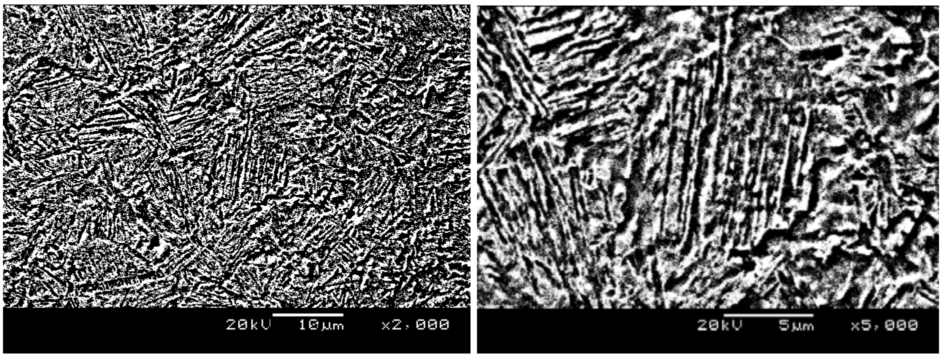

(e) (f)

Figure 6.2 (e) and (f): Backscatter scanning electron microscopy of steel I (M_S = 309°C). (e) x2000 and (f) x5000

The same observation was made by scanning electron microscopy of the samples when still unetched. Samples with thicknesses ranging from 1 to 2 mm were cut from the plates of steels E through to I, mechanically polished using a 1 micron diamond paste and cleaned 30 seconds in an ultrasonic cell containing pure ethanol.

These samples were then austenitised at 900°C for 10 minutes in a high vacuum atmosphere in the THETA Dilatometer and quenched to room temperature in a Helium-gas flow. The backscatter scanning electron microscopy micrographs of these samples are shown in Figure 6.3. The free-surface features of the martensite are coarser in steel E (shown in Figure 6.3(a)) which has the lowest martensite start temperature of 196°C and is finer in steel I (shown in Figure 6.3(e)) whose martensite start temperature is the highest at 309°C. The steels H, F and G whose martensite start temperatures were respectively 210°C, 255°C and 271°C, had intermediate sized free-surface martensite features as shown in Figures 6.3(b), 6.3(c) and 6.3(d) respectively. The small packets formed in steels whose martensite start temperatures are higher than 250°C, present less resistance against the combination of dynamic loading and localised high temperatures produced in zone 1 during ballistic impact.

It was noted in Chapter 4, that the free-surface martensite was not fully constrained during its formation as is the case inside the bulk of the steel, hence the differences in martensite plate widths between Figures 6.2 and Figure 6.3.

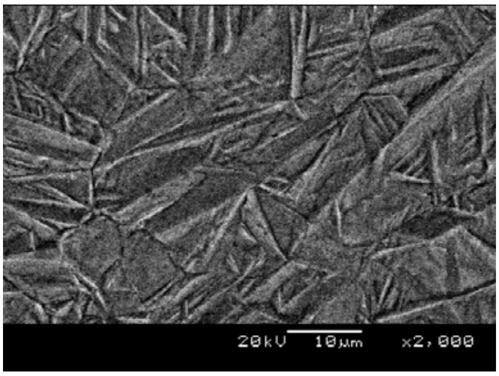

Figure 6.3(a): Backscatter scanning electron micrographs of steel E with M_s=196°C, finely polished before austenitising at 900°C for 10 minutes in high vacuum and quenched in a helium-gas flow. The sample was not polished or etched after quenching.

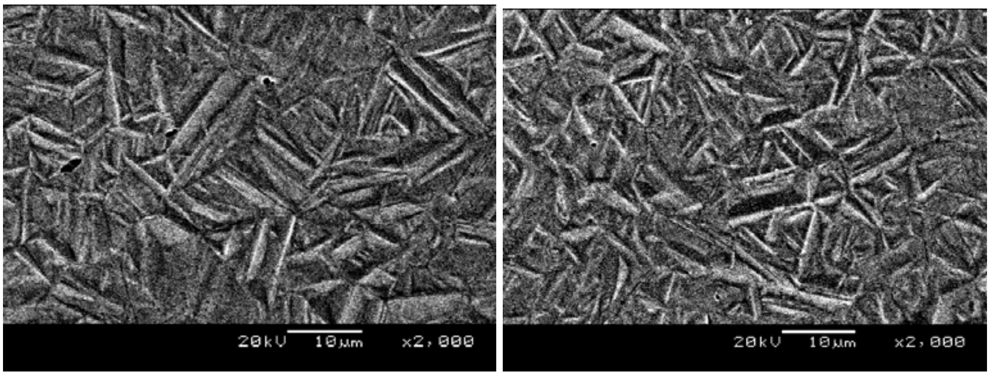

(b) **(c)**

Figure 6.3: (b) Backscatter scanning electron micrographs of steel H with M_s=210°C and **(c)** steel F with M_s=255°C, both finely polished before austenitising at 900°C for 10 minutes in high vacuum and quenched in a Helium-gas flow. The samples were not polished or etched after quenching.

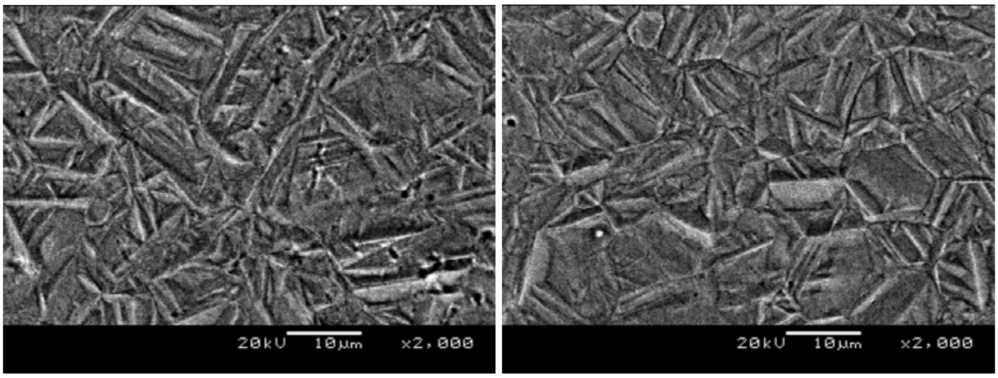

(d) **(e)**

Figure 6.3: (d): Backscatter scanning electron micrographs of steel G with M_s=271°C and **(e)** steel I with M_s=309°C, both finely polished before austenitising at 900°C for 10 in high vacuum and quenched in a Helium-gas flow. The sample was not polished or etched after quenching.

6.3.2. Quantitative analysis of the surface relief by means of Atom Force Microscopy

6.3.2.1: Plate martensite in steel E

Atomic Force Microscopy of steels E through to I was presented in Figure 4.4.36 of Chapter 4. The qualitative comparison of the surface relief apparently reveals different mechanisms of martensite formation in these steels. In Chapter 4, a qualitative classification of the surface relief of these armour steels was done according to their martensite start temperatures.

It was observed that in steel E which had a low martensite start temperature with M_s=196°C, internally twinned martensite formed by a shear mechanism accompanied by sub-twins. Two groups of twins were present and formed in two different directions A and B as shown in Figure 6.4. The twinning ratios of these two groups as well as their frequency were analysed using the Discrete Fourier Transform calculated by the Fast Fourier Transform algorithm of their spatial distributions and are compared in this paragraph.

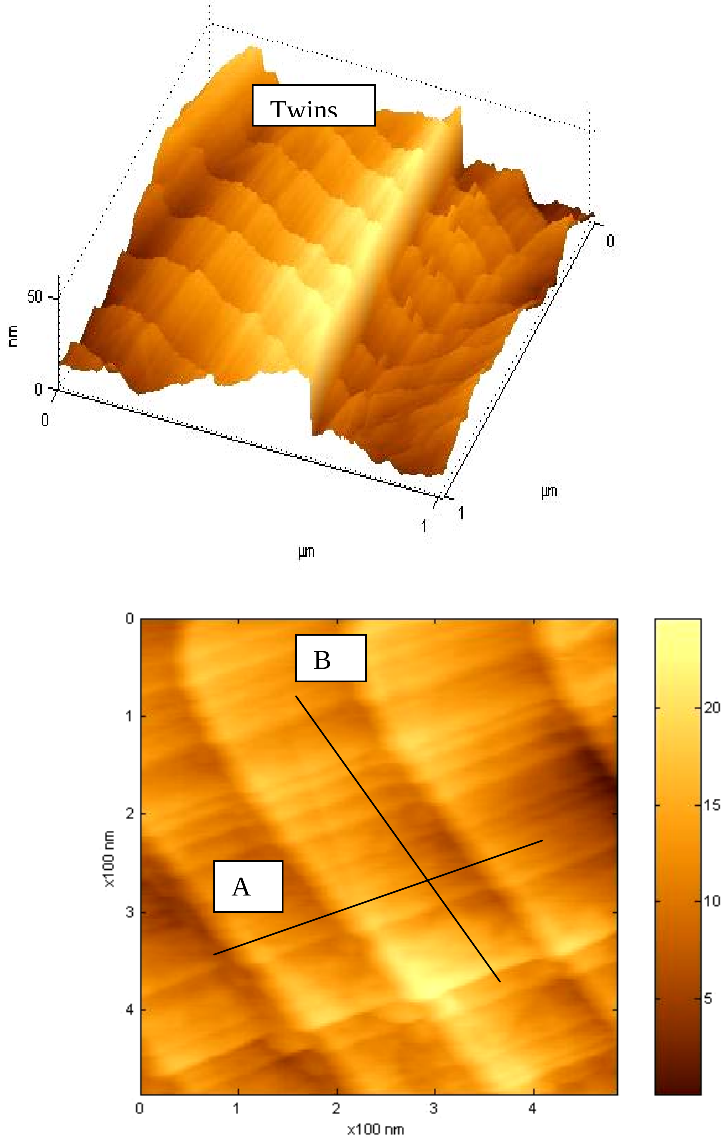

Figure 6.4: Atomic Force Microscopy of steel E with M_s=196°C, showing the twins (100 to 200 nm wide) and other finer parallel lines (sub-twins) approximately transverse to the twins (and approximately parallel to the habit plane)

Normal lines were considered relative to each direction A or B. The corresponding surface relief profiles along the two directions A and B with the corresponding Fast Fourier Transforms are illustrated in Figure 6.5 for the direction A and in Figure 6.6 for the direction B.

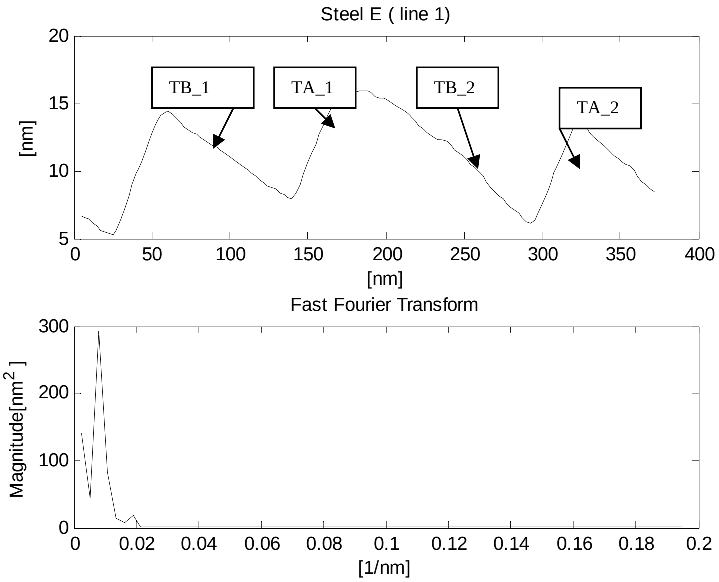

Figure 6.5(a): Surface relief profile of steel E along line 1 in the direction A and the corresponding Fast Fourier Transform

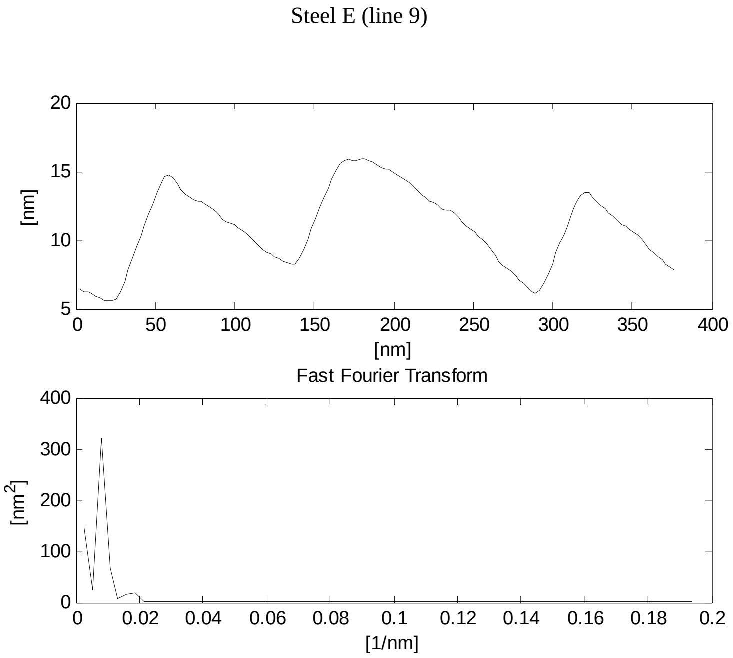

Figure 6.5(b): Surface relief profile of steel E along line 9 in the direction A and the corresponding Fast Fourier Transform.

The measured widths of the twins and the twinning ratios are presented in Table (6.2) and Appendix A6.2 where (dx) is the horizontal distance between a minimum and the following maximum or vice versa and (dy) is the height difference between the two points.

Table (6.2): Measured geometric characteristics of the twins along lines parallel to the direction A in steel E.

line 1	**TA_1**	**TB_2**	**TA_2**	**TB_3**	**TA_3**	
dx [nm]	35.71	79.61	33.48	24.55	95.98	
Height [nm]	9.05	-6.44	8.03	-8.75	7.35	
Relief angle [Degrees]	14.23	-4.62	13.50	-4.84	13.55	
Width [nm]	36.84	79.87	34.43	55.84	26.42	
Slope [nm/deg]	2.58	-17.25	2.54	-11.6	1.94	
Twinning ratio TB/(TB+TA)		0.69		0.68		
Line 9	**TA_1**	**TB_1**	**TA_2**	**TB_2**	**TA_3**	**TB_3**
dx [nm]	35.67	79.70	26.56	92.61	31.12	55.41
Height [nm]	9.17	-6.50	6.64	-9.06	7.37	-5.60
Relief angle [Degrees]	14.43	-4.66	14.04	-5.59	13.34	-5.78
Width [nm]	36.84	79.97	27.38	93.05	31.98	55.69
Slope [nm/deg]	2.55	-17.12	2.00	-16.63	2.39	-9.63
Twinning ratio TB/(TB+TA)	0.74		0.74		0.63	

The twinning ratio $\frac{TB\_i}{TB\_i + TA\_i}$ normal to the direction A in steel E spread from 0.6 to 0.81.

Twins TB_i are regular shapes whose relief angle is about 5.2±0.6°. Twins TA_i are rather regular shapes whose relief angle is about 13.5±2.0°.

The frequency spectrum contains a narrow bandwidth peak at about $0.008\,nm^{-1}$. This indicates that the plates are not exactly the same width but are rather continuously distributed around the mean width value which equalled $125\,nm$.

The surface relief profile along the direction B is illustrated in Figure 6.6.
The geometric measurement along the lines in the direction B are shown in Table 6.3. The twinning ratio $\frac{TB\_i}{TB\_i + TA\_i}$ along the normal to the direction B in steel E was spread within the range 0.55±0.03.

The surface relief was again N-shaped with twins TB_i whose relief angle was about 5.0±1.0° and twins TA_i whose relief angle was about 6.0±2.0°.

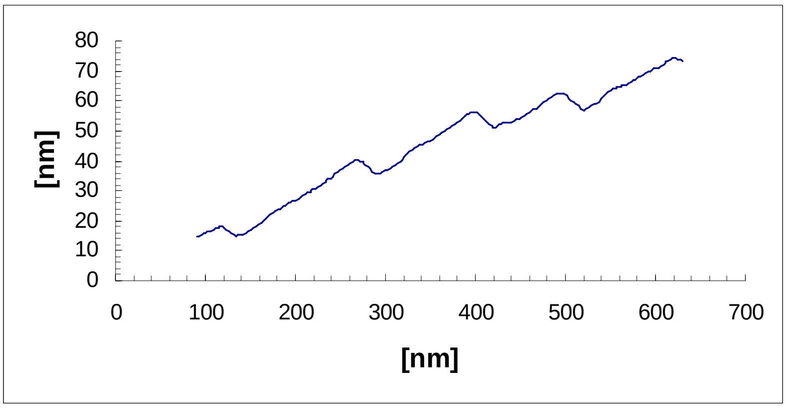

Figure 6.6(a): Typical surface relief profile along the direction B

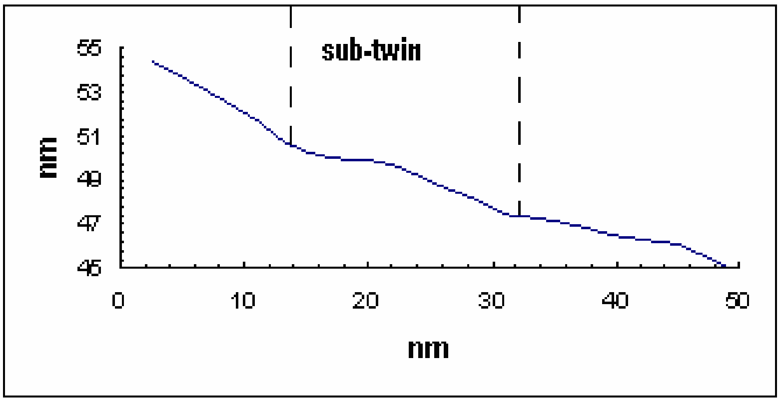

Figure 6.6(b): Typical surface relief profile of the sub-twins along the direction B

The total width of the sub-twin pairs normal to the direction B ranges from 10 to 20 *nm* which are smaller than 125 *nm* measured normal to the direction A.

Table (6.3): Measured geometric characteristics of the twins along lines in the direction B in steel E.

	TA_1	TB_2	TA_2	TB_3	TA_3	TB_4	TA_4
dx [nm]	42.03	48.32	33.62	31.52	27.32	52.53	37.82
height [nm]	3.29	-4.98	3.56	-2.73	1.13	6.59	-3.91
Relief angle [Degrees]	4.477	-5.89	6.05	-4.96	2.37	7.153	-5.91
Width [nm]	42.15	48.58	33.81	31.64	27.34	52.95	38.03
Slope [nm/deg]	9.414	-8.24	5.58	-6.37	11.49	7.40	-6.43
Twinning ratio TB/(TB+TA)		0.58		0.53		0.58	

The twinning ratio is also smaller normal to the direction B than normal to the direction A. Lin Xiaoping and co-workers [47, 96] have determined the crystallographic characteristics of the $\{2\ \ 2\ \ 5\}_\gamma$ and of the $\{2\ \ 5\ \ 9\}_\gamma$ martensite in a Fe-23%Ni-0.55%C and a Fe-8%Cr-1%C alloy respectively using Atomic Force Microscopy.

They have observed that the relief angles of the $\{2 \quad 5 \quad 9\}_\gamma$ and the $\{2 \quad 2 \quad 5\}_\gamma$ martensite range respectively from 4 to 5.8° and from 1 to 9°. The relief angles measured for steel E which ranged from 4 to 6°, was in good agreement with those measured by Lin Xiaoping and co-workers for the $\{2 \quad 2 \quad 5\}_\gamma$ martensite. However the widths of the plates measured for steel E ranging from 90 to 125 nm, were at least two times smaller than those measured by Lin Xiaoping and co-workers [95]. It seems from this comparison that the relief angle of the $\{2 \quad 2 \quad 5\}_\gamma$ martensite may be less sensitive to the chemical composition than the width of the plates.

The austenitisation temperature seems to have an effect on the widths of the plates but not on the relief angles. Indeed, the data from Table 1 of the work done by Lin Xiaoping and co-workers [95] shows that the heights and the widths of the plates increase when the austenitisation temperature increases from 1173K to 1473K.

A number of areas of the steel E consist of zigzag-shaped, while the rest consisted of twin martensite. The adjacent plates of zigzag-shaped martensite share the same conjugate habit plane. According to the Nishiyama-Wasserman-I (NW-I) and Nishiyama-Wasserman-II (NW-II) orientation relationships, the adjacent plates that share the same conjugate habit plane may grow in two symmetrical directions, so a tent-shaped surface relief is formed by their mutually back-to-back accommodation growth [93].

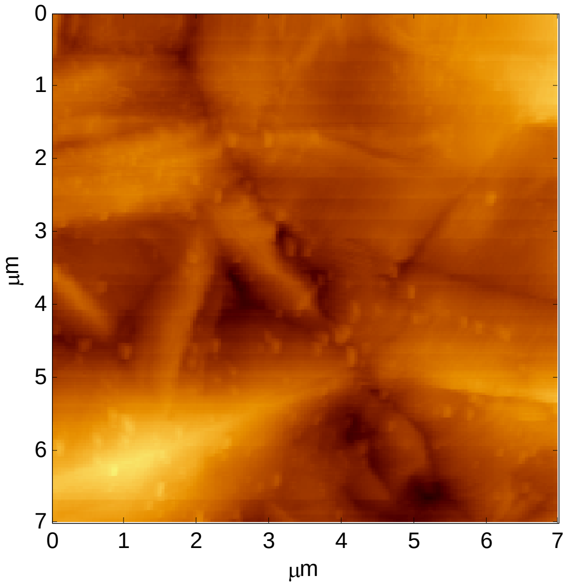

Figure 6.7: Zigzag-shaped martensite appears to have been formed in some parts of steel E

6.3.2.2: Lath martensite in the steel I

The martensite start temperature of steel I is 309°C. Figure 4.4.35(e) of Chapter 4 showed the thin foil TEM bright field image of this steel. Lath morphology of the martensite in this steel was found after austenitisation at 900°C for 20 minutes and water quenching. Figure 6.8 illustrates the surface relief accompanying the martensite formation in this steel. Contrary to steel E's surface relief, is that of steel I irregular and N-shaped, which is not in agreement with the prediction of the invariant plane strain [95, 96].

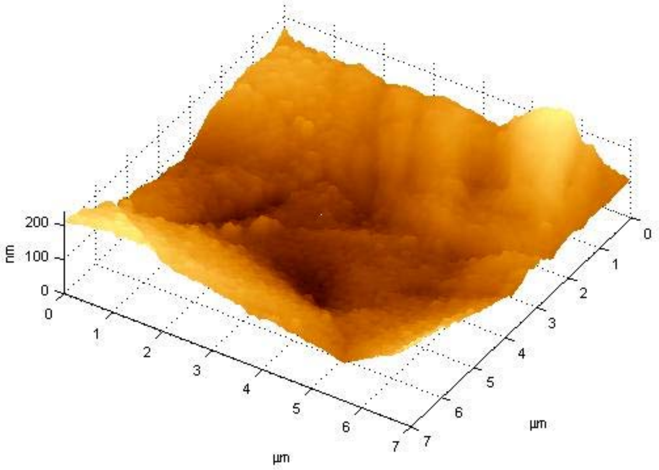

Figure 6.8 (a): Surface relief accompanying the formation of slipped martensite in steel I showing the irregular N-shape.

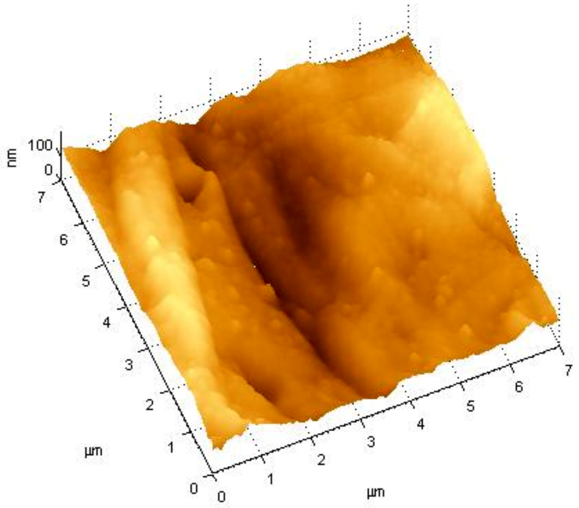

Figure 6.8 (b): Surface relief accompanying the formation of slipped martensite in steel I (Ms =309°C) showing the irregular N-shape.

A typical surface relief profile accompanying the formation of the martensite in steel I is illustrated in Figure 6.9. Relief deterioration is possible in the case of this relatively high Ms temperature through thermal smoothing and oxidation.

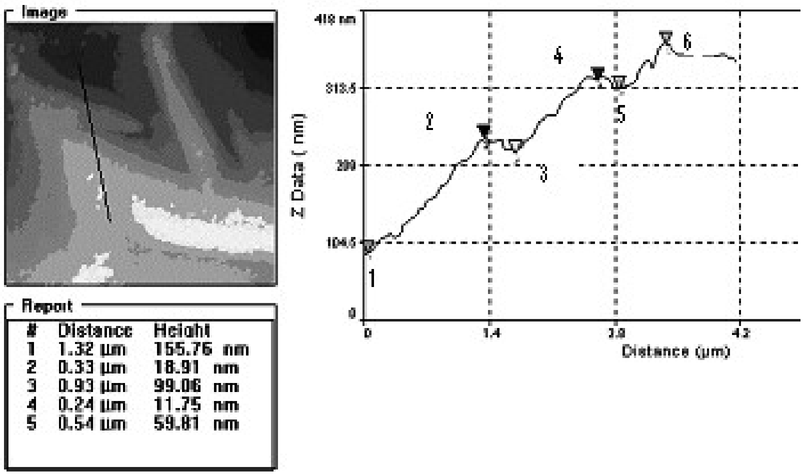

#	Distance	Height
1	1.32 µm	155.76 nm
2	0.33 µm	18.91 nm
3	0.93 µm	99.06 nm
4	0.24 µm	11.75 nm
5	0.54 µm	59.81 nm

Figure 6.9: Typical surface relief profile after martensite formation in steel I and the corresponding geometric characteristics. The number in the first column indicates the segment number, i.e. 1 correspond to segment 1-2, 2 corresponds to segment 2 –3.

The laths are larger than 1.1 µm. This is about 2 times the width of the martensite plates formed in steel E. The size of the laths or of the plates may have an effect on the effective "grain size" in resisting fracture or perforation due to ballistic impact.

The transition of the martensite morphology in the armour steels as determined by Atomic Force Microscopy was illustrated in Figure 4.4.36 of Chapter 4. AFM images reveal three different morphologies of the martensite formed in these armour steels depending on the specific martensite start temperatures. Based on the work of Davies and Magee [99], the AFM results presented in Figure 4.4.36 and the crystallographic parameters using the Bowles and Mackenzie model as presented in Table (6.1) and Figure 6.1, the lattice invariant shear for the various martensite habit planes for the armour steels E through to I would be as follows:

Table (6.4): Habit planes of the armour steels E through to I as defined using the AFM results, the work of Davies and Magee and the crystallographic parameters from the BM model

	M_S [°C]	Illustrated in	Habit plane	Invariant lattice shear angle [°]	Total strain
Steel E	196	Figure 4.25(a)	{2 2 5}- twinning in ferrite	8.19	0.28
Steel H	210	Figures 4.25(b); 6.2(a)		8.40	0.29
Steel F	255	Figure 4.25(c)	{2 2 5}and {5 7 5} slip in austenite and twinning in ferrite	8.38	0.29
Steel G	271	Figures 4.25(d); 6.2(c)		8.48	0.30
Steel I	309	Figures 4.25(e); 6.2(e)	{5 7 5} or{1 1 1}- slip in austenite and ferrite	8.47	0.30

6.4. Orientation relationship between martensite and retained austenite

The orientation relationship between martensite and retained austenite in the armour steels W (M_s =130°C), U (Ms =170°C), and H (M_s =210°C), were determined by the electron diffraction technique. It is concluded in Figure 6.10 that, in the Steel W, the orientation between the martensite and the retained austenite obeys the Nishiyama-Wasserman orientation relationship with:

$$(1\ \ 0\ \ 0)\alpha \,//\, (1\ \ 1\ \ 0)\gamma$$
$$\langle 0\ \ 1\ \ 1\rangle\alpha \,//\, \langle 1\ \ \bar{1}\ \ 1\rangle\gamma$$

Figure 6.10(a): TEM thin foil bright field of the steel W (Ms = 130°C). Label mark: 500 nm

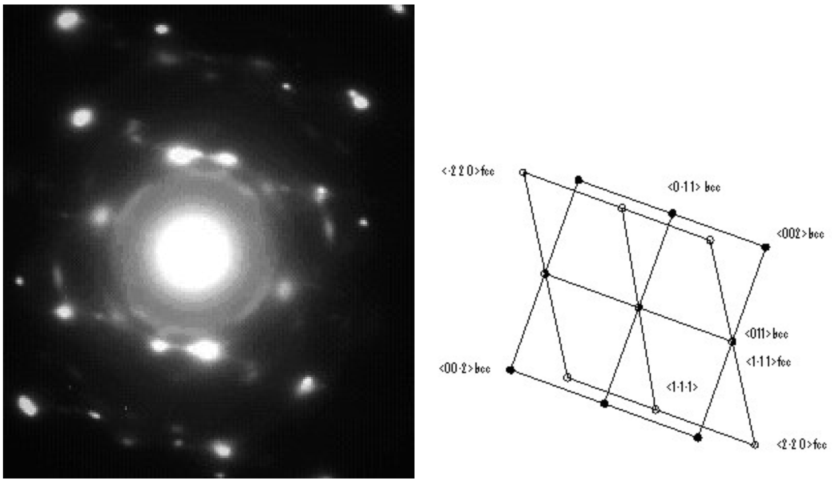

Figure 6.10(b) **Figure 6.10c**

Figure 6.10(b): Selected Area Diffraction Pattern from Figure 6.10(a). **Figure 6.10(c)**: Corresponding indexing

The dark field images corresponding to the spots $\langle 0\ \ \bar{1}\ \ 1\rangle bcc$ and $\langle \bar{2}\ \ 2\ \ 0\rangle fcc$ are shown in Figure 6.10(d) and 6.10(e) respectively.

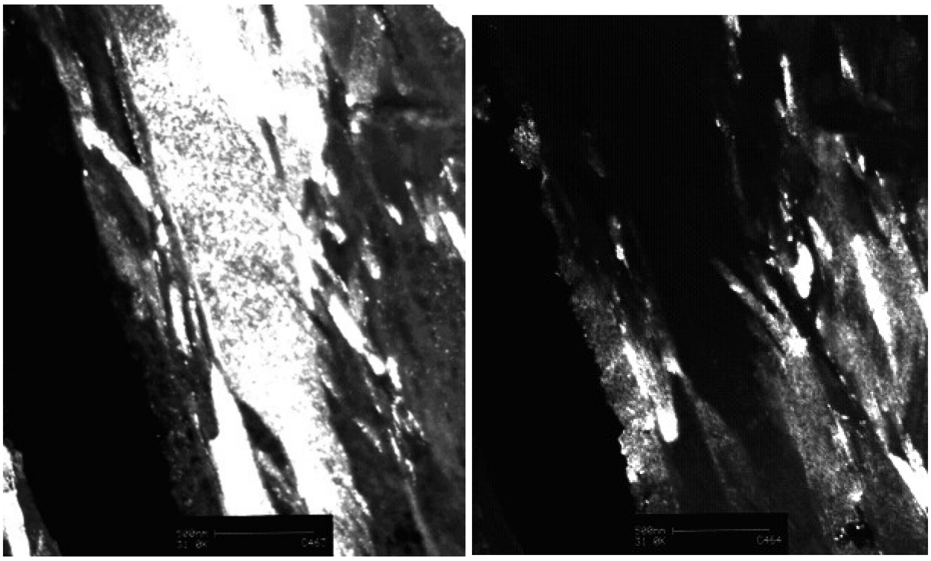

Figure 6.10(d) **Figure 6.10(e)**

Figure 6.10(d): TEM thin foil dark field image corresponding to the spot $\langle 0\ \ \bar{1}\ \ 1\rangle bcc$ showing the martensitic matrix. **Figure 6.10(e):** TEM thin foil dark image corresponding to the spot $\langle \bar{2}\ \ 2\ \ 0\rangle fcc$ showing nodular retained austenite. Label mark: 500 nm

The same orientation relationship was observed in the Steel U, with M_s = 170°C. The typical TEM thin foil bright image of this steel is shown in Figure 6.11(a).

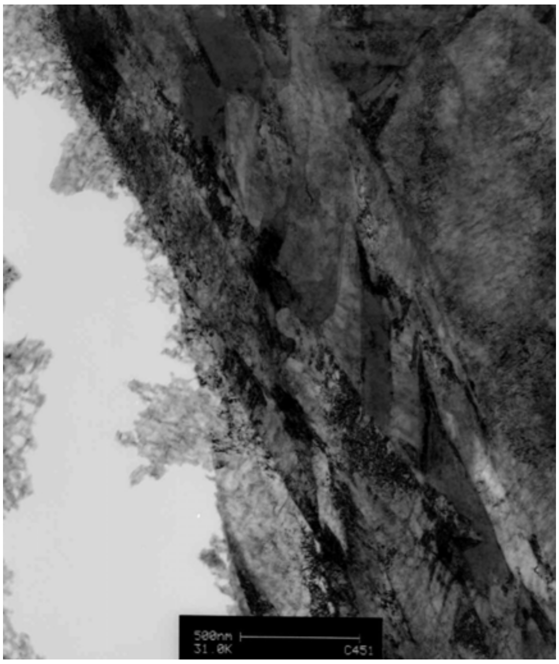

Figure 6.11(a): TEM selected area bright field of the steel U. Label mark: 500 nm

The Selected Area Diffraction Pattern and the indexing map of this steel are presented in Figure 6.11(b) and 6.11(c).

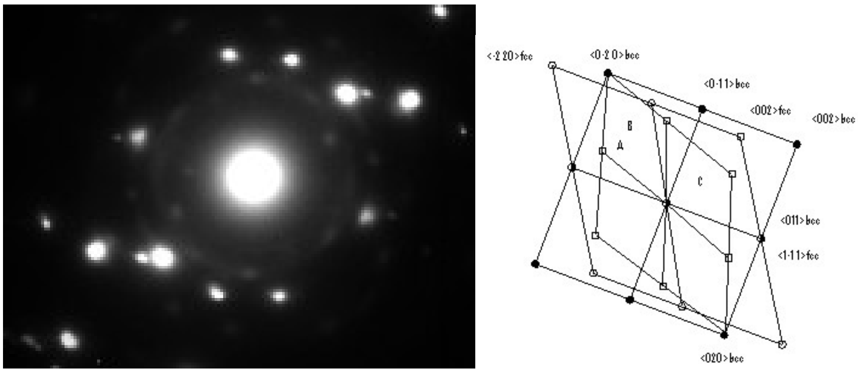

Figure 6.11(b) **Figure 6.11(c)**

Figure 6.11(b): Typical SADP of the Steel V, M_s = 145°C. **Figure 6.11(c):** corresponding indexing map.

It is concluded from this mapping that the Nishiyama-Wasserman orientation between the parent austenite and the martensite is obeyed in this steel.

$$(1 \quad 0 \quad 0)\alpha \,//\, (1 \quad 1 \quad 0)\gamma$$

$$\langle 0 \quad 1 \quad 1\rangle\alpha \,//\, \langle 1 \quad \bar{1} \quad 1\rangle\gamma$$

The spacing of the planes that produced the extra spots A, B and C are close to the lattice parameters of cementite, however the corresponding angles differ by about 2°. They may be formed by the reflexions from a structure that is very close to the orthorhombic cementite, possibly an iron carbide formed by autotempering during the quenching.

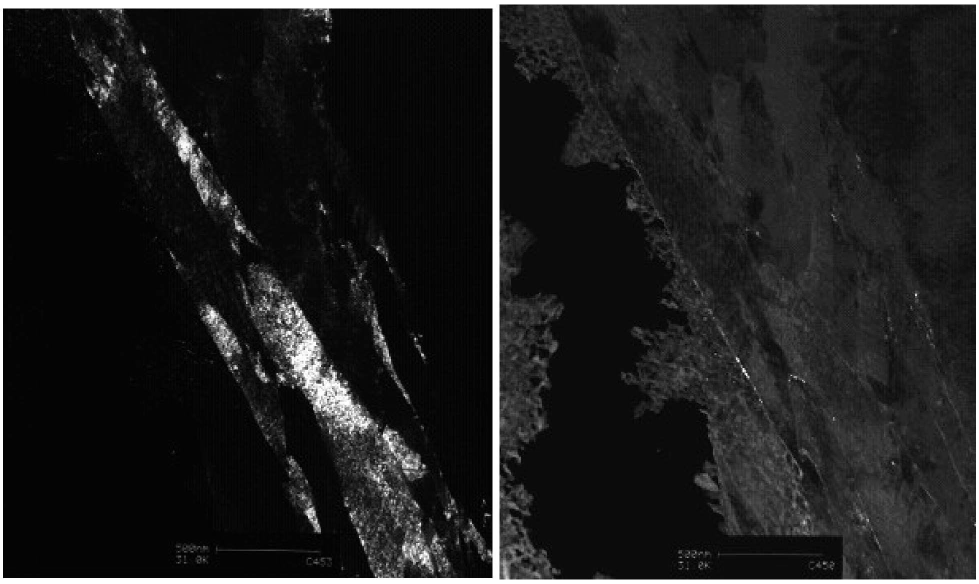

Figure 6.11(d) **Figure 6.11(e)**

Figure 6.11 (d) and **(e):** TEM dark field images corresponding to the spots $\langle 0\ \bar{1}\ 1\rangle bcc$ showing the martensitic matrix and $\langle \bar{2}\ 2\ 0\rangle fcc$ revealing the retained austenite along the martensite twinned plates. Label mark: 500 nm

Formatted

In steel H, M_s = 210°C, the SADP presents the orientation relationship

$$(1\ 0\ 0)\alpha // (1\ 1\ 2)\gamma$$
$$\langle 0\ 1\ \bar{1}\rangle \alpha // \langle 1\ \bar{1}\ 1\rangle \gamma$$

which deviates from the Nishiyama-Wasserman by 7°.

In this steel also the spacing of the planes that produced the extra spots A,B,C,D and E are close to those of cementite and suggest the possibility of autotempering and the formation of fine carbide particles of a carbide such as $Fe_{2.4}C$ or ε-carbide.

Figure 6.12(a) presents a typical TEM thin foil bright field image of the steel H. The SADP corresponding to the region near the boundary indicated with an arrow, is shown in Figure 6.12(b) and the indexing map in Figure 6.12(c).

Figure 6.12(a): TEM selected area bright field of the steel H (M_s = 210°C)

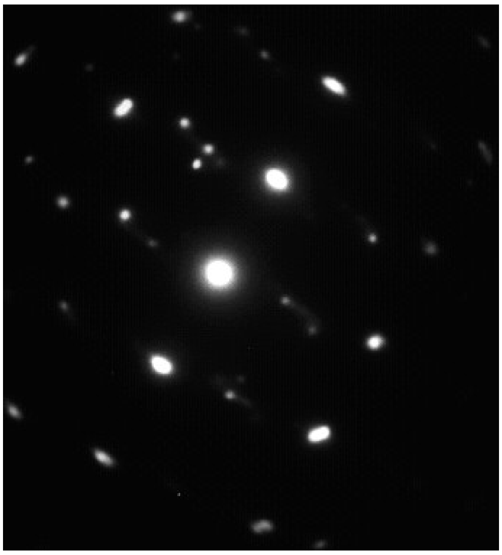

Figure 6.12(b)

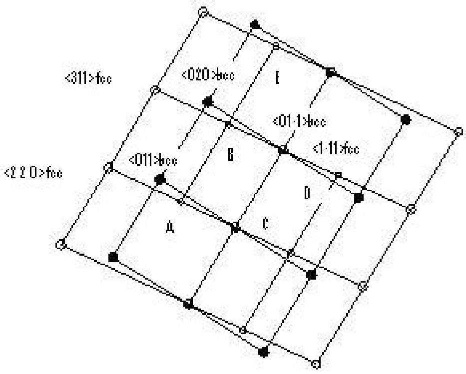

Figure 6.12(c)

The dark field images corresponding to the spots $\langle 0 \quad 2 \quad 0 \rangle \alpha$ and $\langle 3 \quad 1 \quad 1 \rangle \gamma$ are presented in Figure 6.12(d) and Figure 6.12(e).

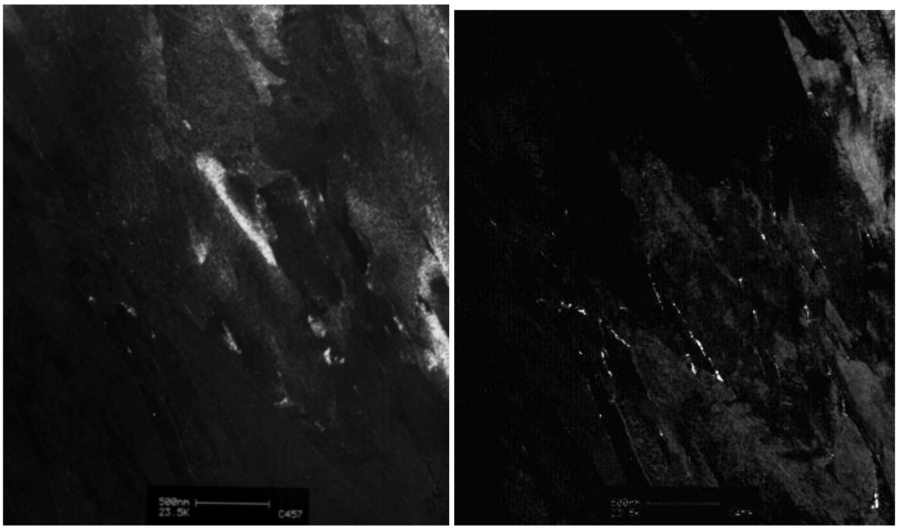

Figure 6.12(d) **Figure 6.12(e)**

Figure 6.12(d): Dark field image from the spot $\langle 0 \quad 2 \quad 0 \rangle \alpha$ showing the martensite. **Figure 6.12(e)** from the spot $\langle 3 \quad 1 \quad 1 \rangle \gamma$ showing the retained austenite

The N-W orientation relationship seems to prevail in these martensitic armour steels where the M_s temperature is lower than 200°C. The orientation relationship deviates from the N-W when the Ms temperature is higher. Spots suggesting autotempering appear in steels with M_s temperatures higher than 170°C.

CHAPTER 7. REQUIREMENTS FOR ADVANCED PERFORMANCE ARMOUR STEELS

7.1 Introduction

The optimisation of the microstructures and mechanical properties of the armour plates in a quenched and tempered condition has been undertaken with the intention of improving the ballistic performance of the steels A, B, C and D currently produced and used for military, civil and security purposes. Standardised ballistic testing of plates of new armour steels with 6 mm thickness assessed the improved resistance against ballistic impact. The reliability of the 6 mm armour plates was assessed by the ability of thinner plates ranging from 4.7 to 5 mm to withstand the direct impact of 5.58 mm rounds fired by a R4 rifle at zero degree obliquity from a distance of 30m at muzzle velocities ranging between 930 and 1050 m/s, as specified currently for civil and military applications with armour plates thicker than 8.5 mm. Since armour plates with thickness of 8.5 to 20 mm are currently being used to obtain the same ballistic performance, this makes the new alloys a significant improvement in weight reduction. It represents a reduction in weight of the plate used in manufacturing light vehicles for security and combat purposes from 66.3 kg/m^2 to less than 35.1 kg/m^2, a possible reduction of almost 50% in weight of the protected areas in these vehicles. This will reduce fuel consumption and increase the maximum speed attainable in these vehicles and will also open new global markets for the local steel industry. Thirteen advanced performance armour plate steels have been tested successfully in the conditions mentioned above. Through thin foil transmission electron microscopy, scanning electron microscopy and X-ray diffraction techniques from carefully sectioned samples at and near the impact areas after ballistic testing, it was confirmed that the success of these new alloys lies in their ability to undergo Transformation Induced Plasticity or "TRIP" of retained austenite upon impact together with a transition from twinned plates to slipped lath martensite that consume a significant part of the kinetic energy of the fired rounds.

Three groups of armour steels were identified by considering together the martensite start temperature, the volume fraction of retained austenite and the morphology of the martensite.

7.2. **Group 1:** consists of armour steels containing 1 to 6% volume fraction of retained austenite. Steels of this group have a higher ability to withstand rounds from R4 rifles fired from a distance of less than or equal to 30 metres from the plate. The martensite start temperatures of these steels range from 130 to 210°C. The morphology of the martensite formed in this temperature range is twinned plates containing nodules of retained austenite in the plate interfaces and on grain boundaries. Thin foil Transmission Electron Microscopy of the regions of the 4.5 to 5.0 mm thick plates of Group 1 deformed upon multiple ballistic impacts reveals the combination of two operating mechanisms in resisting ballistic perforation. The kinetic energy of the fired rounds is absorbed in the impacted regions in two ways:

- The transformation of the retained austenite to martensite by the well known TRransformation-Induced Plasticity or TRIP effect; and
- through reaustenitisation subsequent to the heating up of the plate martensite by entropy trapping inside the so called "adiabatic region" at the centre of the impacted zone and the formation of new slipped martensite upon being cooled down by the surrounding material. It needs to be recognized,

however, that the reaustenitised material probably has a higher M_s temperature than originally as little carbide dissolution may take place under the dynamic conditions of shock wave propagation

7.3. Group 2: comprises armour steels whose martensite start temperatures are between 210 and 280°C. This Group 2 armour steels has a combination of high strength, high Charpy-V impact energy at -40°C and a high hardness. The yield strengths of the steels in this group are higher than 1500 MPa, the ultimate tensile strength higher than 2000 MPa, the elongations on 50 mm gauge length are higher than 7% at room temperature, the Charpy-V impact energies of sub-sized specimens is above 13 Joules at -40°C and the hardness values are higher than 570 BHN.

The combination of high mechanical properties has inspired the design of armour steels in the past. The current martensitic armour steels such as steels A, B, C and D belong to Group 2. The minimum thickness of the plates of these armour steels required to withstand the R4 rifles fired in the same conditions than above, is 8.5 mm. The volume fraction of retained austenite in these plates is less than 1% and the martensite formation is generally accompanied by slip of dislocations. Some regions of the martensite contain twins on a background of laths. The coexistence of the laths and the twinned regions within the martensite was clearly observed in the three-dimensional surface relief AFM images and was also observed by thin foil transmission electron microscopy. The retained austenite in these steels is present as thin films along the lath interfaces and does not appear to undergo any TRIP. It remains untransformed upon ballistic impact, contrary to the nodular austenite located on plate interfaces and grain boundaries of the Group 1 armour steels.

7.4 Group 3: comprises armour steels whose martensite start temperatures are higher than 280°C. They contain less than 1% retained austenite and have the highest Charpy-V impact energy at -40°C and % elongation at room temperature. Their yield and ultimate tensile strength are intermediate between those of Group 1, the lowest, and those of Group 2, the highest. Armour steels of Group 3 are very sensitive to auto-tempering upon quenching.

7.5. General requirements of high performance armour steels

The location and the morphology of the retained austenite in all of these steels seem to be a function of the martensite start temperature. The TRansformation Induced Plasticity effect appears to be more effective when the martensite is formed at lower temperatures rather than at higher temperatures. Furthermore, nodular retained austenite seems to transform more readily by the strain-induced mechanism. Further investigation is needed for a better understanding of the conditions that determine the location and the morphology of the retained austenite in these martensitic armour steels.

The mechanical properties and ballistic performance of martensitic armour steels are strongly dependent on the chemical composition and the heat treatment cycle. The tensile properties are difficult to measure in untempered conditions for the armour steels of Groups 1 and 2 because of their brittle behaviour. On the other hand the martensitic armour steels of Group 3 are ductile from auto-tempering during quenching and their tensile properties are measurable in the as-quenched condition. The steels of Group 3 also have a high Charpy-V impact energy of sub-sized specimens in the untempered condition. The tensile properties as well as their impact energy at -40°C of all of these armour steels are improved by tempering between 200°C and 250°C for times less than 1 hour. Tempering above

300°C for the same time leads to a reduced tensile strength due to the precipitation of coarse cementite particles in the martensitic matrix.

Thin foil transmission electron microscopy of the tempered steels confirmed the well-known effect of Silicon in retarding the decomposition of the supersaturated martensite and the formation of cementite. Martensitic armour steels containing 0.8 to 1.2%Si may resist over-tempering at 300 to 350°C without forming coarse cementite that is detrimental to the mechanical properties as well as to the resistance against ballistic perforation. Thin carbides start precipitating along the twinned plate interfaces upon tempering of these armour steels, which is in agreement with the results published by Kelly [100], who has confirmed that the cementite thus formed obeys the Bagaryaski orientation relationship with the ferrite.

7.6. Design philosophy of high performance armour steels

From the comparison between mechanical properties and ballistic performance of the 13 steels tested in the conditions described in Chapters 4 and 5, it appears that the highest ballistic performance is reached by heat treatment conditions that are contrary to those required for the combination of the highest mechanical properties for a given chemical composition of the steel. This observation is in agreement with the published results on the ballistic performance of armour steels in general and, thereby, constitutes the basis for the development of advanced performance armour steels. This observation is, therefore, in contradiction to the current design philosophy for armour steels used hitherto. Neither the high tensile properties nor the high Brinell hardness number of the steel are ideal criteria within themselves in predicting the ballistic performance of armour plates or the dynamic resistance of structures to impact loading [6,7, 12, 13, 14, 15, 16, 17, 18]. Instead, the ratio of the yield strength to the ultimate tensile strength of the material and the volume fraction of retained austenite contained in the martensite are an improved indication of the steel's ability to resist localised yielding that favours ballistic perforation. The steels whose YS/UTS ratio is lower than 0.6 and contain 1% to 7% of retained austenite in twinned martensite, appear to present a low tendency to localised yielding upon high velocity impact loading.

This behaviour may be quantified through a function that includes the diameters of the impact affected zones around the incidence point after ballistic testing. However, it is difficult to establish a direct relationship between mechanical properties and ballistic performance of armour steels. The differences between mechanical properties and ballistic performance for a given armour steel and the reason why an armour steel plate performs ballistically better than another, should rather be explained in terms of their microstructures as well as their response to high velocity dynamic loading. Indeed, published data have reported measured dynamic tensile stresses in steel plates subjected to ballistic impacts of as high as 28 GPa [16,17,18]. The dynamic measurable maximum stress is, therefore, 12 times higher than the ultimate tensile strength of current high strength steels. This fact renders the current criteria that are largely based on the absolute values of the yield or the ultimate tensile strength in predicting the ballistic performances of armour steels, inappropriate.

In this study the resistance to localised yielding by the ballistic impact has been quantified by the diameters of three concentric zones formed around the incidence point. It appears that the diameter of the inner zone 1 is almost equal for all the steels and is slightly larger than the fired round's diameter. On the other hand the diameters of the outer zone 3 are larger for those steels whose volume fraction of retained austenite is higher and their yield strength to ultimate strength ratios are lower. The relationship between the volume fraction of retained austenite in the martensitic steel, the diameter of the outer zone 3 and the thickness of the plate may then be used in defining a criterion for its ballistic performance. The yield strength to ultimate tensile strength ratio (YS/UTS), which also appears to be a function of the volume fraction of retained austenite in the martensitic steel through the TRIP effect, may be introduced as a dependent variable in this relationship. The uncertainty in predicting the ballistic performance of the steels considered in this study using the Ballistic Performance Index (BPI) proposed by Srivathsa and Ramakrishnan [6,7] may be explained by the lack of a relationship between the independent variable, i.e. the volume fractions of the phases present in the microstructure and the dependent variable, expressed as the yield strength to ultimate tensile strength ratio. The Ballistic Parameter BP has, therefore, been defined in Chapter 5 to account for the effect of the volume fraction of retained austenite and the thickness of the steel plates on the diameters of the outer zone 3 of the ballistic impact-affected regions, which indicate the resistance to localised yielding due to impact loading upon high velocity ballistic impact. It has been observed in this study that the combination of a high austenitisation temperature ranging between 870 and 950°C together with a low tempering temperature ranging between 170 and 200°C, is favourable for a low YS/UTS ratio and this provides a high resistance to localised yielding of the plates in thicknesses smaller than 5 mm. When the Silicon content of the armour steel is high the plates may be tempered at 350°C and still have a high ballistic performance. Contrary to this design philosophy, a low austenitisation temperature of 800 to 850°C and a high tempering temperature of 250 to 300°C, generally improve all the tensile properties and the sub-zero impact energy but reduce the steel’s resistance to ballistic perforation.

7.7 Localised microstructural features of impact loading

Shock induced transformations and transitions occur respectively inside zones 1 and 3 of the impact affected regions. Quasi-adiabatic conditions prevailing inside zone 1 are favourable for the conversion of kinetic energy into heat. The localised temperatures in those zones are high enough to induce melting and welding of the fired round’s material onto the steel plates, dynamic reaustenitisation of the twinned plate martensite and subsequent formation of slipped lath martensite together with auto-tempering. The new lath martensite forms from austenite with likely a higher M_s than originally as it is unlikely that carbides will fully dissolve during the brief and dynamic temperature rise. The Vickers micro-hardness profiles across the sections of the impacted regions show global hardening of these regions but with relative softening of zone 1 compared to zones 2 and 3. Inside zone 3 many dislocations are produced. Thin foil transmission electron microscopy of zone 3 shows dislocation pile-ups at twinned plate interfaces, demonstrating the high resistance of the twin interface to shear by slip of dislocations. New martensite is formed by a strain-induced mechanism of the retained austenite, i.e. the TRIP effect. No retained austenite was detected by X-ray diffraction of the impact-affected regions after ballistic testing. Rather, thin foil transmission electron microscopy of the same regions revealed new untwinned martensite that was formed by transformation of nodular retained austenite located in plate interfaces.

Scanning electron microscopy of the three-dimensional cracks revealed the character of dynamic cracking with microscopic cracks propagating along the grain boundaries. This observation may be a consequence of the high resistance provided by the twinned plate interfaces against the movement of dislocations throughout the martensite crystals and throughout the grains. Former parent austenite grain boundaries are then less resistant for the propagation of microcracks induced by the transmission of that part of the kinetic energy of the fired round that is converted into potential energy of the compressive and tensile stress waves crossing the plates. From the simulation using an adaptation of the stress distribution model in space and time upon impact loading proposed by Hopkinson and modified by Taylor [5] and taking into account the likely true fracture stress as reported in the literature, the fracture of the untempered plates is predicted to occur 11 to 20 cm away from the incidence point for an incidence velocity of the fired rounds between 930 and 950 m/s. Tensile stresses near to 12 GPa may be developed within the armour plate after three or four reflections of the tensile stress wave from the edges of the plates, which were 30 cm long and 20 cm wide. The profiles of the shear bands across the fractured sections of the untempered plates suggested a vibratory dynamic response of the plates to the ballistic impact loadings that excited some natural frequencies within the plates according to their harmonics. The sizing of the plates to be used should then consider a lowest natural frequency of the plate structure larger than the highest firing frequency of the R4 to avoid synchronisation. Smaller and thinner plates may be the remedy for mechanical resonant failures.

7.8 Martensite characterisation in these advanced performance armour steels

The martensite was characterised using the lattice parameters of the martensite and of the retained austenite as measured by X-ray diffraction, as inputs in predicting the crystallographic features by the Bowles and Mackenzie model of the Phenomenological crystallographic Theory of the Martensitic Transformation. This was found to be in good agreement with the predictions of the existence of three plateaux distinguishing the martensite formed by an internal twinning mechanism, $\{2\ \ 2\ \ 5\}_\gamma$ butterfly martensite formed by a slip mechanism in the austenite and $\{1\ \ 1\ \ 1\}_\gamma$ lath martensite formed by a slip mechanism in both the austenite and the ferrite. The three formation mechanisms of the martensite were observed by qualitative AFM analysis of the surface relief accompanying the martensite formation.

- Surface relief of armour steels in Group 2 whose martensite start temperatures ranged from 210 to 280°C, were irregular N-shaped which revealed no character of the IPS. The three-dimensional AFM images and the thin foil TEM of these steels showed the coexistence of twinned plates and dislocated lath martensite. Thermodynamic data reported by Morozov et al [21] suggest that this transition in morphology is likely to occur between 232 and 284°C for Fe-C-X systems.

- The surface relief accompanying the formation of martensite at temperature above 300°C in Group 3, indicated high plastic strain accommodation. However, relief deterioration is also possible in the case of this relatively high Ms temperature through thermal smoothing and oxidation.

- The Bowles and Mackenzie model of the PTMT predicts a crystallographic orientation between the martensite and the austenite close to the Kurdjumov-Sachs orientation relationship in the armour steels of Group 1.

For the other two groups the PTMT predicts a larger deviation from the Kurdjumov-Sachs orientation relationship, suggesting the existence of an influence from the relative crystallographic orientation between the martensite and austenite crystals within the plates or laths on the ability that grain boundaries have in resisting spallation and crack propagation by dynamic loading. Indeed, backscattered scanning electron microscopy in Figures 6.2 and 6.3 show big differences between the plates and laths formed within the grains that may have some influence on the microscopic geometric configuration of the grain boundaries. It is well known from the theory of formation and growth of martensite that the growth of plates and laths is arrested at parent austenite grain boundaries. The microscopic configuration of the grain boundaries will then be the result or consequence of the formation history of the martensite inside the grains.

An effective control of the state of the grain boundaries and of the subsequent ballistic performance or of the mechanical properties, depending on the application, may then be achieved by controlling what is happening inside the grains through appropriate design of the chemical composition of the armour steel and by applying the relevant heat treatment.

7.9. Proposed revised specification for advanced performance armour steels

The specifications for the advanced performance plate armour steels may be revised as follows:

- The optimum chemical composition should range between:

Element	**%C**	**%Mn**	**%Si**	**%Mo**	**%Cr**	**%Ni**	**%Cu**	**%P**	**%S**
Range in weight percentage	0.38 - 0.43	0.4 - 2.0	0.4 - 1.2	0.4 - 0.6	0.4 - 1.5	1.0 - 4.5	<0.2	<0.005	<0.005

- The martensite start temperature of the steel should be lower than 210°C;
- The volume fraction of retained austenite in plate martensite should be higher than 1%;
- The heat treatment should consist of austenitisation at temperatures between 850 and 950°C for less than 1 hour, followed by water quenching to room temperature;
- Tempering should be undertaken at temperatures ranging from 150 to 180°C for 20 to 60 minutes when the Silicon content is lower than 0.6%. The tempering temperature may be raised to 300°C when the Silicon content is higher than 1%;
- The design methodology should be based on the YS/UTS ratio which should preferably be below 0.6 as well as on a value of the Ballistic Parameter of 0.018 to 0.060 to predict the ballistic performance;
- Small size and thin armour plates should be preferred to reduce the risk of mechanical resonance of the armour plate with the firing frequency;
- Manganese sulphide and coarse carbides are detrimental to ballistic performance as well as to mechanical properties of the tempered plates; and
- Under these conditions armour steels with a Brinell hardness of 475 BHN and a Charpy impact energy at -40°C as low as 10 Joules, are acceptable.

CHAPTER 8: CONCLUSION

From this experimental and theoretical study, it is concluded that:

- There is a constitutional/morphological dependence of the ballistic performance of martensitic armour steels;
- A high hardness or strength are not accurate indicators for good ballistic performance;
- The lack of correlation between high strength and high ballistic performance may be explained in terms of the effect of retained austenite on the YS/UTS, which determines the resistance to localised yielding;
- The Ballistic Parameter BP which takes into account the volume fraction of retained austenite RA and the thickness of the armour plate, gives a better prediction of the ballistic performance;
- The combination of twinned martensite and nodular retained austenite appears to be favourable to a good ballistic impact resistance;
- Reaustenitisation of the twinned plate martensite in the centre of the impact region absorbs a significant part of the kinetic energy of the fired round;
- Twinned plate interfaces act as barriers for dislocation movement upon ballistic impact. This produces a high hardness in zone 3 of the ballistic affected region;
- Lath martensite with films of RA have poor ballistic resistance;
- Coarse carbides and needlelike manganese sulphide are also detrimental;
- The impact loading induces transient vibration within the steel plates. The mechanical design of the structure should optimise their size to avoid resonance with the frequency of the firing rifle.

Further work

It was observed in this study that the nodular retained austenite in plate interfaces or on grain boundaries is more susceptible to strain induced transformation than RA with a film morphology in lath interfaces. The stabilisation of the austenite upon quenching of the armour steels and the reason why the retained austenite is nodular or film shaped were not analysed in this study. Further investigation on the conditions of formation, the location and the morphology of the retained austenite in the martensitic steel armour plates will be necessary for further improvement of the ballistic performance and reduction of the plate thickness by exploiting the TRIP effect in these steels.
Analyse the following:
Effect of increased Mo, C and Si
Effect of Cobalt
Ballistic limit in terms of %RA and thickness of the plates

REFERENCES

1. ISCOR, Technical notes, 2003

2. SP WOLSKY and AW CZANDERNA, Methods and Phenomena 5, Ballistic Materials and Penetration Mechanics, Elsevier Scientific Publishing Company, 1982

3. von F. Wever, W. Peter; Atlas zur Warmebehandlung der Stahle. Hrsg. Vom Max-Planck-Institut fur Eisenforschung in Zusammenarbeit mit dem Werkstoffausschuss des Vereins Deutscher Eisenhuttenleute; Dusseldorf 1954-1958.

4. Isao Kozasu. Metallurgical Framework of Direct-Quenching of steel; The Minerals, Metals & Materials Society; 1997

5. Jonas A ZUKAS, T NICHOLAS, Halloock F SWIFT, Longin B GRESZCZUK, Donald R CRRAN, Impact Dynamics, John Wiley and Sons editors,1982

6. B. Srivathsa and N Ramakrishnan, Ballistic performance maps for thick metallic armour, International Journal of Impact Engineering, Volume 24, Issue 2, 2000.

7. B. Srivathsa and N Ramakrishnan, A ballistic performance index for thick metallic armour, Computer Simulation Modelling in Engineering, 3(1998), pp. 33-40

8. N Ramakrishnan, Ballistic test procedures for armour materials, Technical Report DMRL, Hyderabad, India, 1986

9. Young-Wong Lee and Tomasz Wierbicki,Fracture prediction of thin plates under localized impulsive loadind. Part II: discing and petalling, International Journal of Impact Engineering, Volume 31, Issue 10, 2005 pp. 1277-1308

10. AG Atkins and YW Mai, Crack and craze nucleation In: elastic and plastic fracture, Ellis Horwood, Chichester (1985), p. 369-431.

11. AK Takuda, K. Mori, N Takakura and K Yamaguchi, Finite element analysis of limit strains in biaxial stretching of sheet metals allowing for ductile fracture, Int J Mech Sci 42 (2000), pp. 785-798

12. T Borvik, M Langseth, OS Hopperstad and KA Malo, Ballistic penetration of steel plates, International Journal of Impact Engineering 22,(1999), pp. 855-886.

13. T Borvik, OS Hopperstad,T Berstad and M Langseth, A computational model of viscoplasticicty and ductile damage for impact and penetration, Eur J Mech A/Solids 20(2001), pp 685-712

14. T Borvik, OS Hopperstad,T Berstad and M Langseth, On the influence of stress triaxiality and strain rate on the behaviour of a structural steel. Part II. Numerical study, Eur J Mech A/Solids 22(2003), pp. 15-32

15. S Dey, T Borvik, OS Hopperstad, JR Leinum and M Langseth, The effect of target strength on the perforation of steel plates using three different projectile nose shapes, Engineering Fracture Mechanics, Volume 70, Issue 18, December 2003, pp. 2543-2558

16. B.I. Hammond and W.G. Proud, Does the pressure-induced alpha-epsilon transition occur for all low-alloy steels, The Royal Society, 2004

17. Yu I Mescheryakov, A K Divakov and N I Zhigacheva, Shock induced structural transitions and dynamic strength of solids, International Journal of Solids and Structures, Volume 41, Issue 9-10, May 2004

18. Z Rosenberg and E Dekel, On the role of material properties in the terminal ballistic of long rods, RAFAEL, Ballistic Center, Haifa, Israel, 2004

19. Fisher JC, Trans. AIME, 1949, 185, 688

20. T.Y. Hsu (Xu Zuyao), J. Mater. Sci. 20, 23 (1985)

21. Yiwen Mou and H.I. Aaronson, The carbon-carbon interaction energy in alpha Fe-C alloys, Acta Metallurgica, Volume 37 No. 3 pp. 737-765, 1989

22. G J. Shiflet, J.R. Bradley and H.I. Aaronson, Metall. Trans. 9A, 999, 1978

23. C. Zener, Trans. Am. Inst. Min. Engrs 203, 619(1955)

24. J Wang, PJ van der WOLK, S van der ZWAAG, Metals Trans JIM: 41 (2000) p. 761

25. Pickering FB, Physical Metallurgy and the Design of Steels, London, Applied Science Publication, 1978

26. M. Tanino, C. . Liu, A. Tsuchiya, and T. Matsuo; Effect of C, N, Mn and Mo on the Ms and Md temperatures in High Purity Fe – 18% Cr – 10% Ni stainless steels; The Minerals, Metals and Materials Society, 1977

27. P Payson and C.H. Savage, Trans. ASM33 (1944), pp. 261-281

28. R.A. Grange and H.M. Stewart, Trans. AIME 167 (1945) pp. 467-494

29. KW Andrews, JISI 203 (1965), pp. 721-727

30. T Sourmail and C. Garcia-Mateo, Critical assessment of models for predicting the M_S temperature of steels, Computational Materials Science, Volume 34, Issue 4, December 2005

31. Hayzelden et al, The martensite transformation in Fe-Ni-C alloys, Acta Metallurgica, Vol. 34, No 2, pp. 233-242, 1986

32. Ueda M, Yasuda H Y, Umakoshi Y, Controlling factor for the nucleation of martensite at grain boundary in Fe-Ni bicrystals, Acta Materialia 51 (2003) 1007-1017

33. Eshelby J, Proc R Soc 1957; A241:376
34. Christian J., Acta Metallurgica 1958; 6:377

35. Borgenstam A and Hillert M, Driving Force for fcc→bcc martensite in Fe-X alloys, Acta Metallurgica, Volume 45, No 5, PP. 2079-2091, 1997.

36. Nishiyama Z, Martensitic Transformation, Materials Science and Technology, Academic Press, New York, 1978

37. Johnsson, CH, Arch Eisen., 1937, 11, 241

38. Zener C, Trans. AIME, 1949, 1167, 550

39. Kaufman L. and Hillert M., in Martensite – A Tribute to Morris Cohen, ed. Oslon and WS OWEN. ASM International, Materials Park, Ohio, 1992

40. Koistinen DP, Marburger RE, Acta Metallurgica 1959; 7; 59

41. Magee CL. The nucleation of martensite. Phase transformations. Metals Park, OH: American Society of Metals; 1970. p. 115

42. Fisher JC, Hollomon JH, Turnbull D, AIME Trans 1949; 185,:69

43. SMC van Bohemen, J Sietsma, MJM Hermans, IM Richardson, Kinetics of the martensitic transformation in low-alloy steel studied by means of acoustic emission, Acta Materialia 51 (2003) 4183-4196

44. Christian, J.W. Martensite, A tribute to Morris Cohen, (G.B Olsen and W.S. Owen. Eds.), ASM International, 1992, p103.

45. Christian, J.W. Theory of Transformations in Metals and Alloys, Pergamon, Oxford, 1965, p.869

46. Kennon, N.F. and Dunne P. Druce· Acta Met., 1982, 30, p.429

47. Xiaoping Lin, Y. Zhang, N. Gu and Z Meng, Crystallographic analysis of {225} martensite in Fe-Cr-C alloy, Hebei University of Technology, Tiajin, China, 2003

48. Tadaki and Shimizu. Scripta Met., 1971, 9, p.771

49. Dunne P. Druce and N.F.Kennon, Materials Science Forum Vols. 189-190(1995) pp.

273-278

50. Morito, H. Tanaka, R. Konishi, T. Furuhara and T. Maki , The morphology and crystallography of lath martensite in Fe-C alloys, Acta Materialia 51 (2003) 1978-1999.

51. George Krauss, Martensite in steel: strength and structure, Materials science and Engineering A 273 – 275 (1999) 40-57

52. J.M. Marder, A.R. Marder, Trans. ASM 62 (1969) 1

53. T. Maki, K. Tsuzaki, I. Tamura, Trans. Iron Steel Inst. Jpn. 20 (1986) 207

54. P.M. Kelly, A. Jostsons, R.G. Blake, Acta Metall. Mater. 38 (1990) 1075

55. Dongyu Liu, Bingzhe Bai, Hongsheng Fang, Wenzheng Zhang, Jailing Gu, Kaidi Chang, Effect of tempering temperature and carbide free bainite on the mechanical characteristics of a high strength low alloy steel, Materials Science and Engineering A, Volume 371, Issues 1-2, 25 April 2004, p. 40-44

56. T. Inoue, S. Matsuda, Y. Okamura, K. Aoki, Trans Jpn Inst. Metals 11 (1970) 36.

57. S. Matsuda, T. Inoue, H. Mimura, Y. Okamura, Trans. Iron Steel Inst. Jpn. 12 (1972) 325

58. G.B. Olson, in: G. Krauss, Deformation, Processing and Structure, ASM, Materials Park, OH, 1984, p. 391

59. Patrick M. Kelly, Martensite Crystallography – the Apparent controversy between the Infinitesimal Deformation Approach and the Phenomenological Theory of Martensitic Transformations; Metallurgical and Materials Transactions A; Volume 34A; September 2003 – 1783

60. R.H. Aborn, Trans. ASM 48 (1950) 51

61. C.S. Roberts, Trans. TMS-AIME 197 (1953) 203

62. L. Chang, S.J. Barnard, G.D.W. Smith, in: G. Krauss, P.E. Repas. Fundamentals of aging and Tempering in Bainitic and Martensitic Steel Products, ISS-AIME, Warrendale, PA, 1992, p. 19

63. G. Krauss and A. R. Marder, Met. Trans., 2, 2243-2257 (1971)

64. J. McMahon and G. Thomas, in Proc. Third Int. Conf. on Strength of Metals and Alloys, The University of Cambridge (UK), 1973, PP. 180-184

65. Daozhi Liu and Druce Dunne.
Interfacial Structure of Twinned Martensite in Shape-Memory Alloys
Materials Science Forum Vols. 394-395 (2002) pp. 201-204
2002 Trans Tech Publications, Switzerland

66. Liu Cheng, N.M. van der Pers, A BöTTGER, Th. H. de Keijser and E.J. Mittemeijer, Lattice Changes of Iron-carbon martensite on aging at Room-Temperature, Delft University of Technology, The Netherlands, 1990

67. L.I. Lyssak and O Andrushchik, Fiz. Metal. Metalloved, 28(1969), 348

68. S. Kajiwara and T. Kikuchi, Acta Metall. Mater. 39(1991) 1123

69. S Uehara, S Kajiwara, and T Kikuchi, Origin of abnormally large tetragonality of Martensite in High Carbon Iron alloys containing Aluminium, Materials Transactions, JIM, Volume 33, No 3, (1992), pp. 220 to 228.

70. M. Bowles and C. M. Wayman, Bain Strain, Lattice Correspondences, and Rotations Related to Martensitic Transformations, Metallurgical Transactions, Volume 3, May 1972

71. N. Gu, X. Song, J. Zhang, F. Yin and R. Wang, Effects of Self-Accommodation and Plastic Accommodation in Martensitic Transformations and morphology of Martensites, Metallurgical and Materials Transactions A, volume 26A, August 1995.

72. STEEL. A Handbook for Materials Research and Engineering. Volume 1: Fundamentals, Verein Deutscher Eisenhuttenleute, Dusseldorf 1992

73. Waldo Sumpf, Lecture notes on Phase transformations in Metals and their Alloys, 2003, University of Pretoria

74. S.D. Antolovich, R.O. Ritchie, W.W. Gerberich, MECHANICAL Properties and Phase Transformations in Engineering Materials, Committees of the Metallurgical Society, TMS Annual Meeting in New Orleans, Louisiana,, 1986
    Article: W.M. Garrison, Jr.; The micromechanisms of Ductile Fracture and the Design of Ultra High Strength Steels

75. Badeshia HKDH. Bainite in steels. London: The Institute of Materials, 2001

76. R.E. Schramm and R.P. Reed, Stacking fault energies of Austenitic Stainless Steels; Metall. Trans. A, 6A(1975), 1345-1351

77. Bhadeshia HKDH. Carbon content of retained austenite in quenched steels. Metal Science 1983; 17 (March): 151-2

78. Woie-Shyan Lee and Tzay-Tian Su, Mechanical properties and microstructural features of AISI 4340 high-strength alloy steel under quenched and tempered conditions, Journal of Materials Processing Technology, Volume 87, Issues 1-3, 15 March 1999, Pages 198-206.

79. P.K. Ray, R.I. Ganguly and A.K. Panda, OPTIMIZATION of Mechanical Properties of an HSLA-100 Steel through control of Heat Treatment variables; Materials Science and Engineering A, Volume 346, Issues 1-2, 15 April 2003, Pages 122-131

80. J. Speer, DK Matlock, BC De Cooman, JG Schorth, Carbon partitioning into austenite after martensite transformation, Acta Materialia 51 (2003) 2611-2622

81. Hillert M, Purdy GR. On the misuse of the term bainite. Scripta Materialia 2000; 43(9); 831-3

82. Kozasu, I., T. Shimizu, K. Tsukada: Trans. Iron Steel Institut Japan 12(1972) S. 305/13

83. Magonon, O.L.; Metallurg. Trans. 7A (1976) S. 1389/400

84. Edwards, R.H., N.F. Kennon: Metallurg. Trans. 9A(1978) S. 1801/09

85. Pietikainen, Considerations about tempered martensite embitterment, Materials Science and Engineering A, 1999, pages 466-470

86. A. Nakashima and J.F. Libsch, Trans. ASM 53 (1961), p. 753]

87. F. Zia-Ebrahimi and G. Krauss. Acta metal. 32 (1984), p. 1767

88. Bimal K. Jha and Nirmalendu S. Mishra, Materials science and engineering A 263 (1999 42-55)

89. R.C. Thomson and M.K. Miller ,Carbide precipitation in martensite during early stages of tempering Cr- and Mo-containing low alloy steels, Acta materialia, Vol 46, pp. 2203-2213, 1998,

90. A.J. McEvily, R.C. Ku, T.L. Johnston, Trans. TMS-AIME 236 (1966) 108

91. R.H. Richman, Trans. TMS-AIME 227 (1963) 159

92. G. Krauss, ISIJ International 35 (1995) 349

93. Gu Baozhu, J.M.B. Losz, G. Krauss, Proceedings ICOMAT, The Japan Institute of Metals, 1986, p. 367

94. Enders A. Robinson, Least squares regression analysis in terms of Linear algebra, Goose Pond Press, Texas, 1981

95. J Speer, D.K. Matlock, B.C. De Cooman, J.G. Schroth; Carbon partitioning into austenite after martensite transformation. Acta Materialia 51 (2003) 2611-2622.

96. Lin Xiaoping, Gu Nanju, Zhang Yong, Meng Zhaowei and Ma Xiaoli, AFM quantitative analysis and determination of shear angle of $\{2\ \ 5\ \ 9\}_f$ martensite surface relief, Progress in Natural Science, March 2002.

97. Yu D.G. et al, Bainite transformation theory, Shangai Jiaotong University Press, 1998

98. Zhang X.M., Gauthier E. and Simon A., Martensite morphology and habit plane transitions during tensile tests for Fe-Ni-C alloys, Acta Metallurgica, Volume 37, N0. 2, 1989.

99. Davies R.G. and Magee C.L., Metallurgical Transactions, 2. 1939 (1971)

100. Kelly PM, Acta Metallurgica; 1965; 13; 635

101. Waldo Stumpf, Lecture notes on Mechanical Metallurgy, 2003, University of Pretoria

102. M.S. Wechsler , D.S. Lieberman and T.A. Read, Trans AIME 197, 1503 (1953)

103. J.S. Bowles and J.K. Mackenzie, Acta Metall. 2, 129, 224 (1954)

APPENDIX 2

A2: Fitting parameters and equations of the mechanical property surfaces

A2.1:Steel F

Table A2.1(a): The fitting parameters for the YS/UTS ratio of steel F, in Equation (4.3)

		Fitting parameters in Equation (4.3)			
Austenitisation temperature	**Normalised austenitisation temperature T**	**a**	**b**	**c**	**Correlation coefficient**
800°C	-1	0.0365	0.0495	0.5224	0.992
850°C	-0.33333	0.0298	0.0477	0.5094	0.979
900°C	0.333333	0.0134	0.0522	0.496	0.975
950°C	1	0.0148	0.0501	0.4786	0.982

Table A2.1(b) The fitting parameters for the YS/UTS ratio of steel F, in Equation (4.4)

	Fitting parameters in (4.4)				**Correlation coefficients**
	A	**B**	**C**	**D**	
a	0.0155	0.0046	-0.0263	0.0211	1
b	-0.0073	-0.0002	0.0076	0.05	1
c	-0.002	-0.0025	-0.0199	0.503	1

Table A2.1(c): Fitting parameters for the ultimate tensile strength of steel F in Equation (4.3)

		Fitting parameters in Equation (4.3)				
Austenitisation temperature	**Normalised austenitisation temperature**	**a**	**b**	**c**	**d**	**Correlation coefficients**
800°C	-1	117.6	-390.52	33.642	2163.8	0.97
850°C	-0.33333	202.71	-452.26	-230.58	2348.8	0.939
900°C	0.333333	122.3	-316.52	-316.87	2365.8	0.996
950°C	1	13.969	-195.43	-74.625	2029	0.978

Table A2.1(d): Fitting parameters for the tensile strength of steel F in Equation (4.4)

	Fitting parameters in Equation (4.4)				**Correlation coefficients**
	A	**B**	**C**	**D**	
a	0	-108.81	-58.695	174.6	0.95
b	0	102.84	108.15	-395.82	0.94
c	0	284.89	-61.664	-305.38	0.99
d	0	-293.51	-58.11	2389.9	0.98

Table A2.1(e): Fitting parameters for the Charpy impact energy of steel F in Equation (4.3)

		Fitting parameters in Equation (4.3)				
Austenitisation temperature	**Normalised austenitisation temperature T**	**a**	**b**	**c**	**d**	**Correlation coefficients**
800°C	-1	-1.6946	2.3901	5.3945	10.33	0.995
850°C	-0.33333	-0.2232	1.2026	2.9669	6.2403	0.9946
900°C	0.333333	0.3044	0.3166	2.3285	8.6423	0.97
950°C	1	0.3809	0.5326	1.4276	7.5503	0.906

Table A2.1(f): Fitting parameters for the Charpy impact energy of steel F in Equation (4.4)

	Fitting parameters in Equation (4.4)				Correlation coefficients
	A	**B**	**C**	**D**	
a	0.2771	-0.7846	0.7606	0.1278	1
b	0.4503	0.7895	-1.379	0.6719	1
c	-1.1541	0.8588	-0.8294	2.5523	1
d	-5.617	1.68682	4.2271	7.2539	

A2. Eq1. Equations for the mechanical properties of steel F

$$\frac{YS}{UTS}=\left(0.0155T_{an}{}^{3}+0.0046T_{an}{}^{2}-0.0263T_{an}+0.0211\right)\times T_{tn}+\left(-0.0073T_{an}{}^{3}-0.0002T_{an}{}^{2}+0.0076T_{an}+0.05\right)\times$$
$$T_{tn}+\left(-0.002T_{an}{}^{3}-0.0025T_{an}{}^{2}-0.0199T_{an}+0.503\right)$$

(A2.Eq1(a))

$$UTS=\left(-108.81T_{an}{}^{2}-58.695T_{an}+174.6T_{an}\right)\times T_{tn}{}^{3}+\left(102.84T_{an}{}^{2}+108.15T_{an}-395.82\right)\times T_{tn}{}^{2}$$
$$+\left(284.86T_{an}{}^{2}-61.664T_{an}-305.38\right)\times T_{tn}+\left(-293.51T_{an}{}^{2}-58.11T_{an}+2389.9\right)$$

(A2. Eq1(b))

$$CIE\left(-40^{0}C\right)=\left(0.2771T_{an}{}^{3}-0.7846T_{an}{}^{2}+0.7606T_{an}+0.1278\right)\times T_{tn}{}^{3}+\left(0.4503T_{an}{}^{3}+0.7895T_{an}{}^{2}-1.379T_{an}+0.6419\right)$$
$$\times T_{tn}+\left(-1.1541T_{an}{}^{3}+0.8588T_{an}{}^{2}-0.8294T_{an}+2.5523\right)\times T_{tn}+\left(-5.617T_{an}{}^{3}+1.68682T_{an}{}^{2}+4.2271T_{an}+7.2539\right)$$

(A2.Eq1©)

A2.2: Steel G

Table A2.2(a): The fitting parameters for the yield to tensile strength ratio of steel G in Equation (4.3)

		Fitting parameters in Equation (4.3)			
Austenitisation temperature	**Normalised austenitisation temperature**	**a**	**b**	**c**	**Correlation coefficients**
800°C	-1	0.0287	0.0442	0.6758	0.99
850°C	-0.33333	0.0273	0.0621	0.6844	0.81
900°C	0.333333	0.0271	0.0592	0.5196	0.9881
950°C	1	0.0069	0.0739	0.5166	0.9249

Table A2.2(b): Fitting parameters for the objective function for Steel G

	Fitting parameters in Equation (4.4)				Correlation coefficients
	A	**B**	**C**	**D**	
a	-0.0119	-0.0106	0.001	0.0284	1
b	0.0216	-0.0018	-0.0067	0.0609	1
c	0.1885	-0.0065	-0.2681	0.6027	1

Table A2.2(c): Fitting parameters for the tensile strength of steel G in Equation (4.3)

Austenitisation temperature	**Normalised austenitisation temperature T**	Fitting parameters in (4.3)				**Correlation coefficients**
		a	**b**	**c**	**d**	
800°C	-1	265.22	-670.08	-92.36	2177.8	0.963
850°C	-0.33333	122.37	-308.53	-261.59	2110.8	0.962
900°C	0.333333	38.471	-166.74	-245.45	2090	0.965
950°C	1	123.55	-289.29	-282.04	2036.6	0.986

Table A2.2(d): Fitting parameters for the tensile strength of steel G in Equation (4.4)

	Fitting parameters in Equation (4.4)				Correlation coefficients
	A	**B**	**C**	**D**	
a	0	128.21	-76.336	66.175	0.98
b	0	-272.31	192.62	-207.38	0.999
c	-133.93	74.61	39.091	-261.81	1
d	-44.325	7.65	-26.275	2099.6	1

Table A2.2(e): Fitting parameters for the Charpy impact energy of the sub-sized specimens of steel G

		Fitting parameters in Equation (4.3)				
Austenitisation temperature	**Normalised austenitisation temperature**	**a**	**b**	**c**	**d**	**Correlation coefficients**
800°C	-1	1.4866	-4.2306	2.6199	18.178	0.9968
850°C	-0.33333	0.1438	-2.0506	3.9178	15.008	0.995
900°C	0.333333	0.7649	-2.7295	3.1999	16.611	0.986
950°C	1	-0.275	-1.0173	3.5676	14.176	0.993

Table A2.2(f): Fitting parameters for the Charpy impact energy of steel G in Equation (4.4)

	Fitting parameters in Equation (4.4)				**Correlation coefficients**
	A	**B**	**C**	**D**	
a	-2.039	0.1704	1.1582	0.4354	1
b	2.95531	-0.2631	-1.3465	-2.3608	1
c	1.7445	-0.5232	-1.2707	3.617	1
d	-4.9562	0.4134	2.9552	15.764	1

A2. Eq2. Equations for the mechanical properties of steel G

$$\frac{YS}{UTS} = \left(-0.0119T_{an}{}^{3} - 0.0106T_{an}{}^{2} + 0.001T_{an} + 0.0284\right)\times T_{tn}{}^{2} + \left(0.0216T_{an}{}^{3} - 0.018T_{an}{}^{2} - 0.0067T_{an} + 0.0609\right)\times$$
$$T_{tn} + \left(0.1885T_{an}{}^{3} - 0.0065T_{an}{}^{2} - 0.2681T_{an} + 0.6027\right) \tag{A2.Eq2(a)}$$

$$UTS = \left(128.21T_{an}{}^{2} - 76.336T_{an} + 66.175\right)\times T_{tn}{}^{3} + \left(-272.31T_{an}{}^{2} + 192.62T_{an} - 207.38\right)\times T_{tn}{}^{2}$$
$$+ \left(-133.93T_{an}{}^{3} + 74.61T_{an}{}^{2} + 39.091T_{an} - 261.81\right)\times T_{tn} + \left(-44.325T_{an}{}^{3} + 7.65T_{an}{}^{2} - 26.275T_{an} + 2099.6\right) \tag{A2.Eq2(b)}$$

$$CIE\left(-40^{0}C\right) = \left(-2.039T_{an}{}^{3} + 0.1704T_{an}{}^{2} + 1.1582T_{an} + 0.4354\right)\times T_{tn}{}^{3} + \left(2.955T_{an}{}^{3} - 0.2631T_{an}{}^{2} - 1.3465T_{an} - 2.3608\right)$$
$$\times T_{tn}{}^{2} + \left(1.7445T_{an}{}^{3} - 0.5232T_{an}{}^{2} - 1.2707T_{an} + 3.617\right)\times T_{tn} + \left(-4.9562T_{an}{}^{3} + 0.4134T_{an}{}^{2} + 2.9552T_{an} + 15.764\right) \tag{A2.Eq2©}$$

A2.3: Steel H

Table A2.3(a): The fitting parameters in Equation (4.3) for the YS/UTS ratio of steel H

		Fitting parameters in Equation (4.3)			Correlation coefficients
Austenitisation temperature	**Normalised austenitisation temperature**	**a**	**b**	**c**	
800°C	-1	0.0224	0.0545	0.4888	0.92
850°C	-0.33333	0.0193	0.058	0.4754	0.95
900°C	0.333333	0.0137	0.0378	0.4662	0.99
950°C	1	0.0129	0.0273	0.4444	0.9833

Table A2.3(b): The fitting parameters in Equation (4.4) for the YS/UTS ratio of steel H

	Fitting parameters in Equation (4.4)				Correlation coefficients
	A	**B**	**C**	**D**	
a	0	0.0013	-0.0051	0.0164	0.96
b	0.0188	-0.0079	-0.0324	0.0488	1
c	0	-0.0047	-0.0214	0.4713	0.99

Table A2.3(c): The fitting parameters for the ultimate tensile strength of steel H in Equation (4.3)

		Fitting parameters in Equation (4.3)				Correlation coefficients
Austenitisation temperature	**Normalised austenitisation temperature**	**a**	**b**	**c**	**d**	
800°C	-1	231.81	-791.9	489.98	1932.8	0.994
850°C	-0.33333	230.63	-704.14	388.36	1864.1	0.996
900°C	0.333333	262.13	-668.63	100.07	2151.2	0.992
950°C	1	166.59	-563.7	286.23	1839.1	0.996

Table A2.3(d): The fitting parameters for the ultimate tensile strength of steel H in Equation (4.4)

	Fitting parameters in Equation (4.4)				Correlation coefficients
	A	**B**	**C**	**D**	
a	-89.842	-53.078	57.232	252.28	1
b	68.439	9.6581	45.661	-687.46	1
c	371.88	161.88	-473.75	226.23	1
d	-537.19	-136.91	490.34	2022.9	1

Table A2.3(e): The fitting parameters of the Charpy impact energy for steel H in Equation (4.3)

		Fitting parameters in (4.3)				
Austenitisation temperature	**Normalised austentisation temperature**	**a**	**b**	**c**	**d**	**Correlation coefficients**
800°C	-1	1.9032	-7.6936	2.2175	19.296	0.988
850°C	-0.33333	2.2313	-5.9804	-0.9373	15.176	0.972
900°C	0.333333	3.3711	-9.3431	-0.2485	18.372	0.9657
950°C	1	0.597	-4.4147	1.8897	13.246	0.926

Table A2.3(f): The surface fitting parameters of the Charpy impact energy for steel H in Equation (4.4)

	Fitting parameters in Equation (4.4)				Correlation coefficients
	A	**B**	**C**	**D**	
a	-2.6581	-1.745	2.005	2.9951	1
b	7.5189	1.8086	-5.8795	-7.8627	1
c	-1.3467	2.9773	1.1828	-0.9237	1
d	-8.7964	-0.5659	5.7714	16.837	1

A2. Eq3. Equations for the mechanical properties of steel H

$$\frac{YS}{UTS} = \left(0.0013T_{an}^{2} - 0.0051T_{an} + 0.0164\right)\times T_{tn}^{2} + \left(0.0188T_{an}^{3} - 0.0079T_{an}^{2} - 0.0324T_{an} + 0.0488\right)\times$$
$$T_{tn} + \left(-0.0047T_{an}^{2} - 0.0214T_{an} + 0.4713\right)$$

(A2.Eq3(a))

$$UTS = \left(-89.842T_{an}^{3} - 53.078T_{an}^{2} + 570232T_{an} + 252.28\right)\times T_{tn}^{3} + \left(68.439T_{an}^{3} + 9.658T_{an}^{2} + 45.661T_{an} - 687.46\right)$$
$$\times T_{an}^{2} + \left(371.88T_{an}^{3} + 161.88T_{an}^{2} - 473.75T_{an} + 226.23\right)\times T_{tn} + \left(-537.19T_{an}^{3} - 136.91T_{an}^{2} + 490.34T_{an} + 2022.9\right)$$

(A2.Eq3(b))

$$CIE\left(-40^{0}C\right) = \left(-2.6581T_{an}^{3} - 1.745T_{an}^{2} + 2.005T_{an} + 2.9951\right)\times T_{tn}^{3} + \left(7.5189T_{an}^{3} + 1.8086T_{an}^{2} - 5.8795T_{an} - 7.8627\right)$$
$$\times T_{an}^{2} + \left(-1.3467T_{an}^{3} + 2.9773T_{an}^{2} + 1.1828T_{an} - 0.9237\right)\times T_{tn} + \left(-8.7964T_{an}^{3} - 0.5659T_{an}^{2} + 5.7714T_{an} + 16.837\right)$$

(A2.Eq3©)

A2.4: Steel I

Table A2.4(a): The fitting parameters for the yield strength to ultimate tensile strength ratio of steel I in Equation (4.3)

		Fitting parameters in Equation (4.3)			
Austenitisation temperature	**Normalised austenitisation temperature**	**a**	**b**	**c**	**Correlation coefficients**
800°C	-1	0.0018	0.069	0.7226	0.96
850°C	-0.33333	0.005	0.1014	0.702	0.96
900°C	0.333333	0.0117	0.0737	0.5473	0.9577
950°C	1	0.0147	0.063	0.5193	0.98

Table A2.4(b): The fitting parameters for the yield strength to ultimate tensile strength ratio of steel I in Equation (4.4)

	Fitting parameters in Equation 4.4				Correlation coefficients
	A	**B**	**C**	**D**	
a	-0.004	-0.0001	0.0105	0.0084	1
b	0.0434	-0.0242	-0.0464	0.0902	1
c	0.1467	-0.0042	-0.2484	0.6251	1

Table A2.4(c): The surface fitting parameters for the tensile strength of steel I in Equation (4.3)

		Fitting parameters in Equation (4.3)				
Austenitisation temperature	**Normalised austenitisation temperature**	**a**	**b**	**c**	**d**	**Correlation coefficients**
800°C	-1	89.705	-159.9	-370.57	1982.3	0.992
850°C	-0.33333	60.44	-135.38	-284.47	1869	0.971
900°C	0.333333	62.015	-127.64	-284.9	1859	0.99
950°C	1	64.553	-226.13	-110.66	1725.3	0.993

Table A2.4(d): The fitting parameters for the tensile strength of steel I in Equation (4.4)

	Fitting parameters in Equation 4.4				Correlation coefficients
	A	**B**	**C**	**D**	
a	-16.806	17.889	4.2298	59.24	1
b	-50.316	-69.193	17.201	-123.82	1
c	146.92	49.579	-16.97	-290.19	1
d	-127.69	-11.475	-0.8125	1865.3	1

Table A2.4(e): Fitting parameters for the Charpy impact energy of steel I in Equation (4.3)

		Fitting parameters in Equation (4.3)				
Austenitisation temperature	**Normalised austenitisation temperature**	**a**	**b**	**c**	**d**	**Correlation coefficients**
800°C	-1	0.3737	-1.0494	0.8835	18.097	0.87
850°C	-0.33333	0.5935	-1.1198	0.519	18.97	0.95
900°C	0.333333	0.5948	-1.1983	0.7491	19.246	0.92
950°C	1	0.5647	-0.9749	0.9475	19.273	0.95

Table A2.4(f): Fitting parameters for the Charpy impact energy of steel I in Equation (4.4)

	Fitting parameters in Equation 4.4				Correlation coefficients
	A	**B**	**C**	**D**	
a	0.1052	-0.1406	-0.0097	0.6098	1
b	0.1744	0.1653	-0.1371	-1.1774	1
c	-0.3523	0.3166	0.3843	0.5989	1
d	0.1958	-0.4759	0.3923	19.161	1

A2. Eq4. Equations for the mechanical properties of steel I

$$\frac{YS}{UTS}=\left(-0.004T_{an}^{\ 3}-0.0001T_{an}^{\ 2}+0.0105T_{an}+0.0084\right)\times T_{tn}^{\ 2}+\left(0.0434T_{an}^{\ 3}-0.0242T_{an}^{\ 2}-0.0464T_{an}+0.0902\right)$$
$$\times T_{tn}+\left(0.1467T_{an}^{\ 3}-0.0042T_{an}^{\ 2}-0.2484T_{an}+0.6251\right)$$

(A2.Eq4(a))

$$UTS=\left(-16.806T_{an}^{\ 3}+17.889T_{an}^{\ 2}+4.2298T_{an}+59.24\right)\times T_{tn}^{\ 3}+\left(-50.316T_{an}^{\ 3}-69.193T_{an}^{\ 2}+17.201T_{an}-123.82\right)$$
$$\times T_{tn}^{\ 2}+\left(14.92T_{an}^{\ 3}+49.579T_{an}^{\ 2}-16.97T_{an}-290.19\right)\times T_{tn}+\left(-127.69T_{an}^{\ 3}-11.475T_{an}^{\ 2}-0.8125T_{an}+1865.3\right)$$

(A2.Eq4(b))

$$CIE\left(-40^{0}C\right)=\left(0.1052T_{an}^{\ 3}-0.1406T_{an}^{\ 2}-0.0097T_{an}+0.6098\right)\times T_{tn}^{\ 3}+\left(0.1744T_{an}^{\ 3}+0.1653T_{an}^{\ 2}-0.1371T_{an}-1.1774\right)$$
$$\times T_{tn}^{\ 2}+\left(-0.3523T_{an}^{\ 3}+0.3166T_{an}^{\ 2}+0.3843T_{an}+0.5989\right)\times T_{tn}+\left(0.1958T_{an}^{\ 3}-0.4759T_{an}^{\ 2}+0.3923T_{an}+19.161\right)$$

(A2.Eq4©)

APPENDIX A6.2:

Geometric characteristics of the steel E measured by means of Atomic Force Microscopy

Line 4								
dx	39.1997	79.168	33.8193	11.5293		109.1442	29.2076	58.4152
dy	9.259	-7.058	8.343	-0.06741		-10.5198	7.2356	-5.4776
Inclination(Degrees)	13.29647	-5.09716	13.86483	-0.33517		-5.50821	13.92083	-5.35968
Width	40.27835	79.482	34.83318	11.5295		109.65	30.09049	58.67146
Slope (nm/deg)	3.029251	-15.5934	2.512342	-34.3994		-19.9067	2.161545	-10.9468
TB/(TB+TA)		**0.69**				**0.78**		
Line 5								
dx	32.98	80.6177	40.3089	115.4299		29.3155	102.6044	
dy	9.4593	-6.142	9.3723	-10.5284		5.9052	-9.158	
Inclination(Degrees)	16.01203	-4.35897	13.09602	-5.21419		11.39481	-5.10303	
Width	34.30975	80.85133	41.38414	115.9091		29.90435	103.0123	
Slope(nm/deg)	2.142748	-18.5483	3.160055	-22.2295		2.624384	-20.1865	
TB/(TB+TA)		**0.66**			**0.79**			
Line 6								
dx	29.6402	67.3642	15.2692	26.0475		126.6447	27.8439	142.8121
dy	6.6714	-4.1958	0.019344	8.0066		-8.614	6.9449	-13.2485
Inclination(Degrees)	**12.69115**	**-3.56589**	**0.072623**	**17.09529**		**-3.89307**	**14.01221**	**-5.30278**
Width	30.38172	67.49474	15.26921	27.25028		**126.9373**	28.69694	**143.4253**
Slope(nm/deg)	2.39393	-18.9279	210.2539	1.594023		-32.606	2.047995	-27.0472
TB/(TB+TA)		**0.61**			**0.74**			
Line 7								
dx	36.6428	75.1648	33.8241	124.9614		27.2472	147.5109	
dy	7.9903	-4.7493	7.9828	-8.4291		6.9117	-13.1597	
Inclination(Degrees)	**12.30755**	**-3.61727**	**13.28607**	**-3.86092**		**14.24101**	**-5.10054**	
Width	37.50386	75.31469	34.75334	125.2454		28.11017	148.0967	
Slope(nm/deg)	**3.047224**	**-20.8209**	**2.615772**	**-32.4393**		**1.973889**	**-29.0355**	
TB/(TB+TA)		**0.68**			**0.81**			
Line 8								
dx	32.071	69.153	13.0288		34.0754	116.2573	32.071	
dy	9.8142	-7.1363	0.48034		9.4498	-11.4269	7.3269	
Inclination(Degrees)	**17.02352**	**-5.89482**	**2.11247**		**15.50764**	**-5.6164**	**12.87539**	
Width	33.53905	**69.52024**	13.03765		35.36144	**116.8175**	32.8973	
Slope(nm/deg)	1.97016	-11.7935	6.171757		2.28026	-20.7993	2.555052	
TB/(TB+TA)		**0.60**			**0.77**			